Spectroscopic Studies of Small Molecule Adsorption and Oxidation on TiO_2-Supported Coinage Metals and Zr_6-based Metal-Organic Frameworks

Darren M. Driscoll

Dissertation submitted to the faculty of the Virginia Polytechnic Institute and State University in partial fulfillment of the requirements for the degree of

Doctor of Philosophy

In

Chemistry

John R. Morris, Chair

Brian Tissue

Diego Troya

Gordon Yee

March 21, 2019

Blacksburg, Virginia

Keywords: surface chemistry, infrared spectroscopy, heterogeneous catalysis, propene epoxidation, chemical warfare agent decomposition

Copyright © 2019, Darren M. Driscoll

Spectroscopic Studies of Small Molecule Adsorption and Oxidation on TiO_2-Supported Coinage Metals and Zr_6-based Metal-Organic Frameworks

Darren M. Driscoll

Abstract

Developing a fundamental understanding of the interactions between catalytic surfaces and adsorbed molecules is imperative to the rational design of new materials for catalytic, sorption and gas separation applications. Experiments that probed the chemistry at the gas-surface interface were employed through the utilization of *in situ* infrared spectroscopic measurements in high vacuum conditions to allow for detailed and systematic investigations into adsorption and reactive processes. Specifically, the mechanistic details of propene epoxidation on the surface of nanoparticulate Au supported on TiO_2 and dimethyl chlorophosphate (DMCP) decomposition on the surface of TiO_2 aerogel-supported Cu nanoparticles were investigated. *In situ* infrared spectroscopy illustrates that TiO_2-supported Au nanoparticles exhibit the unprecedented ability to produce the industrially relevant commodity chemical, propene oxide, through the unique adsorption configuration of propene on the surface of Au and a hydroperoxide intermediate (-OOH) in the presence of gaseous hydrogen and oxygen. Whereas, TiO_2-supported Cu aerogels oxidize the organophosphate-based simulant, DMCP, into adsorbed CO at ambient environments. Through a variety of spectroscopic methods, each step in these oxidative pathways was investigated, including: adsorption, oxidation and reactivation of the supported-nanoparticle systems to develop full mechanistic pictures. Additionally, the perturbation of vibrational character of the probe molecule, CO, was employed to characterize the intrinsic μ_3-hydroxyls and molecular-level defects associated with the metal-organic framework (MOF), UiO-66. The adsorption of CO onto heterogeneous surfaces effectively characterizes surfaces because the C-O bond vibrates differently depending on the nature of the surface site. Therefore, CO adsorption was used within the high vacuum environment to identify atomic-level characteristics that traditional methods of analysis cannot distinguish.

Spectroscopic Studies of Small Molecule Adsorption and Oxidation on TiO_2-Supported Coinage Metals and Zr_6-based Metal-Organic Frameworks

Darren M. Driscoll

General Audience Abstract

The interaction between small gas molecules and solid surfaces is important for environmental, industrial and military applications. In order to chemically change molecules, surfaces act to lower activation barriers and provide a low energy plane to create new chemical bonds. To study the fundamental interactions that occur between gas molecules and surfaces, we employ infrared spectroscopy in order to probe the vibrations of bonds at the gas–surface interface. By tracking the chemical bonds that break and form on the surface of different materials, we can develop surface reaction pathways for a variety of different chemical reactions. We focus our efforts on two different applications: the conversion of propene to propene oxide for industrial applications and the decomposition of chemical warfare agents. Using the techniques described above, we were able to develop reaction pathways for both propene oxidation and chemical warfare agent simulant degradation. Our work is critical to the further development of catalysts that harness the specific structural and chemical properties we identify as important and exploit them for further use.

Acknowledgements

My time at Virginia Tech was quite enjoyable. My scientific intellect grew immensely during my time here but specifically, I enjoyed the daily challenges of scientific questions that needed to be solved. Leaving Virginia Tech, I feel confident as a chemist and thank those faculty members who were instrumental in the skills I developed.

I would like to thank my fiancée, Nicolletta. Without her encouragement throughout this entire process I would not be here today. Having a helpful family of dogs and cats back at my apartment was not only stress relieving but also a great way to take a break from science (just a little break of course). My advisor, John Morris, was critical in my progression as a PhD student as he taught me the importance of 1) reading that literature EVERYDAY and 2) sometimes taking a step back to think. Also, the John Morris handshake is legendary. I would also like to thank Mitko, who was so helpful in my early time as a PhD student. Still today when going through an experiment with an unexpected result, I think, “what would Mitko do right now?” and almost always I end up adding some CO to probe those surface sites.

I like to thank my other PhD students in the Morris group for helping, preparing and working with me during my years here. Specifically, Tyler and Conor who were great friends but also great scientific minds to bounce ideas off of. I spent countless hours arguing with Tyler from topics ranging from hydrogen bonding to organophosphate reaction and I think those “heated” discussions were quite helpful in our scientific development. I finally would like to thank my family for their countless help and support throughout my years of graduate school.

Table of Contents

Attributions

Portions of the work in Chapter 3 of this dissertation has been published previously in the journal of *Surface Science* and the *Journal of Physical Chemistry C*, with the following references:
Panayotov, D.; McEntee, M.; Burrows, S.; Driscoll, D.; Tang, W.; Neurock, M.; Morris, J., Infrared Studies of Propene and Propene Oxide Adsorption on Nanoparticulate Au/TiO_2. *Surface Science* **2016**, *652*, 172-182 and Driscoll, D. M.; Tang, W.; Burrows, S. P.; Panayotov, D. A.; Neurock, M.; McEntee, M.; Morris, J. R., Binding Sites, Geometry, and Energetics of Propene at Nanoparticulate Au/TiO_2. *Journal of Physical Chemistry C* **2017**, *121*, 1683-1689.

In these multi-author works, Darren Driscoll preformed the majority of vacuum-based experiments with guidance from D. Panayotov and also contributed to the construction of the manuscript. S. Burrows was instrumental in the initial propene studies as well as the implementation of vacuum components used during experimentation. M. Neurock and W. Tang performed the density functional theory calculations provided in Figure 3.2. M. McEntee was crucial in the construction of portions of the manuscripts as well.

Chapter 4 of this dissertation has been taken from a manuscript in preparation for submission with the following author reference:
Panayotov, D. A.; Driscoll, D. M.; Tang, W.; Burrows, S. P.; Neurock, M.; McEntee, M.; Morris, J.R.

In this multi author manuscript, Darren Driscoll performed the majority of vacuum-based experiments under the guidance of D. Panayotov and also contributed to the construction of the manuscript. S. Burrows was instrumental in the implementation of the vacuum chamber components. M. Neurock and W. Tang performed the entirety of the density function theory calculations provided in Figure 4.9 and 4.10. M. McEntee was crucial in the construction of portions of the manuscript.

Portions of the work in Chapter 7 of this dissertation has been previously published in the *Journal of Physical Chemistry C* and the journal *Physical Chemistry Chemical Physics*, with the following references:
Driscoll, D. M.; Troya, D.; Usov, P. M.; Maynes, A. J.; Morris, A. J.; Morris, J. R., Characterization of Undercoordinated Zr Defect Sites in UiO-66 with Vibrational Spectroscopy of Adsorbed CO. *Journal of Physical Chemistry C* **2018**, *122*, 14582-14589 and Driscoll, D. M.; Troya, D.; Usov, P. M.; Maynes, A. J.; Morris, A. J.; Morris, J. R., Geometry and Energetics of CO Adsorption on Hydroxylated UiO-66. *Physical Chemistry Chemical Physics* **2019**, *21*, 5078-5085.

In these multi-author works, Darren Driscoll performed the entirety of the vacuum-based experiments described in the two published works with the help of A. Maynes. P. Usov provided the metal-organic frameworks used in the experimental sections of the work. D. Troya performed the density functional theory calculations shown in Figure 7.5 and contributed to the construction of both manuscripts.

Publications

Grissom, T. G.; Driscoll, D. M.; Sapienza, N. S.; Troya, D.; Usov, P. M.; Morris, A. J.; Morris, J. R., Molecular-Level Insight into CO_2 Adsorption on the Zirconium-Based Metal-Organic Framework, UiO-66: A Combined Spectroscopic and Computational Approach. *Journal of Physical Chemistry C*. Submitted

Lu, Y.; Kuo, C.; Kovarik, L.; Hoffman, A.; Boubnov, A.; Driscoll, D.; Morris, J.; Bare, S.; Karim, A., A Versatile Approach for Quantification of Surface Site Fractions using Reaction Kinetics: The Case of CO Oxidation on Supported Ir Single Atoms and Nanoparticles. *Journal of the American Chemical Society*. Submitted

Desario, P. A; Pitman, C. L.; Delia, D. J.; Driscoll, D. M.; Maynes, A. J.; Morris, J. R.; Pennington, A. M.; Brintlinger, T. H.; Rolison, D. R.; Pietron, J. J., Low-Temperature CO Oxidation at Persistent Low-Valent Cu Nanoparticles on TiO_2 Aerogels. *Applied Catalysis B.* **2019** https://doi.org/10.1016/j.apcatb.2019.03.073

Driscoll, D. M.; Troya, D.; Usov, P. M.; Maynes, A. J.; Morris, A. J.; Morris, J. R., Geometry and Energetics of CO Adsorption on Hydroxylated UiO-66. *Physical Chemistry Chemical Physics* **2019**, *21*, 5078-5085.

Driscoll, D. M.; Troya, D.; Usov, P. M.; Maynes, A. J.; Morris, A. J.; Morris, J. R., Characterization of Undercoordinated Zr Defect Sites in UiO-66 with Vibrational Spectroscopy of Adsorbed CO. *Journal of Physical Chemistry C* **2018**, *122*, 14582-14589.

Kaledin, A.; Driscoll, D. M.; Troya, D.; Collins-Wildman, D.; Hill, C.; Morris, J.; Musaev, D., Impact of Ambient Gases on the Mechanism of the [Cs8Nb6O19]-Catalyzed Nerve-Agent Decomposition. *Chemical Science* **2018**, 9, 2147-2158.

Driscoll, D. M.; Tang, W.; Burrows, S. P.; Panayotov, D. A.; Neurock, M.; McEntee, M.; Morris, J. R., Binding Sites, Geometry, and Energetics of Propene at Nanoparticulate Au/TiO_2. *Journal of Physical Chemistry C* **2017**, *121*, 1683-1689.

Panayotov, D.; McEntee, M.; Burrows, S.; Driscoll, D.; Tang, W.; Neurock, M.; Morris, J., Infrared Studies of Propene and Propene Oxide Adsorption on Nanoparticulate Au/TiO_2. *Surface Science* **2016**, *652*, 172-182**.**

Chapter 1

Introduction

Thesis Statement

In situ infrared spectroscopy interrogated the gas-surface adsorption and reaction processes that occur between small molecules and solid-phase catalytic surfaces. Overall, these studies provided the fundamental understanding of gas-surface interactions necessary to develop new strategies for the synthesis and application of the next generation of catalytic materials.

1.1 Motivation

The overall motivation for the scientific work presented within this thesis is to provide a fundamental understanding of the atomic-level processes involved in small molecule adsorption and reaction on surfaces in order to develop new synthetic strategies for catalytic materials. Heterogeneous catalysis, where a chemical reaction is promoted with the aid of a solid catalyst, requires surface atoms to adsorb and react with incoming reactant molecules.[1] Surface atoms are in fact very different chemically and electronically compared to bulk atoms. These surface atoms often promote substantial chemical reactivity because of the high chemical potential these low-coordinated atoms exhibit.[2-3] While many researchers synthetize nanomaterials (with a high concentration of surface atoms relative to bulk atoms) and study the catalytic properties of these nanomaterials, I focus on the fundamental processes that answer the question of why specific materials exhibit fascinating catalytic behavior. The studies presented herein utilize experimental techniques that observe the chemical processes as they occur.

1.2 Supported Nanomaterials Used for Heterogeneous Catalysis

1.2.1 Why Gold?

In the bulk form, gold is considered to be "the noblest of all the metals."[4] The inability of bulk gold to form chemical bonds at the gas or liquid–surface interface can be explained by the so-called "*d* band model", which attributes weak Au–adsorbate interactions to: a filled *d* band that resides below the Fermi energy level (E_f) of Au and weak coupling of the 5d states to the adsorbate molecule.[4] As an adsorbate molecule approaches a surface, the adsorbate energy level broadens due to mixing with a near-infinite sea of electrons, which decreases the lifetime of the discrete state.[5] Upon interaction with the *d* electrons, the adsorbate orbitals split into a bonding orbital and an antibonding orbital (Figure 1.1).[6] In contrast to Pt, the *d* band of Au is completely filled and overlaps energetically with the newly formed antibonding orbital to produce repulsive interactions.[7] In contrast to Au, Cu (which also has a filled *d* band) couples much more strongly to adsorbates through its 3*d* band. For a further, more quantitative discussion of periodic trends in adsorbate–metal coupling, see the work of Hammer and Norskov.[4,8] Below, the focus turns to chemistry that is activated, not on bulk gold, but within nanoparticulate systems.

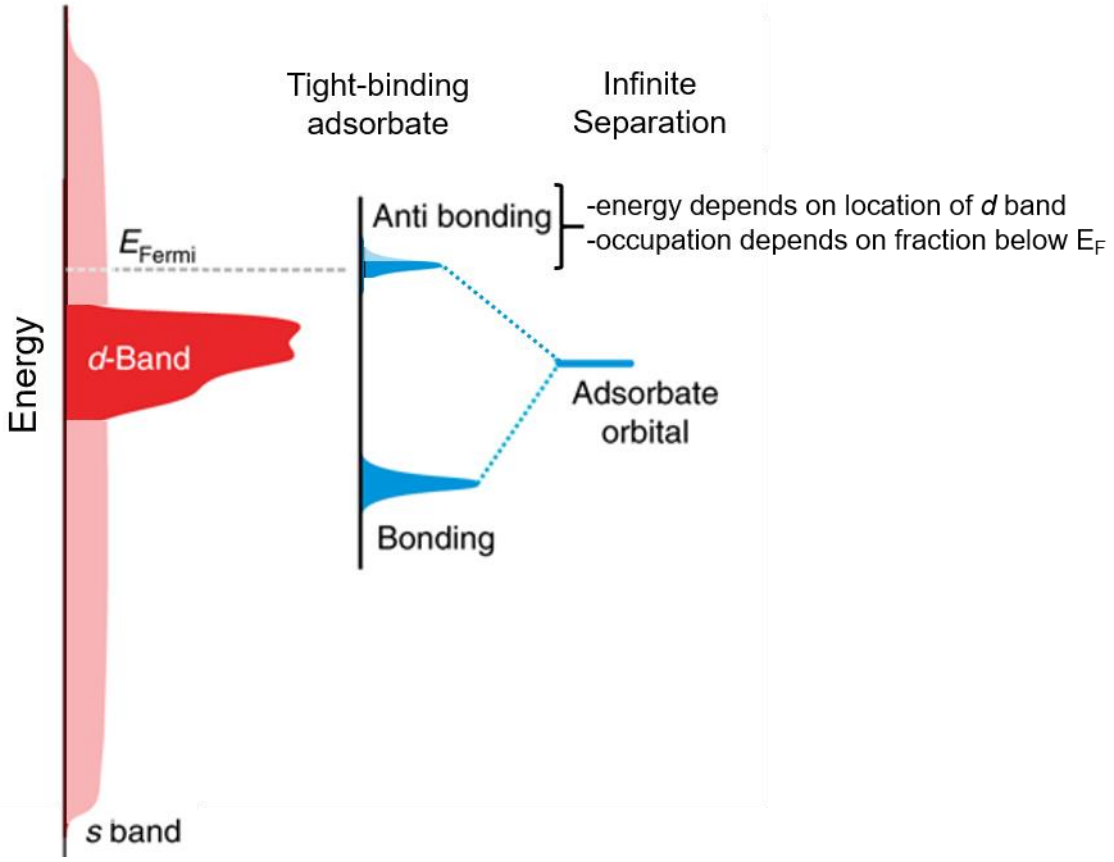

Figure 1.1. Schematic of the density of states (DOS) between an adsorbate interacting with a metal *s* band and a metal *d* band of a late transition metal. Adapted by permission from Springer Nature: Greiner et al. Free-atom-like *d* states in single-atom alloy catalyst, *Nature Chemistry* 2018, 10, 1008-1015. Copyright 2018.

Although bulk Au is unreactive, Au nanoparticles exhibit remarkable catalytic properties unforeseen from bulk Au chemistry.[9-12] Two separate theories help to elucidate the reasons behind this phenomenon. First, the gold nanoparticle's catalytic activity increases as the curvature, surface area and surface tension of the Au particle increase and as the diameter of the Au nanoparticle decreases. Haruata et al. first showed this remarkable experimental observation in the oxidation of CO into CO_2 while varying the diameter of the gold nanoparticle on a variety of metal oxide surfaces.[10-11] Another proposed theory behind the heightened reactivity of supported-gold

nanoparticles relates to the concept that as the coordination of a site changes (as occurs for nanoparticles) the *d* band center rises and promotes adsorption processes as shown in Figure 1.2.[13-15] Therefore, upon bond formation between an adsorbate and the metal surface, the antibonding orbitals of the metal-adsorbate complex would lie above E_F and not be entirely filled—unlike the case of bulk gold. These two theories help to explain the unprecedented activity of Au nanoparticles compared to bulk Au. The early scientific discoveries on nanoparticle-based Au compounds have opened the door for thousands of researchers to identify unique nanomaterials (including Au, Cu, Ag, Pt, Ir, etc.) that exhibit promising catalytic activity for a variety of environmental and industrial purposes.[16-20]

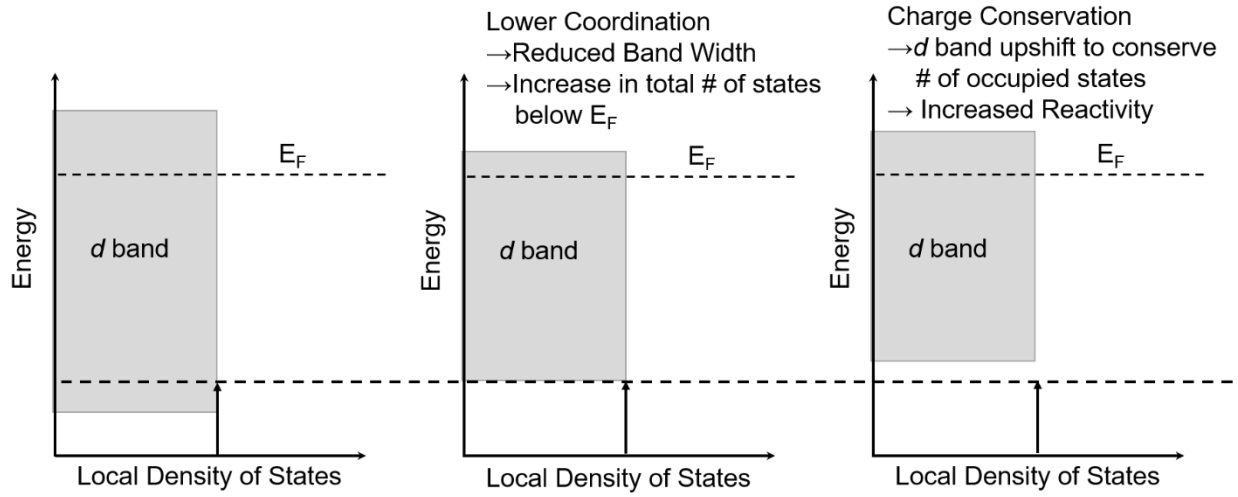

Figure 1.2. Representative energy diagrams of the *d* band for a late transition metal as a result of lower coordination. Lower coordination results in a reduced band width and the *d* band shifts upwards as a result of charge conservation.

1.2.2 General Catalyst Structure

Traditional solid catalysts used for heterogeneous catalysis incorporate an active species onto a high surface area support.[21] The support material, like silica or titania, provides an anchor

for the active portion (Au, Pt, Pd, Cu, etc…) of the catalyst to be exposed to reactants.[10,22-27] The support can also have a significant impact on the type of chemistry that occurs on the surface of these materials. Strong metal-support interactions (SMSI) significantly affect the electronic structure of the metal, which affects binding and reactivity.[15-16,26,28-29] These findings have led researchers to develop materials, such as aerogel-supported metal nanoparticles (shown in Figure 1.3) that increase the number of contact points between the metal particle and support.[30-32]

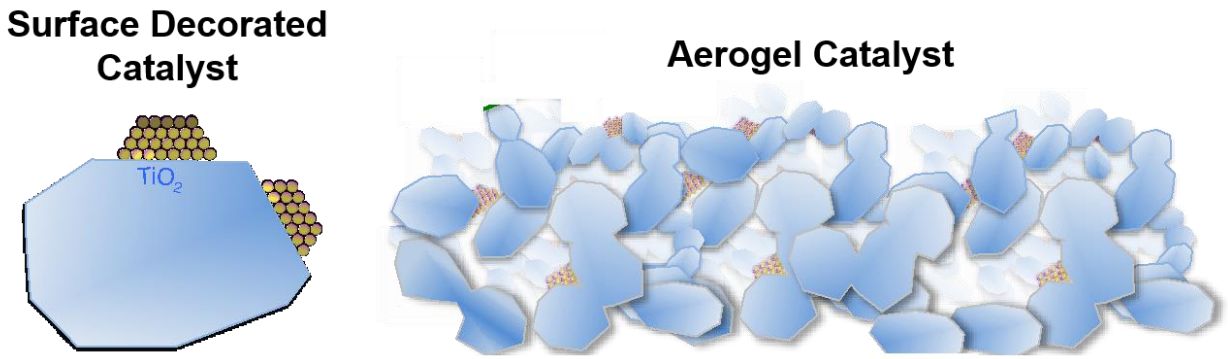

Figure 1.3. Cartoon representation of a surface decorated Au/TiO_2 catalyst with only a single Au-Ti contact plane and the 3-dimensional aerogel supported Au/TiO_2 catalyst with multiple Au-Ti contact planes.

Titanium dioxide (TiO_2) surfaces, and other reducible oxide supports, are particularly attractive as support materials.[12,33-34] The metal-oxygen bonds of reducible supports are lower in energy and have the tendency to cleave and further reduce the support. This reducing behavior of certain metal oxide supports allows for strong chemical interactions between the support and small nanoparticle materials, like gold.[34] Two main structures of TiO_2, anatase and rutile (shown in Figure 1.4), are important to both the catalysis and the surface science communities because of their economic value and their stability under a wide range of thermal and chemical environments.[33] Both of these crystal structures contain a single Ti atom surrounded by six oxygen

atoms in a octahedral configuration. Oxygen vacancies, known to occur due to the weak Ti-O bond strength, have been computationally shown to promote nanoparticle adhesion onto the support materials.[35]

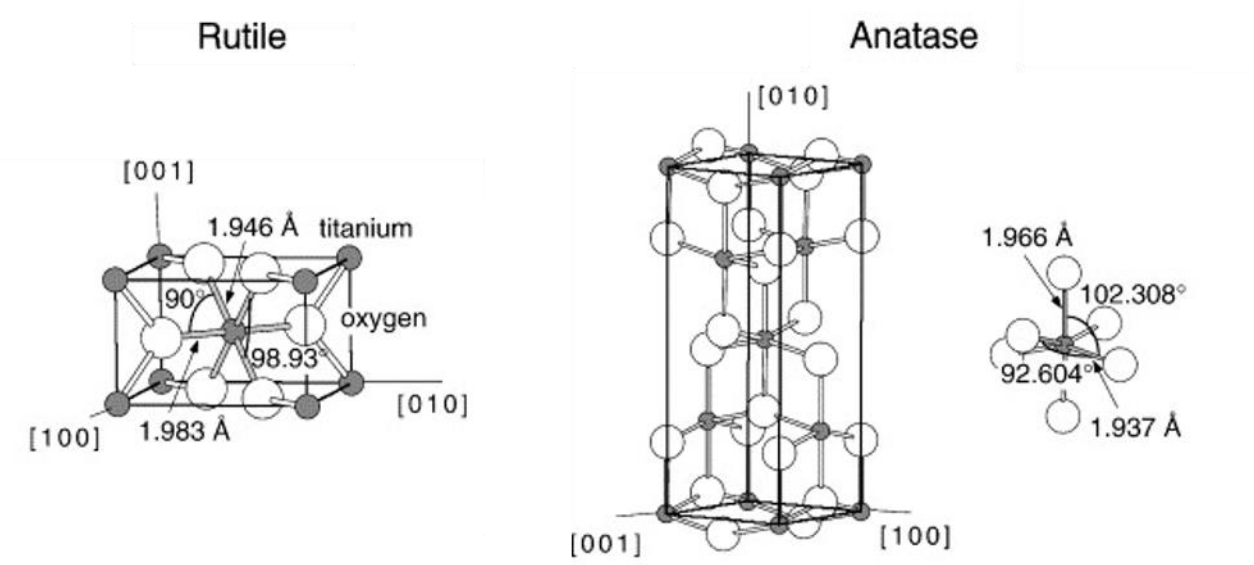

Figure 1.4. Unit cell structures of rutile and anatase TiO_2. Adapted from *Surface Science Reports*, 87, Ulrike Diebold, The surface science of titanium dioxide, 53-229, 2003 with permission from Elservier.[33]

One specific synthetic method to deposit Au nanoparticles onto a TiO_2 support is the deposition-precipitation method.[11,36] In this method, a metal precursor is added to an aqueous suspension of TiO_2. By gradually adding hydroxide ions, the Au is deposited as a gold hydroxide and anchored to the TiO_2 precipitating from the solution.[36] The support acts as a nucleating agent during the reaction. This method allows for Au nanoparticles of roughly 3 nm is size to be anchored to a TiO_2 support. It is important to note that the Au must be calcined in elevated temperatures to drive off the hydroxide layer and expose metallic Au atoms.[37-40] These synthetic steps provide a

nanoparticle Au surface bound to a TiO_2 support and can be applied to similar nanoparticle systems such as Cu/TiO_2.[32]

1.2.3 A New Generation of Catalysts: Metal-Organic Frameworks

More recently, metal-organic frameworks (MOFs) have been identified as materials for heterogeneous catalysis. These materials consist of a metal cluster bound to multiple organic linkers to form a 3-dimensional porous, high surface area nanostructure.[41] MOF's tunability includes the chemical composition of metal or metal node and the organic linker. These changes result in a vast array of different structures based on a size, electronic structure and active surface sites and will be further discussed in a later section.[42-44]

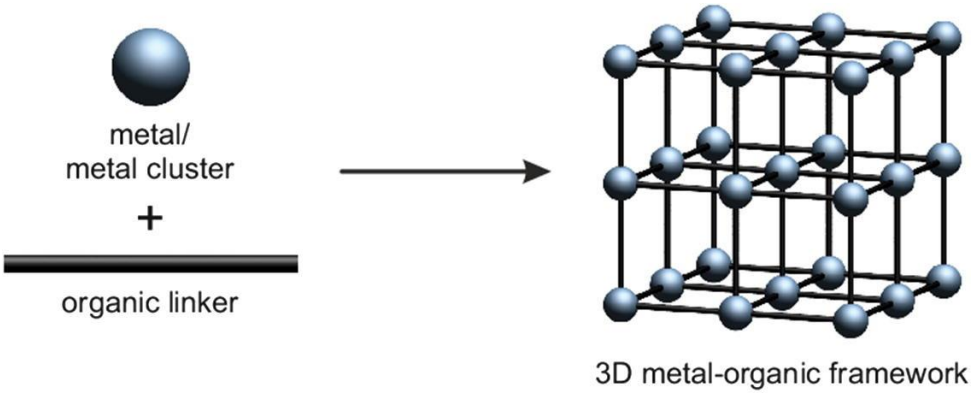

Figure 1.5. Cartoon representation of a metal-organic framework. Reprinted from *Coordination Chemistry Reviews*, 349, Ren, J. et al., Structural defects in metal–organic frameworks (MOFs): Formation, detection and control towards practices of interests, 169-197, 2017 with permission from Elsevier.[41]

1.2.4 Fundamental Studies of Adsorption onto Catalytic Materials

Both traditional supported-metal catalysts (like TiO_2-support Au and Cu nanoparticles) and metal-organic frameworks have been experimentally and theoretically shown to convert a gas or a liquid phase compound into a desired product. In order to develop the next generation of materials

with desired functionality, a fundamental understanding of the adsorption and reactive processes that occur during these heterogeneous reaction events is needed. Therefore, through the entirety of this thesis, I will focus research efforts on materials used for two main applications: the production of propene oxide, an industrially relevant commodity chemical and the detoxification of the vapor phase nerve-inhibiting chemical warfare agents know as G-series nerve agents. Many similarities between these two vastly different fields revolve around the type of materials used to catalytically convert propene and organophosphorus-based compounds into the desired products.

1.3 Propene Epoxidation

Propene oxide (PO) is a commodity chemical within the chemical industry. The major industrial importance of propene oxide is for use in the production of polyether polyols, propene glycol and propene glycol ethers for the downstream production of polyurethane, polyesters, and use as a solvent, respectively.[45-46] For the past sixty years, there have been two major global industrial-level production methods: the chlorohydrin process and the hydroperoxide process. However, both of these processes have significant environmental and economical drawbacks. The chlorohydrin process is environmentally unfriendly due to the production of chlorinated byproducts—produced as a result of the propene chlorohydrin intermediate required during the synthesis.[47] Additionally, the dehydrochlorination reaction step to produce propene oxide results in significant $CaCl_2$ production. Brine, produced at 40 times more than propene oxide, has no commercial value and thus creates a disposal problem.[46] On the other hand, the hydroperoxide method avoids the environmental issues of the chlorohydrin process. Yet, this method suffers from economic drawbacks. The hydroperoxide method requires the production of ethylbenzene hydroperoxide, which is then sent to a second reactor to produce propene oxide and a coproduct alcohol as shown in equation (1.1)

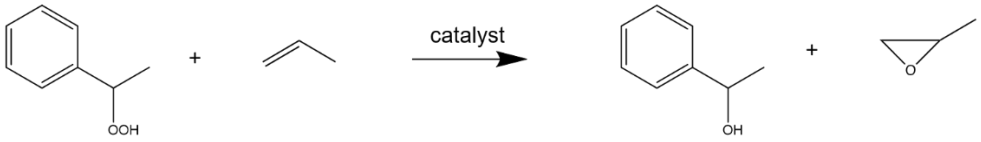

(1.1)

Traditionally, a homogenous tungsten, molybdenum, or vanadium complex is incorporated into the reaction as the catalyst and is thus expensive to separate.[46-47] The aromatic-containing alcohol is then converted to styrene for commercial uses. The overall success of this method is fixed to the commercial price of both styrene and propene oxide. For these reasons, the propene oxide industry desires catalytic materials that would directly convert propene to propene oxide.

Recently, the scientific community has focused significant efforts on developing new supported catalysts for alternative routes to PO production. These alternative routes to PO production utilize the direct-gas phase conversion of propene into propene oxide over a solid catalyst. In these catalytic systems, the selective production of propene oxide, instead of oxidized by-products such as acrolein, acetone and propanal (shown in Figure 1.6), is crucial to the success of the catalytic material in industrial-level applications.[48]

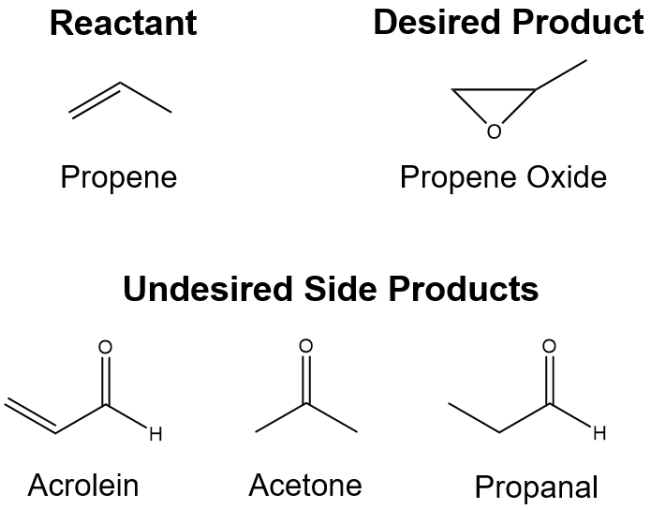

Figure 1.6. Chemical structures of propene, propene oxide and common by-products of propene oxidation over heterogeneous catalysts.

For example, researchers have found that moderate selectivity and nearly 1% conversion of propene in oxygen to PO could be achieved over a Au/SiO_2 catalyst at 600 K (Reaction 1.2): [49]

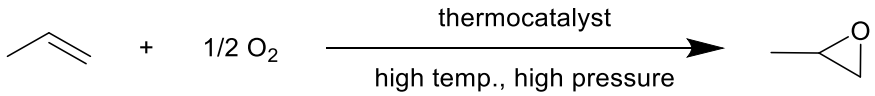

(1.2)

This direct conversion reaction is ideal in many respects; however, the high temperatures and low conversion rate lead to poor chemical and energetic efficiencies. In contrast, alternate approaches that require a feedstock of propene, hydrogen, and oxygen have been shown to provide significantly higher conversions as the reaction closely resembles the hydroperoxide industrial method without any coproduct requirement (such as styrene mentioned above) as shown in Reaction 1.3 [50-51]

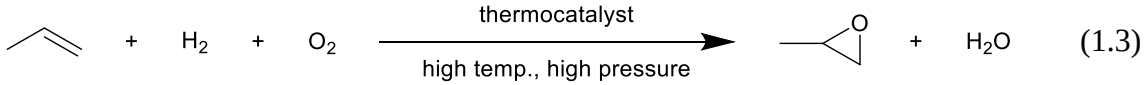

(1.3)

For example, scientists recently reported the vapor-phase epoxidation of propene over a titania-supported Au (Au/TiO_2) nanocatalyst.[50-54] For the Au/TiO_2 catalysts, the proposed mechanism requires the formation of a hydrogen-peroxy (-OOH) intermediate to selectively oxidize propene into propene oxide.[52,55-56] While many researchers have identified Au/TiO_2 materials as active in the conversion of propene into propene oxide, few studies have identified the unique adsorption and reactive properties that these supported metal nanostructures demonstration.

1.4 CWA Detoxification

Chemical warfare agents continue to harm individuals and communities across the globe. Since the development of CWAs during World War I, scientists have been tasked to develop the necessary countermeasures to mitigate any potential harm. Specifically, materials that can

sequester, decontaminate, and catalytically produce benign gas phase products are of particular interest to military personnel.

One specific class of CWAs is the G-series nerve agents. These chemical compounds, shown in the top line of Figure 1.7, are potent acetylcholinesterase inhibitors. The G-series' biological toxicity originates from the organophosphonate structure (RO(O=P(R')OR'') which irreversibly binds to the serine moiety of the acetylcholinesterase protein.[57] Once the chemical warfare agent is bound to the protein, acetylcholine is unable to react to produce choline and thus a buildup of acetylcholine within the post-synaptic membrane occurs. As the post-synaptic membrane continues to build-up with acetylcholine, the constant firing of electrical signals occurs. These electrical impulses can continue to fire and can cause symptoms ranging from uncontrolled twitching to convulsions and death.

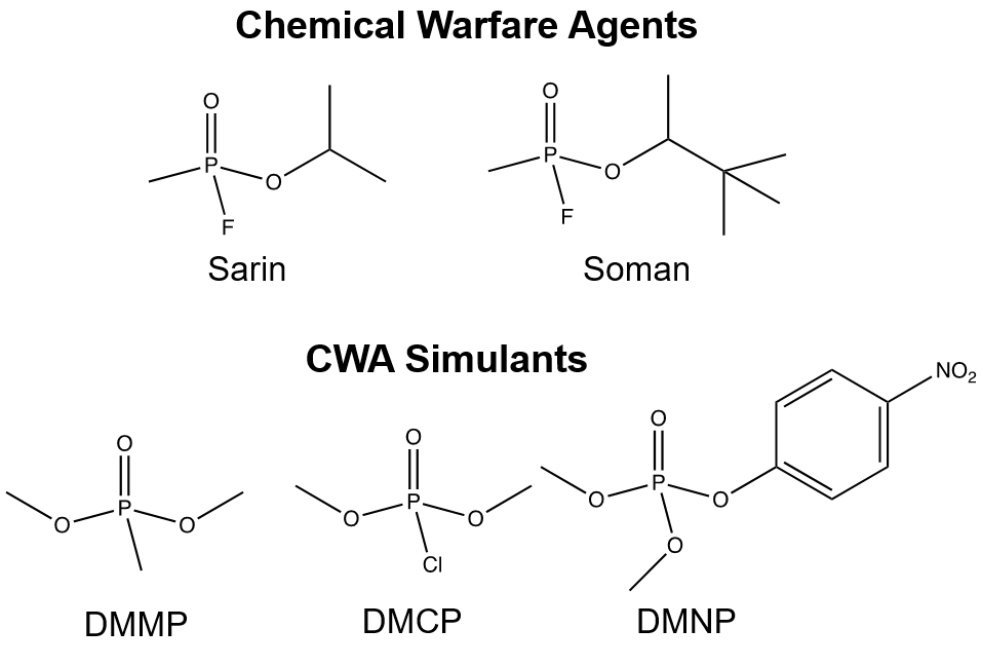

Figure 1.7. Chemical structures of common G-series chemical warfare agents and CWA simulants: dimethyl methyl phosphonate (DMMP), dimethyl chlorophosphate (DMCP) and dimethyl 4-nitrophenyl phosphate (DMNP).

In attempts to counteract the utilization of G-series nerve agents, the scientific community has investigated the degradation of sarin and soman on a wide-range of different materials with the hope of identifying materials that effectively degrade these compounds into less toxic derivatives.[58-60] However, few research locations have the safety capabilities to study such deadly materials. Therefore, CWA simulants of significantly reduced toxicity have been studied as structural and chemical mimics of the CWAs. CWA simulants, shown in the bottom of Figure 1.7, contain similar functionality as sarin or soman with significantly less toxicity.[61]

General decomposition pathways of nerve agents focus mainly on hydrolysis. Some reaction products associated with the hydrolysis of nerve agents are shown in the Scheme 1.1. The hydrolysis of the P-F bond of sarin and soman still results in the production of HF, a highly toxic chemical and is not an ideal gas-phase product for biological systems.[61] Additionally, many researchers have shown that hydrolysis occurs at the hydroxyl groups of metal oxide surfaces.[62-63] However, the reaction of hydroxyl groups with these organophosphorus (OP)-based adsorbates produces multiple P-O bonds and these phosphoryl functional groups bind tight to metal surfaces.[59,64]

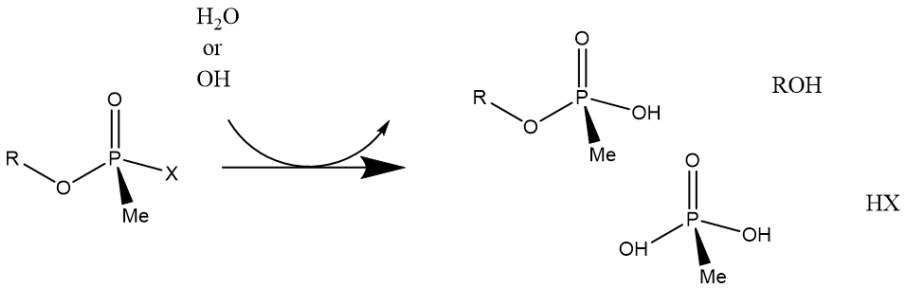

Scheme 1.1. Neve agent hydrolysis in the presence of H_2O or OH groups on a surface. The reaction could produce a variety of different compounds depending if the P-X or the P-OR bond is cleaved.

1.4.1 Metal/Metal Oxide Materials for G-agent Detoxification

Both organophosphate and organophosphonate adsorption and degradation have been studied on a variety of high-surface-area nanoparticulate surfaces–notably silicon dioxide,[58,65-66] titanium dioxide,[67-69] and zirconium hydroxide,[70] as well as other materials.[61-63,71-76] Both hydrolytic reactions and oxidative pathways have been investigated for the degradation of CWA simulants.[64] In fact, many known metal-oxide materials dissociatively adsorb gas-phase OP-based molecules and detoxify the compounds; however, product inhibition or low stability limit the success of these materials in air-based detoxification.[64,68,77] The dissociation of chemical warfare agents and simulants result in the formation of multiple bonds between the oxygen atoms from the adsorbed organophosphate or organophosphonate compound and the surface. Pictorially depicted in the Figure 1.8, these adsorbates bind very strongly to surface of metals or metal oxides and resist desorption into the gas phase.[59,68,72]

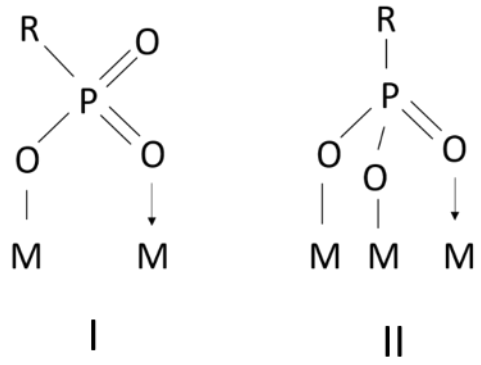

Figure 1.8. Representation of the bond formation between a bidentate-bound organophosphorus compound and tridentate-bound organophosphorus compound on metal or metal oxide surface.

For example, the common CWA-simulant, dimethyl methylphosphonate (DMMP), dissociates upon adsorption on aluminum oxide films by initial binding at surface hydroxyl sites or unsaturated metal sites to form surface bidentate methyl methylphosphonate (MMP) and a

methoxy ligand.[62] Surface-bound bidentate and even tridentate phosphates develop over extended reaction times and block reactive surface sites. Recent DFT calculations predict dissociation products of DMMP on clean TiO_2 surfaces to exhibit binding energies of over 200 kJ/mol.[59] These highly stable adsorbates require significant thermal treatment to remove.[68,78-79] Although dissociation of DMMP occurs readily on TiO_2 at temperatures as low as 214 K, the surface-bound phosphates passivate the titania and thus prevent sustained chemistry, even upon extensive thermal cycling.[67-69] These previous studies suggest that effective strategies for sustained CWA destruction at surfaces will likely require multicomponent materials where (a) initial weak-binding interactions sequester or activate the OPs, (b) activated co-reactants (e.g. O_2 or H_2O) are proximal to the bound OPs, and (c) the resulting products migrate to low surface-energy areas of the catalyst where they desorb.[61] The use of low-surface-energy metallic nanoparticles may play a key role in moving these strategies forward.

1.4.2 Metal Organic Frameworks for G-agent Detoxification

A new class of materials known as Zr-based MOFs has garnered significant attention within the scientific community in regard to CWA detoxification. The chemical composition of the Zr-MOFs is unique in that they contain Zr_6 oxide metal nodes or clusters anchored by organic linkers to form a highly porous, crystalline material. The general structure of Zr-MOFs is provided in Figure 1.9 and depicts how the metal nodes contain many of the same features that metal/metal oxide materials contain but also exhibit unique properties that arise from the linkage of the organic components between each node.

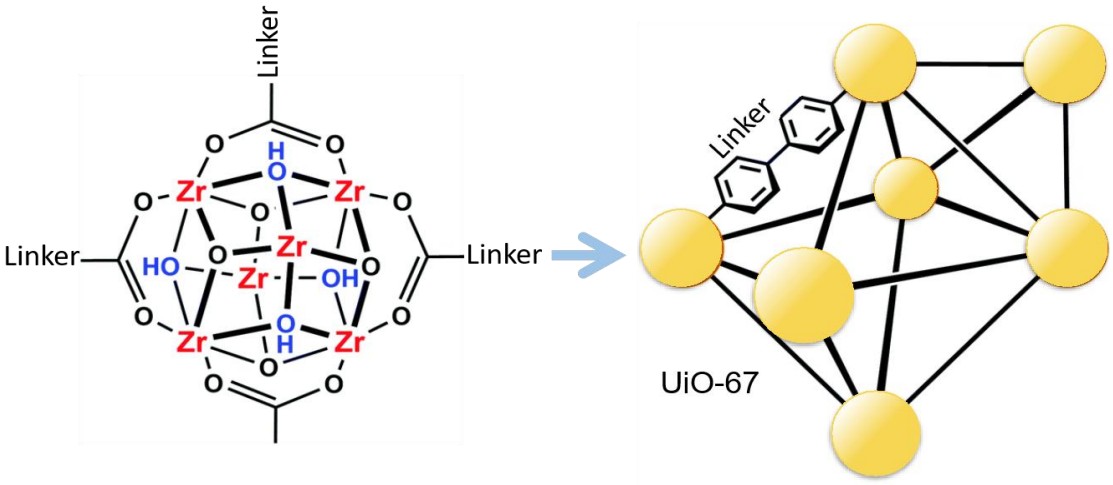

Figure 1.9. Illustration of the node structure (left) and the linker + node structure (right) for the metal-organic framework, UiO-67. Adapted with permission from Katz et al., One Step Backward Is Two Steps Forward: Enhancing the Hydrolysis Rate of UiO-66 by Decreasing [OH^-]. *ACS Catalysis*, 2015, 4637-4642. Copyright 2015 American Chemical Society.[80]

In particular, the Zr_6-based MOF series of UiO-66 [$Zr_6(\mu_3\text{-}O)_4(\mu_3\text{-}OH)_4(bdc)_6$; bdc: benzene1,4-dicarboxylate], UiO-67 [$Zr_6(\mu_3\text{-}O)_4(\mu_3\text{-}OH)_4(bpdc)_6$; bpdc: biphenyl-4,4′-dicarboxylate], MOF-808 [$Zr_6(\mu_3\text{-}O)_4(\mu_3\text{-}OH)_4(OH)_6(H2O)_6(btc)_2$; btc: benzene-1,3,5-tricarboxylate], and NU-1000 [$Zr_6(\mu_3\text{-}O)_4(\mu_3\text{-}OH)_4(OH)_4(H2O)_4(tbapy)_2$; tbapy: tetratopic 1,3,6,8-tetrakis(p-benzoate) pyrene] exhibit promising solution-phase and gas-phase detoxification of the G-series nerve agents and simulants.[42,81-85] The major difference between the MOFs shown above is the linker connectivity to each metal node. For example, each metal node of UiO-66 and UiO-67 connect to 12 organic linkers; whereas, each metal node of NU-1000 only connects to 6 organic linkers.[86-87] The decrease in metal connectivity provides coordinatively unsaturated Zr atoms (Zr_{cus}) that exhibit chemically reactive properties.[88-90] Specifically, Mondloch et al. identified that a dehydrarated-NU-1000 framework exhibited a remarkable improvement in the solution-based hydrolysis of DMNP and soman compared to the non-dehydrated NU-100 variant.[84] These results,

along with the research of others,[60,91-92] clearly suggest the incorporation of undercoordinated metal centers improves the chemical reactivity of the CWAs within MOFs. However, direct characterization of these coordinatively unsaturated Zr sites within metal-organic frameworks has remained elusive.

1.5 The Characterization of Surface Sites with the Probe Molecule, CO

For the past sixty years, the surface science community has employed gas-phase probe molecules that adsorb onto surface sites in order to characterize the electronic nature of the associated surface site. These probe molecules provide *in situ* characterization of catalysts and answer the fundamental atomic-level structural questions that kinetic analysis of a series of different materials cannot. One particularly useful gas phase probe molecule, CO, has the been critical in identifying characteristics of both Brønsted and Lewis acidic surface sites.[93-99]

The unique nature of adsorbed CO, also called $CO_{(ads)}$, is due to the vibrational transition associated with the ν(CO) and the molecular orbitals of CO, shown in Figure 1.10. The highest occupied molecular orbital (HOMO) of CO is the 5σ orbital and the electron density associated with the 5σ orbital is found mainly on the carbon end of the molecule. CO coordinates with electron deficient Lewis acidic surface sites through a sigma bond, which results in an increase in the bond order of CO.[96,98] This phenomenon suggests that the 5σ orbital is antibonding in nature and the electron density that is removed from this orbital will result in a vibrational blueshift (increase in frequency from the fundamental vibration in the gas phase, 2143 cm^{-1}) of the $\nu(CO)_{ads}$. This sigma interaction, depicted in Figure 1.11b, suggests that electron density from CO interacts with empty orbitals of the metal cation surface site. It is generally accepted that a greater blueshift in frequency of the $\nu(CO)_{ads}$ correlates to a stronger interaction with the Lewis acid.[99]

Conversely, when a surface site contains significant electron density, backdonation from the surface site into the 2π antibonding orbital of CO occurs. This effect causes an associated red shift in the adsorbed CO vibrational transition because the $\nu(CO)_{ads}$ bond is weakened (see Figure 1.11c).[98-99] The π-backbonding donation effect is typically found in addition to the sigma interaction and the overall $\nu(CO)_{ads}$ observed is some synergistic combination of both components.[96,99] Therefore, depending of the electronic nature of the surface site to which CO is bound, the associated vibrational transition for the adsorbed CO molecule will blueshift (via sigma donation through the 5σ orbital) or redshift (via a strong backdonation of electron density into the 2π orbital).

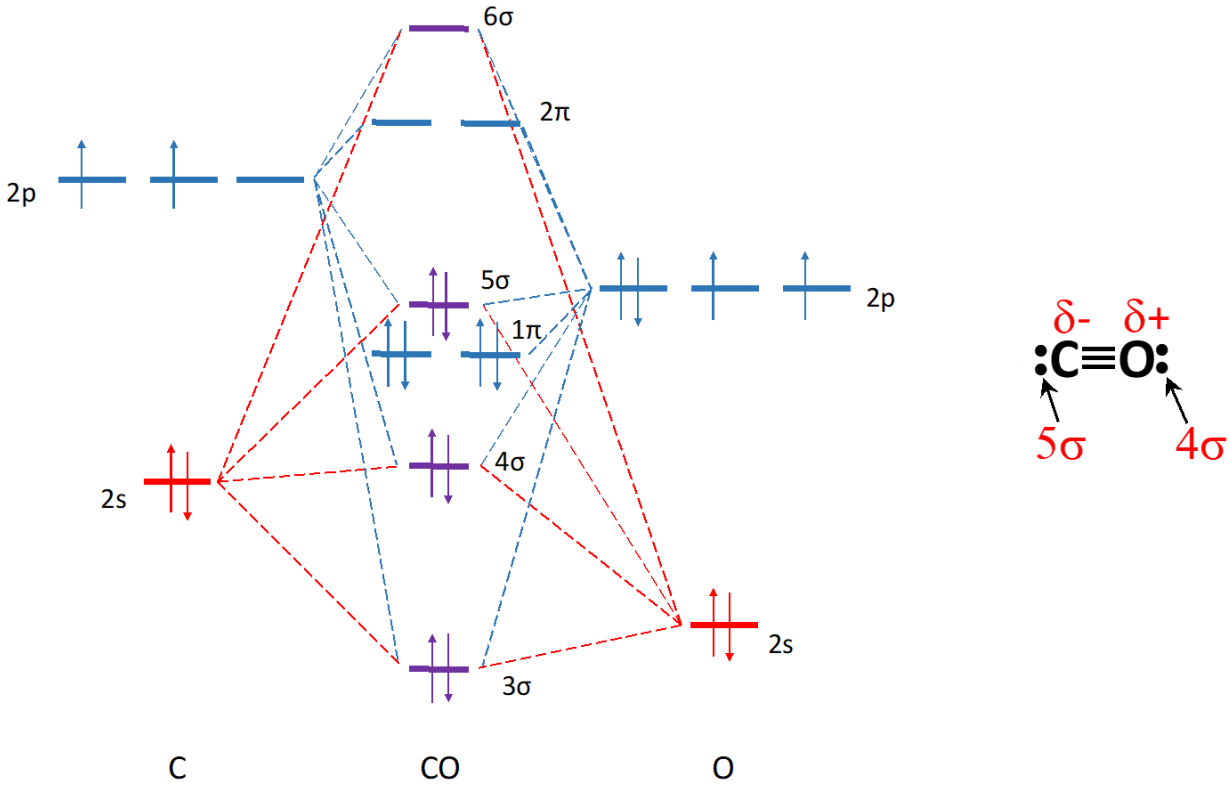

Figure 1.10. Molecular orbital structure of CO and the associated orbital positions in which the 5σ orbital is manly around the carbon atom while the 4σ orbital is manly around the oxygen atom.

In addition to covalent-like interactions, electrostatic interactions between the adsorbed CO molecule and surface species induce specific changes to the vibrational character of CO. The electric field created by the positive charge (like an alkali metal cation or the H of a hydroxyl group) induces a polarization of the CO molecule according to the Stark effect.[99] As shown in equation 1.4, the electric field at the adsorption site, *E*, correlates with the vibrational shift of the C-O bond:

$$\Delta\nu(CO) \propto E \propto \frac{q}{d^2} + E_{anions} \tag{1.4}$$

where *q* is the cation effective charge, *d* is the distance between M to CO center of bond and E_{anions}, is the vector sum of neighboring anions. An increase in the charge separation (C is partially negative, O is partially positive) is proportional to the strength of the local electric field and results in a further blueshift of the $\nu(CO)_{ads}$ compared to the gas phase. Therefore, as shown in Figure 1.11a, the closed shell configuration of the alkali metal cations induces electrostatic interactions on the adsorbed CO molecule and the stronger interaction results from the electric field associated with the surface site.

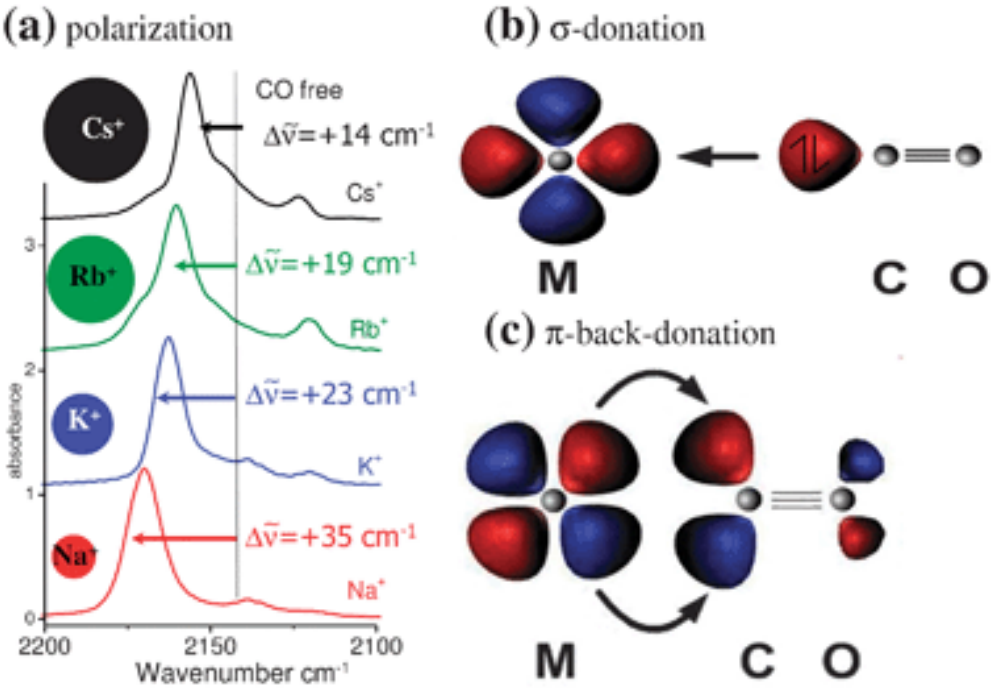

Figure 1.11. Three possible interactions between CO and a metal center (M). (a) Electrostatic or polarization, (b) σ-bonding interaction, and (c) π backbonding interaction. Reproduced from Ref. [99] with permission from The Royal Society of Chemistry.

The interaction between CO and hydroxyl groups is also electrostatic and the magnitude of the change in vibrational frequency compared to the gas phase fundamental vibration at 2143 cm^{-1} [$\Delta\nu$(CO)] depends on the strength of the electrostatic field according to the Stark effect.[96] Therefore, interactions with an electric field through the carbon end of the CO molecule induce a blueshift in frequency of the C-O bond. Whereas, interactions with these same hydroxyls through the oxygen end, or the 4σ orbital, induce a redshift in frequency of the C-O bond because of the depopulation of the fully bonding 4σ orbital.[100-101] Overall, it can be seen that CO adsorption onto a variety of different materials can easily identify unique adsorption sites. The properties of CO adsorption upon active surface sites for catalytic materials will be further explored in the upcoming chapters.

1.6 Specific Aims of the Chemical Systems of Interest

The utilization of *in situ* spectroscopic techniques provides the ability to probe the gas–surface interface during gas molecule adsorptive and reactive processes. In this thesis, I focus on two main oxidation pathways: the photoepoxidation of propene into propene oxide and the oxidation of organophosphorus-based CWAs. First in Chapter 3, I focus on the adsorption of propene onto a titania-supported Au nanocatalyst (Au/TiO_2). The Au/Ti interface has been cited as critical in the epoxidation of propene into propene oxide, however, the binding geometries and energetics of propene on Au/TiO_2 were not well understood. Through the utilization of *in situ* infrared spectroscopy, I identified two propene adsorption sites distinguishable through the ν(C=C) vibrational mode of propene. Propene adsorption is the critical first step in the entire epoxidation process that also includes H_2 and O_2.

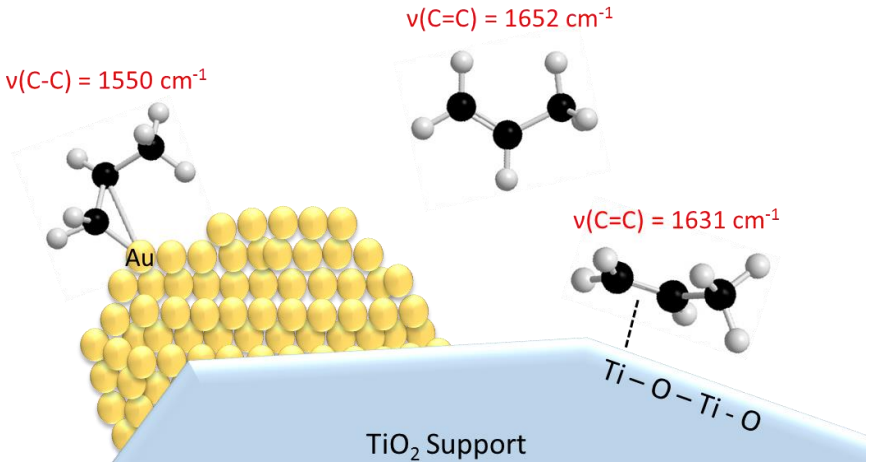

Scheme 1.2. Schematic depiction of the binding sites, geometry, and energetics of propene at nanoparticulate Au/TiO_2.

In Chapter 4, the propene adsorption conclusions generated from Chapter 3 were built upon by the addition of both H_2 and O_2 into the experimental reaction mixture on the same Au/TiO_2 nanocatalyst. By using the same spectroscopic approach, I identified specific intermediates,

products, and by-products produced when propene, H_2 and O_2 simultaneously react on a Au/TiO_2 surface. Specifically, spectroscopic evidence of the hydroperoxide intermediate ($-OOH/H_2O_2$) suggested the importance of H_2 dissociation and reaction with oxygen, prior to interactions with propene. Through the utilization of the probe molecule, CO, the surface location of propene oxide was identified at Au sites near the Au/Ti interface.

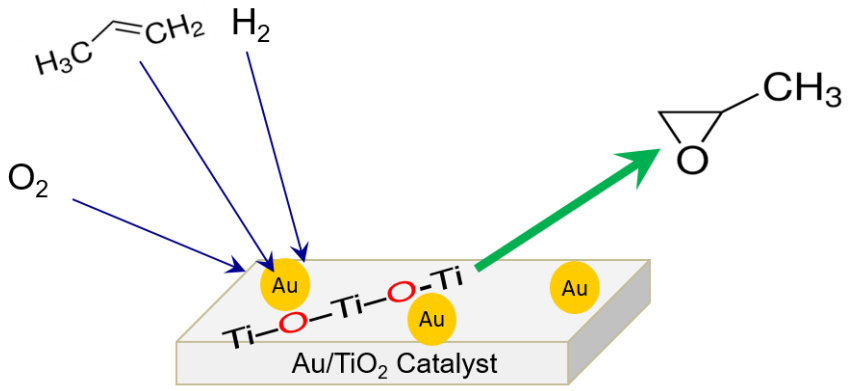

Scheme 1.3. Schematic description of Chapter 4 including the adsorption and reaction of propene, O_2, and H_2 to form propene oxide on Au/TiO_2.

In order to remove the necessity of hydrogen from the reaction feedstock during propene epoxidation, UV was incorporated into the epoxidation reaction on a TiO_2-SiO_2 binary catalyst. In Chapter 5, *in situ* infrared spectroscopy of the photocatalytic reaction identified the production of trace amounts of propene oxide. However, propene oxide was further degraded in the presence of UV light to form undesirable side products including acetone and acrolein.

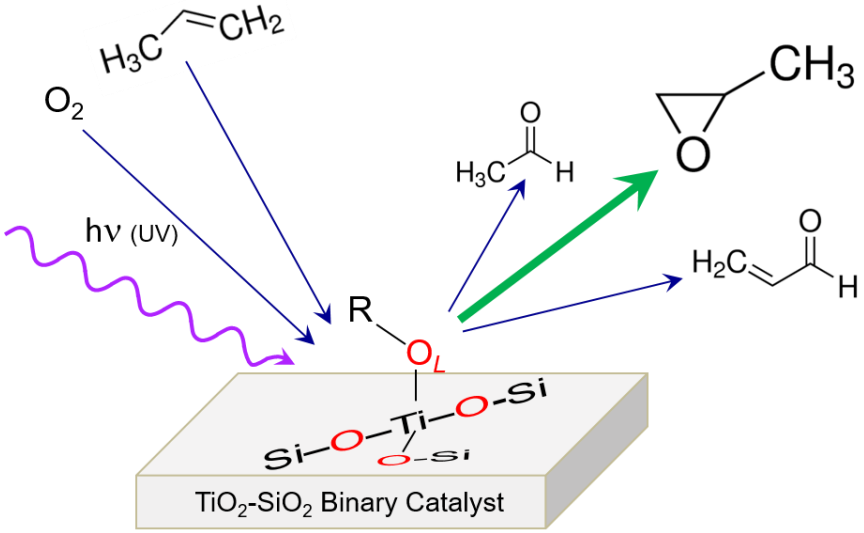

Scheme 1.4. Schematic description of Chapter 5 including the surface adsorption and photooxidation of propene into propene oxide, acrolein, and acetone over a TiO_2-SiO_2 binary catalyst.

In Chapter 6, I describe the oxidative mechanistic pathway of the chemical warfare agent simulant, dimethyl chlorophosphate (DMCP), over a titania aerogel-supported Cu (Cu/TiO_2) nanomaterial. Through spectroscopic interrogation of the both surface adsorbates and the underlying electronic structure of surface sites, DMCP was found to oxidize first to a methoxy intermediate and then to copper-bound CO. As more organophosphorus-containing species adsorbed onto the surface, the oxidative decomposition pathway was quenched. This study suggests further synthetic advancement to utilize mixed oxide aerogel supported-copper, where oxidized phosphorus-containing species will more easily desorb, will aid in the continued decomposition activity of OP-based molecules.

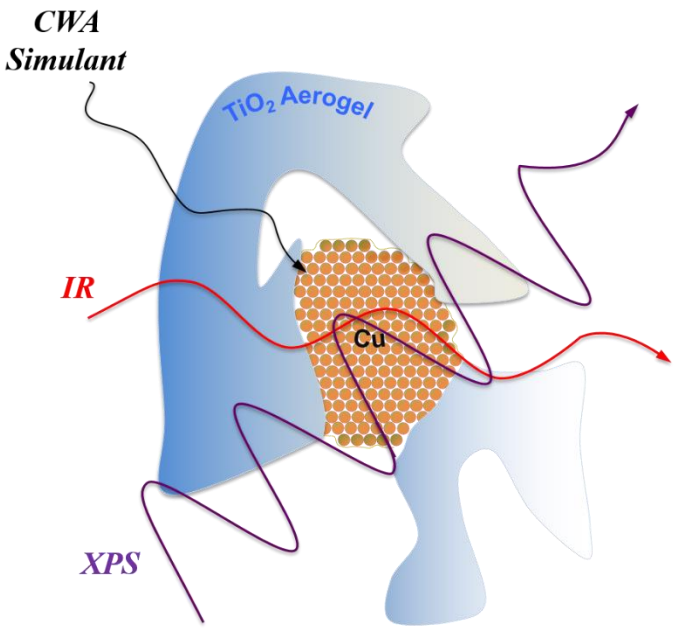

Scheme 1.5. Schematic description of Chapter 6 in which infrared light and x-ray light reveal adsorption and decomposition of dimethyl chlorophosphate over a TiO_2 aerogel-supported Cu nanoparticle.

Finally, in Chapter 7, I utilize the adsorption of the small molecule, CO, in order to characterize the acidic surface sites within a series of Zr-based metal-organic frameworks. CO adsorption on the hydroxyl groups (shown in Scheme 1.6) and CO adsorption on the coordinatively unsaturated Zr atoms are distinguishable through the ν(CO) vibrational motion of $CO_{(ads)}$. The high-vacuum, *in situ* spectroscopic methods described in Chapter 7 provide the first systematic characterization of Zr_{cus} within the Zr-based MOF family. The CO adsorption experiments provide the benchmark to further study how Zr active sites within Zr-based MOFs change as a result of continued catalytic activity and as a result of MOF synthetic variability.

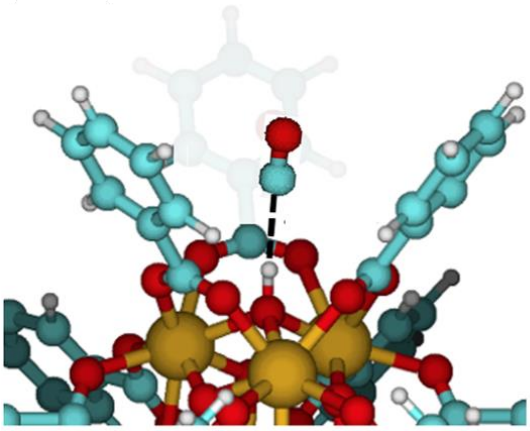

Scheme 1.6. Schematic illustration of Chapter 7 in which the probe molecule, CO, binds to the acid sites of Zr-based metal-organic frameworks in order to characterize the materials.

Through each of these specific aims, I have developed a fundamental understanding of the adsorption, diffusion and reaction processes that occur on relevant materials critical for industrial, environmental, and defense related applications. These studies will aid further development and design of catalysts synthesis. Finally, the careful experimental detail and analysis provided within this thesis is critical to understanding the molecular-level processes that occur when a gas molecule interacts with a solid surface.

1.7 Concluding Remarks

Supported-metal nanoparticles and metal-organic frameworks are well-known for their ability to catalyze molecular transformations. However, many questions remain in terms of the atomic-level adsorption and reactive processes that occur on these materials. The studies performed in this thesis depict fascinating atomic-level behavior of small molecule adsorption and reaction processes. I have employed spectroscopic techniques to characterize the bonds that form upon adsorption and track the bonds that break upon reaction. These studies identify unique adsorption configuration for adsorbates and mechanistic pathways that adsorbed molecules partake

on to react and form desired products or in some cases undesired products. The fundamental nature of these studies will aid future research with the next-generation of catalytic material for industrial and environmental usage.

Chapter 2

Experimental Approach for Studies of Gas–Surface Adsorption and Reaction

2.1 Experimental Considerations

Ultra-high vacuum (UHV)-based surface science instruments have revolutionized the field of gas-surface chemistry. Ranging from single-crystal metal surfaces to complex heterogeneous nanostructured systems, UHV environments have provided fundamental thermodynamic binding energies and single atom resolution imaging of the gas-surface interface.[102-105] Unfortunately, the gap between typical materials studied within an UHV environment and the materials of practical relevance can be significant. To address this so-called "materials gap", we have a developed a controlled environmental apparatus to study complex materials with the ability to cover vast temperature and pressure ranges. The main goal of the instrument developed is to better understand how materials such as powders, polymers, atmospheric aerosols, and chemical warfare agents, function in realistic environments while quantifying fundamental thermodynamic energetics of the gas-material interactions. The instrument was designed to address four key challenges and provide specific analytical capabilities:

(1) ***In situ* spectroscopic characterization.** Infrared spectroscopy has been incorporated into the instrument to interrogate the surface-adsorbed species, reaction intermediates, and emergence of products in real-time as atmospheric molecules collide on the surface of a material of interest.

(2) **Variable pressure environment.** Precision controlled vapor dosing, gas handling, and vacuum pump baffling have been applied to provide the ability to study interfacial reactions at pressures ranging from 100 Torr to 10^{-9} Torr.

(3) **Wide-range temperature control.** A sample mount for particles and other materials has been designed that provides the ability to rapidly heat and cool the sample from liquid nitrogen temperatures to 1000 K.

(4) **Gas phase detection.** Detection of gas-phase products released from a surface has been achieved via the implementation of a differentially pumped line-of-sight quadrupole mass spectrometer with a mass range from 1 to 300 amu.

The chamber described in this chapter was built at Virginia Tech and sent to Edgewood Chemical Biological Center for studies involving chemical warfare agent adsorption onto complex nanomaterials. An analogous chamber remained at Virginia Tech for studies presented in Chapters 3 – 7.

2.2 Specific Vacuum Chamber Capabilities

A schematic representation of the experimental vacuum chamber described above is shown in Figure 2.1. The vacuum system is divided into two chambers separated by a pneumatic gate valve (VAT Valve). Each chamber is pumped by a magnetically levitated turbomolecular pump (400 L/s Pfeiffer Vacuum). A manual gate valve (VAT Valve) is placed below the main chamber (blue compartment, Figure 2.1) to isolate the sample and chemical reactants from the turbomolecular pump. The manual gate valve serves as a pumping baffle that allows the main chamber to quickly cover pressure ranges between 1×10^{-9} Torr – 100 Torr. The main reaction chamber includes 16 Conflat® flange ports that are used to introduce chemicals, photons (green – Visible/UV and red- infrared lines), samples, and other instrumentation into the chamber. The entire apparatus is mounted on an aluminum framework (80/20 Inc.).

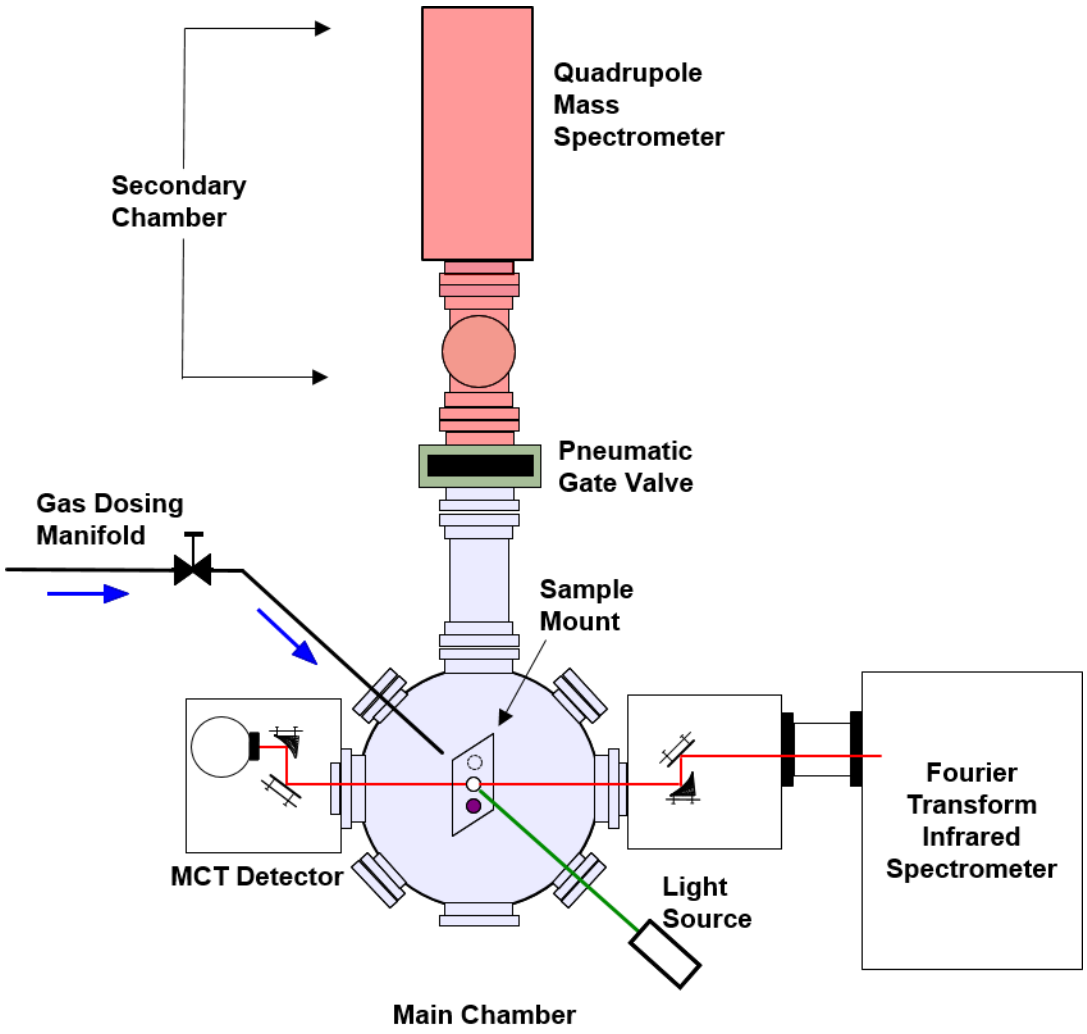

Figure 2.1. General schematic of the instrument. The main chamber, where the sample is located, is shown in blue. The secondary chamber is shown in red. The FTIR and mirror are not under vacuum and shown in white. Components not drawn to scale.

For the detection of surface species during experimental operation, transmission Fourier transform infrared spectroscopy (FTIR) is incorporated into the chamber (red solid line, Figure 2.1). Two 4.5” CF flanges are fixed with KBr windows to allow for the transmission of infrared light through the chamber. In combination with the *in situ* detection of surface species, a quadrupole mass spectrometer is attached to the secondary chamber (red compartment, Figure 2.1)

to monitor the gas phase reactants and products that desorb from the surface. Together, these methods provide simultaneous probes of reactants as they adsorb onto a surface and products as they are released into the gas phase.

2.3 Sample Mount

The custom designed and constructed sample mount, shown in Figure 2.2, utilizes stainless steel clamps that immobilize a tungsten grid. Samples can either be pressed into the voids of the grid, deposited onto the grid via an aerosol generator, or drop-casted to produce a thin film of material. The grid allows for a variety of materials to be integrated into the instrument for exposure to reactive species. The sample holder is mounted to an external manipulator (McAllister) for precision alignment at the crossing coordinate of the mass spectrometer and infrared beam. A pinhole aperture below the sample position is used to align the IR light by locating the beam path in the center of the chamber. For temperature control, the stainless steel clamps are attached to copper leads and the mesh is resistively heated with applied current from an external power source. A k-type thermocouple is used to monitor temperature of the sample and as a feedback loop to the external power source. Finally, a liquid nitrogen reservoir is used as a heat sink to cool the copper leads and mesh. Both the liquid nitrogen and the resistive heating provide a working sample temperature range of < 90 K to 1000 K.

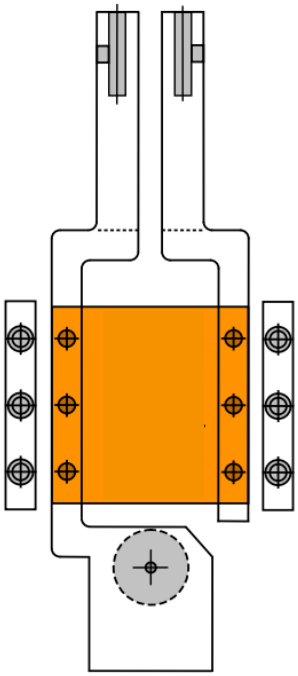

Figure 2.2. Schematic representation of the sample used for gas-surface studies. The orange region represents the tungsten mesh that is either coated with sample or hydraulically-pressed to hold solid powders in the void space of the mesh. A pinhole aperture is located below the sample (circle, shadowed). Figure adapted from Steven Burrows with permission.

2.4 Mass Spectrometer

The secondary vacuum chamber has been manufactured to provide detailed information on the gas phase species originating from surface desorption or reaction. The residual gas analyzer (RGA, SRS 300) is mounted to a custom six-way CF cross (Kurt J. Lesker) where the center of the ionizer is positioned directly in line with the center of the sample (located in the main chamber). This allows for line-of-sight detection of the gas phase products that have desorbed from the surface. The pneumatic gate valve between the two vacuum chambers actuates and closes during high-pressure experiments to preserve the mass spectrometer (SRS-RGA filaments cannot exceed

pressures above 1×10^{-6} Torr). A gas leak valve is attached between the two chambers to allow for real time sampling by the RGA when the main chamber is held at high pressure for heterogeneous chemical reactions.

The residual gas analyzer coupled to the high-vacuum chamber has been benchmarked by desorption measurements of NH_3 adsorbed into a polyvinylidene fluoride (PVDF) film. The desorption of gas molecules from the polymeric coating was tracked in a test experiment by heating the sample while monitoring product desorption with the line-of-sight mass spectrometer. Initially, the PVDF sample was exposed to NH_3 at 123 K. Once equilibrated, the temperature of sample was increased linearly while the mass analyzer was used to monitor the gas phase composition. As shown in Figure 2.3, the gas phase mass-to-charge ratio (m/z) for NH_3, 17, increased over time as the temperature of the gas-saturated sample increased. The increase in detection of the specific m/z is associated with NH_3 desorbing from the polymer surface and traveling to the mass spectrometer ionizer for detection. The monitoring of other gas phase species such as H_2O, CO_2, and CO did not exhibit this same analyzer response for the associated mass fragments during the temperature ramp.

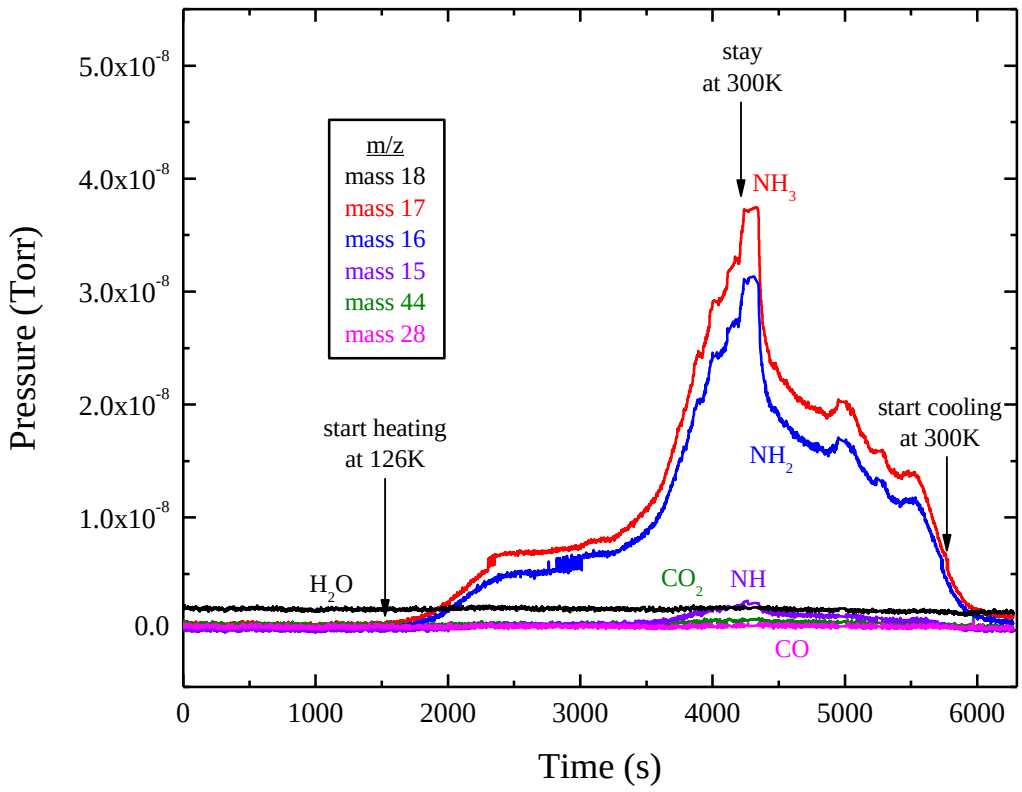

Figure 2.3. Temperature programmed desorption profile of NH_3 bound to PVDF. Pressures of each mass fragment over time were acquired with the RGA. Mass-to-charge ratios of 18, 17, 16, 15, 44, and 28 are associated with H_2O, NH_3, NH_2, NH, CO_2 and CO/N_2 respectively.

2.5 Infrared Spectroscopy

Transmission Fourier transform infrared spectroscopy (FTIR) effectively elucidates the atomic-level vibrational features that occur within materials and upon perturbation of materials. To experimentally approach this, infrared spectra are acquired prior, during and after the adsorption of gas molecules on a surface to identify bond rupture and bond formation events occurring at the atomic level.

The infrared light used to detect vibrational features associated with gas adsorption and reaction is coupled to the variable pressure chamber through two KBr windows and custom

designed optics compartments. Infrared light is extracted from a commercial FTIR spectrometer through an external port. A dry-air purge is used to remove residual gas molecules and vapors from the custom optics compartments (Figure 2.4A). In the entrance optics compartment, one flat mirror (Edmund Optics) and one parabolic mirror (Thor Labs focal length = 228.6 mm) are inverted and attached to a micrometer stage (Newport) to allow for fine focal adjustment towards or away from the sample. The parabolic mirror is adjusted to focus the infrared energy onto a 1 mm^2 spot on the sample. Once focused, infrared light passes through the sample and enters a dry-air purged detector box where a flat mirror (Edmund Optics) reflects the light onto a parabolic mirror (Thor Labs, focal length = 152.4 mm). Finally, the light is focused onto an external MCT/A detector for analysis.

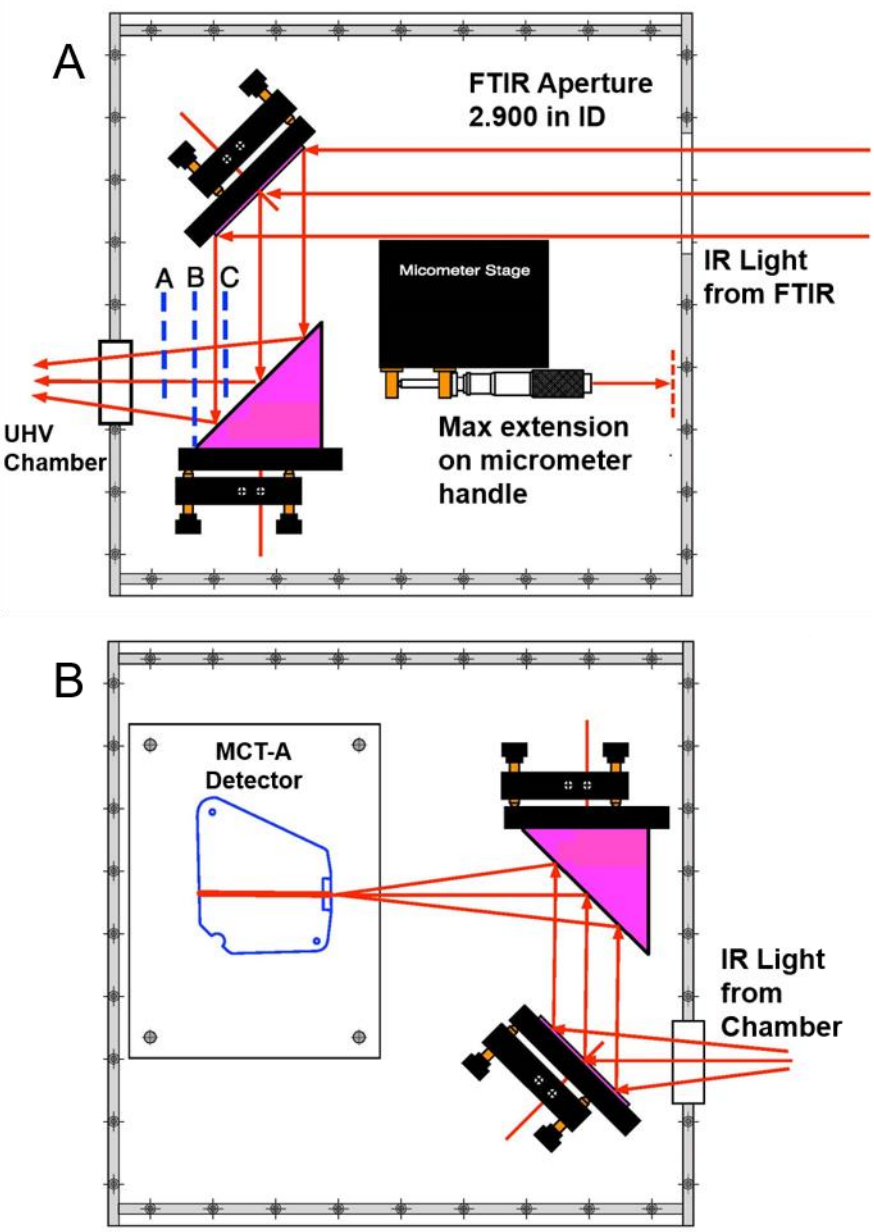

Figure 2.4. Infrared light mirror boxes. (A) Mirror box that directs infrared light from the FTIR housing to the vacuum chamber. (B) Mirror box that directs the infrared from the vacuum chamber into the MCT detector. Parabolic mirrors are depicted as pink triangles. Figure adapted from Steven Burrows with permission.

The *in situ* infrared system has been benchmarked by measurements on a test polymeric sample of the MOF, UiO-66-NH_3, incorporated into PVDF. Figure 2.5 displays the infrared spectra for the UiO-66-NH_3 incorporated into the β-PVDF sample. Spectra were recorded over the temperature range of 298 K to 116 K. The final spectrum recorded at low temperature (Figure 2.5, red spectrum) has a few minor differences in infrared absorbance around 740-760 cm^{-1} and 790 – 805 cm^{-1} compared to the material at room temperature (Figure 2.5, black spectrum). The small vibrational shifts that occur in the MOF-composite are easily identified using the aforementioned *in situ* infrared spectroscopic techniques. This experimental methodology allows for systematic studies of the vibrational changes that occur upon gas molecule adsorption and temperature or pressure effects.

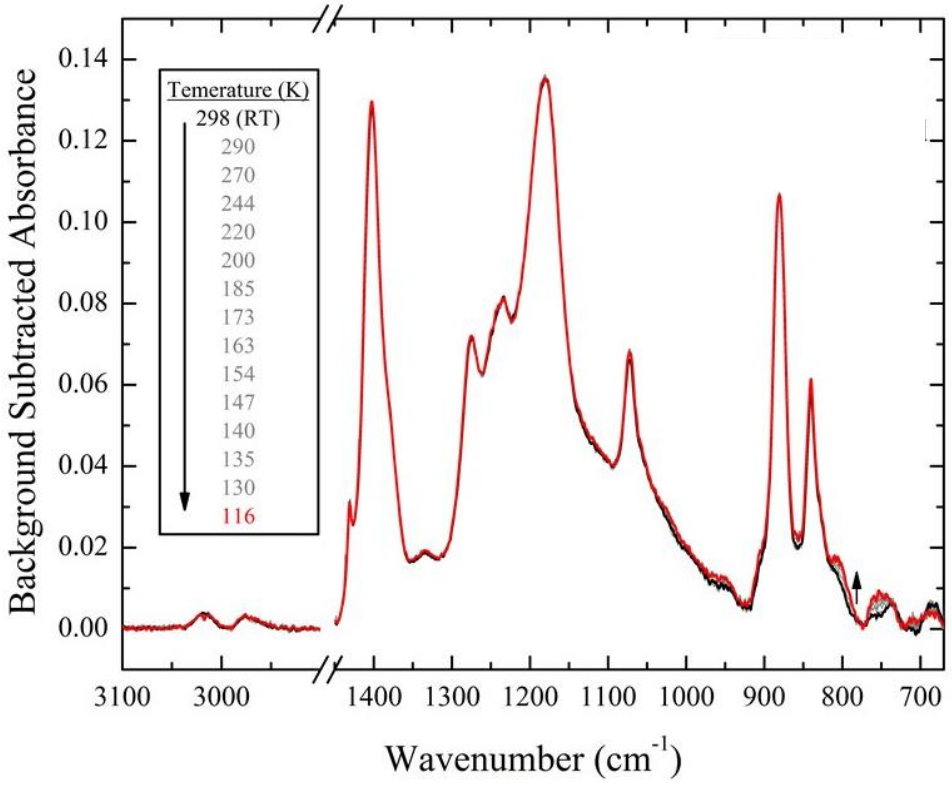

Figure 2.5. Infrared spectra of UiO-66-NH_3 incorporated into β-PVDF at decreasing temperatures.

2.6 Variable Temperature Infrared Spectroscopy

A critical part of understanding the characteristics of gas-molecule adsorption involves defining and quantifying the energetics of the adsorption of gas molecules on a single surface site. Variable-temperature infrared spectroscopic (VTIR) measurements characterize the energetics of gas-surface interations.[106] VTIR requires a fixed partial pressure of small gas molecules interacting with a material within the closed vacuum system. The equilibrium constant for the gas molecule adsorption depends on temperature according to the van't Hoff equation:

$$ln\,K(T) = \left(-\frac{\Delta H^{\circ}_{ads}}{RT}\right) + \left(\frac{\Delta S^{\circ}_{ads}}{R}\right) \tag{2.1}$$

where K is the equilibrium constant of the adsorption process while both ΔH°_{ads} and ΔS°_{ads} are assumed to be temperature independent values of the standard enthalpy and entropy of adsorption, respectively.

The VTIR method utilizes the assumption of Langmuirian adsorption for gas phase molecules. The fractional coverage of the molecule on the surface, θ, defined by the Langmuir adsorption model is related to the intensity of the characteristic gas molecule–surface IR absorption band, A. Within this construct, one can express surface coverage as:

$$\theta = \frac{A}{A_M} = \frac{exp\left[\frac{\Delta S^{\circ}_{ads}}{R}\right] exp\left[-\frac{\Delta H^{\circ}_{ads}}{RT}\right] p}{(1 + exp\left[\frac{\Delta S^{\circ}_{ads}}{R}\right] exp\left[-\frac{\Delta H^{\circ}_{ads}}{RT}\right] p)} \tag{2.2}$$

where A_M is the intensity under full coverage of the adsorbed molecule on the surface site and p is the pressure of the closed system.

In the studies presented, an increase in the sample temperature resulted in an observed decrease in the concentration of gas–surface interactions. No measurable pressure increases within the chamber accompanied the decrease in concentration of the gas—surface species. This results

from a variety of reasons including the large volume of the chamber, the sensitivity of the full range pressure gauge (Pfeiffer, Full range vacuum gauge) and the low coverage of gas molecules bound to the surface. As a result, the relationship between integrated absorbance and the standard enthalpy of adsorption ($\Delta H°_{ads}$) eqn. 2.3 can be written as:

$$A \approx A_M \exp\left[\frac{\Delta S^{\circ}_{ads}}{R}\right] N_{tot}\left(\frac{RT}{V_g}\right) e\exp[-\frac{\Delta H^{\circ}_{ads}}{RT}] \propto T \exp[-\frac{\Delta H^{\circ}_{ads}}{RT}] \quad (2.3)$$

where N_{tot} is the total number of adsorbate moles in the system (both in the gas phase and adsorbed) within a fixed volume, V_g. From this point, we assume the surface coverage is negligible ($\theta \ll 1$) and only $\Delta H°_{ads}$ can be evaluated.

2.7 Summary

A variable temperature and pressure vacuum apparatus was designed in order to study complex materials with *in situ* spectroscopic methodology over a wide magnitude of pressures and temperatures. The main chamber, which incorporates infrared spectroscopy, was built to study the vibrational features that appear and disappear during the uptake and reaction of small gas molecules onto a variety of solid and film-like materials. From the preliminary results in this chapter and through the experimentation provided in the chapters herein, we have shown that transmission infrared spectroscopy of small molecule adsorption onto high-surface area, complex nanomaterials provides fundamental adsorption, reaction, and desorption characteristics within a well-defined, isolated vacuum environment. This instrumentation described in this chapter provides the means to bridge the "materials gap" between low temperature, low pressure UHV experimentation and environmentally and industrially relevant experimental conditions.

Chapter 3

Binding Sites, Geometry, and Energetics of Propene at Nanoparticulate Au/TiO_2

Adapted with permission from Driscoll et al., Binding Sites, Geometry, and Energetics of Propene at Nanoparticulate Au/TiO_2. Journal of Physical Chemistry C, 2017, 121 1683-1689. Copyright 2017 American Chemical Society and from Panayotov et al., Infrared Studies of Propene and Propene Oxide Adsorption on Nanoparticulate Au/TiO_2. Surface Science, 2016, 652, 172-182 2016 with permission from Elsevier.

3.1 Introduction

3.1.1 Propene Oxide Production

Since the early 2000s, over 6 million tons of propene oxide have been synthesized each year for the production of polyurethane films, propene glycol, and important ethers.[45-46] However, the two main propene oxide production methods, the chlorohydrin process and the hydroperoxide process, have major environmental and economical drawbacks.[46,107] These drawbacks have led researchers to develop a new class of heterogeneous catalysts that can directly and selectively convert gas-phase propene into propene oxide. One of these materials, nanoparticulate Au/TiO_2, contains an abundance of low-coordinated Au sites and Au-Ti interfacial regions, both of which have been cited as major structural contributors for the high catalytic activity of the material.[12,23,108-111]

3.1.2 Au/TiO_2 Nanoparticle Catalysts for Propene Oxide Production

In several important studies, researchers have shown that TiO_2-supported Au nanoparticles are active for the direct conversion of propene to propene oxide in the presence of oxygen and

hydrogen.[48,51-52] Initial propene oxidation research on Au/TiO_2 demonstrated the high selectivity for propene oxide compared to other possible oxidation products; however, the excessive consumption of hydrogen and low propene oxide yield during the epoxidation hindered large-scale processes.[46,51] Studies of propene epoxidation kinetics have led to improvements in propene oxide yield and hydrogen efficiency. Unfortunately, the advances in efficiency generally occur at the expense of selectivity with increased production of other oxidized compounds such as acetone, propanal, CO_2, and acrolein.[50,52,54,56] The key mechanistic step in oxide formation, olefin activation, appears to occur at low coordinated Au sites through activation of the carbon double bond.[55,112-114] The binding geometry of propene on Au plays a critical role in whether the epoxidation reaction pathway[115] or the abstraction of the allylic hydrogen, to form acrolein and unsaturated aldehydes, is preferred.[116-117] Additionally, others have suggested that the oxidation of the Au–propene adsorption complex on a Au/TiO_2-SiO_2 surface produced acrolein and therefore acts to lower the selectivity of propene oxide.[118-119] Such disparity between different researchers' conclusions suggests the importance of further study into Au/TiO_2-based catalysts for propene epoxidation.

3.1.3 **Fundamental Studies of Propene Adsorption onto Au/TiO_2**

Many studies highlight the importance of propene–Au binding in the activation of propene during epoxidation.[55-56,115,120] However, direct spectroscopic evidence of propene–Au interactions on supported Au surfaces remains elusive.[38,52,112,121-122]. Theoretical predictions on the nature of sites in which propene interacts with under-coordinated Au (on a variety of Au crystal faces) have also been discussed.[38,113,116,123-125] Despite these insightful studies, the field lacks a fundamental understanding of the chemistry involved in the adsorption of propene on the surface of Au/TiO_2.

Few published studies have explored the binding energetics of propene on Au (111) and Au/TiO_2 (110) single crystal surfaces. Campbell and coworkers utilized temperature programmed desorption to examine the adsorption and desorption processes of propene on a Au/TiO_2(110) planar model catalyst.[126] They found that propene bound to Au islands persisted on the surface at higher temperatures (265-310 K) compared to Ti sites and Ti sites at the edges of Au islands (190 K and 240 K respectively).[126] Davis and Goodman discovered, on a Au (111) crystal surface, that propene desorbs from terrace sites prior to low-coordinated Au sites at edges.[127] Both studies suggest that propene binds strongly to low coordinated Au sites. However, direct identification of propene binding sites on nanoparticulate Au/TiO_2 catalysts has yet to be provided.

The objective of the work described below is to provide a fundamental understanding of the chemistry involved with propene adsorption onto Au/TiO_2. The experiments provided below couple high-vacuum surface-science based methods with *in situ* infrared spectroscopy to track the adsorption and desorption of propene on Au/TiO_2 surfaces. Fourier transform infrared spectroscopy is a powerful tool for exploring differences in surface site dependence for molecule-surface interactions. In conjunction with experimental studies, density functional theory (DFT) calculations, performed by our collaborators, were used to help interpret and assign infrared bands to particular binding geometries on a model Au/TiO_2 catalyst. Results from both experiments and DFT calculations provide stretching frequencies and binding energies of propene in different orientations on the surface of Au/TiO_2. Together, our studies provide new insight into the adsorption and activation of propene on the surface of Au/TiO_2.

3.2. Procedural Methods

3.2.1 Au/TiO_2 Synthesis

For this work, a Au/TiO_2 sample was prepared according to the urea hydrolysis precipitation-deposition synthesis procedure developed by Zanella et al.[36] The synthesis procedure produced approximately 3 nm diameter Au particles (8% w/w gold loading), highly dispersed on TiO_2 (Degussa P25) nanoparticles with an average size of 25 nm. Au/TiO_2 particles synthesized in the same manner have been previously characterized.[18,28,128] The TiO_2 reference material, Degussa P25, was used as a reference sample in the experiments presented below.

3.2.2 Sample Installation into High-Vacuum Chamber and Sample Activation

Infrared spectroscopic experiments were performed in a stainless-steel high-vacuum chamber with a base pressure of ~ 1×10^{-8} Torr. Samples were pressed, as 7 mm diameter disks, into a tungsten grid and then clamped onto a sample mount coupled to a precision manipulator. Au/TiO_2 and reference TiO_2 samples were pressed into the same mesh allowing studies to be performed on the two materials under identical experimental conditions. An empty region of the grid was used to monitor gas phase species in the chamber and was used as a background for surface adsorption and desorption studies. Details on the vacuum chamber and sample mount can be found in Chapter 2. An FTIR spectrometer (Thermo, Nexus 470 FTIR) with an external liquid-N_2 cooled MCT-A detector and a spectral resolution of 2 cm^{-1} was used for the collection of IR data. For this work, the sample pretreatment procedure followed an oxidative treatment with O_2 at 573 K for 60 minutes and evacuation at the same temperature for an additional 30 minutes. The oxidative pretreatment fully removes the residual products from both samples and activates both samples for further adsorption of propene.

3.2.3 Propene Adsorption

Once cooled to chemical adsorption temperatures, the samples were exposed to varying amounts of C_3H_6 (99.99 % purity, Matheson TriGas CP) and propene-1-^{13}C (99% atom ^{13}C, CDN Isotopes). Propene was either introduced into the chamber by backfilling to a specific pressure or by flowing propene into the chamber under continuous vacuum pumping. Adsorbate–surface interactions were monitored by tracking changes in IR spectra before, during, and after exposure to propene on both the Au/TiO_2 and TiO_2 surfaces. Additionally, infrared spectra acquired during a thermal temperature ramp of 0.13 K/s qualitatively identified the relative binding strengths between different propene geometries on the Au/TiO_2 surface.

3.2.4 Variable Temperature Infrared Spectroscopy

Quantitative energetics of propene–surface interactions were attained by introducing 4 Torr of propene into the vacuum chamber at 170 K. Following propene introduction, the sealed chamber equilibrated at a given temperature for a ten-minute period prior to data collection. The acquisition of infrared spectra ranged from 180 K – 230 K and composed of an average of 250 scans.

The energetics of the propene—surface interactions were quantified through a van't Hoff analysis of the VTIR experimental data shown in eqn. 3.3. This analysis has been shown to be highly successful in characterizing gas-surface binding energetics in a number of studies, and reviewed here.[106] The infrared vibrational feature used to quantify the concentration of propene on the surface of Au/TiO_2 was the 1631 cm^{-1} ν(C=C). Only propene interactions with titania regions of the materials were evaluated.

3.2.5 CO—Propene Coadsorption

CO (99.3%, Airgas CP300) and propene co-adsorption studies were performed at pressures ranging from < 0.1 to 2 Torr of CO being added before, co-fed, and after propene adsorption to

determine where the propene adsorption sites were located. Small changes in the character of the adsorbates were monitored via infrared spectroscopy by subtracting the spectrum of a clean Au/TiO_2 or TiO_2 catalyst from the spectrum obtained following or during exposure of the sample to propene.

3.2.6 Density Functional Theory Calculations of Propene Adsorption

Density functional theory calculations were carried out to determine the binding energies and vibrational frequencies of adsorbed propene on a model Au/TiO_2 system. All DFT calculations were performed by Wenjie Tang and Matthew Neurock at the University of Minnesota. A 3 nm Au particle supported on TiO_2 was simulated by creating a Au nanostructure on a rutile TiO_2 (110) surface—one of the most stable planes on TiO_2 nanoparticles.[33,129-130] The nanostructure consisted of a 3-atomic-layer-high close-packed Au nanorod anchored to the TiO_2 (110) surface. The TiO_2 surface was simulated using a (2 × 3) unit cell, with four O–Ti–O trilayers. The top half of the TiO_2 surface was fully relaxed whereas the bottom half was held fixed to the bulk TiO_2 lattice. All of the Au atoms in the nanorod were allowed to relax in the Z-direction to maintain good lattice matching with the oxide surface. The model Au nanorod on a rutile TiO_2 (110) surface approximates the reactive sites for the supported Au nanoparticles by providing a variety of lower coordinated Au sites that interact with the support. This model has been used previously to successfully simulate chemical processes on supported Au nanoparticles on P25 TiO_2.[18,128,131-132]

All of the DFT calculations reported herein were carried out using the Vienna *ab initio* Software Package (VASP)[133-135] program. The Kohn-Sham one-electron valence states were expanded in a basis of plane waves with a kinetic energy cutoff of 400 eV. The core electrons were described by pseudopotentials constructed with the projector augmented-wave (PAW) method.[136-137] The exchange-correlation energy was evaluated within the generalized gradient approximation

with the PW91 functional.[138] The DFT + U method with a U value of 4.0 eV was implemented to produce a match of band features observed experimentally.[139-140] Spin-polarization was considered for all calculations. The Au/TiO_2 model has a 10 Å vacuum gap in the Z-direction to prevent any image-image interactions caused by the periodic boundary condition. The (2×3) Au/TiO_2 unit cell was sampled with a $(2 \times 2 \times 1)$ k-point mesh.[141] Geometries were considered optimized until the forces on each atom were less than 0.03 eV/Å.

3.3 Results and Discussion

The adsorption mechanism of gaseous propene onto two particulate surfaces, P25 TiO_2 and Au/TiO_2, has been studied via *in situ* vibrational spectroscopy and DFT calculations. The objective of this work is to characterize propene–Au interactions, which occur on the surface of TiO_2-supported Au nanoparticulate catalysts that have been previously explored for facilitating the propene epoxidation reaction.[38,51] Below, we provide experimental and theoretical evidence that propene binds to Au/TiO_2 through two separate adsorption sites. These two binding configurations, characterized by significantly different C=C stretching frequencies, binding energies, and differing CO coadsorption behavior provide insight into the key propene activation step associated with epoxidation to propene oxide.

3.3.1 Propene Adsorption at Low Temperatures

The initial stages of propene adsorption were studied by exposing thermally activated Au/TiO_2 and TiO_2, to 1 Torr of pure propene at 170 K, a temperature low enough to achieve extended surface residence time and limited reactivity. Infrared spectra, recorded *in situ* and referenced to the pre-exposed samples, are provided in Figure 3.1. The difference spectra display a number of positive-going bands that indicate new vibrational features associated with surface

adsorbates and one high-energy negative-going band that represented a decrease in absorbance due to a change in the character of the surface-bound hydroxyl groups following propene adsorption.

The characteristics of propene adsorbed on TiO_2 and Au/TiO_2 were similar, as evidenced by the strong overlap in infrared spectral features for the two samples. The high wavenumber spectral region, shown in Figure 3.1A, strongly suggests that only a small fraction of propene either displaced or interacted with previously existing surface hydroxyl groups, as revealed by a small depletion feature above 3700 cm^{-1}. However, the coverage of hydroxyl groups was minor relative to exposed Au and Ti sites due to the high temperatures used to pretreat and dehydroxylate the sample. In addition, the bands assigned to the ν(CH) stretching motions of the adsorbed molecules are nearly identical in terms of both peak position and intensity. The similarities between the Au/TiO_2 and TiO_2 spectra indicate that most of the propene binding in the Au/TiO_2 sample occurred at Ti sites remote from the Au particles or that propene bound to Au does not significantly affect the C-H stretching frequency of adsorbed propene.

Consistent with similarities in the IR spectra for propene adsorption in the high wavenumber region, Figure 3.1B shows strong spectral overlap for the two samples in the fingerprint region from 1900 to 900 cm^{-1}. In particular, spectra for ^{12}C-propene on both surfaces (spectra depicted in red and black) show an intense band at 1631 cm^{-1}, which previous studies attributed to the interaction of propene π electrons with Ti sites remote from the Au nanoparticles.[38,122] Upon coordination of the π electrons with surface Ti sites, the C=C band redshifts by 20 cm^{-1} relative to the same band in the gas phase (the ν(C=C) stretch of the gas-phase molecule absorbs 1652 cm^{-1} photons).[142] The 20 cm^{-1} redshift in vibrational energy of the double bond suggests that the π–Ti interaction only slightly affects the electronic structure of propene; therefore, adsorption at this site is likely molecular in nature and weak, relative to other more

covalent interactions. Stronger interactions are expected to have a more profound effect on the stretching frequency of the double bond.[143] The two samples also exhibit similar C-H bending vibrations (1450 – 1300 cm^{-1}) except for a small band located at 1406 cm^{-1} for the Au/TiO_2 sample. This unique band is most likely the δ(CH) vibration of propene adsorbed onto Au.[38] The most profound difference in the IR spectra for the two samples is a feature at 1550 cm^{-1}, which only appears in the spectrum following propene exposure to Au/TiO_2.

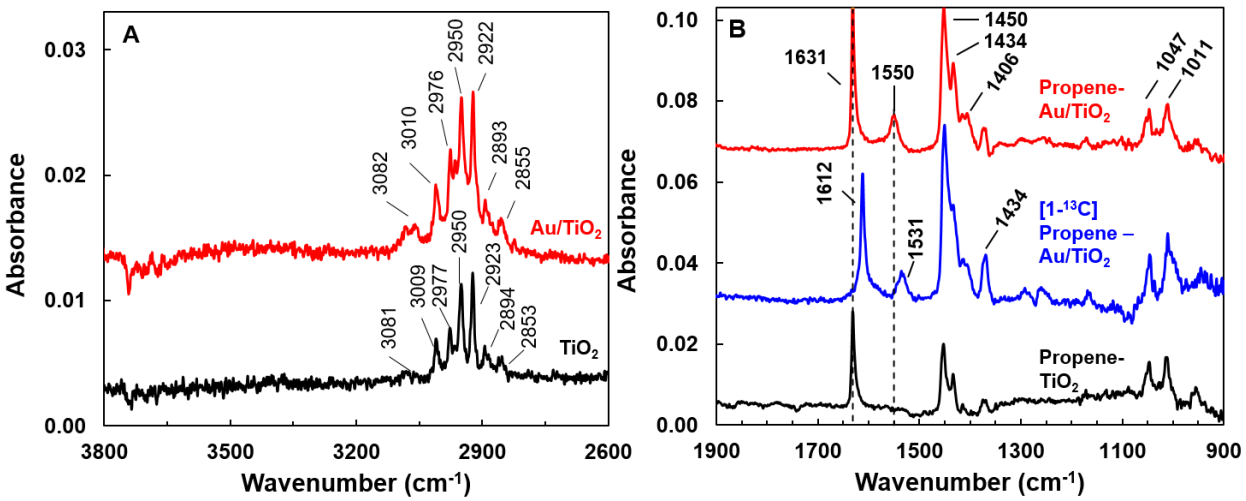

Figure 3.1. Infrared spectra recorded during the adsorption of ^{12}C-propene onto activated Au/TiO_2 (black trace) and TiO_2 (red trace) at 170 K. Panel A provides the high wavenumber region (4000 – 2500 cm^{-1}). Panel B shows the fingerprint wavenumber region (1900 – 900 cm^{-1}). Each spectrum shown above represents an average of 250 scans. Included in panel B is the adsorption of [1-^{13}C] propene on Au/TiO_2 (blue trace).

We hypothesize that the 1550 cm^{-1} feature (identified only on Au/TiO_2) results from a further red-shifted C=C stretch for molecularly adsorbed propene on Au particles. The infrared spectrum for isotopically labeled propene, $CH_3CH=^{13}CH_2$, adsorbed onto Au/TiO_2 (blue spectrum in Figure 3.1B) confirms the assignment of the band at 1550 cm^{-1} to that of the C=C stretch of

propene. The redshift associated with the ν(C=C) of [1-^{13}C] propene follows Hooke's Law. Specifically, Hooke's law for a classical harmonic oscillator model states:

$$\nu = \frac{1}{2\pi}\sqrt{\frac{k}{\mu}} \tag{3.1}$$

where ν is the vibrational frequency, μ is the reduced mass, and *k* is the spring constant. Hooke's law predicts an approximate 30 cm^{-1} redshift of the ν(C=C) band for the [1-^{13}C] propene molecule compared to the naturally occurring propene sample—similar to our observation and the observations of others.[144] The reason for the large vibrational energy difference between propene bound to Ti sites and propene bound to Au sites ($\Delta\nu$ = 81 cm^{-1}) is likely due to significant charge redistribution. The significant electron density associated with the Au atom perturbs the sp^2 hybridization of the double bond and thereby reduces the bond order.

Significant charge redistribution from Au to the antibonding π orbital of propene would reduce the bond order, elongate the bond, and lower the stretching frequency of the molecule. Previous studies suggest that this type of adsorbate–metal interaction may be attributed to either (a) a di-σ interaction, where the two carbon atoms involved in the propene double bond form bonds with two adjacent metal atoms (Figure 3.2D-F), or (b) a (πσ)-interaction, where the two carbon atoms are bound to a single metal site (Figure 3.2A-C). In the case of the (πσ)-interaction, the hybridization of the C-C bond lies somewhere between the sp^2 π interaction and the nearly sp^3 di-σ interaction and thus the shift in ν(C=C) is less significant compared to typical di-σ binding.[143,145]

3.3.2. Site-Specific Band Assignment through Density Functional Theory

Density functional theory was employed to further elucidate the binding sites and configurations of propene on Au/TiO$_2$. Both the (πσ)- and the di-σ interactions between propene and Au were identified in previous computational studies of olefin adsorption on small Au clusters.[120,125,146] In the current study, the vibrational frequencies for both the (πσ)- and the di-σ

interactions were calculated for propene adsorbed onto a Au nanorod anchored to a titania support. Figure 3.2 provides calculated vibrational frequencies of the C=C bond and subsequent binding enthalpies for the minimum energy configuration at a particular Au site (Au coordination: 7) in both the (πσ)- and the di-σ configurations. Propene bound to Au through the (πσ)-coordinated model provided calculated ν(C-C) vibrational frequencies between 1551 – 1536 cm^{-1}, dependent on the environment around the adsorbed molecule (Figure 3.2A-C). Upon (πσ)-adsorption, the propene C=C bond elongates, with a bond length between 1.38 - 1.39 Å, which is 0.05 - 0.06 Å longer than the C=C bond length for the isolated molecule in the gas phase (1.33 Å). The di-σ interaction of propene bound to two adjacent Au atoms produced vibrational energies for the ν(C-C) stretch between 1471 – 1460 cm^{-1} (Figure 3.2D-F), with the propene C=C bond length between 1.43 -1.45 Å. Previous studies have shown that the large redshift in the ν(C-C) vibrational energy for the di-σ interaction is due to greater sp^3 character of the carbon atoms involved in the bond with the surface.[145] The DFT calculations for propene adsorbed through the (πσ)-interaction and the di-σ interaction on Au provided similar frequencies for ν(CH) and δ(CH) motions for a variety of environments.

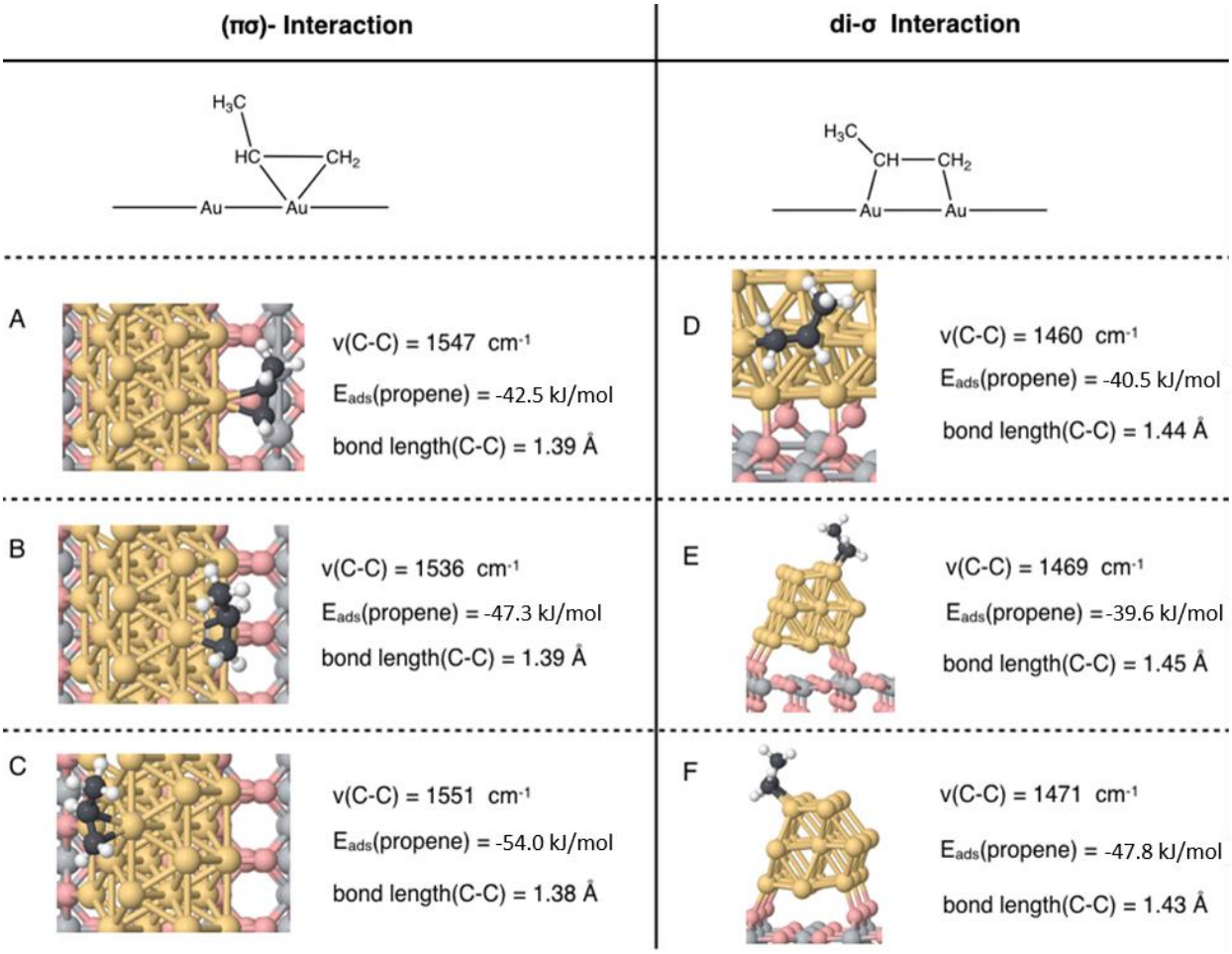

Figure 3.2. Density functional theory calculations for adsorption energies and stretching frequencies of the ν(C-C) upon propene adsorption to a Au site in the (πσ)-coordination (A, B, C) and the di-σ coordination (D, E, F). The Au atoms, Ti atoms, O in the TiO_2, adsorbed C atoms, and H atoms are shown in gold, gray, pink, black, and white, respectively. E_{ads} represents the adsorption energy.

Comparison of the experimental IR spectra to the DFT-calculated vibrational frequencies strongly suggest that propene binds to Au exclusively through the double bond in a (πσ)-configuration at a single atomic Au site. The experimentally obtained IR vibrational bands and DFT calculated frequencies for propene adsorbed on Au/TiO_2 are tabulated in Table 3.1.

Therefore, the thermally activated Au/TiO_2 sample appears to present two modes of adsorption for propene: the ($\pi\sigma$)-interaction of propene on Au and the π interaction with Ti sites on the TiO_2 support.

Table 3.1. IR frequencies of C_3H_6 in gas phase, on TiO_2, on Au/TiO_2 and DFT calculated stretching frequencies for C_3H_6 on Au in two coordinated orientations (($\pi\sigma$) & di-σ).

Vibrations	Gas phase[142]	TiO_2	Au/TiO_2	DFT ($\pi\sigma$)-Propene–Au	DFT di-σ Propene–Au
$\nu_{as}(CH_2)$	3090	3081	3082	3085	3078
$\nu(CH)$	3013	3009	3010	3012	3008
$\nu_s(CH_2)$	2992	2977	2976	2977	2969
$\nu_{as}(CH_3)$	2954, 2933	2950, 2922	2950, 2922		
$\nu_s(CH_3)$	2870	2894, 2853	2893, 2855		
$\nu(C=C)$	1652	1632	1631		
$\nu(C\text{-}C)$ $\pi\sigma$	--	--	1550	1547	--
$\nu(C\text{-}C)$ diσ	--	--	--	--	1460
$\delta_{as}(CH_3)$	1474, 1443	1452, 1434	1452, 1434	1448, 1431	1452, 1434
$\delta(CH)$ on TiO_2	1419, 990	1415	1415		
$\delta(CH)$ on Au	--	--	1406	1408	1407
$\delta_s(CH_3)$	1378	1368	1373	1371	1373
$\delta(CH_2)$	1298	1309	1309	1308	1306
$\rho(CH_3)$	1171, 1045	1172, 1047	1171, 1047		

3.3.3 Propene—Au and Propene—TiO_2 Binding Energetics

The relative stabilities of each propene–surface interaction were studied experimentally through temperature programmed desorption. A continuous thermal rate of 0.13 K s^{-1} heated the Au/TiO_2 sample while IR spectra were continuously recorded. A 3D plot of the IR spectra is shown

in Figure 3.3A. During the temperature ramp, the propene adsorbed to TiO_2 regions through the π-interaction (IR band at 1631 cm^{-1}) desorbed from the surface at a lower temperature and a faster rate compared to the propene molecules adsorbed on Au (IR band at 1550 cm^{-1}) through the (πσ)-bond. Figure 3.3B provides a plot of the normalized integrated absorbance for both the 1631 cm^{-1} and 1550 cm^{-1} IR bands at different temperatures. The propene bound through the (πσ)-interaction with Au appears to persist on the surface over a greater temperature range than propene bound to the titania regions of the sample. This temperature-dependence to surface concentration demonstrates that propene molecules bound to Au are much more thermally stable than propene molecules bound to titania through π-interactions. In fact, propene on titania regions of the sample completely desorbed by 270 K, while propene on Au persisted above 350 K.

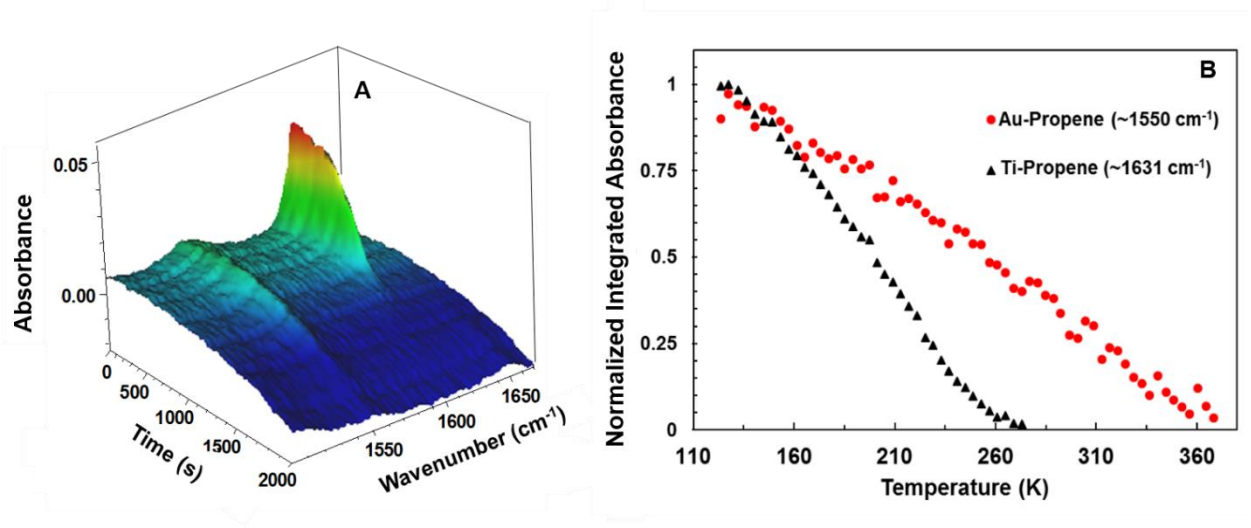

Figure 3.3. Temperature programmed desorption profiles for propene leaving the Au/TiO_2 surface. Panel A provides the IR spectra recorded during the 0.13 K s^{-1} temperature increase. Each spectrum in the temperature profile represents an average of 30 scans. Panel B shows the integrated absorbance of the 1550 and 1630 cm^{-1} IR bands (plotted as normalized surface coverage) at specific temperatures throughout the temperature ramp. The 1550 cm^{-1} band was integrated over the range 1510 - 1585 cm^{-1} and the 1631 cm^{-1} band was integrated over the range 1585 – 1650 cm^{-1}.

Quantitatively, I applied the principles of the van't Hoff analysis to extract the enthalpy of adsorption for the propene–TiO_2 interaction. Briefly, the Au/TiO_2 sample was exposed to a fixed amount of propene and the temperature was increased while acquiring infrared spectra (Fig. 3.4A). The propene–TiO_2 concentration at 1630 cm^{-1} decreased as the temperature increased and therefore a Van't Hoff analysis was performed to extract the energetics of the adsorption event. Using the low coverage assumption (Eq. 2.3), we identified the standard enthalpy of adsorption for propene binding on Ti^{4+} sites to be -15.3 kJ/mol. Under the same thermal conditions, the Au–propene vibrational feature remained constant and therefore the van't Hoff analysis cannot be applied to determine the standard enthalpy of adsorption. Since propene binds much stronger to Au compared to TiO_2 (as shown in both Figure 3.3 and 3.4), we speculate that the standard enthalpy of adsorption for propene–Au interactions is significantly more favorable compared to the propene–TiO_2 interaction.

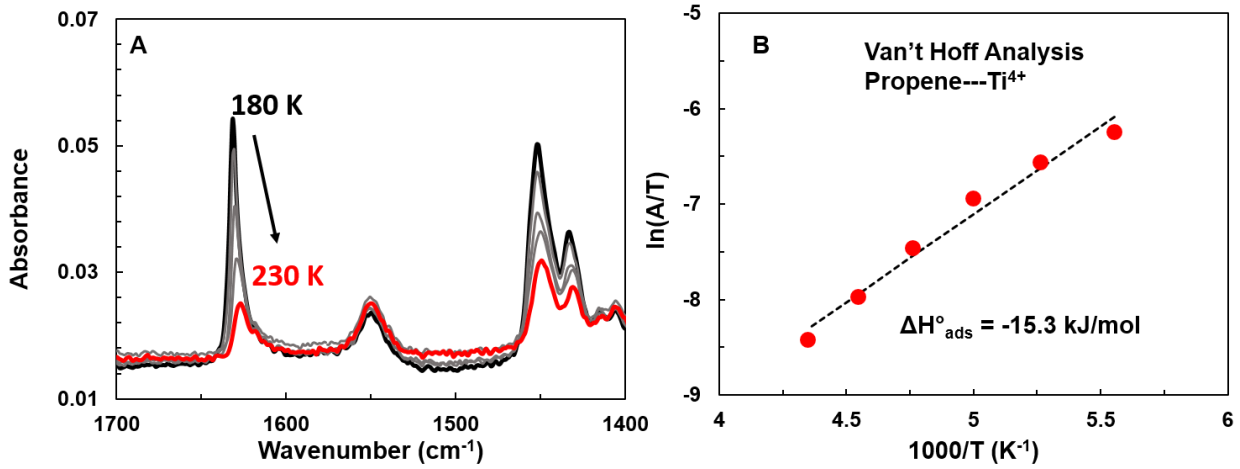

Figure 3.4. Variable temperature adsorption of propene over an Au/TiO_2 sample. (A) Infrared spectra acquired at 180 K, 190 K, 200 K, 210 K, 220 K, and 230 K. (B) Van't Hoff analysis of the integrated intensity of 1631 cm^{-1} feature associated with the propene—TiO_2 interaction.

In order to provide quantitative measures of the enthalpy of adsorptions for both the propene–TiO_2 and the propene–Au interactions, we sought the help of DFT calculations provided by our collaborators at the University of Minnesota. The DFT calculated binding enthalpies for the minimum energy configurations of different (πσ)-interactions on Au provide information about the relative strength of the propene–Au interaction compared to other binding locations on the surface (propene–TiO_2). For the propene–TiO_2 interactions, previously reported binding enthalpies for this same Au/TiO_2 model surface have been reported as -41.5 kJ/mol and -28.9 kJ/mol for propene–TiO_2 remote from and propene–TiO_2 near the Au/TiO_2 interface, respectively.[38] In the current study, the largest DFT-calculated binding enthalpy for a propene–Au (πσ)-interaction was found to be -54.0 kJ/mol (Figure 3.2C). Our DFT results indicate, consistent with the experimental data of Figure 3.3 and Figure 3.4, that propene (in minimum energy configurations) binds much more strongly to Au than to TiO_2.

3.3.4 Connections with Previous Work

With the data gathered in these low temperature studies, we conclude that two binding mechanisms occur when propene adsorbs onto the surface of Au/TiO_2 – a π interaction with titania and a (πσ)-interaction with Au. The propene double bond elongates upon coordination to the Au nanoparticle as electron density from the Au particle perturbs the sp^2 hybridized orbital of the bond. The (πσ)-interaction of propene bound to a single Au atom could explain the high selectivity for propene oxide during the hydro-epoxidation of propene on Au/TiO_2 surfaces as shown by a variety of other research.[48,50-52] Recent literature has suggested that propene is activated on the Au particle during the epoxidation process.[53,55,147] Nijhuis et al. utilized delta-mu analysis within *in situ* XANES experiments of a Au/SiO_2 sample to discover a feature at the Au L_3-edge in the presence of propene, oxygen, and hydrogen. They attributed this spectral change to propene

adsorbed to Au through a π-interaction.[112] Our results are consistent with this interpretation while providing additional insight into the details of the binding mechanism. Recent theoretical studies by Baker et al. agree with this suggestion as they determined an oxygen covered, defective Au(111) surface depletes the electron density from the π orbital of propene and subsequently accumulates charge between each sp^2 carbon and the Au adatom where adsorption occurs (similar to the (πσ)-interaction).[116] Our results highlight the favorable binding energy of propene with Au, in addition to the elongation of the propene double bond upon coordination and suggest that propene bound through the (πσ)-interaction is the activated species necessary for epoxidation on the surface of Au/TiO_2. However, in order to identify how propene adsorbs at temperatures required for propene epoxidation (300 – 400 K), room temperature studies of propene adsorption are necessary.

3.3.5 Propene Adsorption at Room Temperature and Competitive Adsorption with the Probe Molecule, CO

In order to elucidate the adsorption characteristics of propene at temperatures high enough for epoxidation to occur, room temperature adsorption and competitive adsorption studies were required. Competitive adsorption experiments with CO can identify specific locations the propene molecules bind by observing the displacement of CO molecules and identify local perturbations of the surface site electronic structure as evidenced by vibrational shifts in the ν(CO). Additionally, adsorption at realistic temperatures provides a clear picture of the catalyst surface structure that would be present during an epoxidation reaction.

The CO coverage, stretching frequency, and binding characteristics all identify specific electronic structure characteristics on the Au/TiO_2 sample and also provide insight into the adsorption characteristics of propene on Au/TiO_2. The infrared spectrum for CO adsorbed on the O_2-activated Au/TiO_2 sample at room temperature is provided in Figure 3.5A. The ν(C-O)

associated with CO bound to Au (Figure 3A, black curve) at 2120 cm^{-1} is shifted to higher frequencies, relative to highly reduced Au/TiO_2 samples.[28,38] The large blueshift in frequency may be due to a decrease in negative charge for the Au particles as oxygen species present on or near the Au sites scavenge electrons.[128] In fact, the Au–CO IR band appears to be composed of two components. The two blue Lorentzian curves in Figure 3.5A provide an excellent model fit to the data. We assign the band at 2133 cm^{-1}, based on previous literature[128,148] to CO on $Au^{\delta+}$ sites that reside at the Au perimeter. Others[23,149-150] have shown that the under-coordinated Au sites that reside at the perimeter, bind to O atoms from the TiO_2 lattice, form Au-O-Ti linkages, and shift electron density away from the Au atoms. The activated oxygen species at the Au/TiO_2 interface act to further oxidize the Au to provide positively charged surface sites for CO adsorption. The positively charged sites attract more CO than the Au^0 sites[151] and induce a blueshift in the stretching frequency of the adsorbed CO.[152] The surface characterization of CO adsorption is critical because, as stated above, propene is expected to bind to these same undercoordinated surface sites near the Au/Ti interface.

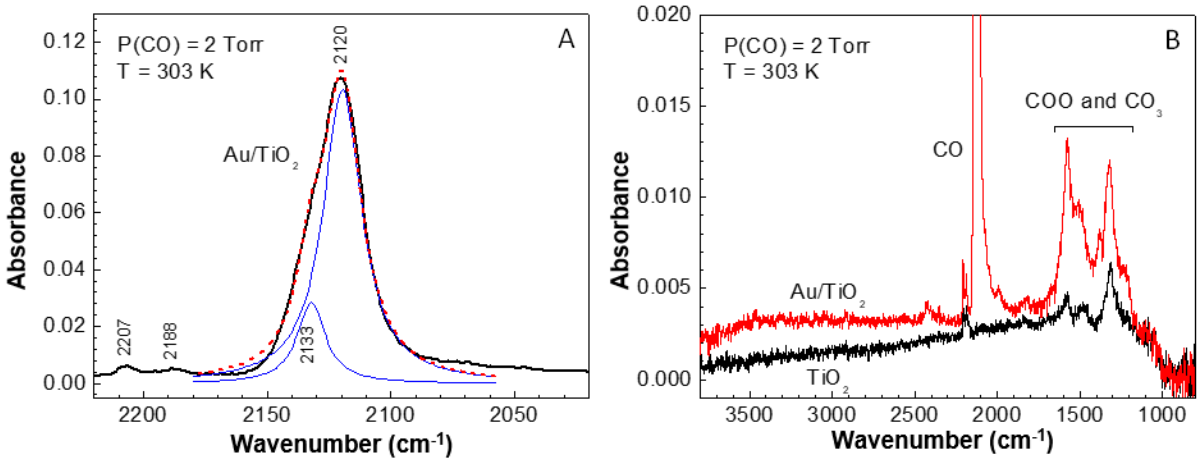

Figure 3.5. Samples activated with 10 Torr of O_2 at 573 K for 60 minutes and evacuated at 573 K for an additional 30 minutes. (A) CO/Au infrared region after adsorption of 2 Torr CO at 303 K on activated Au/TiO_2. The blue curves are bands obtained after Lorentzian fitting of the Au-CO absorbance band. (B) Full mid-IR spectrum for the adsorption of 2 Torr CO at 303 K on activated Au/TiO_2 (red trace) and TiO_2 (black trace) samples.

It should also be noted that additional absorbance bands in the 1600-1300 cm^{-1} region can be assigned to vibrational motions of carbonate and carboxylate species[40] as highlighted in Figure 3.5B. The Au/TiO_2 catalyst (red trace) produced a significantly larger amount of carbonates/carboxylates than the TiO_2 catalyst (black trace), which is expected due to the presence of oxygen at dual perimeter sites where Au-O-O-Ti interactions activate the O_2 bond.[18]

Experiments with pre- and co-adsorbed CO–propene were also performed for the activated catalysts as a means of gaining insight into the surface site dependence to propene adsorption on the activated surface at room temperature. When 2 Torr of CO was pre-adsorbed on the Au/TiO_2 catalyst at 303 K, CO quickly reacted with some of the active oxygen species available at the Au/Ti perimeter to produce carbonate/carboxylate species. The CO that remained was mainly adsorbed at partially charged gold sites as $Au^{\delta+}$-CO species giving rise to an IR band at 2140 cm^{-1} and at

low-coordinated gold sites near the perimeter as Au^0-CO species, identified at 2120 cm^{-1} (see Figure 3.6A, spectrum i). Co-adsorption of propene by incremental admission of up to 2 Torr C_3H_6 produced the spectral developments shown in Figures 3.6A, 3.6C and 3.6D, ii-ix. In Figure 3.6A, the addition of C_3H_6 causes the Au-CO band intensity to decrease and redshift to a frequency as low as 2087 cm^{-1}.

As described above, the large ~30 cm^{-1} redshift reflects the Au oxidation state change due to electron density transfer from C_3H_6 to the Au sites. The decrease in the Au-CO band intensity is due to the displacement of CO adsorbates on Au sites by C_3H_6 molecules. The loss of CO on Au sites (blue open triangles) and the redshift in the Au-CO band frequency (blue closed triangles) during propene exposure are quantitatively shown in Figure 5B. A comparison of these two curves indicates that the CO intensity (an indication of CO coverage) changes at a greater rate than the vibrational frequency of Au-CO. The lack of correlation in the rates of change for these two spectral features implies that CO is directly displaced by propene molecules, rather than driven from the surface by extensive charge transfer.

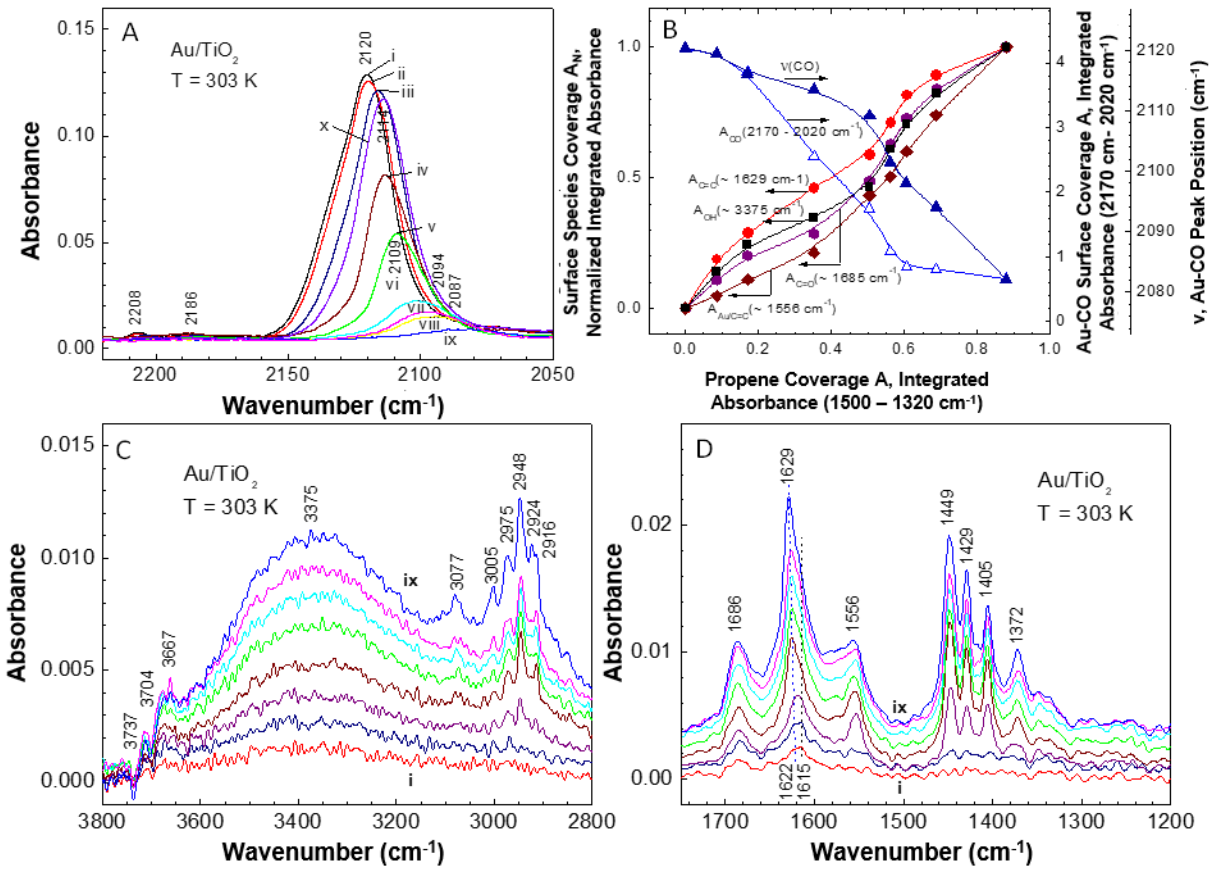

Figure 3.6. Samples activated with 10 Torr O_2 at 573 K for 30 minutes and evacuated at 573 K for 30 minutes. (**i**) Adsorption of 2 Torr CO on activated samples; (**ii-ix**) co-adsorption of propene on CO pre-covered surface. Incremental (**ii-ix**) increase of propene partial pressure (0.01 - 2 Torr) in the chamber; (**x**) re-adsorption of 2 Torr of CO on evacuated sample. (A) CO/Au IR absorbance region, (B) Surface coverage of propene-derived species (left), Au-CO surface coverage (right) and Au-CO peak position (right) changes as propene coverage increases; C and D. OH, C-H and fingerprint regions of the IR spectrum as propene partial pressure increases after CO pre-adsorption.

The IR absorbance bands due to propene vibrational modes (on the CO pre-covered surface) in both the CH-stretch and the fingerprint regions do not differ from those observed with

the clean surface at low temperature, as revealed by Figure 3.6C, D. However, the adsorption associated with propene bound to Au at 1556 cm^{-1} was initially inhibited (see Fig. 3.6D, spectrum i, ii). This suggests that CO bound to undercoordinated Au atoms or carbonate/carboxylates produced during CO adsorption bind and resist competitive adsorption from gas phase propene molecules. The production of an aldehyde species (band at 1686 cm^{-1}, and a result of propene reaction) suggests propene reacts with the Au/TiO_2 surface at 300 K but is much less reactive than propene adsorption onto a clean-oxidized surface at room temperature.[38] These differences observed during room temperature propene adsorption compared to low temperature adsorption suggest partial passivation of the active oxygen-containing Au/TiO_2 perimeter zone by carbonate/carboxylate species produced during CO pre-adsorption and oxidation. Overall, exposure of CO resulted in competition with low concentrations of propene exposure. However, as larger concentrations of propene filled the chamber similar absorption configurations were identified as was the case during low temperature propene adsorption.

After the CO and propene co-adsorption experiment, the IR cell was evacuated and the state of Au sites was again probed by CO adsorption. Subsequent CO adsorption onto Au/TiO_2 (spectrum x in Figure 3.6A) revealed a smaller intensity of the Au-CO band compared to the concentration that was initially observed (Figure 3.6A, spectrum i) and the Au-CO feature position was shifted to 2114 cm^{-1}, indicative of propene and/or propene oxidation products remaining adsorbed on Au—likely at the perimeter and low-coordinated Au sites. The redshift in vibrational frequency relative for the Au-CO feature is likely due to the reaction of propene with O species—previously scavenging electron density away from the Au particles.

The spectroscopic data for the adsorption and co-adsorption of propene and CO on the Au/TiO_2 surface strongly suggest that at room temperature propene reversibly adsorbs both at TiO_2

and at low coordinated Au sites; however, some oxidation products bind more strongly. The high temperature oxidative (573 K) activation of the Au/TiO_2 sample produced active oxygen species at the Au/Ti perimeter that were involved in irreversible adsorption of propene via its oxidation to aldehyde products. These oxidation products alter Au/TiO_2 electronic structure, block surface sites responsible for propene adsorption and modify overall propene chemistry at room temperature as evidenced by co-adsorption of the probe molecule, CO. Overall, we can state with certainty that at room temperature propene still binds through two different geometries on the surface of Au/TiO_2: a π-interaction with TiO_2 and a (πσ)-interaction with low coordinated Au sites.

3.4. Summary

In this work, we have provided evidence for two discrete adsorption sites for propene on nanoparticulate Au/TiO_2. On Au, propene binds through a (πσ)-interaction where electron density from the propene double bond interacts with a single Au surface atom. On TiO_2, propene binds through a π-interaction at Ti sites. These two binding motifs are distinguishable by the ν(C-C) stretching frequency of the propene double bond. Furthermore, experimental TPD and VTIR results as well as DFT calculations indicate that the propene–Au adsorption interaction is significantly stronger than the propene–TiO_2 interaction. We hypothesize that propene binding to low-coordinated Au surface sites results in an elongation of the propene double bond, which may activate the molecule for epoxidation in the presence of hydrogen and oxygen.

Chapter 4

Mechanistic Insights of Propene Epoxidation to Form Propene Oxide on Au/TiO_2: IR Spectroscopic Studies

4.1 Introduction to Au Nanoparticle Catalysis

Gold particles in the nanometer diameter range have unique properties that make them ideal catalysts for oxidation reactions.[12] Other nanoparticles such as Pt, Cu, and Fe are extremely reactive in the presence of O_2; so much so that they form stable oxide surface layers, which deactivate the catalysts.[153-154] Gold, in contrast, provides an active site for O_2 adsorption without reacting directly with molecular O_2 to form an oxide. Recent studies have shown that molecular oxygen adsorbs on Au/TiO_2, and likely on other Au supported catalysts, at a highly reactive area at the interface between the Au nanoparticle and the TiO_2 support.[18,132] The Au/TiO_2 interface allows for electron density to transfer from the Au to the Ti^{4+} sites near the perimeter, and subsequently into the $2\pi^*$ antibonding orbital of the O_2 molecule.[23] The electron transfer to the O_2 antibonding orbital results in the elongation of the O_2 molecule, which lowers the activation energy for dissociation to ~0.5 eV compared to ~2.2 eV on a Au (111) single crystal as the adsorbed O_2 species contains excess negative charge.[23,155-156] Similar electron transfer effects occur at the Au-O-Ti linkages that allow for activation of organics and other molecules.[157] Another factor contributing to the enhanced activity of Au nanoparticles is the abundance of low-coordination sites, which are known to activate H_2 and olefins.[158] For example, H_2 is known to spillover to the support after dissociation on under-coordinated Au sites.[109,159-161] The Au/TiO_2 interfacial region where O_2, H_2 and olefins adsorb, activate, and react, make Au/TiO_2 a good potential catalyst for epoxidation reactions.

4.1.1 Epoxidation of Propene over Supported-Au

Motivated by the promise of supported gold particles, numerous groups have studied propene epoxidation over Au/TiO_2,[50-53,56,123-124,162-164] Au/TS-1 (mesoporous titanosilicate),[115,118,165-171] Au/SiO_2,[121] Au/CeO_2[172] and Au/Al_2O_3.[173] Several main unifying results and theories have emerged from these previous studies:

1. H_2 dissociates on the Au sites and reacts with O_2 to form HOOH and/or OOH, which is then transferred to the support in the form Ti-OOH;
2. Propene adsorbs at the Au-Ti interface and reacts with the OOH intermediate to produce propene oxide (PO);
3. Bidentate propoxy species are formed during the reaction as deactivating species; and,
4. Carbonates/carboxylates are produced and deactivate the catalyst.

Despite this progress in understanding the PO formation mechanism over Au/TiO_2 catalysts, several key questions remain. Interestingly, one of the largest controversial questions regarding the propene epoxidation reaction revolves around the identity of the oxidizing intermediate. The likely intermediate for this system is OOH, which is a short-lived and extremely reactive intermediate in the presence of organics.[158] Thus, directly observing the OOH species with any surface technique is challenging. Recent studies[167,174-175] have claimed to experimentally observe the Ti-OOH species while theoretical DFT calculations[123-124] have identified Au-OOH sites as possible oxidizing intermediates. In order to elucidate the oxidizing intermediate mechanism and the role the intermediate plays in the epoxidation reaction, the initial mechanistic steps needs to be fully characterized including the location of the reactants and of the active sites. In Chapter 3, we showed experimental and computational evidence that the sites for propene adsorption are on low-coordinated Au atoms near the Au/TiO_2 interface and at TiO_2 sites away

from the perimeter.[37] Interestingly, propene adsorbs specifically through a ($\pi\sigma$)-interaction at Au sites, which provides a weakening of the C=C bond and likely lowers the activation barrier for epoxidation (see Chapter 3 for details).[37] Furthermore, the target product, PO, has also been found to adsorb on both the Au sites and on TiO_2 sites at the Au/Ti interface.[38]

With this knowledge, a detailed and systematic look at each step in the epoxidation reaction has been performed in addition to studies between the product, PO, and the $H_2 + O_2$ reaction mixture. For these studies, we have employed infrared spectroscopy in conjunction with density functional theory to explore the active sites of the reactants, intermediates and products for propene oxidation over a prototypical Au/TiO_2 nanoparticle catalyst.

4.2 Procedural Methods

4.2.1 Experimental Measurements

The experiments were performed using a high vacuum IR cell with a base pressure of 1×10^{-8} Torr, and the cell is described in Chapter 2. The commercial Degussa P25 TiO_2 nanoparticles and as-synthesized Au/TiO_2 nanoparticles via the deposition-precipitation method[36] were pressed separately on the same tungsten grid and transferred into the cell for comparison studies under the same environmental conditions. The Au particles were previously characterized to have an average diameter of ~3 nm and ~8% by weight Au loading for the Au/TiO_2 catalyst.[128] A Thermo, Nexus 470 FTIR spectrometer was used for measuring the spectral data with each spectrum containing 250 scans at a resolution of 2 cm^{-1}. A separate region on the W-grid with no nanomaterial was used to provide a background spectrum for adsorption studies in addition to monitoring gas phase species.

Before every experiment, the catalysts were heated to 573 K under vacuum and exposed to 10 Torr O_2 for 60 minutes, and then the cell was evacuated for an additional 30 minutes at the

same temperature. The above pretreatment process removed any hydrocarbon or H_2O impurities either due to air contamination during catalyst transfer or from previous gas exposures. After evacuation at 573 K, the samples were cooled to 303 K and the desired gas or gas mixture was introduced. The gases used include propene (C_3H_6, 99.99 % purity, Matheson TriGas CP), O_2 (99.994 % purity, Airgas Ultra High Purity), H_2 (99.999 % purity, Airgas Ultra High Purity), CO (99.3 % purity, Airgas CP300), and propene oxide (C_3H_6O, PO, 99 % purity, Sigma Aldrich). The adsorption of the probe molecule, CO, effectively characterized the exposed surface site before and after adsorption of epoxidation reactants. Evaluation of the infrared spectra associated with CO adsorption discerned where the reactant and product species adsorbed on the surface of the catalysts. Additionally, PO adsorption and reaction studies were performed to assign IR bands in the epoxidation reaction study as well as to determine which products formed due to interaction with PO, instead of being intermediates to form PO.

4.2.2 Theoretical Methods

All DFT calculations were performed by Wenjie Tang and Matthew Neurock at the University of Minnesota. First principle periodic plane wave density functional theory (DFT) calculations were carried out using the Vienna Ab Initio Simulation Program (VASP)[133] in order to determine the binding energies, activation energies, and reaction energies associated with the intermediate reaction pathways within the overall propene epoxidation mechanism. The results were used to examine previously proposed mechanisms for the formation of the OOH intermediate in the epoxidation of propene over a model Au/TiO_2 interface.

A (2x3) unit cell with four O-Ti-O tri-layers was used to model the rutile TiO_2(110) surface. The top two tri-layers of the TiO_2 surface were allowed to fully relax while the atoms in the bottom two tri-layers of the TiO_2 slab were fixed to the atoms' lattice positions to mimic the bulk. The 3

nm Au nanoparticles on TiO_2 were simulated by using a close-packed Au nano-rod anchored to a model TiO_2(110) surface. The model provides various interfacial Au and Ti sites, different coordination number (ranging from 7 to 9) Au sites, and has proven to be reliable in mimicking important reactive sites for supported Au catalysts.[18,131-132] All of the Au atoms in the nano-rod were allowed to relax in the Z-direction to maintain good lattice matching with the oxide surface. All of the calculations reported herein were carried out using the PW91 gradient approximation (GGA) exchange correlation functional,[138] and the projector augmented-wave (PAW) method was used to simulate the core electrons.[136-137] The valence electrons were described with Kohn-Sham single-electron wave functions and expanded in the plane-wave basis with an energy cutoff of 400 eV. The DFT+U method was employed to correct the on-site Coulomb interactions with U=4.0 eV to generate experimentally observed electronic structures.[139-140] The Au/TiO_2 model was sampled with a (2 × 2 × 1) k-point mesh.[141] Spin-polarization was considered for all calculations. To prevent any image-image interactions caused by the periodic boundary condition, a 10 Å vacuum gap was added in the z-direction for the Au/TiO_2 model. Geometries were considered optimized when the forces on each atom were less than 0.03 eV/Å.

The reaction pathway and activation barriers were found by the climbing image nudged elastic band (NEB) method,[176-177] combined with the dimer method.[178] The NEB method was used to find the minimal reaction path between the reactant and product states to the point where the perpendicular forces on all of the images along the band were lower than 0.1 eV/Å. The dimer method was subsequently used to isolate the transition state to the point where the force acting on the transition state dimer was lower than 0.03 eV/ Å.

4.3 Results and Discussion

We have employed *in situ* infrared spectroscopy to decipher the details of the propene epoxidation reaction mechanism on the Au/TiO_2 catalyst. Our previous work provided the adsorption sites of propene and propene oxide on Au/TiO_2 to be at Au sites near the perimeter and TiO_2 sites away from the Au/TiO_2 interface. Using this knowledge, we were able to elucidate the likely active sites and mechanism for epoxidation by systematically adding each reactant (C_3H_6, O_2, and H_2) separately to the system and comparing the resulting reactions to the epoxidation reaction results. The conclusions developed from this chapter provide new insight into the overall mechanism that governs the transformation of propene to propene oxide over a prototypical Au/TiO_2 catalyst.

4.3.1 Propene Adsorption on Au/TiO_2 and TiO_2 Nanocatalysts

Previously, we identified propene adsorption on both Au and TiO_2 sites on the Au/TiO_2 catalyst.[37-38] Figure 4.1 shows 2 Torr of propene adsorbed at 303 K on both Au/TiO_2 and TiO_2 catalysts after the previously described oxidative pretreatment. The IR bands at 1630 and 1416 cm^{-1} correspond to the ν(C=C) and δ(CH) modes of propene adsorbed on TiO_2 sites, respectively; on the other hand, the IR bands at 1551 and 1407 cm^{-1} correspond to the ($\pi\sigma$)-configuration of the ν(C-C) mode from the C=C moiety and the δ(CH) mode of propene adsorbed on Au sites, respectively.[37] The adsorption of propene on Au/TiO_2 can be depicted by the following reactions:

$$C_3H_6 + Ti^{4+} \leftrightarrow (CH_2{=}CHCH_3) - Ti^{4+} \quad (4.1)$$

$$C_3H_6 + Au \leftrightarrow (CH_2{-}CHCH_3) - Au \quad (4.2)$$

Further evidence of propene adsorption on Au sites is confirmed by the lack of IR bands at 1551 and 1407 cm^{-1} from the TiO_2 catalyst alone. Reactant adsorption prior to the introduction of epoxidation reaction gases (H_2 and O_2) allows for time-resolved formation of propene oxide in

addition to tracking the depletion of propene on the surface. The additional IR band at 1475 cm^{-1} on the Au/TiO_2 catalyst is believed to be a δ(C-O-H) vibrational motion from an oxidation product formed from propene and residual O on the surface after O_2-pretreatment.

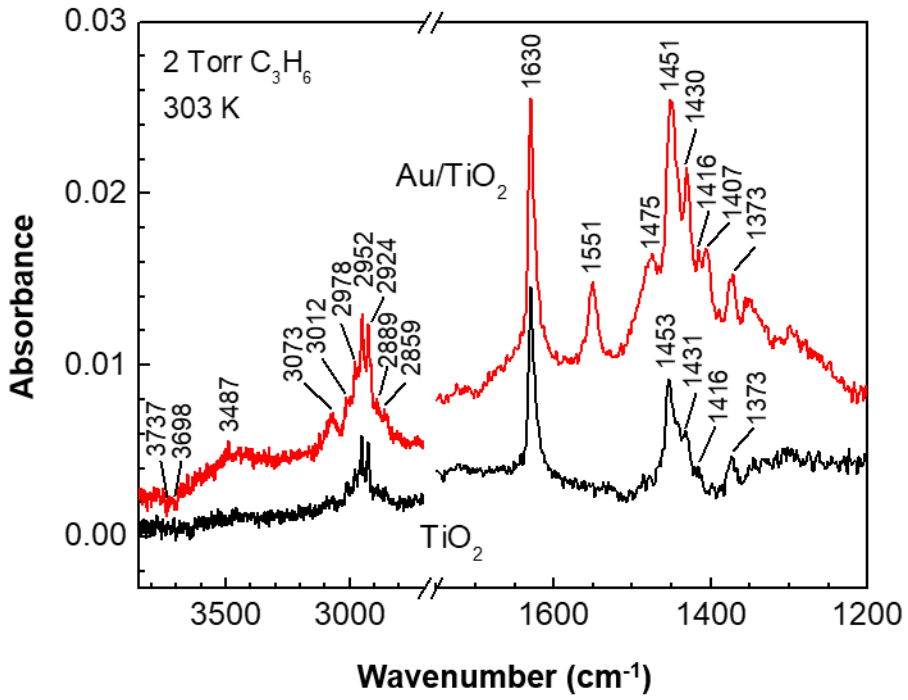

Figure 4.1. Infrared spectrum acquired during propene adsorption on an oxygen activated Au/TiO_2 (red) and a TiO_2 (black) sample. All adsorption experiments were carried out at 303 K.

4.3.2 Propene Epoxidation on Au/TiO_2 using a Mixture of C_3H_6, O_2 and H_2

After propene adsorption on both the Au/TiO_2 and TiO_2 catalysts, the sample was exposed to a gas mixture of 2 Torr H_2 and 2 Torr O_2. The reaction was monitored using IR for 2 hours as shown in Figure 4.2. In order to see small changes, the spectrum before the addition of the H_2 + O_2 gas mixture was subtracted from each spectrum after the gas mixture exposure and therefore negative-going vibrational features are associated with the reaction of propene on the Au/TiO_2 surface. Figure 4.2A reveals an increase in the IR absorbance region 3600-3100 cm^{-1}, which

corresponds to the formation H_2O from the gas mixture of H_2 + O_2 on the Au/TiO_2 catalyst. The water formation mechanism has been previously studied and the activation energy to form H_2O is < 0.3 eV,[158] which signifies an energetically favorable mechanism for H_2O formation at 303 K.

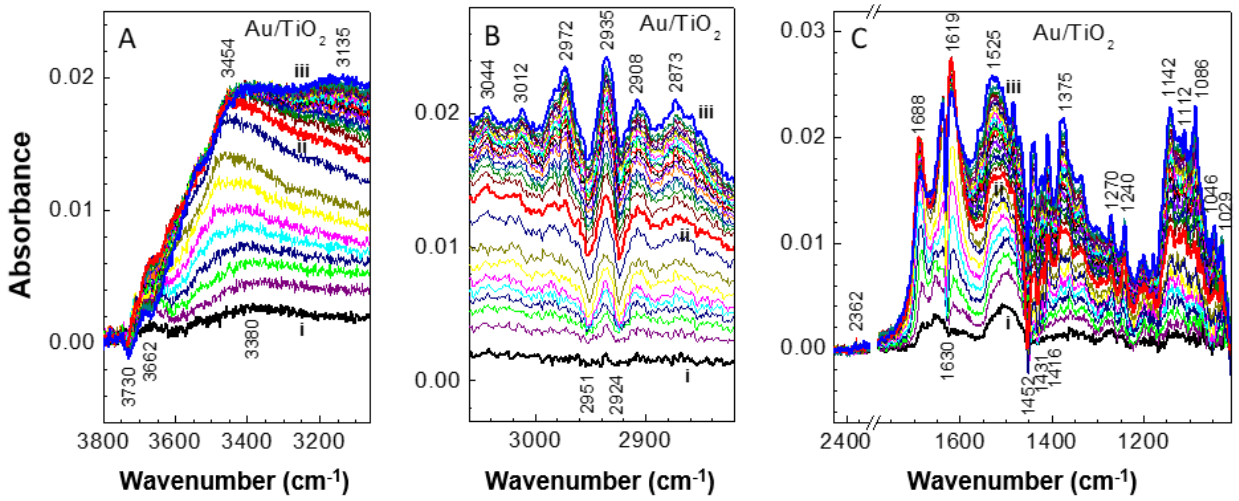

Figure 4.2. Spectra obtained during the interaction of propene-saturated Au/TiO_2 with the epoxidation reactant H_2 + O_2 gas mixture for 2 hours; spectra i-iii: 2 Torr propene (pre-adsorbed) + gas mixture of 2 Torr H_2 and 2 Torr O_2 added. All spectra are referenced to the spectrum of propene adsorbed onto Au/TiO_2.

The C-H region (3100 – 2800 cm^{-1}) of the infrared spectra exhibit vibrational features that both emerge throughout the 2-hour oxidation reaction as well as deplete during the oxidation reaction. Figure 4.2B shows the C-H region with IR bands forming at 3044, 3012, 2972, 2935, 2908, and 2873 cm^{-1} with two distinct IR bands at 2951 and 2924 cm^{-1} disappearing. The IR bands at 2951 and 2924 cm^{-1} are assigned to the $\nu_{as}(CH_3)$ stretches of propene.[37-38,52,122] This is consistent with the reaction of propene to form a new product containing new C-H vibrational features. The positive-going infrared features at 3044, 3102, 2972, 2935, and 2873 cm^{-1} are assigned to $\nu_{as}(CH_2)$, $\nu(CH)$, $\nu_s(CH_2)$, $\nu_{as}(CH_3)$, and $\nu_s(CH_3)$, respectively, for the reaction product, propene oxide (PO).[52] Previous infrared adsorption studies, confirmed by DFT calculations, were performed by

adsorbing PO on the Au/TiO_2 catalyst, and the same IR bands were observed.[38] Further studies of PO adsorption and reactivity are described in more detail in Sections 4.3.5 and 4.3.6.

In the fingerprint region between 1700-1000 cm^{-1} (Figure 4.2C), numerous new vibrational features emerge as the reaction proceeds in addition to the decrease in vibrational features associated with propene, all consistent with the other regions of the infrared window. The negative IR features occur at 1630, 1452 and 1431, and 1416 cm^{-1}, which can be assigned to ν(C=C), $\delta_{as}(CH_3)$, and δ(CH) modes, respectively, for propene adsorbed on TiO_2. Negative propene vibrational features associated with adsorption onto Au, like 1550 cm^{-1}, are convoluted with other IR formation peaks and cannot be observed. Likely, propene adsorbed on both Au and TiO_2 sites is being consumed and forming propene oxide and other side-products. In addition to vibrational features that are associated with the production of propene oxide in the high wavenumber region, other positive-going features at 2362, 1688, 1619, 1525, 1375, 1270, 1240, 1142, 1112, 1086, 1046, and 1029 cm^{-1} are also identified in the spectra. From our previous study focusing on PO adsorption on Au/TiO_2,[38] propene oxide bands appear at 1375 ($\delta_s(CH_3)$), 1270 (symmetric ring breathing), while bands at 1142 (C-O-Ti), 1104 (C-O-Ti), and 1029 (C-O-Ti) cm^{-1} are assigned to propoxy bi-dentate species formed after PO adsorption on TiO_2 regions of the catalyst as shown in Figure 4.3. Bidentate propoxy species can also form after PO adsorption on TiO_2 alone (see Section 4.3.5) and are thought to form through an acid-catalyzed (via a hydroxyl group) epoxide ring opening reaction on the surface of TiO_2.[38,52] Other product bands can be tentatively assigned to CO_2 at 2362 cm^{-1} and H_2O bending at 1619 cm^{-1}.

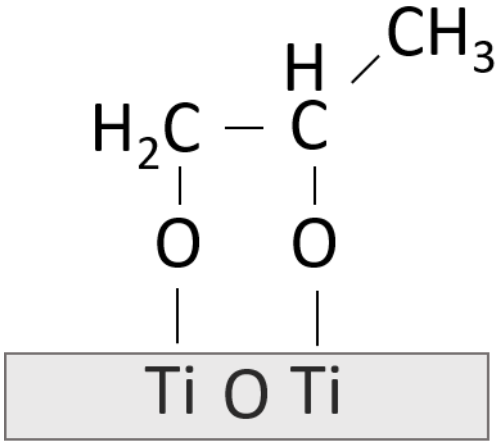

Figure 4.3. Schematic representation of propoxy bidentate species bound to TiO_2.

A comparison study with the reference TiO_2 material shows PO does not form, which provides evidence that Au sites are required for this epoxidation reaction. The next sections dissect the possible mechanisms involved in the epoxidation reaction by describing the studies which systematically leave out one or more of the reactants to observe the possible interactions separately.

4.3.3 Systematic Evaluation of Reactant Interactions on Catalysts

The initial systematic evaluation of reactant interactions with the catalyst surface involved the adsorption of H_2 onto Au/TiO_2 and then adding mixtures of O_2 and propene in order to determine if PO forms with lattice oxygen or requires molecular O_2. The infrared vibrational features associated with H_2 adsorption and reaction with propene suggest propene oxide is not formed and can likely be ruled out as part of the epoxidation mechanism. Figure 4.4A shows H_2 interaction with both the Au/TiO_2 and TiO_2 materials alone. The increase in the IR background over time can be attributed to the excitation of shallow trap electrons in the conduction band (CB) of TiO_2[109,159,179] or to increased scattering as a result of increased concentrations of Ti^{3+} near the

Au particles.[180] Either mechanism to produce the broad-band infrared absorbance requires H_2 adsorption and subsequent dissociation on Au sites (reaction 4.3) or on the Au/TiO_2 interface, where the H atoms then diffuse (or spillover) to the TiO_2 support to form OH sites with lattice O atoms of the TiO_2 support (reaction 4.4):

$$H_2 + Au \leftrightarrow 2(H–Au) \quad (4.3)$$

$$H–Au + Ti–O–Ti \rightarrow Ti–(O\text{-}H)–Ti + Au \quad (4.4)$$

The IR light either excites these electrons into the conduction band as a continuum of states resulting in the rise in the IR background or scatters due to the formation of Ti^{3+}. This background rise effect can be used to observe the availability of the active sites for H_2 dissociation, which have been described at low-coordinated Au sites for the homolytic dissociation of H_2[109,159] or Au/Ti interfacial sites for the heterolytic dissociation of H_2[161]—both of which likely play a critical role in the propene epoxidation mechanism.

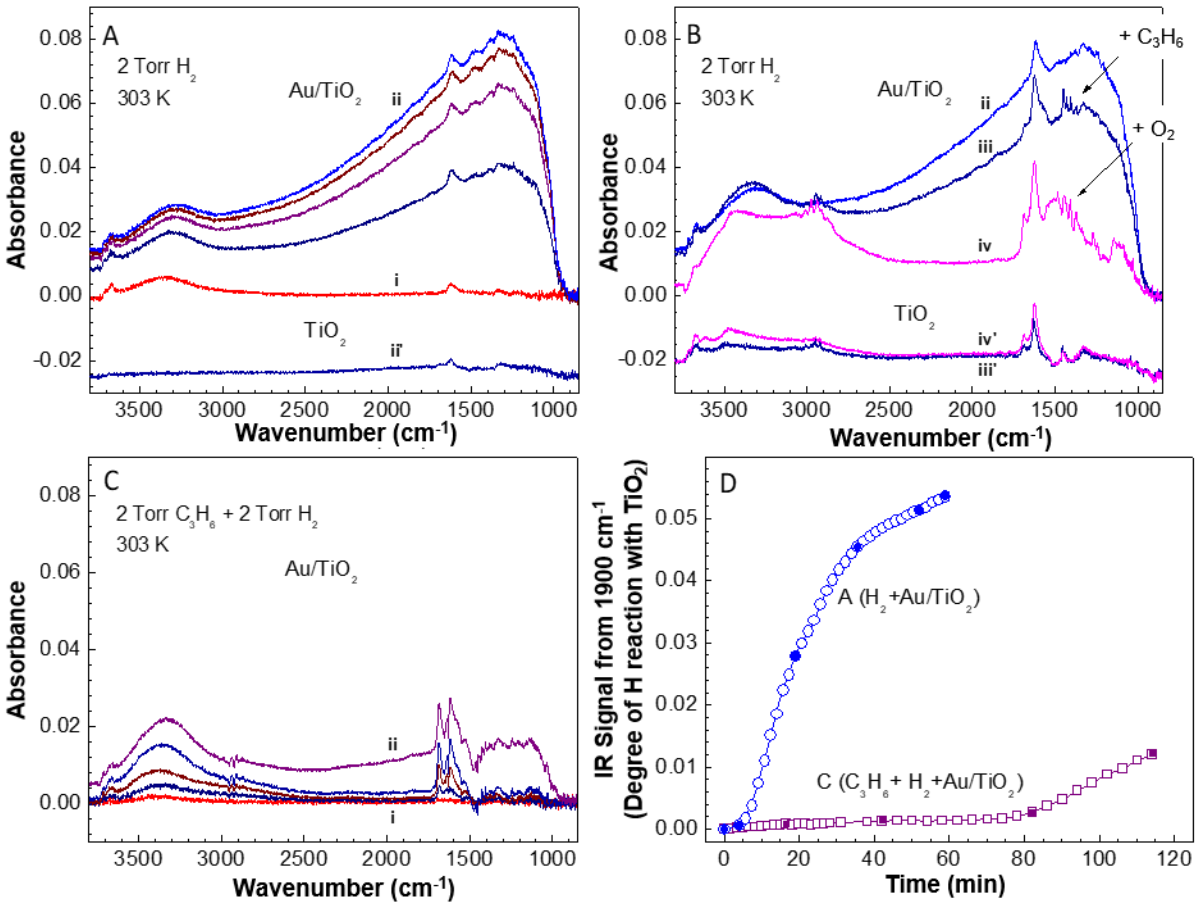

Figure 4.4. Interaction of activated Au/TiO_2 sample with hydrogen. The role of co-adsorbed propene and oxygen. (A.) Interaction of 2 Torr H_2 with activated Au/TiO_2 (i-ii) and TiO_2 (ii') for 60 min. (B.) Co-adsorption of 2 Torr C_3H_6 on H_2-treated Au/TiO_2 (iii) and TiO_2 (iii'); Co-adsorption of 2 Torr O_2 on Au/TiO_2 (iv) and TiO_2 (iv'). (C.) Interaction (co-adsorption) of 2 Torr H_2 with Au/TiO_2 sample pre-covered with C_3H_6 (in the presence of 2 Torr C_3H_6), (i-ii). (D.) Kinetics of charge accumulation in the TiO_2 component of Au/TiO_2 via H-spillover and n-doping or scattering, observed during the experiments shown in A (i-ii) and C (i-ii). The filled in circles and squares in D correspond to the spectra in A and C, respectively.

Figure 4.4B depicts the comparison of H_2 interaction on Au/TiO_2 (blue curve, ii), C_3H_6 interaction on the H_2-treated Au/TiO_2 catalyst (dark blue curve, iii), and subsequent O_2 interaction

on the C_3H_6 + H_2 – treated Au/TiO_2 catalyst (pink curve, iv). The same experimental parameters were also measured for TiO_2, and no IR background rise was observed—providing further evidence that the Au sites play a crucial role in the H_2 dissociation process. After H_2 interaction (blue curve, ii) with the Au/TiO_2 catalyst, the addition of C_3H_6 shows a small decrease in the IR background, which could be attributed to the reaction of propene with H atoms or the quenching of free electrons in deep trapping states within the TiO_2 present due to the molecularly adsorbed propene.[28] However, the addition of O_2 significantly decreases the IR background and the IR bands for PO and H_2O formation are observed. Several conclusions are drawn from these observations: 1) O_2 reacts with H atoms to form H_2O, which removes electron density from the system and lowers the IR background; 2) O_2 adsorption is necessary for PO formation and likely must be present at the Au/Ti interface; and 3) O atoms from the lattice do not react directly with propene to form PO.

Another question to be answered is whether propene adsorbs on or near the active sites for PO formation. Figure 4.4C and 4.4D show C_3H_6 pre-adsorbed on the Au/TiO_2 catalyst, then subsequent H_2 molecules are introduced to the cell. Comparing the IR signal of the background for H_2 exposed Au/TiO_2 and the H_2 exposed C_3H_6-pretreated Au/TiO_2 catalyst, the significant lack of an IR background rise for the C_3H_6-precovered catalyst signifies that the propene molecules adsorb either on the active Au and/or interfacial sites for H_2 dissociation or on the TiO_2 sites near the interface blocking hydrogen spillover. Unable to reach the Au/Ti interface, atomic hydrogen would be inhibited from reacting with interfacial oxygen to promote the epoxidation reaction. However, Figure 4.4B, spectrum iv (pink trace) reveals that PO, H_2O and bidentate propoxy species are formed when O_2 adsorbed and interacted with the propene-H_2 mixture. Therefore, the simultaneous presence of all three reagents in the gas phase is need for PO formation.

Figure 4.5 displays the integrated IR absorption at different frequencies during the 2-hour reaction with H_2 and C_3H_6 co-adsorbed. The loss of C-H bands (3015-2870 cm^{-1}) depict the consumption of propene to form new IR bands in the regions 1730-1660 cm^{-1}, 3600-3020 cm^{-1}, and 1900 cm^{-1}. The 1730-1660 cm^{-1} region corresponds to C=O moieties, which likely form propanal, acrylate, and/or carboxylates from residual oxygen left on the surface from pretreatment conditions. Formation of H_2O is evidenced by the increased bands between 3600 and 3020 cm^{-1}. Both the IR background rise (represented by absorbance at 1900 cm^{-1}) and the H_2O bands increase slowly at first then rise exponentially; this trend is likely due to propene adsorption blocking the active sites for H_2 spillover to form H_2O. However, as propene reacts to form the C=O containing products, the active sites become available for H_2O formation.

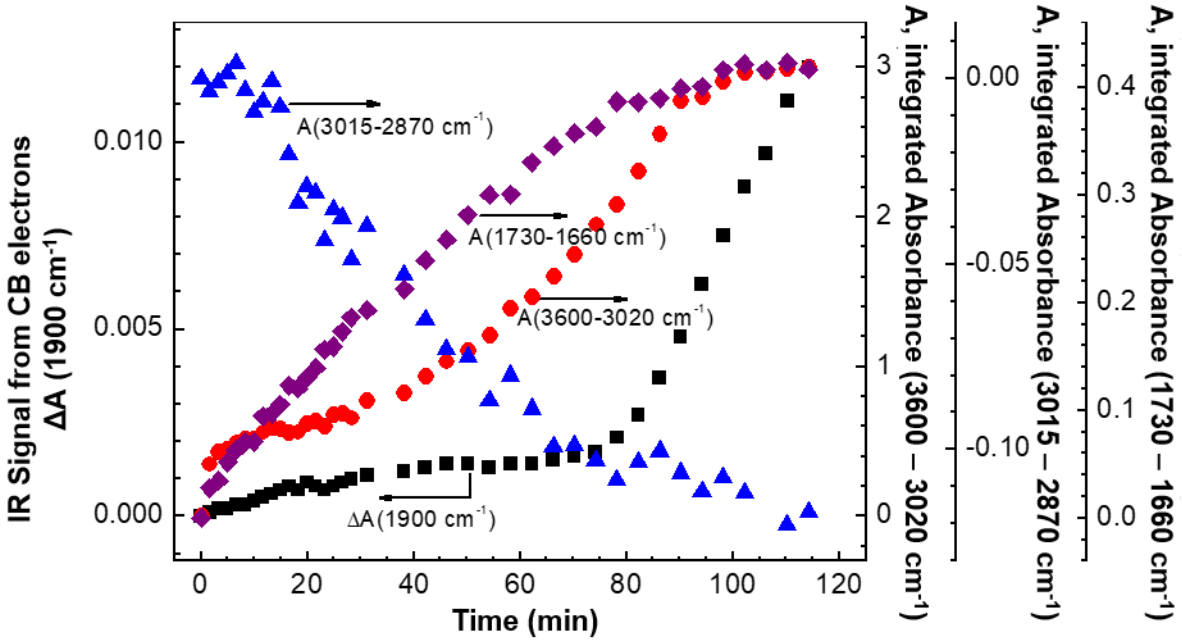

Figure 4.5. Kinetics of products accumulation on Au/TiO_2 during interaction (co-adsorption) of 2 Torr H_2 and 2 Torr C_3H_6. Spectral data presented in the C-panel of Figure 4.4.

Experimental evidence of the $C_3H_6 + H_2$ reaction confirms that lack of PO on Au/TiO_2. Therefore, molecular O_2 must be necessary for the epoxidation reaction. O_2 readily adsorbs to the Au/Ti interface[18] as shown in equation 4.5.

$$O_2 + Au + Ti^{4+} \leftrightarrow Ti^{4+}–OO–Au \quad (4.5)$$

As result of electron donation into the $2\pi^*$ orbital of O_2, the O-O bond elongates and likely exhibits some negatively charge character (can also be written as $O_2^-{}_{ads}$). The bond elongation of the adsorbate promotes reactivity of interfacial oxygen (bound at the Au/Ti interface) and has been previously shown to react with CO,[18] propionic acid,[25] and dimethyl methylphosphonate.[181]

Figure 4.6 shows the comparison of the previous studies (C_3H_6 adsorbed alone – black curve (i), and the $C_3H_6 + H_2$ mixture – red curve (ii)) with the co-adsorption of $C_3H_6 + O_2$ without H_2 reactant gas in the cell on both Au/TiO_2 (Figure 2.6A, iii) and TiO_2 (Figure 2.6B, iii') alone. Several observations can be made: 1) PO does not form, 2) New IR bands around 1688 and 1520 cm^{-1} form, which can be assigned to carbonates (CO_3, 1688 cm^{-1}) and carboxylates (-COO, 1520 cm^{-1}), and lastly, 3) The TiO_2 support in the absence of Au shows no PO formation. Therefore, for PO formation to occur, propene, O_2, and H_2 reactants must be present on the Au/TiO_2 catalyst as shown by the pink curve (spectrum, iv) in Figure 4.6A.

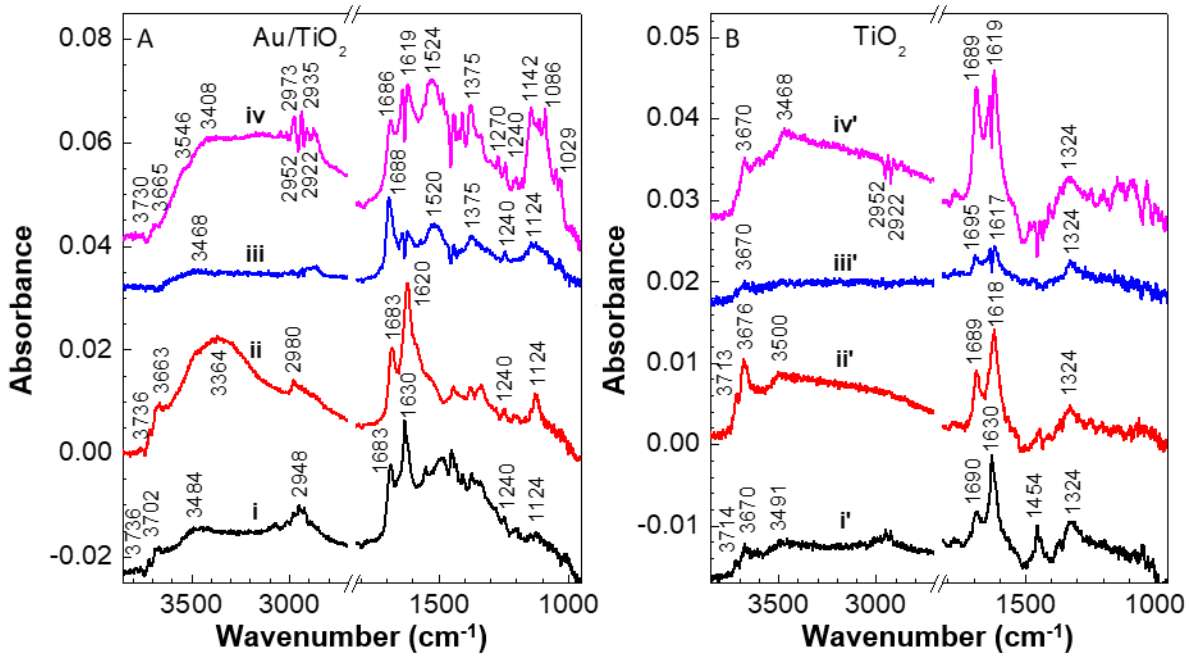

Figure 4.6. Spectra of Au/TiO_2 and TiO_2 samples after a 2-hour interaction with reactant gases: (i, i') 2 Torr propene; (ii, ii') 2 Torr propene (pre-adsorbed) + 2 Torr H_2 added; (iii, iii') 2 Torr propene (pre-adsorbed) + 2 Torr O_2 added; (iv, iv') 2 Torr propene (pre-adsorbed) + gas mixture of 2 Torr H_2 and 2 Torr O_2.

Kinetic studies for the epoxidation reaction ($C_3H_6 + O_2 + H_2$) are shown in Figure 4.7. The integrated absorbance versus time of propene consumption (1460-1380 cm^{-1}) and PO formation (1290-1260 cm^{-1}) follow consistent trends; however, the curves are not exactly mirrored due to the consumption of propene to form other products as well. As shown by the kinetic curves of the other products in Figure 4.7, the H_2O formation (~3450 cm^{-1}) kinetic curve clearly displays a different line shape than propene and propene oxidation products, which is likely due to a separate formation mechanism with solely H_2 and O_2. Additionally, depletion of the 3450 cm^{-1} IR band associated with H_2O, after PO production ceases or reached a steady state, indicated that H_2O reacts further. We speculate that H_2O can act to further degrade PO into the bidentate propoxy

species through an acid-catalyzed reaction or partake in reactions with other carbon-containing species. Therefore, H_2O is ruled out as an active intermediate for PO formation. Formation of another side product - propoxy bidentate species – is revealed by the slowest kinetics measured for the bands in the 1175-1015 cm^{-1} region. This observation precludes the possibility that propoxy bidentate species are active intermediates in the epoxidation of propene to PO.

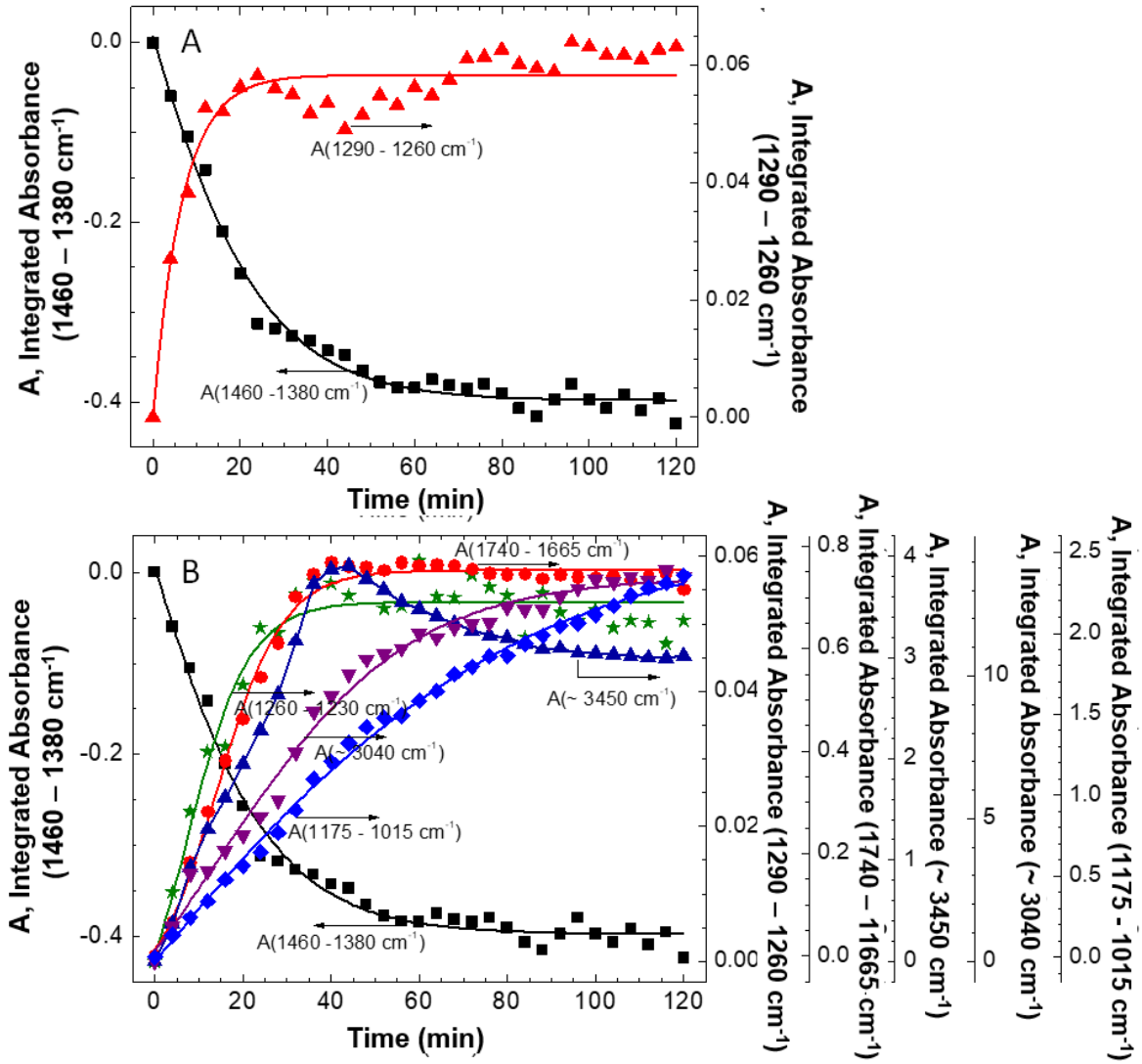

Figure 4.7. Kinetics of species consumption/production during the experiment shown in Figure 4.2. The significant absorbance regions are 1460-1380 (propene, black squares), 1290-1230 (PO, green stars), 1740-1665 (carbonate/carboxylates, red circles), ~3450 (H_2O, dark blue triangles), ~3040 (H-bonded H_2O/OH modes, purple triangles), and 1175-1015 cm-1 (C-O modes, blue diamonds).

4.3.4 $H_2 + O_2$ intermediate reaction on Au/TiO_2 and TiO_2 nanocatalysts

One of the major questions in the mechanism for the epoxidation of propene to PO has revolved around the identity of the oxidizing intermediate. From studies already mentioned above, bound-O_2, bound-H_2 (or a dissociated hydrogen atom), and bound-H_2O can all be ruled out as the required oxidizing species in the epoxidation reaction. For a closer look at the oxidants found on Au/TiO_2 surface during epoxidation, 2 Torr H_2 + 2 Torr O_2 were adsorbed on Au/TiO_2 at 303 K over 60 minutes with propene absent on the surface. Figure 4.8A and 4.8B show that on the Au/TiO_2 catalysts, H_2O forms as evidenced by an infrared feature around 1626-1622 cm^{-1} assigned to the H_2O bending mode. An additional, small feature at 1444 cm^{-1} appears in the time-resolved spectra as well and is attributed to a $\delta_s(OOH)(H_2O_2)$ binary complex previously described in inelastic neutron scattering studies of $H_2 + O_2$ reactions on Au/TiO_2.[175] While the intensity of the H_2O band is significantly larger compared to the OOH/H_2O_2 feature, we cannot confirm the relative concentration of each species on the surface without knowledge of the extinction coefficient for both H_2O and OOH/H_2O_2 on the Au/TiO_2 surface. However, we speculate the OOH/H_2O_2 complex is the major oxidizing intermediate required to produce propene oxide. Once the gas is evacuated from the cell, the H_2O band disappears along with the associated OH modes (3600-3100 cm^{-1}), and this loss of H_2O indicates a weak binding between the H_2O and the catalyst surface. Since the H_2O binding is weak, it is likely that, when in the presence of $H_2 + O_2$, some H_2O desorbs from the Au/TiO_2 catalyst surface.

Further evidence that the Au sites play a crucial role in the formation of both H_2O and OOH was determined through exposures of the probe molecule, CO, onto the clean O_2-pretreated surface and also onto the $H_2 + O_2$ exposed surface. Figure 4.8C shows the CO absorbance bands on Au sites (2150-2075 cm^{-1}) and TiO_2 sites (2207 and 2188 cm^{-1}). The Au-CO band prior to the

addition of H_2 and O_2 can be fit to two Lorentzian components at 2133 and 2120 cm^{-1}. These two IR bands are assigned to $Au^{\delta+}$-CO and Au^0-CO sites, respectively, where the 2133 cm^{-1} site resides next to another Au atom that binds to an O^* atom likely from the TiO_2 lattice at the Au perimeter.[152] After exposure to the H_2 + O_2 mixture, the Au-CO IR band decreases in concentration and decreases in frequency to 2111 cm^{-1}. The redshift of 9 cm^{-1} indicates a reduction of the O_2-pretreated Au sites likely from the H_2 reaction with the O^* atoms to form OH sites or even further reaction to form H_2O. Thus, the likely active Au sites reside at the Au/TiO_2 interface. Furthermore, the molecular O_2 must be consumed by the H_2 in order to keep the Au sites in their metallic Au^0 oxidation state. The OOH/H_2O_2 complex identified spectroscopically when H_2 and O_2 react is not identifiable in the infrared spectra acquired during the oxidation reaction mixture (see Figure 4.2C and 4.6A spectrum iv). We speculate the absence of the oxidizing intermediate to be a combination of the immediate reaction of the OOH/H_2O_2 complex with nearby propene and the negative-going propene vibrational features (at 1452, 1431 and 1416 cm^{-1}) as propene oxidizes into propene oxide as well as other species like acrolein and acetone.[52]

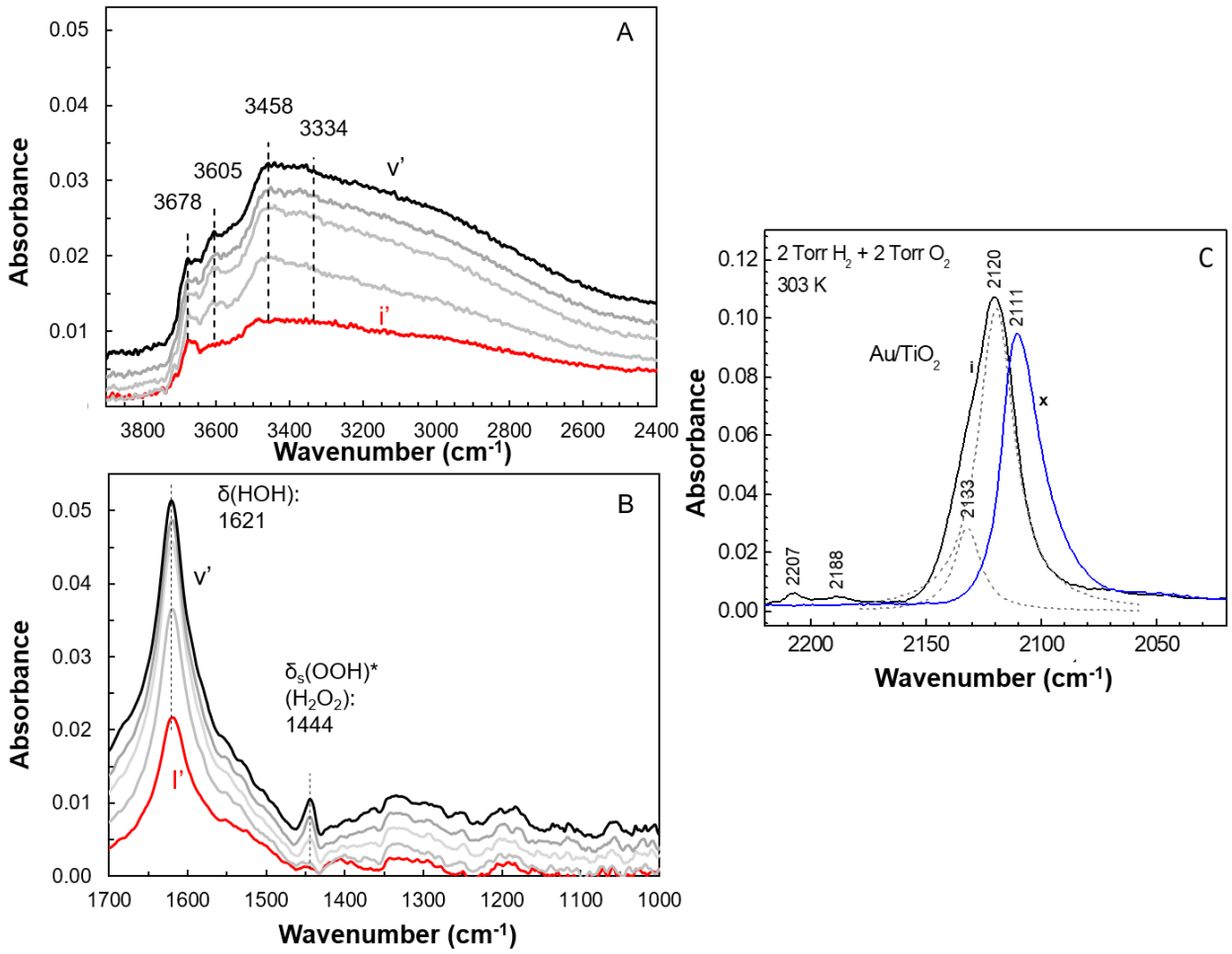

Figure 4.8. (A & B) Interaction of activated Au/TiO_2 with epoxidation gas mixture of 2 Torr H_2 and 2 Torr O_2 for 60 min. spectra i'-v'; (C) Adsorption of 2 Torr CO on Au/TiO_2 sample: Activated sample, spectrum i; After reaction with H_2+O_2 gas mixture and evacuation, spectrum x. The dotted lines represent the model Lorentzian fits.

In order to help confirm the presence of the OOH intermediate on the Au/TiO_2 catalyst, DFT calculations were performed using a Au nanorod anchored to a rutile TiO_2(110) model surface. Figure 4.9 shows the enthalpies of adsorption for O_2 adsorption on the Ti_{5c} site at the perimeter, Au sites, and dual perimeter site to be -179 kJ/mol, -49 kJ/mol, and -97 kJ/mol, respectively. Molecularly-bound O_2 likely contains significant charge density from the Au particle.

This process likely elongates the O-O bond, provides the O_2 adsorbate with excess negative charge and activates the molecules for reaction. Even though the TiO_2 site is preferred, the Au sites are also possible for binding.

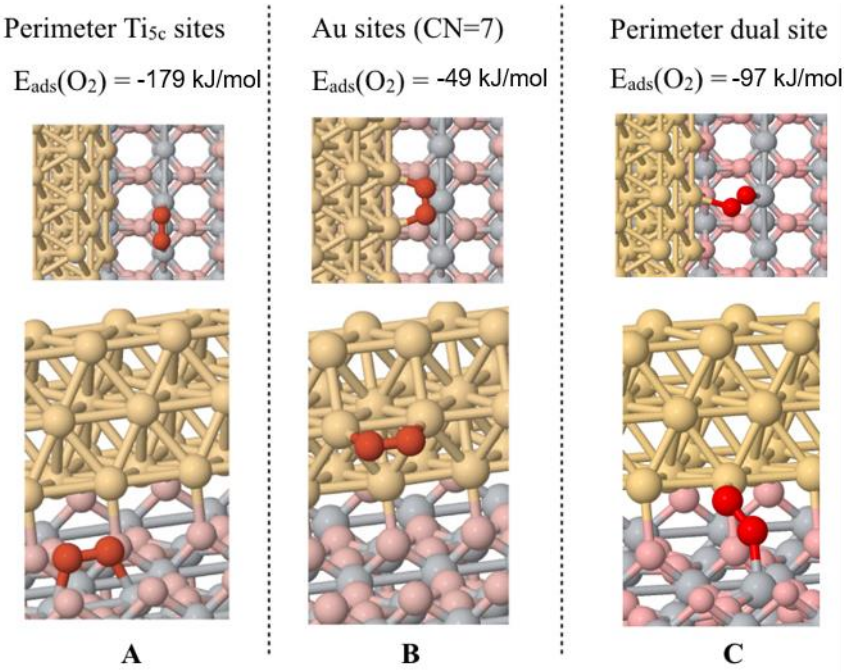

Figure 4.9. O_2 adsorption on the (A) Ti_{5c} sites at the perimeter, (B) Au sites, and (C) perimeter dual site. The Au atoms, Ti atoms, O atoms in the TiO_2 lattice, and O atoms from the O_2 molecule are shown in gold, gray, pink, and red, respectively. The binding energies (E_{ads}) are also shown.

The next step in the reaction involves the addition of an H_2 gas molecule. As shown in Figure 4.10, the reaction mechanism for OOH formation on the Au sites, TiO_2 sites, and the perimeter dual site involves H_2 dissociation with one H attached to the O_2 molecule and the other H atom attached to a Au site for all mechanisms. Both homolytic and heterolytic H_2 dissociation pathways have been previously investigated on low-coordinated Au surfaces.[119,161,182] It is important to note, the heterolytic dissociation of H_2 was previously calculated to have a lower activation barrier (8.53 kcal/mol) compared to the homolytic dissociation (14.76 kcal/mol).[182] In

our Au/TiO_2 model surface, we calculate the heterolytic dissociation of H_2 in which a proton is added to the negatively charged interfacial O_2 molecule to form the OOH species, and a hydride is left on the Au site. For the perimeter dual site case, the generated OOH species ends up on the Ti_{5c} site at the perimeter. The activation barriers for the OOH formation on Au, Ti_{5c} site at the perimeter, and perimeter dual sites were 30.9 kJ/mol, 15.4 kJ/mol, and 27.1 kJ/mol, respectively. The activation barriers are low enough, at 303 K, that all sites can be active for OOH formation. Furthermore, the reaction energy, ΔE_{RXN}, for the OOH formation on Au sites and perimeter dual sites, calculated at -82.0 kJ/mol and -112 kJ/mol, respectively, indicates that the OOH formation is a favorable process. Reaction 4.6 provides the most probable reaction in which the OOH species resides on TiO_2.

$$H^+–Au + Ti^{4+}–OO^-–Au \leftrightarrow Ti^{4+}–OOH + Au \quad (4.6)$$

Thus, the OOH intermediate is likely generated at the Au/Ti interface and reacts quickly when in the presence of propene.

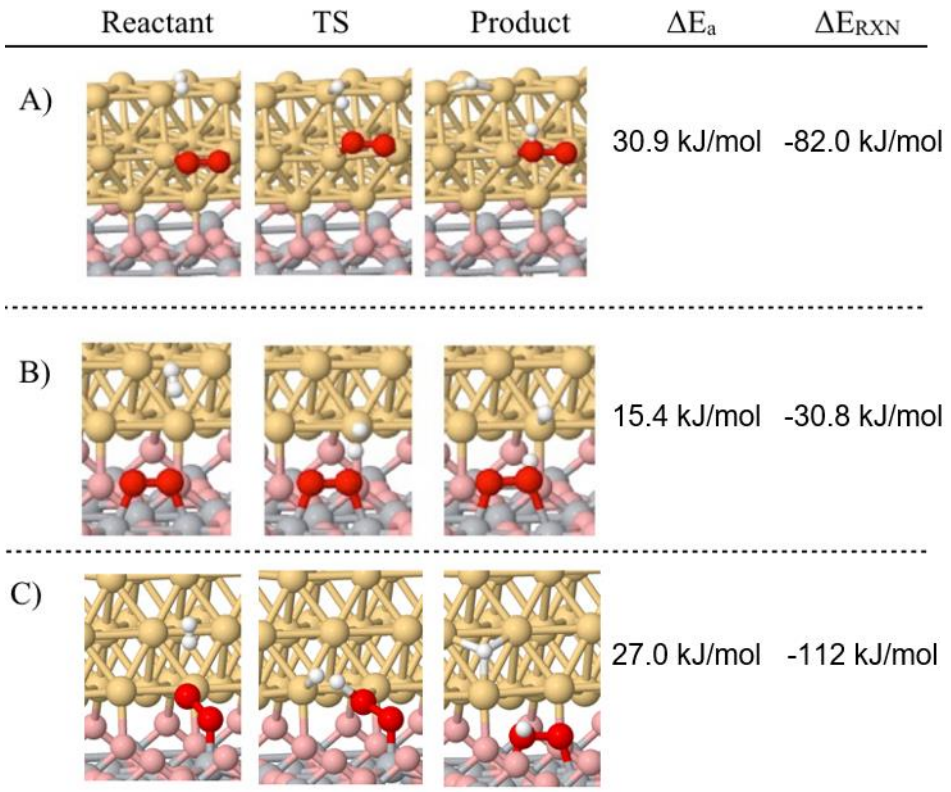

Figure 4.10. O_2 and H_2 can directly form OOH species on the (A) Au sites, (B) Ti_{5c} sites at the perimeter, and (C) perimeter dual sites. The Au atoms, Ti atoms, O atoms in the TiO_2 lattice, O atoms from the O_2 molecule, and H atoms are shown in gold, gray, pink, red and white, respectively. ΔE_a and ΔE_{RXN} represent the activation barrier and reaction energy, respectively.

After propene epoxidation, the reaction gas mixture was removed from the reaction cell as shown in Figure 4.11 (black curves, i). Upon evacuation, propene desorbed from mostly the TiO_2 sites and some of the Au sites, which was observed by the loss of IR bands in the C-H region (2967 – 2912 cm^{-1}) and in the fingerprint region (1630 – 1370 cm^{-1}). Adsorption of CO revealed displacement of propene oxide on Au sites shown by the disappearance of the bands at 1270 cm^{-1} (ring breathing mode) and 1407 cm^{-1} (δ(CH) on Au). Therefore, PO does not degrade on the on the Au sites at the perimeter and further suggests that PO is likely formed on or near these same Au/Ti perimeters sites.

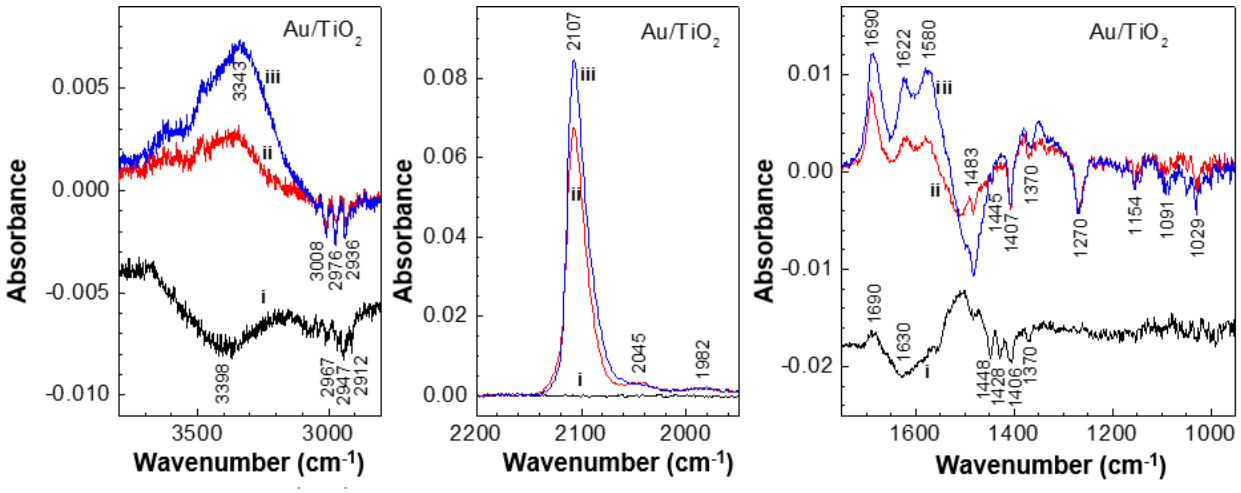

Figure 4.11. Spectra of Au/TiO_2 obtained after: (i) evacuation of the propene, H_2, O_2, gas mixture from the chamber referenced to Figure 2, spectrum iii; (ii-iii) subsequent exposure of Au/TiO_2 to 2 Torr CO for 60 min.

4.3.5 Propene Oxide Adsorption on Au/TiO_2 and TiO_2 Nanocatalysts

Propene oxide formation during the oxidation reaction was further confirmed via the similarity of the propene epoxidation products to that of propene oxide adsorbed on the Au/TiO_2 catalyst. Figure 4.12 displays the vibrational spectra associated with the propene epoxidation reaction mixture (4.12A and 4.12B, from Figure 4.2) and propene oxide adsorption (4.12C and 4.12D). As previously mentioned, the IR bands at 3006, 2970 and 2933 cm^{-1} correspond to C-H stretching modes of PO. The IR bands at 1484, 1408, 1370 and 1270 cm^{-1} are assigned to $\delta_{as}(CH_3)$, $\delta(CH)$, $\delta_s(CH_3)$, and the ring breathing mode of PO, respectively. The slow accumulation of propoxy bi-dentate side products from PO adsorption is also apparent, indicated by bands in the 1145 – 1020 cm^{-1} region.

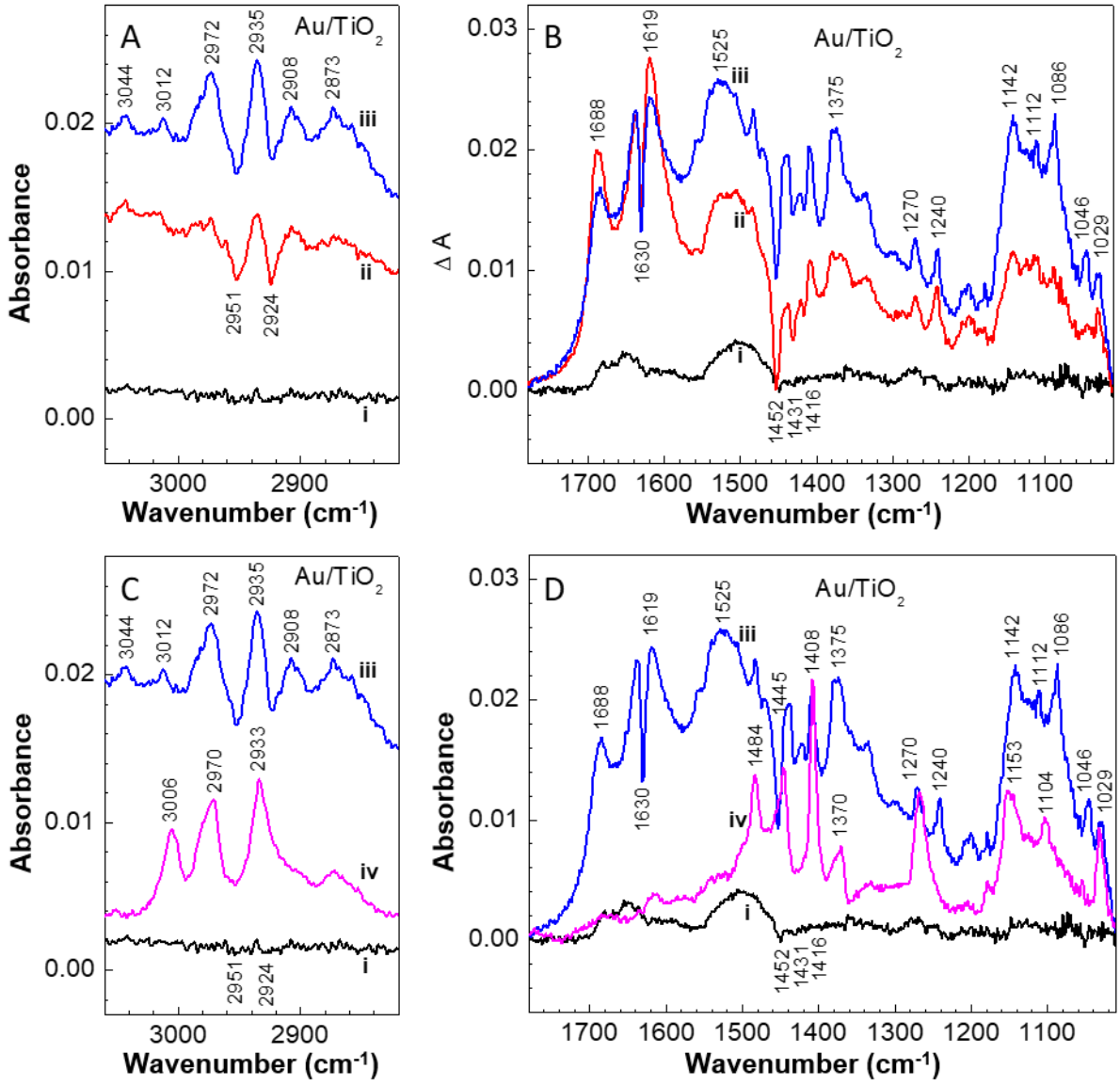

Figure 4.12. Selected spectra (i, ii, iii) from the experiment shown on Figure 4.2. Spectrum iv is obtained after brief exposure of the activated Au/TiO_2 sample to 300 mTorr propene oxide.

In order to determine if propene oxide formed on Au sites and/or TiO_2 sites, the cell was evacuated after propene oxide adsorption. Figure 4.13 depicts, that after gas phase evacuation, a very small amount of PO was removed from the surface and suggests stronger binding between PO and the surface sites compared to propene and the surface. Figure 4.13A shows a comparison

of PO adsorbed on Au/TiO_2 and TiO_2 alone; at first glance, the PO IR bands look very similar for both catalysts suggesting PO adsorbs on the TiO_2 sites alone. However, after evacuation, CO was added to both catalysts and the Au-CO band redshifted to wavenumbers below 2109 cm^{-1} (Figure 4.13B, i). The observed redshift provides evidence that propene oxide is adsorbed on the Au sites and donates electron density to the Au. The IR bands for PO on Au and TiO_2 sites are in the same wavenumber regions. The results are consistent with PO formation on Au sites in the epoxidation reaction. Therefore, we propose in equation 4.7 that propene reacts with the OOH intermediate species at the $AuTiO_2$ interface and the product, PO, binds to Au. Propene originating on TiO_2 and reacting at the Au/Ti interface with OOH is also considered in equation 4.8. In this reaction, the diffusion of PO to the TiO_2 sites after formation is also a possibility. Finally, we cannot rule out the reaction of gas phase propene with the surface-bound OOH.

$$(CH_2–CHCH_3)–Au + Au–OOH–Ti^{4+} \leftrightarrow PO–Au + Ti^{4+}–OH + Au \quad (4.7)$$

$$(CH_2=CHCH_3) –Ti^{4+} + Au–OOH–Ti^{4+} \leftrightarrow PO–Ti^{4+} + Ti^{4+}–OH + Au \quad (4.8)$$

Figure 4.13B (spectrum ii) also shows the loss of PO on just Au/TiO_2 via the IR band assigned to the ring breathing mode at 1270 cm^{-1}. The loss of PO signifies H_2 interaction with pre-adsorbed PO even in the absence of O_2 molecules. The significant intensity loss of PO means PO is either removed from the surface or consumed via H_2. The new positive IR features at 1695 and 1624 cm^{-1} are likely propanal and H_2O, respectively. The loss of PO from the surface via reactivity is a selectivity issue that could possibly be mitigated at higher temperatures where PO would desorb before reacting with H_2.

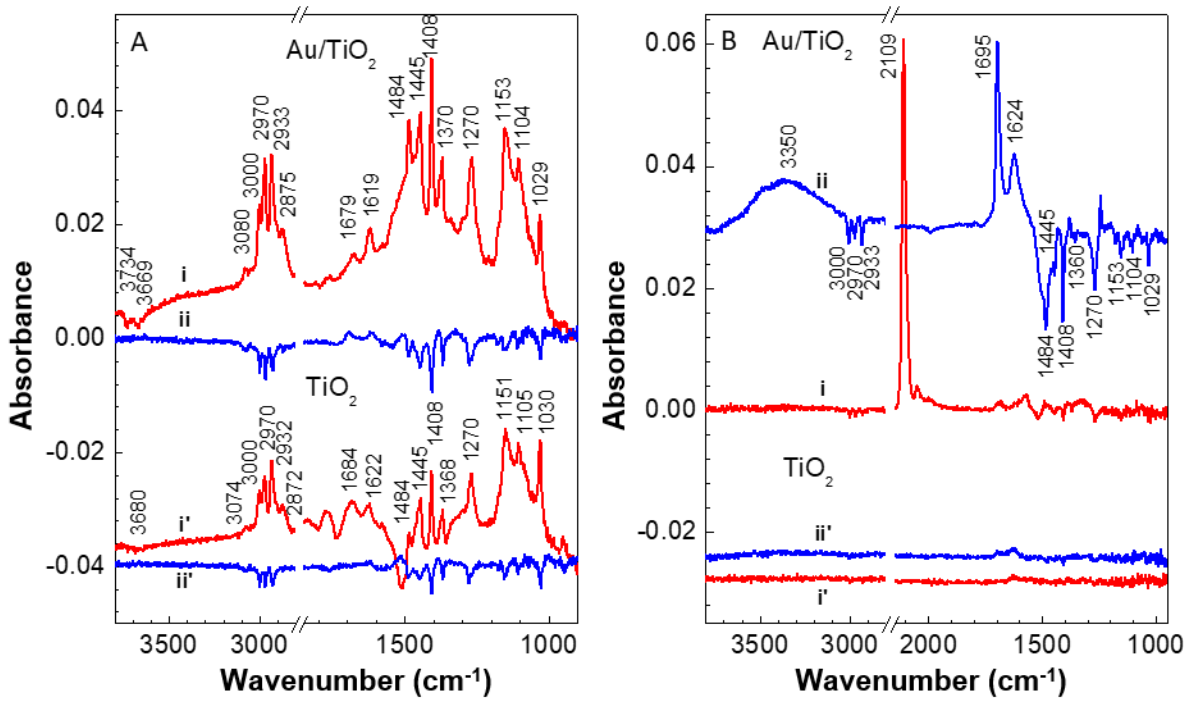

Figure 4.13. (A) Adsorption of 2 Torr propene oxide on activated Au/TiO_2 and TiO_2 samples (i, i') and evacuation (ii, ii'). (B) Sequential exposure of CO and H_2 to Au/TiO_2 sample with pre-adsorbed propene oxide: 2 Torr CO, spectra (i, i') and 2 Torr H_2 (for 60 min), spectra (ii, ii').

3.3.6 Propene Oxide Reaction on Au/TiO_2 and TiO_2 Nanocatalysts

Propene oxide can react further with the oxidizing intermediate and possibly H_2O to form other products. Figure 4.14 shows PO adsorption on both the Au/TiO_2 and TiO_2 catalysts with subsequent addition of the $H_2 + O_2$ gas mixture to the cell. The IR bands at 3404, 1687 and 1624 cm^{-1} form immediately and continue to grow as time increases. The IR bands for PO decrease with time and suggest that PO is being consumed or desorbing as a result of H_2 and O_2 adsorption. The IR bands at 3404 and 1624 cm^{-1} are likely due to H_2O formation as shown by the loss of both bands on both catalysts after evacuation. The positive band at 1687 cm^{-1} together with the growing ill-resolved bands in the 1550-1350 cm^{-1} region can be tentatively assigned to carbonate/carboxylate

products formed via decomposition/oxidation of PO and/or propoxy species. Indeed, the negative bands in the 1150-1030 cm^{-1} region (Figure 4.14B) indicate that propoxy species are leaving the surface of both Au/TiO_2 and TiO_2 catalysts. It can be concluded from Figures 4.13B and 4.14 that both H_2 and $H_2 + O_2$ treatments can react with or desorb the propoxy bi-dentate species.

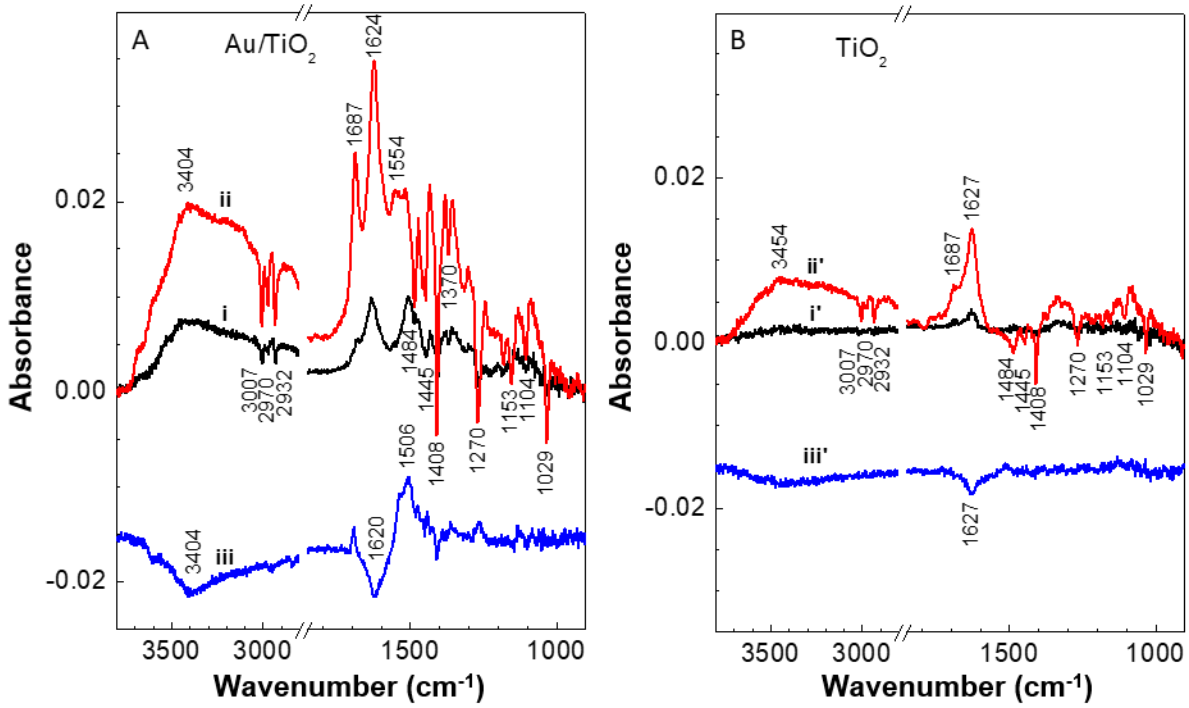

Figure 4.14. Interaction of propene oxide pre-covered samples (after brief exposure to 0.3 Torr propene oxide) with epoxidation reactant H_2+O_2 gas mixture containing 2 Torr H_2 and 2 Torr O_2 for 60 min: Au/TiO_2 sample, spectra i-ii; TiO_2 sample, spectra i'-ii'; Evacuated samples, spectra iii, iii'.

4.4 Summary

The propene epoxidation reaction mechanism was thoroughly studied on the Au/TiO_2 catalyst at 303 K in order to determine each step in the mechanistic scheme:

1. Propene adsorption on both the Au/TiO_2 and TiO_2 catalysts revealed two main adsorption sites for propene with one through a ($\pi\sigma$)-interaction on Au and with the other on a TiO_2 site away from the Au perimeter (See Chapter 3). The Au sites are likely active sites for epoxidation as evidenced by the weakly bound PO molecules that desorbed from the Au sites upon CO adsorption.
2. After the introduction of the $H_2 + O_2$ gas mixture to the propene pre-covered catalysts, PO formation on both Au and TiO_2 sites on the Au/TiO_2 catalyst was observed. No PO formed on TiO_2 indicating that the reaction occurred on the Au sites or at the Au/TiO_2 interface. Since propene only adsorbs on Au sites near the perimeter, the epoxidation must occur on Au sites at the perimeter as well. PO adsorption studies with co-adsorbed CO confirm these results.
3. Systematic studies measuring propene interaction with each reactant separately produced a lack of PO formation unless all three reactants (C_3H_6, O_2, and H_2) were present on the Au/TiO_2 catalyst surface.
4. Since $H_2 + O_2$ are necessary for the epoxidation of propene, the formation of two possible oxidizing intermediates was possible: H_2O and OOH. H_2O was ruled out due to the lack of H_2O consumption during the experiment. DFT calculations confirm that OOH formation on both Au sites and TiO_2 sites near the interface is likely to occur and diffusion of the OOH intermediate from Au sites to isolated TiO_2 regions of the catalyst is less likely.
5. $H_2 + O_2$ exposure over the Au/TiO_2 catalyst revealed a small vibrational feature at 1440 cm^{-1} associated with a OOH/H_2O_2 complex. This species has not been previously identified on a Au/TiO_2 surface at epoxidation temperatures and confirms the presence of a secondary oxidizing intermediate necessary for propene epoxidation over Au/TiO_2.

6. Lastly, PO can also readily react with $H_2 + O_2$ to form possible deactivating species at 303 K.

After all the steps are compiled together, propene epoxidation on the Au/TiO_2 catalyst likely occurs at the Au/Ti interfacial sites at the perimeter. A systematic exploration of the reactant adsorption, intermediate formation and product formation/desorption utilized infrared spectroscopic measurements in conjunction with DFT calculations to observe propene epoxidation reaction surface species not specified in previous literature.

Chapter 5

Infrared Spectroscopic Insight into the Photoepoxidation of Propene over TiO_2-SiO_2 Binary Catalysts

5.1 Introduction

Propene oxide, one of the most important chemical intermediates, is used to produce materials of tremendous consumer, industrial, and military importance, such as polyurethane films and polyethers.[45-46] Currently, over 10^6 tons of PO are produced annually.[45] The great demand for PO is satisfied by two industrial methods: the chlorohydrin and hydroperoxide processes. However, both of these PO production methods have serious environmental and economical drawbacks. The chlorohydrin process generates a significant amount of problematic byproducts, while the hydroperoxide process requires the fixed production of a co-product in high quantities relative to propene oxide.[46] These shortcomings have led researchers to design catalysts that can directly convert propene into propene oxide.

Motivated by the importance of this reaction, we recently employed surface-science methods to investigate the molecular-level details of propene chemistry over a Au/TiO_2 nanocatalyst.[37-38] We have discovered that, on titania, propene coordinates weakly at Ti sites through the electron density in the π-orbital of the double bond (See Ch. 3). On gold, the double bond of propene is significantly elongated due to the high electron density found in Au atoms compared to Ti atoms.[37] The propene double bond elongation likely activates the molecule for the epoxidation reaction. Our results are consistent with computational work that showed evidence for propene bound to under-coordinated Au atoms.[116] Other theoretical studies for propene adsorption on Au clusters have suggested the importance of the propene-Au interaction as the first step in the epoxidation reaction.[120,125,183]

5.1.1 Propene Photoepoxidation

Despite significant strides to improve the efficiency of the chemistry, our work (see Ch. 4) and the findings of others clearly establish that the economic viability of this pathway is limited. Specific inefficiencies include the required H_2 co-reactant and the tendency of supported-metal catalysts to over-oxidize propene to CO_2, acrolein, and propanal.[50,147,184] Therefore, work has begun to identify catalysts for the direct conversion of propene to PO but that harness photonic energy rather than thermal energy for the conversion (Reaction 5.1):[107]

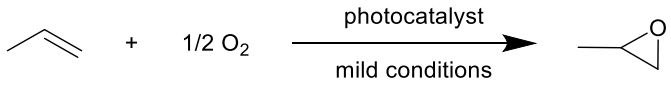

(5.1)

A wide variety of photocatalysts have been tested for the conversion of propene into propene oxide including titania[185] and silica-supported Cr[186], Mg[187-188], Zn[189-190], and V_2O_5.[191-192] A recent survey[193] of over 50 silica-supported systems for photocatalytic performance point to the TiO_x-SiO_2 binary catalyst as preferred for the photocatalytic epoxidation of propene. Consequently, many researchers have focused on titania-silica based photocatalysts to improve the production of PO in the presence of UV light.[194-204] However, few studies have focused on developing a full mechanistic understanding for the reaction.

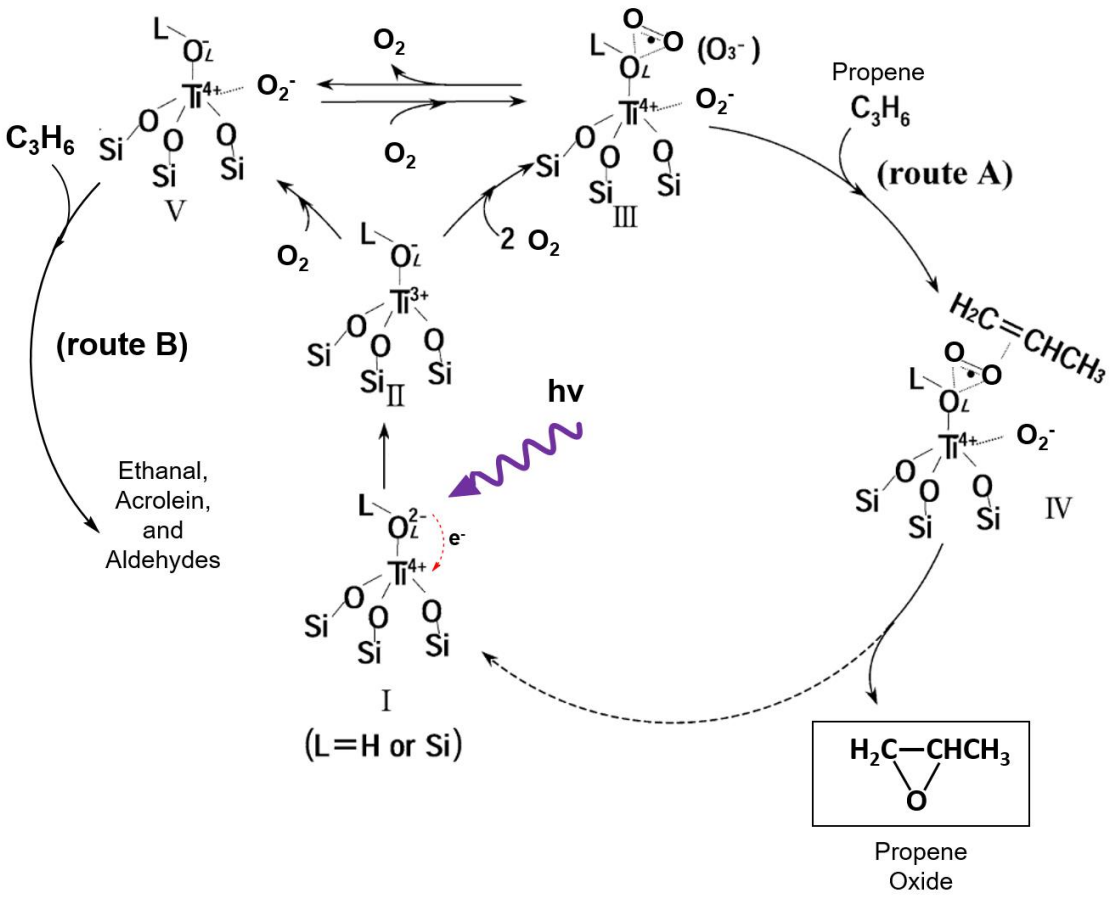

Figure 5.1. The photocatalytic reaction mechanism as suggested by Murata et al. based on electron spin resonance measurements. Propene might to bind directly to the activated O_2 (structure III) to form PO. An alternate pathway, where propene binds to the photo-reduced O_L species, may be responsible for the side products. Adapted with permission from Murata et al., Active Sites and Active Oxygen Species for Photocatalytic Epoxidation of Propene by Molecular Oxygen over TiO2−SiO2 Binary Oxides, *Journal of Physical Chemistry B,* 2003, 4364-4373. Copyright 2003 American Chemical Society.[203]

One notable exception involves a study demonstrating that TiO_2-SiO_2 binary oxides with low Ti content have exceptional selectivity compared to similar materials with larger Ti content.[203]

In that investigation, scientists utilized data from electron spin resonance (ESR) spectroscopy to suggest that O_2 activation to form propene oxide proceeds through the generation of a unique O_3^- intermediate.[204] Their proposed catalytic cycle for the production of propene oxide is shown in Figure 5.1. Upon irradiation by UV light, a ligand-to-metal charge transfer (LMCT) occurs between the O and Ti species in the sample. The photogenerated hole on the lattice oxygen (O_L^-) is thought to react with an O_2 molecule to form the active O_3^-.[204] Propene is suggested to coordinate to the O_3^- intermediate. Experiments that have employed isotopically labeled $^{18}O_{2(g)}$ provided evidence that the PO oxygen originated from the gas-phase, while the side products contained a mixture of lattice oxygen and gas phase oxygen.[204] Others have suggested alternative routes for the photoepoxidation of propene over similar catalysts.[198-199] Such studies suggest that the active form of oxygen is a surface-bound atomic oxyradical ($O^{\bullet}_{ads}$) formed via the dissociation of surface O_2^- as the ion is stripped of an electron by a photo-generated hole. In this proposed mechanism, the $O^{\bullet}_{ads}$ coordinates directly with a gas phase propene molecule to form the desired epoxide.[205] Interestingly, researchers speculated that small catalyst pore sizes were responsible for the reported high selectivity. Our studies complement prior investigations by providing the first systematic exploration into this photoepoxidation reaction with methods that directly probe surface-bound species through vibrational spectroscopy.

5.2. Procedural Methods

5.2.1 Synthesis of TiO_2-SiO_2 Binary Compounds

TiO_2-SiO_2 materials were prepared using a sol gel method. The procedure of the 1, 5, and 10% TiO_2-SiO_2 samples are all the same except for the amount of titanium precursor added. The procedure below is for the 1% Ti/Si (where %Ti = mol Ti / (mol Ti + mol Si), ethoxy and isopropoxy ligands were not included in the calculations). For the 1% by mole Ti sample, 8 mL

of a 50% (v/v) tetraethyl orthosilicate (TEOS, Sigma-Aldrich) in ethanol was placed into a scintillation vial and allowed to stir. 1.5 mL of water was added dropwise, and the pH was adjusted to 2 with 1 M HCl. In a separate vial, 0.1 mL titanium tetraisopropoxide (TTIP, Sigma-Aldrich) was added to 0.65 mL ethanol and 60 µL 5% acetic acid was added dropwise. Both solutions were allowed to stir separately for 90 minutes. The TTIP solution was added dropwise to the TEOS solution and mixed for 30 minutes. The pH of the solution was adjusted to 7 with 1 M NH_3 and allowed to stand until gelation. The resulting gel was soaked in 20% (v/v) TEOS in ethanol for 24 hours, washed in hexanes, and dried at 65 °C. Samples were pulverized in a mortar and pestle before use. In order to produce the 5% Ti sample and 10% Ti sample the ratio of TTIP was adjusted relative to the ethanol and acetic acid. (5%: 0.3 mL TTIP, 2 mL EtOH, 0.2 mL acetic acid; 10%: 0.55 mL TTIP, 3.6 mL EtOH, 0.25 mL acetic acid).

5.2.2 TiO_2-SiO_2 Characterization

Characterization of the synthesized TiO_2-SiO_2 utilized diffuse-reflectance UV/Vis (DR-UV/Vis) and X-ray photoelectron spectroscopy (XPS). For DR-UV/Vis characterization, each sample was placed inside a quartz cell and mixed with the UV-transparent molecule, $BaSO_4$. The monochromator was scanned to provide wavelengths between 200 – 1000 nm at 1 nm resolution. A UV/Vis spectrum of SiO_2 was used to subtract from the TiO_2-SiO_2 samples to remove any SiO_2 absorbance features from the resultant spectra. The acquisition of XPS data used a monochromatic Al K-alpha X-ray source (1486.6 eV) at 100 W over 1400 µm × 100 µm area at 45° angle. Survey scans were acquired at a 1.0 eV step size with 2 sweeps. Individual element scans were acquired at 0.1 eV step size using between 2 - 60 sweeps. All binding energies are referenced to C-C at 284.8 eV.

5.2.3 Sample Installation and Activation in High-Vacuum Chamber

Powder TiO_2-SiO_2 samples have been pressed into the W-mesh and placed into the vacuum chamber using the same sample mount (as previously explained in Chapter 2). Each sample was resistively heated to 573 K in 10 Torr of O_2 for 1 hour and then at 573 K in vacuum for 30 minutes to remove any loosely bound adsorbates. A liquid nitrogen reservoir cooled the sample between 100 K – 300 K depending on the experiment performed.

5.2.4 Propene Photoepoxidation

Photoepoxidation experiments utilized a 1000 W Hg arc lamp coupled to the vacuum chamber. Light reached the sample using a fiber optic cable (Accu-Glass Products, Inc.) attached to a fiber optic flange on the mini CF port of the main chamber (Accu-Glass Products, Inc.). A water filter, attached to the exit port of the light source, removed infrared radiation from the light source. As a result of the light irradiation setup, no measureable sample heating effects have been observed. Inside the chamber, a focusing lens (Accu-Glass Products, Inc.) was attached to the vacuum-side of the fiber optic CF flange and was focused onto a 5 mm diameter spot directly on the sample. Photoepoxidation reactions within the chamber incorporated 2 Torr of O_2 and 2 Torr of propene (99.99 %, Matheson TriGas CP) in addition to irradiation from the Hg arc lamp. Infrared spectra were acquired throughout the entire 2-hour reaction time. The background for each spectrum utilized adsorbed propene and thus propene vibrational modes do not appear as positive features in the infrared spectra during the photoreaction.

Propene oxide adsorption, performed on the same materials, identified reaction products that were produced during the photoepoxidation reactions. A solution of propene oxide (± 99 %, Sigma Aldrich) was placed on the gas manifold and a freeze-pump-thaw treatment was used to

remove atmospheric gases and any impurities within the solution. The addition of 2 Torr of propene oxide onto the surface was used as the product standard.

5.2.5 Isothermal Diffusion of Propene on TiO_2 and SiO_2

Isothermal diffusion studies of propene on both TiO_2 (Degussa P25) and SiO_2 (Aerosil 200) reference materials employed the same vacuum-chamber as reported above. Each sample was cooled to 100 K and propene was introduced at a pressure of roughly 1 $x10^{-5}$ Torr. The temperature of the resistively heated sample was increased to between 103 – 148 K for SiO_2 and 198 – 218 K for TiO_2 under continuous vacuum pumping. At each stable temperature, propene desorbed as infrared spectra were acquired. A diffusion analysis using this experimental method has been previously established for similar porous materials.[206-210] Briefly, the diffusion of propene through SiO_2 and TiO_2 was found to follow Fick's 2nd Law of Diffusion. Transport of a given molecule is governed by a concentration gradient shown here:

$$\frac{\partial C(t,x)}{\partial t} = D\frac{\partial^2 C(t,x)}{\partial x^2} \tag{5.2}$$

where *C* is the concentration of the bound molecule, *t* is the time, *x* is the length position, and *D* is the diffusion coefficient. A solution to Fick's second law can be applied to model the time dependence process as propene diffuses through the material and then desorbs at the surface–vacuum interface:

$$\frac{A_t}{A_0} = \theta \sum_{n=0}^{\infty} \frac{8}{n^2(2n+1)^2} e^{\left[-\frac{D(2n+1)^2\pi^2 t}{l^2}\right]} \tag{5.3}$$

where A_t, is the integrated IR absorbance at time t, A_0 is the integrated IR absorbance at maximum vapor loading, θ is the normalized coverage, *D* is the diffusion coefficient and *l* is the sample thickness (we assume 50.0 μm, the thickness of our W-mesh).

5.3. Results

The photoepoxidation of propene in the presence of the TiO_2-SiO_2 binary compounds was investigated through *in situ* infrared spectroscopic measurements. The objective of this work is to identify specific materials that can produce propene oxide in the presence of only propene, O_2, and light as well as identify specific mechanistic steps during the epoxidation. We provide evidence that a series of TiO_2-SiO_2 materials produce trace amounts of surface-bound propene oxide with UV light; however, propene oxide is shown to degrade on the surface to generate carbonyl-containing species (likely acrolein and acetone). In order to understand the fundamental adsorption and transport properties of propene over different regions of these binary materials, adsorption and isothermal diffusion measurements were performed on silica and titania reference materials.

5.3.1 TiO_2-SiO_2 Characterization

The initial characterization of the TiO_2-SiO_2 materials identified both titania and silica regions on the synthesized TiO_2-SiO_2 samples but can only speculate on the possibility of isolated Ti^{4+} on the low Ti weight percent materials. Scanning electron microscopy images indicated a particle size between 50-100 nm (Fig. 5.2B). Diffuse-reflectance UV/Vis (DR-UV/VIS) spectra, shown in Figure 5.2A, provide evidence of TiO_2 absorption characteristics for the 10%, 5% and 1% Ti samples. The large absorption feature at roughly 300 nm is due to the promotion of the electrons from the valence band of TiO_2 into the conduction band, implying bulk TiO_2 structure. Additionally, the 1% Ti sample contained a more pronounced second absorbance feature at 205 nm. Others have speculated that absorption between 210-205 nm on TiO_2-SiO_2 is due to isolated Ti^{4+} sites (Si-O-Ti-O-Si) deposited within the silica matrix.[198,203] Additionally, we expect the highest concentration of isolated Ti^{4+} to occur in sol-gel synthetic conditions in which the amount of Ti precursor is limited.

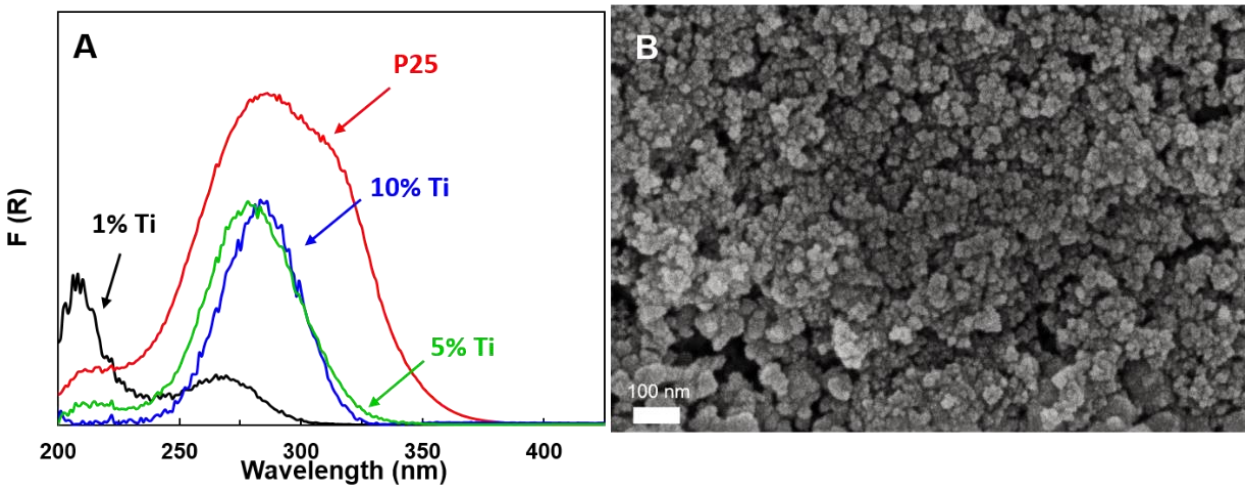

Figure 5.2. (A) DR-UV/Vis absorbance of the synthesized TiO_2-SiO_2 materials. The absorbance spectrum of SiO_2 was subtracted from each material (B) SEM image of the 5% Ti sample.

XPS characterization of the as-synthesized TiO_2-SiO_2 samples identified unique Ti electron structure compared to the P25 reference material. XPS spectra are shown in Figure 5.3 for P25, 1% TiO_2-SiO_2 and 5% TiO_2-SiO_2 samples. For the reference material, P25, one major feature is identified at 458.7 eV (with the second 2p splitting feature appropriately positioned at 464.5 eV) and associated with a TiO_2 structure.[211] The 1% Ti and 5% Ti samples synthesized using the sol-gel method both featured a similar feature at 459 eV in addition to a higher energy shoulder located at 460 eV. We speculate the additional high energy feature on the synthesized TiO_2-SiO_2 materials could be attributed to the structure of an isolated Ti^{4+} if the O-Si-O network around the isolated Ti atom acts to pull some electron density away from the Ti^{4+} site.[212]

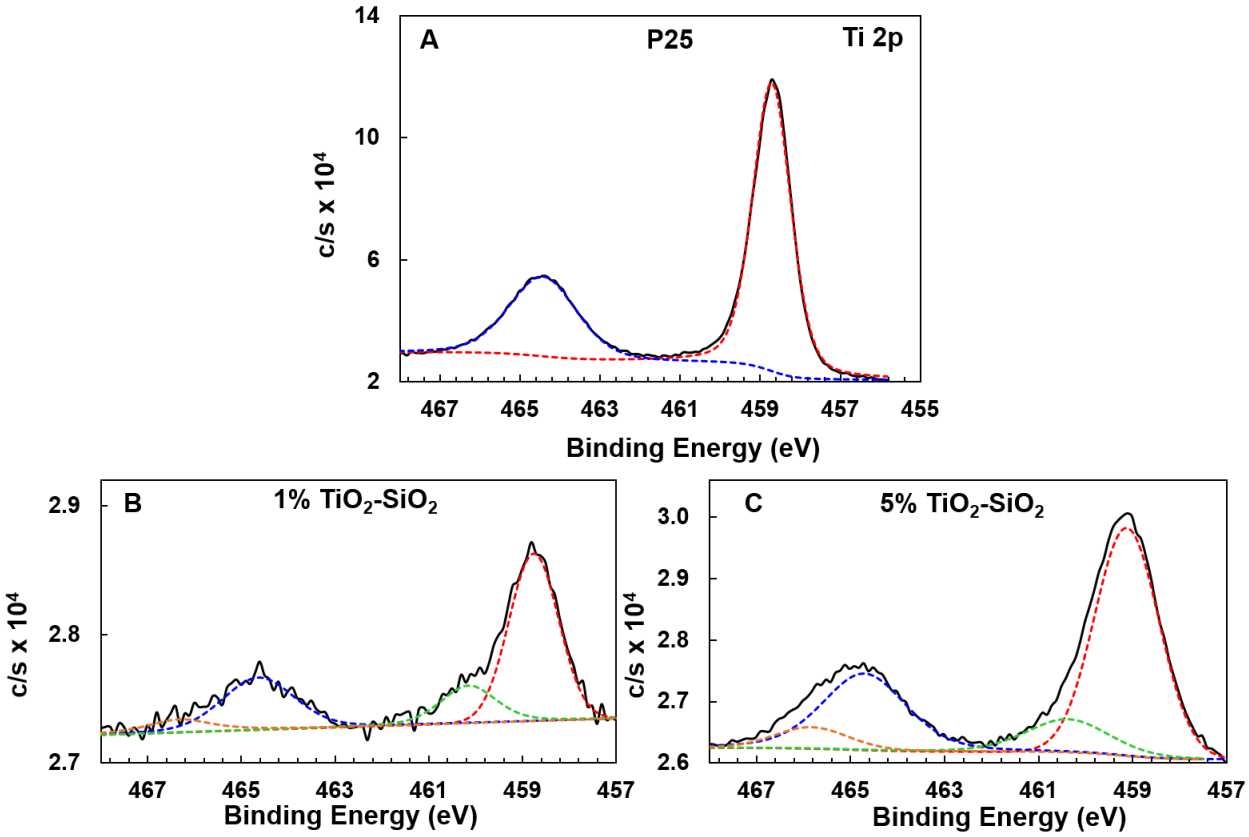

Figure 5.3. X-ray photoelectron spectroscopy of the Ti 2p region for (A) P25, (B) 1% TiO_2-SiO_2, and (C) 5%TiO_2-SiO_2.

CO adsorption onto the TiO_2-SiO_2 samples provided further evidence of both TiO_2 and SiO_2 regions exposed on the surface. The vibrational frequency of $CO_{(ads)}$ is highly dependent on the nature of the surface site for which the CO molecule is bound. Specifically, when CO adsorbs onto a strong Lewis acid, CO coordinates to the surface only through a sigma bond with the electrons from the 5σ orbital located primarily around the carbon atom.[213] A sigma interaction induces a significant blueshift in the frequency of the ν(C-O) vibration as the CO molecule coordinates through the carbon end with surface.[98] Conversely, when CO interacts with a hydroxyl group, the interaction is electrostatic in nature and induces a slight blueshift relative to the gas phase fundamental frequency of CO at 2143 cm^{-1}.[101] Infrared spectroscopy of CO adsorption onto

the TiO_2-SiO_2 materials identified a feature at 2154 cm^{-1} consistent with CO interacting with the abundant hydroxyl groups of SiO_2 regions.[94] The assignment was confirmed with CO adsorption on a SiO_2 reference material (see Fig. 5.4, blue trace). A second absorbance feature at 2185 cm^{-1}, easily identified on the 10% Ti and 5% Ti samples, suggested CO adsorption onto Ti^{4+} sites of TiO_2 regions. This assignment was confirmed when CO was adsorbed onto a TiO_2 reference material (see Fig. 5.4, red trace). However, infrared absorption of CO interacting with the 1% Ti sample did not exhibit a feature at 2185 cm^{-1} associated with TiO_2 surface structure. We speculate that the concentration of TiO_2 surface structure within the 1% Ti sample is below the limit of detection for CO adsorption. Isolated Ti^{4+} species are not expected to adsorbed CO at the temperatures used in this study ($T << 100$ K to observe isolated Ti^{4+}-CO interactions).[96,214] Therefore, we considered the 1% Ti sample the most likely sample to contain isolated Ti^{4+} surfaces sites instead of TiO_2 surface structure.

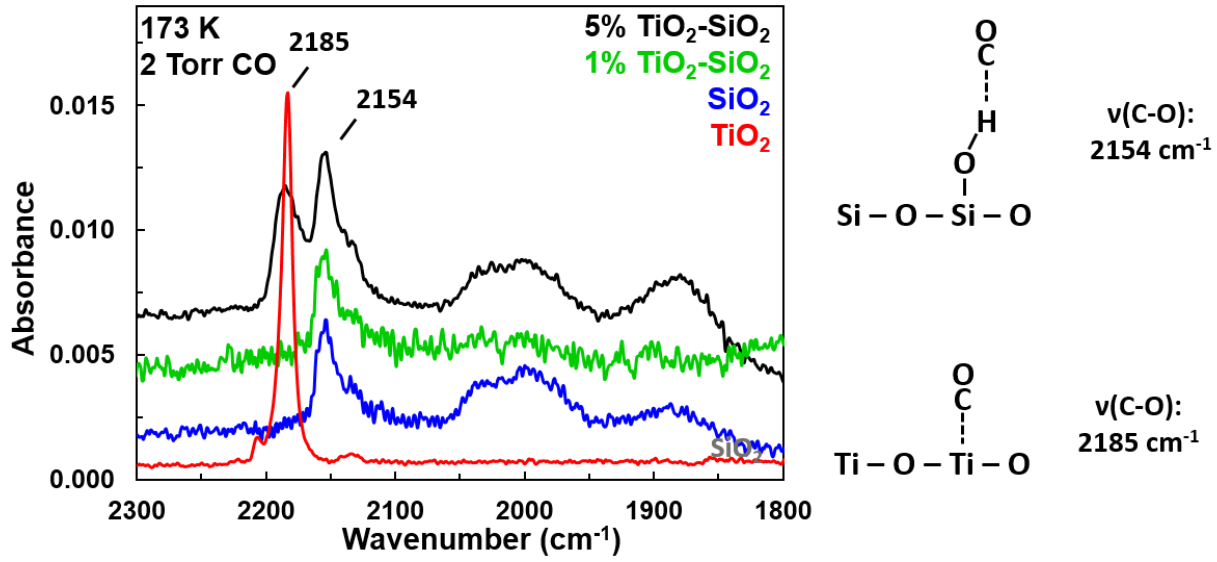

Figure 5.4. Infrared spectra during the adsorption of CO at 173 K on the 1% Ti, 5% Ti, SiO_2, and TiO_2 materials. Schematic representations of the CO adsorption on a Ti^{4+} site and the hydroxylated SiO_2 surface are provided as well.

5.3.2 TiO_2-SiO_2 Photoepoxidation

Photoepoxidation of propene over the synthesized TiO_2-SiO_2 materials was investigated utilizing *in situ* infrared spectroscopy in the high-vacuum chamber. An infrared spectrum of adsorbed propene (2 Torr in chamber) was used as a spectral background and the reaction mixture (2 Torr O_2, 1000 W Hg Arc lamp) was subsequently introduced into the chamber. The mixture of propene, oxygen, and light interacted with the sample and produced surface species during the collection of infrared spectra. Figure 5.5A provides the time-resolved infrared spectra recorded during a 2-hour reaction with the 5% Ti sample. Two major features appear, one at 1680 cm^{-1} and another at 1408 cm^{-1}. It should be noted that less than 1% of the adsorbed propene reacted during the experiment as evidenced by the lack of negative-going vibrational features associated with propene on the surface. We speculate that the reaction temperature of 303 K did not generate

significant reaction products. Additionally, the intensity of light reaching the sample (passing through the fiber optic cable and focusing lens) was likely well below that of the 1000 W source.

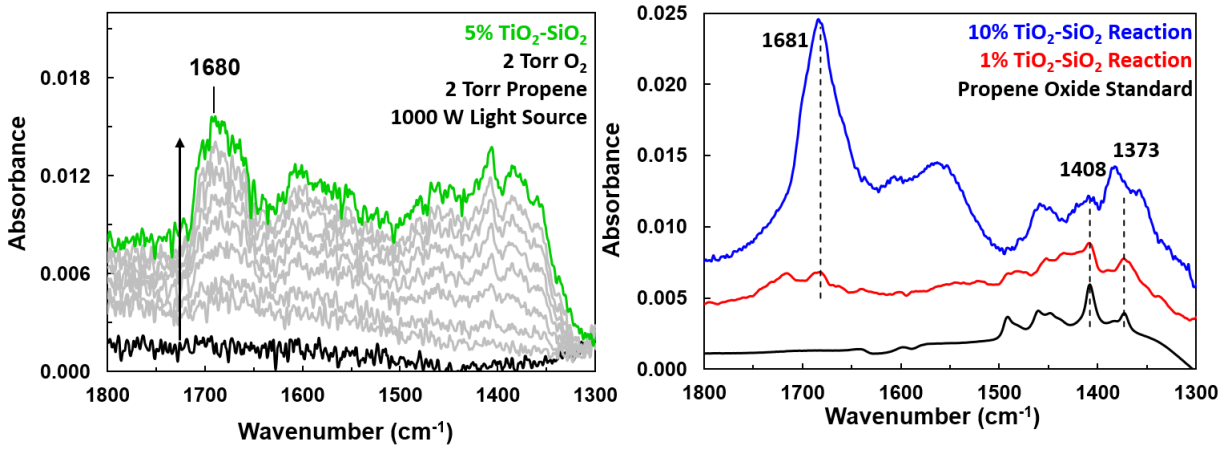

Figure 5.5. Infrared spectra acquired during the photoepoxidation of the propene. (A) Time-resolved infrared spectra acquired over a 2-hour reaction time period on the 5% TiO_2-SiO_2 sample. (B) Infrared spectrum acquired for the 1 % and 10 % TiO_2-SiO_2 samples after 2 hours of photoepoxidation reaction conditions. The black trace represents PO adsorption over the 10% TiO_2-SiO_2 sample.

Infrared spectra acquired after two hours under the same reaction conditions using the 1% Ti and 10% Ti materials are shown in Figure 5.5B. The infrared spectrum of the 10% Ti sample illustrates a significant increase in the 1680 cm^{-1} vibrational feature in addition to large features at 1550 cm^{-1}, 1460 cm^{-1} and 1390 cm^{-1}. The 1408 cm^{-1} feature, identified on the 5% Ti sample, appears in trace amounts on the 10% Ti sample. On the other hand, the infrared spectrum of the 1% Ti sample shows a much smaller vibrational feature at 1680 cm^{-1} and two features at 1408 cm^{-1} and 1373 cm^{-1}. It should be noted that studies, which removed one of the three reactants (propene,

oxygen, or light), exhibited no surface–product formation as evidenced by a lack of positive-going vibrational features over the entire spectral window.

Propene oxide adsorption onto the 10% TiO_2-SiO_2 sample confirmed the formation of propene oxide during the photoepoxidation of propene. The infrared spectrum of propene oxide adsorption, shown in the Figure 5.5B (black trace), confirmed the 1408 cm^{-1} and the 1373 cm^{-1} vibrational features as propene oxide vibrational features (Table 5.1). Additionally, the confirmed propene oxide vibrational features are present in the highest concentration on the 1% Ti sample relative to the concentration of titanium present in the sample. We speculate that the broad features present at 1680 cm^{-1} and 1705 cm^{-1} (identified during all photoepoxidation reactions) are a combination of acrolein and acetone—likely produced as a by-product or as a result of propene oxide degradation.[197]

Table 5.1. Tabulated infrared vibrational frequencies for propene oxide adsorption onto TiO_2-containnig surfaces.

Vibrations	Au/TiO_2[ψ]	TiO_2-SiO_2[#]
$\nu_{as}(CH_2)$	3049	*
$\nu(CH)$	3005	*
$\nu_s(CH_2)$	2970	*
$\nu_{as}(CH_3)$	2931	*
$\nu_s(CH_3)$	2870	*
$\delta_{as}(CH_3)$	1486, 1445	1493, 1459
$\delta(CH)$	1410	1407
$\delta_s(CH_3)$	1373	1374
Sym. Ring breathing	1270	*

[ψ]Vibrational modes and frequencies acquired from Ref.[52]

#This work

*Vibrational features not identified on our TiO_2-SiO_2 materials due to a high absorbance of the clean TiO_2-SiO_2 material

5.4. Discussion

Through the synthesis of multiple TiO_2-SiO_2 materials, with varying amounts of titanium incorporated into the synthesis, we were able to determine that materials with less titania surface structure produced similar amounts of propene oxide and did not exhibit the propensity to produce other oxidized by-products. These studies suggest that TiO_2 regions of the materials vary significantly in terms to the type of chemistry that occurs compared to isolated Ti^{4+} atoms dispersed within a SiO_2 matrix. A fundamental understanding of how propene adsorbs and diffuses will help to gain more insight into how propene binds on different surface structure such as TiO_2 or SiO_2

and help to elucidate the reason propene oxidizes on TiO_2 to form undesired, non-epoxide, products.

5.4.1 Propene Binding on TiO_2 vs. SiO_2

Infrared spectra of propene adsorption on both TiO_2 (P25 reference material) and SiO_2 (Aerosil reference material) identified key differences between the two surfaces. Clean reference materials of SiO_2 and TiO_2 were installed in the high-vacuum chamber to understand the characteristics of propene adsorption. As shown in Figure 5.6, propene binds to both TiO_2 and SiO_2. On SiO_2, a large negative feature at 3749 cm^{-1} and a large positive feature at 3569 cm^{-1} dominate the high wavenumber region of the infrared window. These two features are attributed to propene adsorption onto the hydroxyl groups found on the surface of SiO_2 and depicted in Figure 5.6.[65,215-216] Propene binds through the pi electron density around the C=C. Since electron density from the pi electrons coordinates with the surface site, we would expect a redshift in the frequency for the ν(C=C) when adsorbed because the propene double bond is slightly weakened upon adsorption.[37-38] On SiO_2, the ν(C=C) shifts to 1642 cm^{-1} (a 9 cm^{-1} redshift relative to the gas phase vibration). On TiO_2, the ν(C=C) exhibits a redshift to 1631 cm^{-1}, which suggests the increased strength of the bond between propene and Lewis acidic Ti^{4+} sites.[217] The TiO_2 surface contained minimal hydroxyl groups as evidenced by the lack of the negative vibrational feature at 3600 cm^{-1} and suggests that propene coordination to the surface occurs only by adsorption to Ti^{4+} sites.

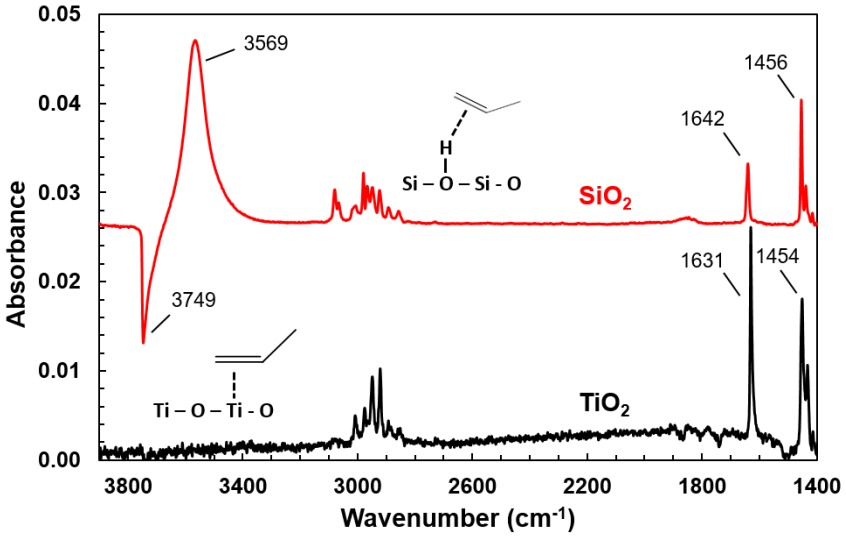

Figure 5.6. Infrared spectrum of propene adsorption onto a SiO_2 and TiO_2 surface.

5.4.2 Propene Diffusion on TiO_2 vs. SiO_2

Isothermal diffusion experiments on both TiO_2 and SiO_2 provided further evidence of increased propene interaction at TiO_2 regions compared to SiO_2 regions. Propene easily diffused across and desorbed off both the titania and silica samples under the thermal conditions provided (see Fig. 5.7 for representative infrared spectra during the desorption/diffusion process). The integrated intensity of the ν(C=C) of propene was plotted with respect to the initial coverage of propene on each surface over the diffusion time scale (Fig. 5.8 A & B). Each experimental data set was modeled using eqn. 5.2 to calculate the diffusion coefficient at each specific temperature (diffusion coefficient values, *D*, tabulated in Table 5.2). The Fickian diffusion model does not appropriately capture the initial diffusion process on SiO_2. The Fickian model still accurately depicts the slow portion of the isothermal experiment and thus a full analysis can be achieved on this portion of the experimental data.

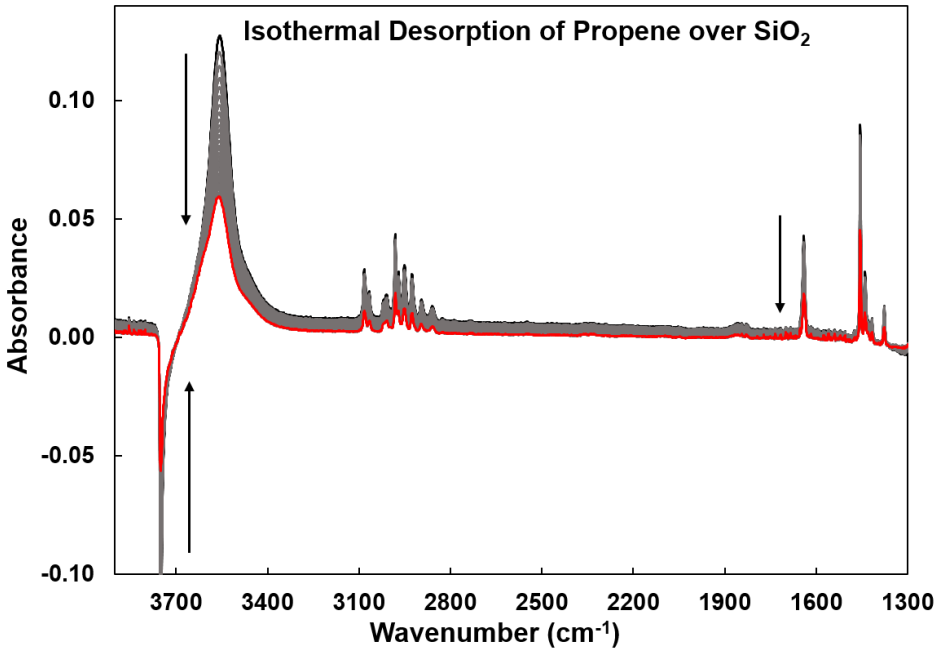

Figure 5.7. Infrared spectra acquired over 40 minutes during the desorption of propene on silica at 103 K. The black spectrum represents propene at the highest coverage while the red spectrum represents propene still adsorbed after 2400 seconds.

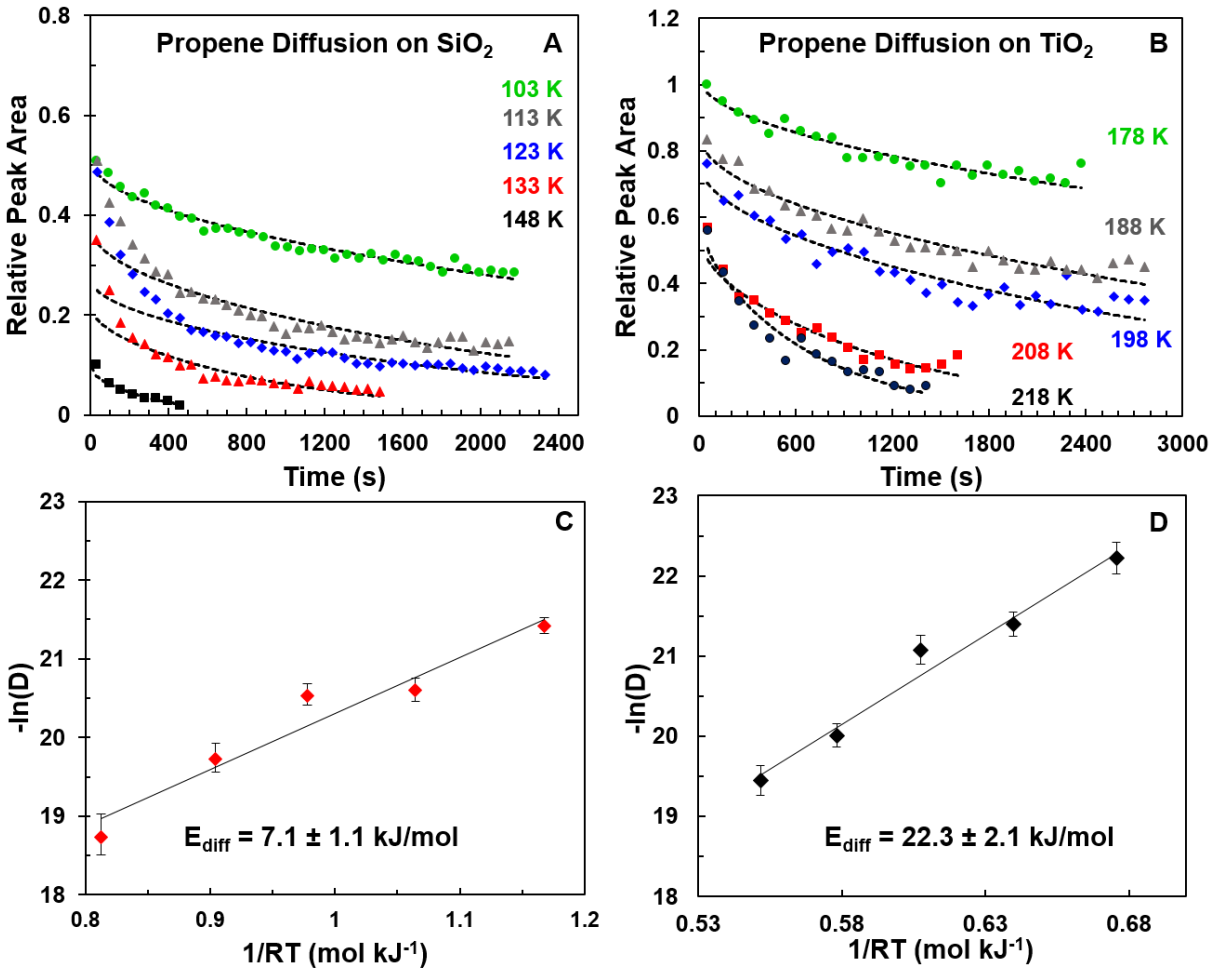

Figure 5.8. Diffusion of propene over silica (A & C) and titania (B & D). Panels A and B provide the relative peak area for propene over time at different temperatures. Dashed lines model the process with Fick's 2nd Law of Diffusion. Panels C and D provide an Arrhenius-like analysis of the diffusion coefficients to attain apparent activation energies of diffusion.

Propene diffuses through silica faster compared to titania. The temperature dependence of propene diffusion on both surfaces (the diffusion coefficient increased with temperature) suggests an Arrhenius-type analysis of the diffusion coefficients for a specific material can be applied using the following equation:

$$D(T) = D_0 e^{(-\frac{E_{diff}}{RT})} \quad (5.4)$$

where E_{diff} is the apparent activation energy of diffusion, $D(T)$ is the experimentally attained diffusion coefficient, D_0 is a prefactor fitting parameter, T is the sample temperature, and R is the ideal gas constant. The E_{diff} for propene diffusion on silica and titania was found to be 7.1 ± 1.1 and 22.3 ± 2.1 kJ/mol, respectively. The experimentally attained energetics of propene diffusion in addition to stronger adsorption interaction (shown via the vibrational shift of the C=C) suggest that propene will interact with TiO_2 regions of a TiO_2-SiO_2 material more strongly. The stronger binding of propene to TiO_2 suggests that potential propene photoepoxidation side-products could be produced in high concentrations on TiO_2 regions because of the stronger propene–surface interactions. Additionally, a major drawback of our synthetic sol-gel method is that even at low %Ti synthetic conditions an observable amount of TiO_2 surface structure is formed.

Table 5.2. Diffusion coefficients for propene on both silica and titania at each temperature studied.

Propene on Silica		Propene on Titania	
Temperature (K)	Diffusion Coefficient (cm^2/s)	Temperature (K)	Diffusion Coefficient (cm^2/s)
103	5.00×10^{-10}	178	2.24×10^{-10}
113	1.14×10^{-9}	188	5.08×10^{-10}
123	1.21×10^{-9}	198	7.02×10^{-10}
133	2.70×10^{-9}	208	2.04×10^{-9}
148	7.31×10^{-9}	218	3.58×10^{-9}

5.4.3 Photodegradation of Propene Oxide on TiO_2-SiO_2

The UV-illumination of propene oxide in the presence of O_2 identified vibrational signatures of degradation products at similar frequencies to those observed during the photooxidation of propene. Propene oxide was pre-saturated onto the 5% TiO_2-SiO_2 sample. With propene oxide adsorbed onto the surface as the spectral background, 2 Torr of O_2 was introduced while the 1000 W Hg arc lamp irradiated the sample for 30 minutes. Infrared spectra of propene oxide degradation, depicted in the Figure 5.9, show negative-going vibrational features at 1480 cm^{-1} and 1408 cm^{-1} associated with the $\delta_{as}(CH_3)$ and $\delta(CH)$ of propene oxide. Additionally, the positive-going vibrational features clearly identified a carbonyl-like vibration on the surface—not present when propene oxide is adsorbed. We speculate that propene oxide easily degrades under UV light and that the low energy bonds of the epoxide ring, break, and reform to produce acrolein or acetone.

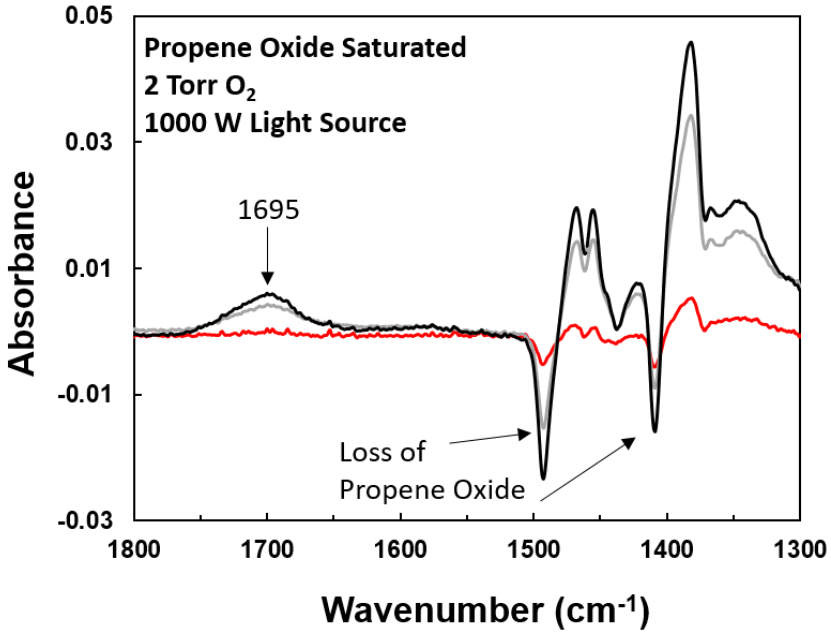

Figure 5.9. Infrared spectra of propene oxidation degradation on the 5% TiO_2-SiO_2 sample in the presence of O_2 and UV light. The red spectrum depicts the reaction of propene oxide after 4 minutes while the black spectrum represents the reaction of propene oxide after 30 minutes.

5.4.4 Insight into the Mechanism of Propene Epoxidation and By-Product Formation

Through the photooxidation experiments and molecular-level adsorption and desorption studies performed, we speculate on important mechanistic factors that occur during the photoepoxidation of propene over TiO_2-SiO_2 materials. Firstly, experimental evidence suggests that the adsorption of propene onto TiO_2 has adverse effects in the production of propene oxide. The stronger adsorption between the pi electrons on propene and the Lewis acidic Ti^{4+} sites of TiO_2 may be a major contributor to the production of other carbon-containing products such as acetone or acrolein. The vibrational spectroscopic techniques used in this chapter do not provide clear evidence of the isolated Ti^{4+} surface sites. However, the low-Ti concentration sample did exhibit a greater propene oxide to side-product ratio. We can only speculate to the surface species

that contribute to the formation of propene oxide. Additionally, propene oxide produced these TiO_2-SiO_2 materials likely diffuses to TiO_2 regions, reacts further and degrades upon the UV irradiation conditions. For further improvement of the photoepoxidation process, we suggest advances in the synthetic method that limit the concentration of extended TiO_2 regions.

5.5 Summary

In summary, we applied *in situ* spectroscopic techniques to study the photoepoxidation of propene into propene oxide over TiO_2-SiO_2 materials. Infrared spectra acquired during the reaction identified trace amounts of propene oxide produced in the presence of the UV light and O_2. However, significant by-products (or over-oxidation) impeded the selective production of propene oxide and the concentration of these by-products increased with the increased amount of Ti used in the synthesis. Systematic evaluation of propene adsorption and diffusion over TiO_2 and SiO_2 reference materials suggested that propene binds more strongly and diffuses slower (with a greater activation barrier) over TiO_2 compared to SiO_2. These results suggest that under the UV conditions required to produce propene oxide, synthetic advances to eliminate extended TiO_2 regions are necessary to promote increased selectivity of the desired product.

Chapter 6

Surface Decomposition of a Chemical Warfare Agent Simulant: Mechanistic Steps of Dimethyl Chlorophosphate Oxidation on a Cu/TiO_2 Aerogel

6.1 Introduction

Organophosphorus (OP)-based compounds have commanded the headlines of international news due to their functionality as chemical warfare agents (CWAs). In particular, the G-series nerve agent sarin (GB) and more recent synthetic derivatives have been identified in current warzones and used in lethal doses on non-military targets.[218-220] Recent global events command the need for new materials that can sequester, detoxify and desorb benign products for continued and catalytic decomposition of these harmful OP-based vapors.

6.1.1 Organophosphate Decomposition on Au and Cu Surfaces

A promising research area associated with the emergence of new heterogeneous catalysts lies in the development of 3D inorganic architectures designed to provide high surface areas and extreme stability in the harsh conditions often required for catalytic conversion of gas-phase compounds. These properties make aerogel supports of metallic particles particularly attractive candidates for the destruction of OP-based CWAs because low vapor pressure reactants and tight surface binding of products necessitate the input of thermal, photonic, or chemical energy into the system. Any reusable catalyst must withstand such energetic challenges.

In order to promote desorption or diffusion of bound products by reducing activation energies, metal particles deposited on metal oxide supports provide materials with interfacial reaction zones for improved chemical reactivity. Particularly noteworthy are TiO_2-supported Au nanoparticles that contain uniquely active surface sites at the TiO_2-Au interface.[12,18,221-222] Recent studies suggest supported-Au nanoparticles oxidize DMMP to form trace amounts CO and CO_2 at

environmentally relevant temperatures.[181] The oxidative chemistry occurs through the assistance of both lattice oxygen and adsorbed O_2 activated at the Au/TiO_2 interface.[181] These findings demonstrate that supported metal/metal oxide materials can drive oxidative chemistry in gas-surface reactions—processes aided by metal-support interactions and bi-functional interfacial contact points.

While supported Au-based materials exhibit intriguing properties, recent demonstrations of 3D aerogel-based materials stabilize metallic Cu against air oxidation and indicate that other, more abundant metals, hold the potential to further advance the field.[32] The utilization of copper particles in heterogeneous catalysis is particularly attractive because of the relative abundance of Cu. Currently, Cu is used to facilitate sorption over high-surface area activated carbon filters.[223] Supported-Cu materials present a variety of oxidation states, including Cu^0, Cu^{1+}, and Cu^{2+} for which the synthetic method and sample history have significant impact. However, the influence of Cu oxidation state on catalysis remains to be fully explained.[32,224-225] For example, recent research demonstrated that the reaction rate for CO oxidation decreases with increasing copper oxidation state, which suggests that metallic Cu is the active species.[226] However, the oxidation state of Cu particles rapidly changes during catalysis from the more reactive metallic or Cu^{1+} state to the less reactive Cu^{2+} state.[227-228]

Copper oxide materials have recently been studied for the decomposition of CWA simulants.[77,229] For example, copper oxide (Cu^{2+}) impregnated into carbon textiles was found to degrade dimethyl chlorophosphate (DMCP) vapor through a hydrolysis pathway that initially forms HCl.[230] The HCl reacts with the methoxy functional groups of the OPs to produce $CH_3Cl_{(g)}$ and a surface-bound phosphate product.[79] Highly-sensitive XPS studies of DMMP adsorption on

CuO identified multiple surface-products produced through rupture of the PO-CH_3, P-OCH_3, and P-CH_3 bonds of DMMP[229] while Cu_2O produced atomic phosphorus at room temperature.[77]

In this study we have synthesized Cu/TiO_2 aerogels with multiple interfacial Cu/Ti contact points to study the decomposition of the CWA simulant, DMCP. Aerogel-based materials resist oxidation to Cu^{2+} while sustaining unique chemistry due to their reducible-support metal nanoparticle structure.[31-32,221] Motivated by the practical importance of CWA decomposition, we applied *in situ* spectroscopic measurements to reveal the adsorption and oxidation tendencies of DMCP over a Cu/TiO_2 aerogel. Identified through the vibrational features of the adsorbed reaction products, CO molecules bound to Cu_2O regions of the material were confirmed as the major decomposition product. We propose a surface-oxidation mechanism for DMCP oxidation in which DMCP first reacts with an interfacial-bound O_2 molecule to produce a surface-bound methoxy species that then reacts further to produce CO.

6.2. Procedural Methods

6.2.1 Synthesis of Cu/TiO_2 Aerogel

All synthetic procedures were performed by the Debra Rolison group at the U.S. Naval Research Laboratory and further details of the synthetic procedure are provide here.[32] Titania aerogels were prepared using a sol-gel method as described elsewhere.[32,231] The titania precursor ($Ti(^iOPr)_4$) was added to a mixture of ethanol, water and nitric acid. The mixture gelled quickly and was cured for an additional 24 hours. The wet gels were rinsed with acetone and then loaded into a supercritical dryer. The aerogels were then calcined in air at 700 K to produce the nanocrystalline anatase structure. Copper was subsequently photodeposited into the TiO_2 aerogel by illuminating a slurry of TiO_2 powder with 2nM of $Cu(NO_3)_2$ in a solution of H_2O/ethanol (pH

adjusted to 9.5 with NaOH and HCl). The composite Cu/TiO_2 aerogels were then centrifuged multiple times with the resultant supernatant removed each cycle.

6.2.2 Material Characterization with X-Ray Photoelectron Spectroscopy

Ex situ XPS characterization was performed with a PHI VersaProbe III scanning XPS microscope using a monochromatic Al K α X-ray source (1486.6 eV). The acquisition of XPS spectra associated with the C1s, Ti2p, O1s, $Cu2p_{3/2}$, P2p, and Cl2p utilized a 26 eV pass energy, which gives a $Ag3d_{5/2}$ full width at half-maximum of 0.59 eV. All binding energies are referenced to C−C at 284.8 eV.

6.2.3 Flow Reactor Studies with Infrared Spectroscopy

Adsorption and oxidation studies of DMCP were performed in an ambient pressure flow reactor for the TiO_2 aerogel, Cu/TiO_2 aerogel and a standard Cu_2O material. Samples were installed into a Thermo Nicolet Nexus 670 infrared spectrometer in diffuse reflectance mode (DRIFTS) using a DRIFTS cell (Pike Technologies HC-900). An *in situ* activation of 1 hour at 150 °C under a 10 mL/min flow of Ar effectively removed loosely-bound surface adsorbates. DMCP vapor, carried by Ar for approximately 30 minutes, adsorbed onto and reacted with each sample at 300 K during the acquisition of infrared spectra.

6.2.4 Vacuum Studies of Adsorption and Oxidation with Infrared Spectroscopy

Systematic studies of adsorption and oxidation were performed in a stainless-steel high-vacuum reactor cell with a base pressure of 1×10^{-8} Torr. Cu/TiO_2 and TiO_2 aerogel samples were pressed into a tungsten mesh, which was then secured onto a precision manipulator. Details of the high-vacuum cell are provided in Chapter 2. An FTIR spectrometer with an external MCT-A detector (Thermo, Nicolet Nexus 470 FTIR, resolution 2 cm^{-1}) is attached to the vacuum chamber to provide the *in situ* infrared spectroscopic measurements.

Samples were pretreated in the vacuum chamber for 1 hour in 673 K in 10 Torr of O_2 followed by 30 minutes at 673 K in vacuum. This procedure, confirmed with infrared spectroscopy of each sample, effectively removes weakly-bound organic species on the surface. For exposures of O_2 (99.994% purity, Airgas Ultra High Purity), $^{18}O_2$ (99% atom, Sigma Aldrich) and CO (99.3% purity, Airgas CP300), a gas manifold affixed to the vacuum chamber allowed for quantifiable amounts of each adsorbate to be introduced into the chamber and exposed onto each material. Materials such as CH_3OH (99.9% HPLC grade, Sigma Aldrich), $CH_3{}^{18}OH$ (95% atom, Sigma Aldrich), and DMCP (97%, Sigma Aldrich) were stored in glass bulbs, attached to the gas manifold, and purified via three freeze-pump-thaw cycles. Gaseous vapor was then subsequently pulled into the manifold for experimental studies.

6.3 Results and Discussion

The adsorption and oxidation pathways of the CWA simulant, DMCP, were investigated through the utilization of *in situ* infrared spectroscopic measurements on a TiO_2-supported Cu aerogel and a TiO_2 aerogel. Direct comparison between the two materials suggest that Cu/Ti interfacial sites—abundant compared to traditional 2-dimensional surface-decorated materials–are active for the decomposition of DMCP. A major decomposition product of DMCP oxidation was found to be copper-bound CO molecules produced through a surface-bound methoxy intermediate. The Cu/Ti interfacial sites, identified through infrared spectroscopic characterization, become blocked over extended oxidation time periods by the production of strongly bound molecules such as phosphate (PO_x) and bidentate-adsorbed formate. These studies highlight the importance of the metal/support interactions, exhibited by these multiple-contact-point aerogel materials, in the detoxification of CWA simulants.

6.3.1 Cu/TiO_2 Characterization

Exposed surface atoms on the Cu/TiO_2 aerogel were characterized utilizing adsorbed CO as a probe molecule. CO was introduced into the chamber at a pressure of 1 Torr and sample temperatures of 180 K and 300 K. The infrared spectra of CO adsorption on the Cu/TiO_2 aerogel is shown in Figure 6.1. Similar to previous infrared spectroscopic studies of TiO_2-supported Cu materials, the low temperature CO adsorption (Fig. 6.1, red trace) results in infrared features at 2108 cm^{-1} and 2180 cm^{-1} associated with CO bound to Cu^{1+} and Ti^{4+} surface sites respectively.[32,232] At low temperatures, CO adsorption onto the Ti^{3+} sites near the Cu/Ti interface is also likely to be found at 2100 cm^{-1}.[233-234] CO adsorption to metallic regions of Cu appears as a small shoulder at 2056 cm^{-1}—likely found at interfacial regions surrounding the Cu particles.[232] The feature associated with Cu^0 appears redshifted relative to the CO-Cu^{1+} feature because the metallic Cu particles induce a greater backdonation of electrons into the $2\pi^*$ antibonding orbitals of adsorbed CO molecules. We speculate that the CO absorption feature at 2155 cm^{-1} is due to CO bound to undercoordinated or isolated Cu^{1+} sites.[96] The infrared spectrum upon CO adsorption at 300 K (Fig. 6.1, black trace) indicates no CO-Ti^{4+} feature, which suggests weak adsorption of CO to the support (note the absence of absorbance at 2180 cm^{-1}). Conversely, CO-Cu^{1+} and CO-Cu^0 vibrational features were present at 300 K, which suggests strong adsorption compared to the Ti surface sites.

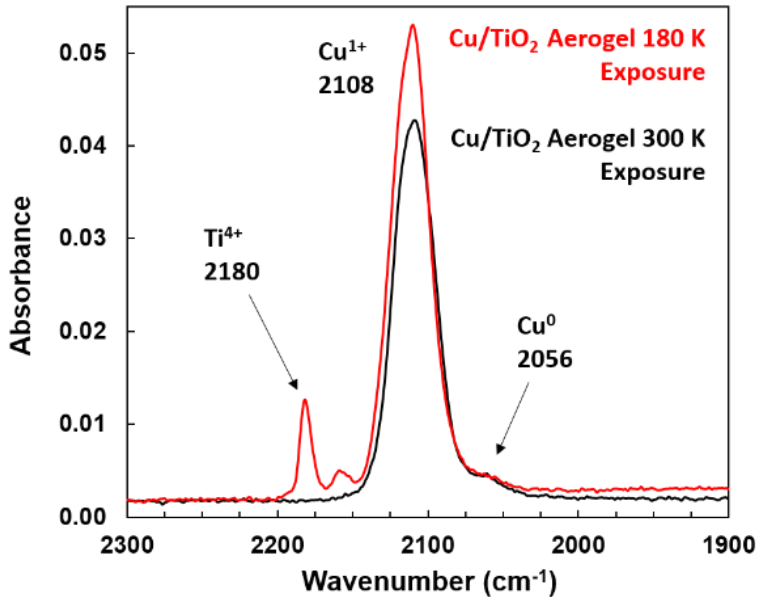

Figure 6.1. Infrared spectrum of CO adsorption at 180 K (red trace) and at 300 K (black trace) on a Cu/TiO_2 aerogel.

6.3.2 DRIFTS Studies of DMCP Degradation

The degradation of the CWA simulant, DMCP, over a Cu/TiO_2 aerogel was studied in a DRIFTS reactor cell under continuous flow conditions. Infrared spectra acquired during DMCP flow over the $CuTiO_2$ aerogel is depicted in Figure 6.2. Over the 30-minute exposure time period, an infrared feature emerged at 2109 cm^{-1} for reactions over the Cu/TiO_2 sample. This feature is consistent with the stretching vibration of CO bound to Cu^{+1} surface sites. In addition, five major features identified in the low-wavenumber region at 1660 cm^{-1}, 1586 cm^{-1}, 1569 cm^{-1}, 1371 cm^{-1}, and 1350 cm^{-1} are associated with the $\nu_{as}(C=O)$ of a mondentate bound carbonyl and two unique bidentate-bound formate vibrational modes ($\nu_{as}OCO$) and ($\nu_{s}OCO$), respectively.[221] The vibrational features between 1500 – 1400 cm^{-1} appear to be the gas phase vibrational signatures of CH_3Cl that either was present in trace amounts in the gas feed or was produced via a DMCP

hydrolysis pathway with the native surface hydroxyls present on TiO_2 or Cu_2O regions of the materials.[79,235]

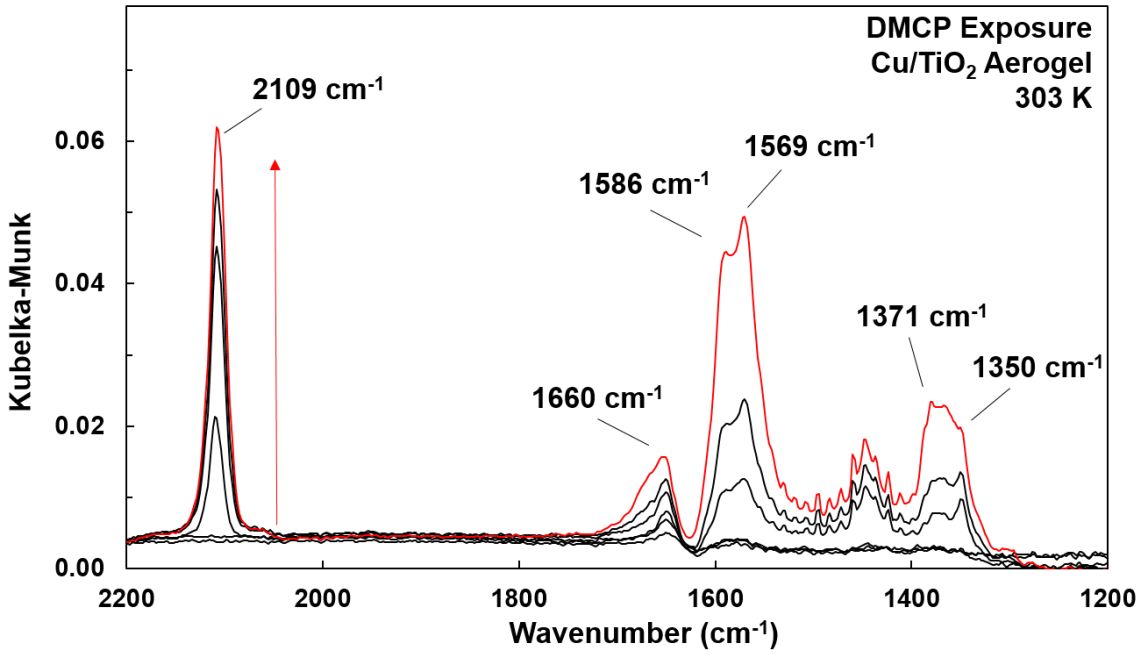

Figure 6.2. DRIFTS spectra acquired during exposure of DMCP over a Cu/TiO_2 aerogel during a 30-minute exposure.

Upon DMCP adsorption onto the TiO_2 aerogel, no features between 2100-2200 cm^{-1} emerged, suggesting no production of surface bound CO. Instead, the DRIFTS spectra showed only three features emerging at 1660 cm^{-1}, 1591 cm^{-1} and 1340 cm^{-1}, consistent with carbonyl vibrational motion ($\nu_{as}C=O$) and formate vibrational motions ($\nu_{as}OCO$ & ν_sOCO), respectively (Fig. 6.3B).[221] DMCP flow over the TiO_2 aerogel for extended time (2 hours) revealed significant loss of features attributed to free hydroxyl vibrations between 3600 – 3700 cm^{-1} (Fig. 6.3A, blue spectrum). Additionally, vibrational features at 1045 cm^{-1}, 1135 cm^{-1} and 1303 cm^{-1} developed; consistent with the $\nu_s(CO)$, $\rho(CH_3O)$ and $\nu(P=O)$, respectively of molecularly adsorbed DMCP.

These studies demonstrated that, like the Cu/TiO_2 sample, the pure TiO_2 aerogel cleaved the P-Cl and P-OCH_3 bonds to produce surface-bound formate species. However, subsequent reactions (observed on Cu/TiO_2) that produce CO do not occur in the absence of the copper nanoparticles. In addition to the pure TiO_2 sample, we repeated the experiments with a Cu_2O standard as the sorbent. Importantly, no infrared features that could be attributed to surface-bound CO emerged in this control experiment, which helps confirm the unique reactivity of the Cu/Ti aerogel toward DMCP decomposition (Fig. 6.3C).

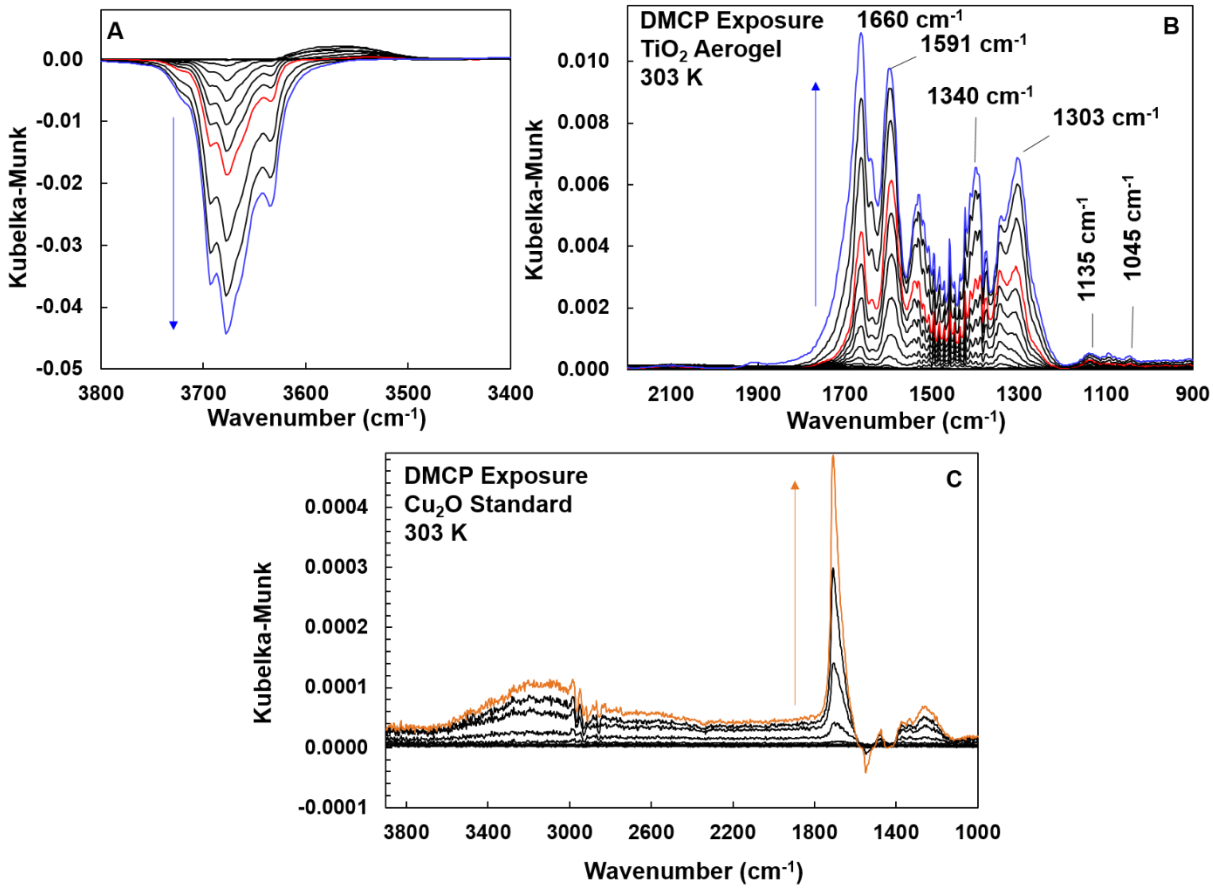

Figure 6.3. DRIFTS spectra acquired during exposure of DMCP over a TiO_2 aerogel (A & B) and a Cu_2O standard (C) during a 2-hour exposure.

6.3.3 Fundamental Studies of DMCP Adsorption

The DRIFTS-based experiments described above show evidence for surface-bound carbonyl-containing species (likely monodentate- and bidentate-bound formate, -OOCH) and carbon monoxide when DMCP is exposed to the Cu/TiO_2 aerogel under atmospheric conditions; therefore, the surface chemistry was explored in more detail through the well-controlled environment of a high-vacuum reaction cell. This system was employed to systematically study DMCP adsorption, first in the absence of gas-phase oxygen, then the presence of oxygen to elucidate specific mechanistic steps toward oxidation.

In the absence of oxygen, DMCP was found to adsorb on the Cu/TiO_2 and TiO_2 aerogels through both molecular and dissociative pathways. Each aerogel was exposed to 2 Torr of DMCP vapor. After an exposure of 1 minute, the DMCP vapor was removed from the chamber, leaving only strongly bound DMCP and degradation products on the surface. Infrared spectra of the DMCP-saturated materials, under vacuum, are shown in Figure 6.4. Consistent with the DRIFTS spectra, the transmission-infrared spectra indicated that DMCP adsorption occurs through the formation of hydrogen bonds to free hydroxyl groups native to both the Cu/TiO_2 and TiO_2 aerogels (note the negative features between 3600-3800 cm^{-1} and an associated broad feature between 3500-2600 cm^{-1}). In addition, large positive features at 2961 cm^{-1} [$\nu_a(CH_3)$] and 2860 cm^{-1} [$\nu_s(CH_3)$] indicate the presence of molecularly adsorbed DMCP on both surfaces. Additionally, a small feature at 2930 cm^{-1} was also identified on both surfaces and attributed to the $\nu_a(CH_3)$ of methoxy groups. The methoxy vibration suggests that the P-OCH_3 bond of DMCP is cleaved through reaction with a surface hydroxyl group[236] or oxidation with reactive oxygen [$O_{2(ads)}$][181,237-238] produced through the thermal pretreatment of the Cu/TiO_2 aerogel. Both reactions are summarized

by the following equations and suggest the formation of bidentate phosphate species (see two O—Ti^{4+} bond) upon methoxy dissociation:

$$Ti^{4+}–OH + Cl(H_3CO)_2P=O —Ti^{4+} + Ti^{4+} \rightarrow Ti^{4+}–OCH_3 + Cl(H_3CO)(HO—Ti^{4+})P=O—Ti^{4+} \quad (6.1)$$

$$Ti^{4+}–O\text{-}O–Cu^{1+} + Cl(H_3CO)_2P=O —Ti^{4+}\rightarrow Cu^{1+}–OCH_3 + Cl(H_3CO)(O—Ti^{4+})P=O—Ti^{4+} + O_{ads} \quad (6.2)$$

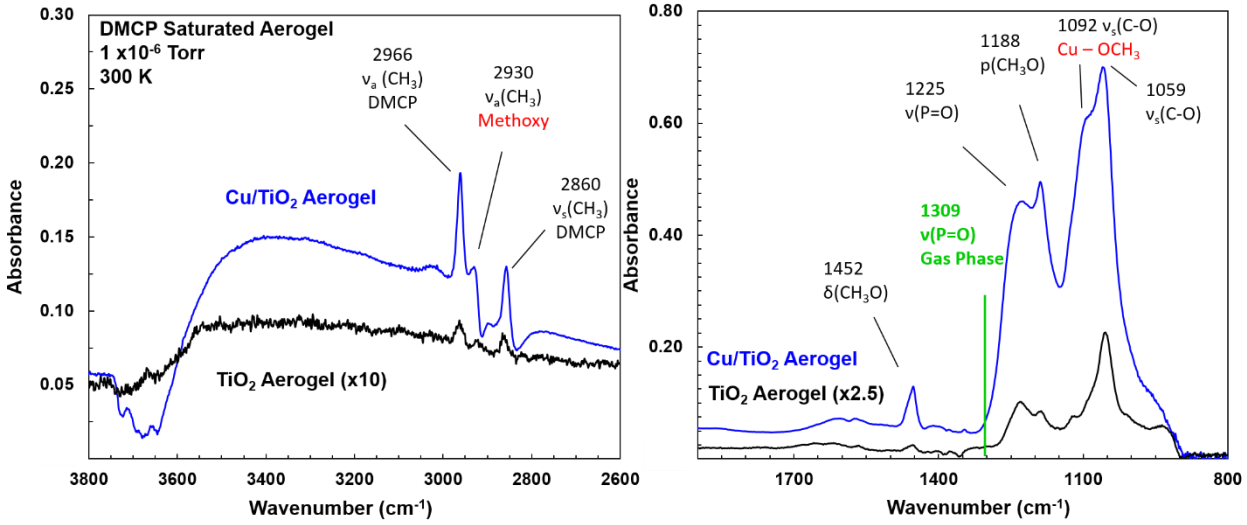

Figure 6.4. DMCP adsorption on a Cu/TiO_2 aerogel (blue trace) and TiO_2 aerogel (black trace). Spectra were acquired after gas phase DMCP was removed from the chamber.

Infrared spectra of the low wavenumber region, recorded after DMCP equilibrium, suggest dissociative adsorption occurs over the Cu/TiO_2 surface–albeit to a much larger extent compared to TiO_2. Infrared absorption features at 1450 cm^{-1}, 1222 cm^{-1}, 1183 cm^{-1}, and 1053 cm^{-1} are consistent with the $\delta(CH_3O)$, $\nu(P=O)$, $p(CH_3O)$, and $\nu_s(C\text{-}O)$ vibrations of DMCP on both materials. The $\nu(P=O)$ vibration appears significantly redshifted relative to the gas phase vibration and indicates a strong adsorption between Lewis acid metal atoms on the surface and the

phosphoryl oxygen atom of DMCP ($Cl(CH_3O)_2P=O$ --- Ti^{4+}). Previous studies suggest the initial adsorption of OP-based molecules through undercoordinated metal centers is the critical first step towards dissociation on metal oxide surfaces.[64,181,229] Infrared spectra during DMMP adsorption on TiO_2 revealed similar adsorption characteristics as evidenced by a redshift in the vibrational frequency of $\nu(P=O)$ (~34 cm^{-1}).[69] The major difference in DMCP adsorption behavior between Cu/TiO_2 and TiO_2 is the appearance of a large shoulder at 1092 cm^{-1} found only on the Cu/TiO_2 aerogel. We speculate this $\nu_s(C-O)$ feature is attributed to a fraction of dissociated DMCP, in form of Cu^{1+}-OCH_3 present on Cu regions of the material, consistent with previous literature of methoxy adsorption on copper oxide surfaces.[229] The dissociation of DMCP into a methoxy group and a bidentate-bound organophosphate species occurs on both TiO_2 and Cu/TiO_2; however, the relative abundance of vibrational features associated with Ti-OCH_3 and Cu-OCH_3 is significantly greater on the Cu/TiO_2 aerogel compared to the TiO_2 aerogel.

Beyond the formation of methoxy-like species during the dissociation of DMCP on the surface of TiO_2 and Cu/TiO_2, we observed spectroscopic evidence for adsorbed CO, identified through the infrared feature between 2108-2119 cm^{-1}, and only present on the Cu/TiO_2 aerogel (Figure 6.5). On both oxidized and reduced Cu/TiO_2 surfaces, trace amounts of DMCP converted into CO as observed by CO vibrational features on both the Cu^{1+} regions of the material and Ti^{4+} regions of the material. The absence of adsorbed CO on the TiO_2 aerogel highlights the importance of the Cu/Ti interface in the degradation of DMCP to CO. The high temperature oxygen pretreatment (673 K in O_2) on TiO_2-supported Au nanoparticles has been previously shown to produce higher concentrations of active oxygen species compared to the reducing pretreatment (673 K in vacuum) and therefore we expect, as shown in Figure 6.5, DMCP absorption onto an oxidized Cu/TiO_2 surface to produce greater concentrations of adsorbed CO.[37-38] Additionally, the

shift in frequency for the ν(C-O) of Cu^{1+}-CO between the oxidized and reduced surface (2108 cm^{-1} vs. 2119 cm^{-1}) suggests the thermal oxygen pretreatment significantly impacts the electronic structure of copper. Interfacial oxygen has previously been shown to scavenge electron density from Au nanoparticles on a Au/TiO_2 surface and alter the catalytic properties of the Au/Ti interface for CO oxidation.[128] Because of these findings, we focus on DMCP oxidation associated with the oxidized pretreatment for the Cu/TiO_2 aerogel (673 K in O_2).

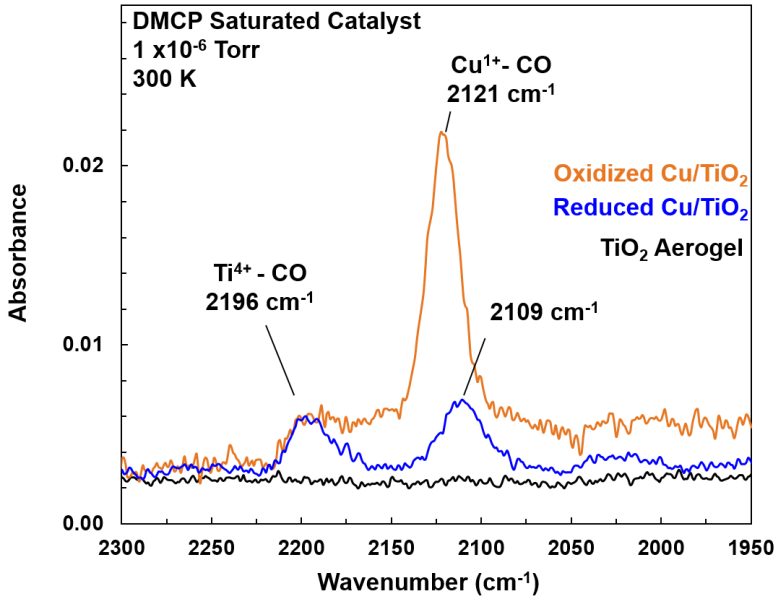

Figure 6.5. Infrared spectra acquired of the ν(C-O) region after DMCP adsorption on a reduced Cu/TiO_2 aerogel (blue trace), an oxidized Cu/TiO_2 aerogel (orange trace), and TiO_2 aerogel (black trace). Spectra have been normalized with respect to sample mass and are referenced to the clean sample.

The mechanism of organophosphorus-based decomposition to CO has been identified previously on TiO_2-supported Au nanoparticles.[181] Similar to the organophosphate decomposition experiments provided above, DMMP oxidation near the Au/Ti interface was found to occur in the

presence of interfacial oxygen species ($O_2^{-}{}_{(ads)}$). The adsorbed O_2 scavenged excess electron density to promote the oxidation of DMMP first to a methoxy adsorbate and then subsequent oxidation to CO and CO_2.[181] The similarities between the Cu/TiO_2 aerogel presented here and the TiO_2-supported Au nanoparticles would suggest similar oxidation pathways to form adsorbed CO.

6.3.4 Oxidation of DMCP in an Aerobic Environment

In order to evaluate the activity of supported-copper materials in air-based environments, DMCP oxidation was further investigated under an aerobic environment. The DMCP-saturated Cu/TiO_2 aerogel (spectra of which was previously shown in Figure 6.4 & 6.5) was exposed to 20 Torr of O_2 and monitored with *in situ* infrared spectroscopy. Figure 6.6A depicts the infrared spectra acquired between 4-25 minutes after the initial introduction of O_2. Immediate production of surface-bound CO (in the form Cu^{1+}-CO) is evidenced by the appearance of a feature at 2118 cm^{-1}. In addition to the immediate production of CO on the Cu/TiO_2 surface, one negative feature at 1240 cm^{-1} and one positive feature at 1115 cm^{-1} emerged in the difference spectra (Fig. 6.5A). We attributed the negative feature at 1240 cm^{-1} to the loss of molecularly-bound DMCP (via the ν(P=O)) and the appearance of the 1115 cm^{-1} feature to the formation of bidentate and tridentate PO_x surface adsorbates, consistent with organophosphate oxidation on TiO_2 surfaces.[68]

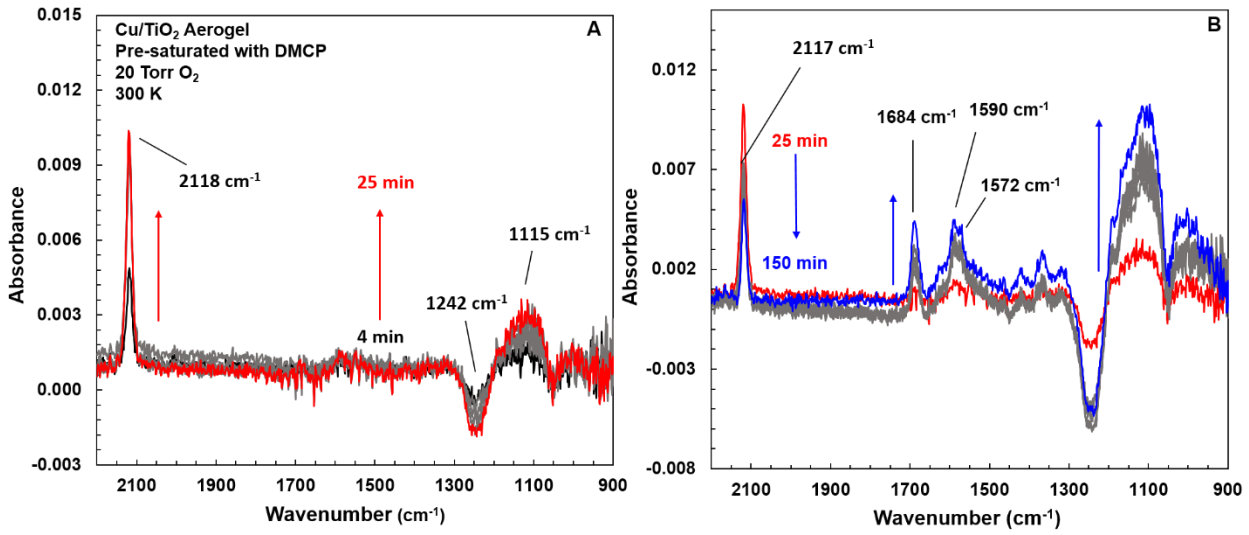

Figure 6.6. Infrared spectra acquired during the oxidation of DMCP between t = 4 -25 minutes (A) and between t = 25 – 150 minutes (B). All spectra are referenced to the spectrum of DMCP adsorbed onto Cu/TiO_2.

The oxidation of the DMCP was allowed to proceed for two hours as shown by the infrared spectra in Figure 6.6B. As the reaction reached a state of equilibrium, the concentration of Cu^{1+}-CO adsorbates decreased and indicated the oxidation of CO in the presence of gas phase O_2. Additionally, prominent positive features started to appear at 1684 cm^{-1} and 1580 cm^{-1}, consistent with the carbonyl stretches of formate adsorbates identified previously with the DRIFTS experiments. The loss of the ν(P=O) and emergence of the ν(P-O_x) continued during the entire oxidation reaction, which suggest multiple DMCP degradation pathways: including the fast reaction pathway to form surface-bound CO and the slow reaction pathway to form surface-bound formate. At the experimental temperatures within this study, we do not expect CO to react further to produce the formate species identified. Infrared spectra acquired during the aerobic oxidation on a DMCP saturated TiO_2 aerogel (see Fig. 6.7) identified no feature at 2100 cm^{-1} and suggested no reactivity to form the surface-bound CO molecules. However, the TiO_2 aerogel in the aerobic

environment produced a large negative feature at 1240 cm^{-1} and a large positive feature at 1115 cm^{-1} in the infrared spectra, consistent with partial DMCP decomposition on the TiO_2 aerogel (the slow reaction pathway as mentioned above). Therefore, we speculate the continued degradation of DMCP occurs on TiO_2 regions of the Cu/TiO_2 aerogel and suggest CO is not produced throughout the entire oxidation reaction. It should be noted that IR intensity do not directly indicate concentrations of surface-bound species due to differences in the extinction coefficients of different vibrational motions.

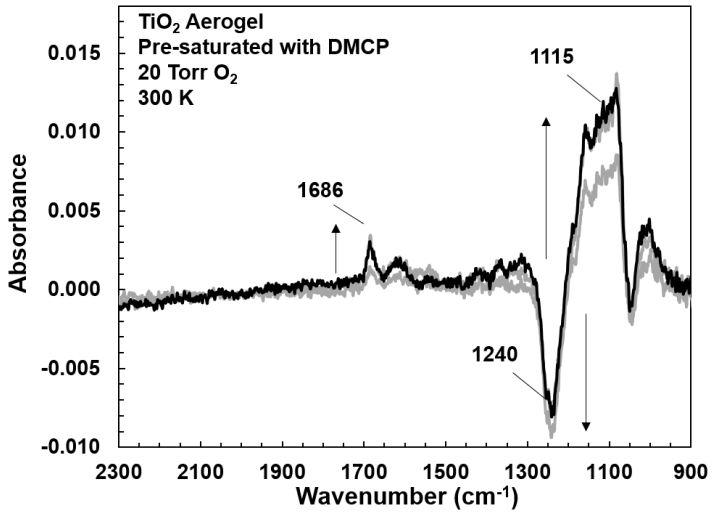

Figure 6.7. Infrared spectra acquired during the oxidation of DMCP between 30 minutes and 1 hour All spectra are referenced to the spectrum of DMCP adsorbed onto TiO_2.

Integration of infrared absorbance bands associated with the formation of CO and the decomposition of the DMCP on the Cu/TiO_2 aerogel further confirmed the hypothesis that CO was only initially produced. As shown in Figure 6.8, both the integrated absorbance of the Cu^{1+}-CO at 2118 cm^{-1} and the negative integrated infrared feature associated with the ν(P=O) of molecularly adsorbed DMCP were tracked with respect to time. The initial production of CO followed pseudo-first order rate kinetics and therefore, a single-exponential rise with an observed rate constant of

k_{obs} = 0.25 min^{-1} was identified. Conversely, the degradation of DMCP does not fit a single exponential decay. We speculate that a DMCP adsorbate on TiO_2 regions of the aerogel reacts slower in relation to DMCP adsorbed near the Cu/Ti interface or on Cu surface sites. Therefore, we fit the rate of DMCP degradation to two exponential components and two associated rate constants, k_{fast} and k_{slow}, associated with the fast production of CO on the surface and the slow production of formates identified between 1700-1500 cm^{-1}, respectively. The k_{fast} term (0.31 min^{-1}) for the degradation of DMCP suggests the initial degradation results in CO production. Whereas, we speculate the k_{slow} term (6.1×10^{-4} min^{-1}) is associated with the production of oxidation products such as the formate-like species on TiO_2 regions of the Cu/TiO_2 aerogel.

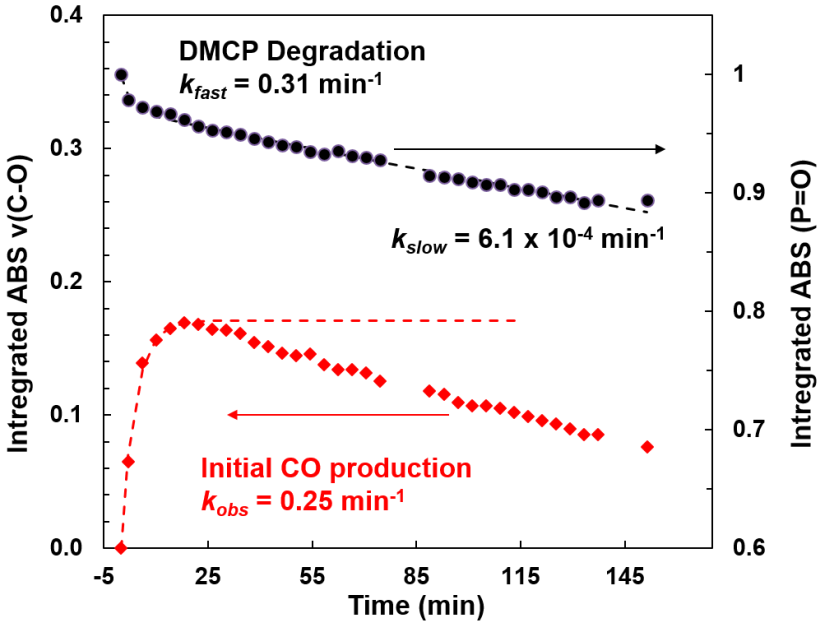

Figure 6.8. Integrated absorbance of the 2110 cm^{-1} infrared feature associated with CO production and the negative-going 1242 cm^{-1} feature associated the degradation of DMCP plotted versus O_2 exposure time at 300 K. The dashed lines represent a single exponential function for CO production and a two exponential function associated with DMCP degradation.

Previous studies on Au/TiO_2 have identified the production of CO upon introduction of molecular oxygen to an OP-saturated surface.[181] The Au/Ti interface was shown to be highly active in the adsorption of O_2 and even induced a change of the charge within the Au nanoparticles from $Au^{\delta+}$ to Au^{1+} due to the activation of the $O_{2(ads)}$ species.[181] Therefore, we speculate that DMCP adsorbed near the Cu/Ti interface likely reacts with O_2 bound at interfacial Cu/Ti sites to produce a methoxy intermediate. The methoxy intermediate then rapidly converts, with another $O_{2(ads)}$ species, to produce the surface–CO adsorbate, identified spectroscopically. These observations suggest that a clean Cu/Ti interface is required to adsorb O_2 and subsequently produce CO from adsorbed DMCP. Therefore, the continued degradation of DMCP into bidentate- or tridentate-bound phosphate species near the interface could deactivate the CO pathway.

The Cu/TiO_2 aerogel was thermally reactivated to study successive additions of DMCP and subsequent oxidation. The reactivation temperature of 673 K in O_2 was used to effectively oxidize and remove weakly bound adsorbates but likely, did not desorb the strongly bound phosphate species leftover from previous adsorption and oxidation procedures.[64,68] Infrared spectra acquired during oxidation experiment for the 2nd DMCP oxidation cycle over the Cu/TiO_2 aerogel are provided in Figure 6.9. Similar to the initial oxidation exposure shown in the Figure 6.6, the 2nd and 3rd oxidation cycle produced surface-bound CO. The infrared feature associated with the Cu^{1+}-CO is further shifted to higher frequencies (centered at 2143 cm^{-1}, Fig. 6.9) relative to the initial oxidation reactions. The blueshift in the vibrational feature associated with Cu^{1+}-CO after DMCP exposure was attributed to the highly oxidized phosphorous-containing (PO_x) species bound to the surface. Bound-PO_x induces an electron withdrawing effect on the Cu_2O particles (whether bound on TiO_2 or Cu) and therefore a decrease in the electron donation into pi antibonding orbital of adsorbed CO is observed.[28,38] This electronic effect has been previously

shown on Au/TiO_2 surfaces when an electron accepting molecule, such as SF_6, binds to the TiO_2 support and effectively withdraws electronic density from nearby metal nanoparticles.[28]

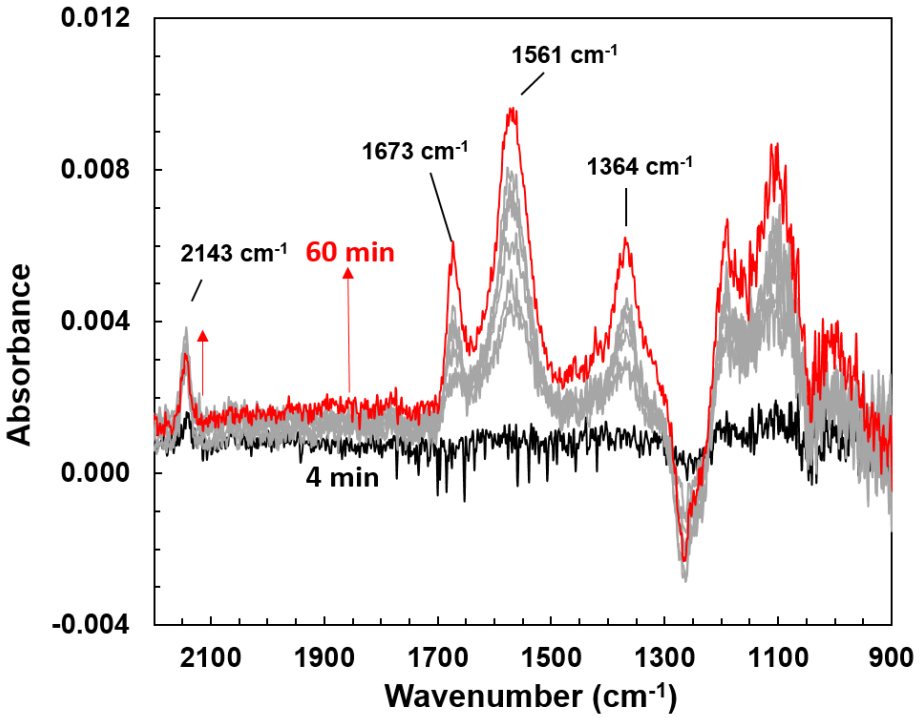

Figure 6.9. Infrared spectra acquired after the 2nd cycle of DMCP oxidation over a Cu/TiO_2 aerogel.

The integrated absorbance of CO produced upon the subsequent oxidations of DMCP on the Cu/TiO_2 surface suggested dramatically reduced activity for DMCP oxidation (Figure 6.10). In both the 2nd and 3rd cycle, CO is produced. However, the concentration of CO bound to the surface and the rate at which CO was formed on the surface both decreased. During each successive oxidation cycle, the infrared spectra indicate the continued production of surface formates and PO_x (see broad feature at 1130 cm^{-1}, Fig. 6.9). With further cycling of Cu/TiO_2, CO production ceased entirely. We speculate the increase in production of formates and PO_x result in the deactivation of the Cu/Ti interface.

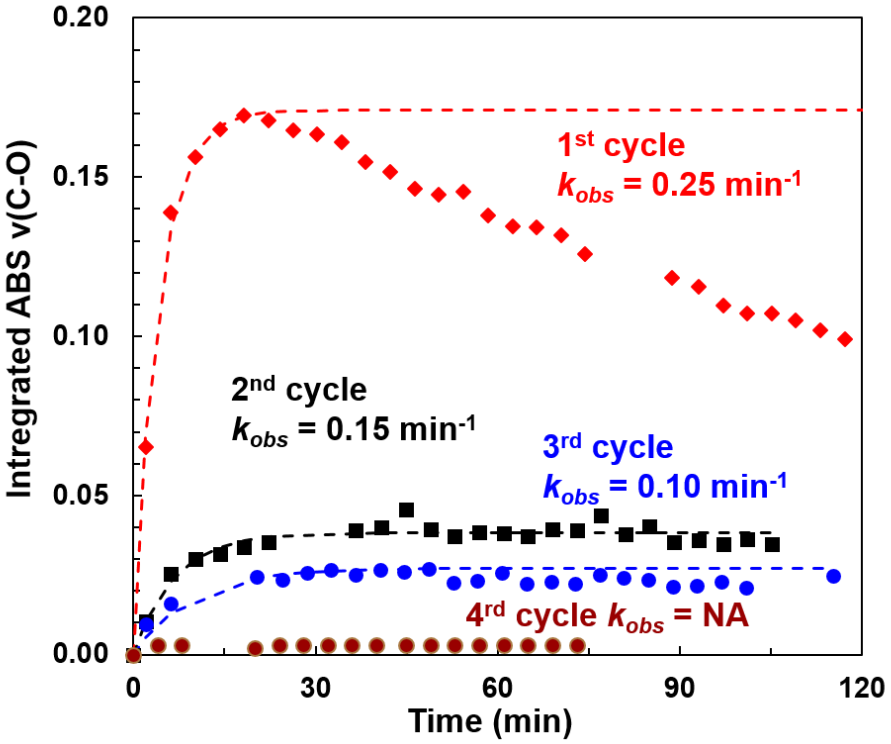

Figure 6.10. Integrated absorbance of infrared feature associated with Cu-CO production during DMCP oxidation over a Cu/TiO_2 aerogel for multiple cycles. The dashed lines represent a single exponential functional for CO production.

6.3.5 Post Oxidation Aerogel Characterization

The accessibility and speciation of Cu/TiO_2 surface sites available after exposure to DMCP were investigated with infrared spectroscopy of the probe molecule CO and *ex situ* XPS as shown in Figure 6.11. *In situ* infrared spectroscopy of CO adsorption was performed to study the nature of the Cu surface sites after DMCP adsorption and oxidation (Fig. 6.11E). The number of available Cu^{1+} surface sites after DMCP oxidation dramatically decreased relative to the clean Cu/TiO_2 aerogel, as evidenced by the decrease in the concentration of CO adsorption on the post-oxidation aerogel relative to the clean aerogel. In addition, the Cu^{1+}-CO infrared feature shifted to

2144 cm^{-1}—a significant increase in frequency relative to the clean material. Upon reactivation of Cu/TiO_2 aerogel at 673 K in O_2, a small percentage of the available copper surface sites are replenished after the oxidative thermal treatment. The blueshift in the vibrational feature associated with Cu^{1+}-CO after DMCP exposure was attributed to the highly oxidized phosphorous-containing species bound to the surface.

Ex situ X-ray photoelectron spectroscopy of the aerogel revealed the appearance of P and Cl on the surface of Cu/TiO_2. Two Cl 2p features at 200.16 eV and 198.56 eV were identified in the post-exposure sample. The higher binding energy feature at 200.16 eV is consistent with a carbon-containing chlorine species—likely a result of hydrolysis and further reaction with formate-like species covering the surface. The low binding energy feature, present on the clean aerogel in trace amounts due to HCl used in the synthesis of the Cu/TiO_2, could be either 1) Cl bound to copper surface sites or 2) the intact P-Cl bond. We expect hydrolysis of the P-Cl bond with surface hydroxyls to occur throughout the adsorption, oxidation and handling of the sample and therefore suggest the P-Cl bond is unlikely to be present during *ex situ* XPS analysis.

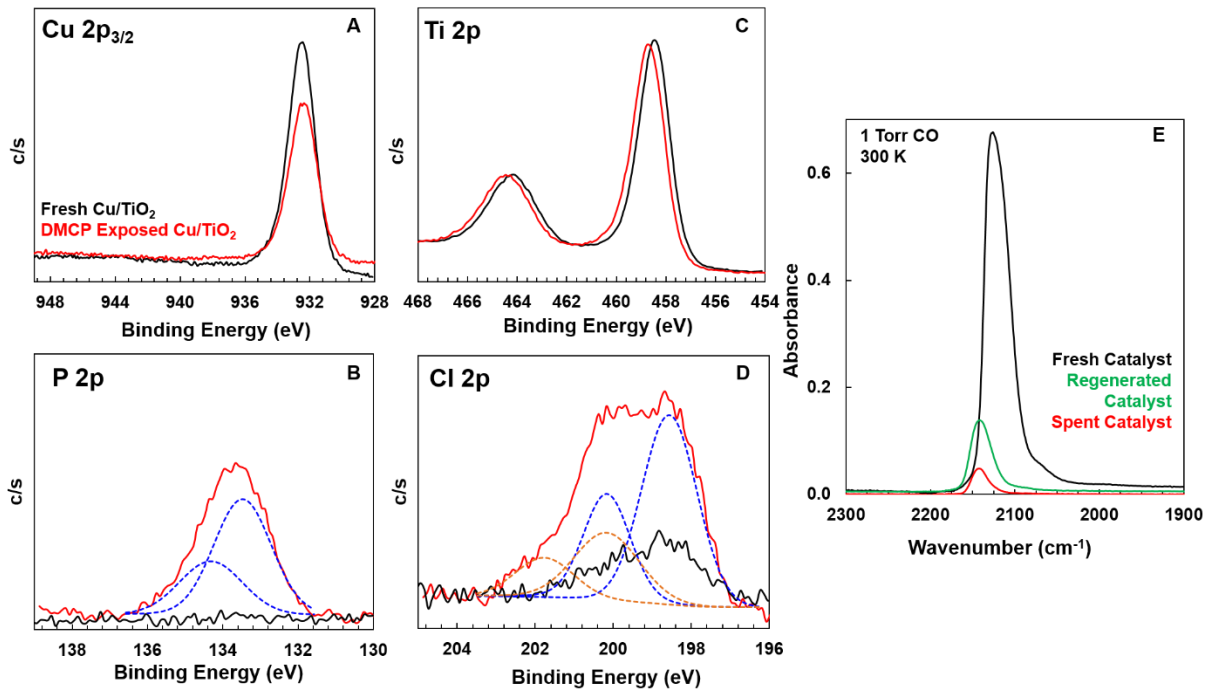

Figure 6.11. Characterization of the Cu/TiO_2 aerogel post-DMCP oxidative cycling. (A-D) *Ex situ* XPS analysis of the Cu/TiO_2 surface prior to and after DMCP oxidation. Individually fitted features are displayed as dashed lines. (E) Infrared spectroscopy of CO adsorption on the Cu/TiO_2 aerogel.

The main P 2p feature located at 133.48 eV is likely associated with the oxidized PO_x-bound adsorbates identified in infrared spectroscopic measurements. These results suggest that highly oxidized phosphorus adsorbates remain on the surface (likely on both Ti and Cu regions) upon thermal oxidation at 673 K. Recent investigations involving the adsorption of DMMP onto Cu_2O utilized XPS analysis to identify DMMP decomposition into atomic P species at 300 K.[77] In this study, binding energies associated with PO_x emerged only when the surface was heated in vacuum.[77] In the XPS analysis present here, we do not identify atomic P species (expected binding energy = 129 eV) on the Cu/TiO_2 aerogel after DMCP exposure. The presence of O_2 during DMCP

oxidation and the presence of O_2 during repeated attempts to reactivate the Cu/TiO_2 aerogels suggest any atomic P produced during the reaction was quickly oxidized. Additionally, no satellite lines associated with Cu^{2+}, typically present in the 940-945 eV region, were identified on the Cu/TiO_2 aerogel.[239] Overall, the XPS analysis identifies reaction products in the form of multiple Cl species and PO_x on the Cu/TiO_2 aerogel after the adsorption and oxidation of DMCP. However, the Cu regions of the material retain significant Cu^{1+} (instead of oxidation to Cu^{2+}) surface structure and we attribute this to the multiple Cu/Ti contact planes the aerogel stabilization exhibits on the nanoparticulate copper.

Through the *in situ* spectroscopic characterization of the decomposition of DMCP over Cu/TiO_2, we identified a carbon monoxide-bound surface adsorbate. Ultra-high vacuum studies of DMCP adsorption suggested CO was formed through a methoxy intermediate located on Cu_2O regions of the aerogel. In addition to CO, formate vibrational features are present between 1500 – 1700 cm^{-1} upon DMCP decomposition and are thought to form as a result of a secondary methoxy oxidation pathway. Previously, infrared spectroscopic measurements have been employed to observe the methoxy to formate oxidation pathway on Au/TiO_2, both thermally and photocatalytically.[221] However, the same Au/TiO_2 material exhibited very little evidence of CO production from the methoxy adsorbate in the presence of the visible light. Supported-copper surfaces have been previously shown to display unique catalytic ability in steam reforming of methanol[240-242] and thus we speculate the Cu/TiO_2 aerogels may exhibit heighted activity in the methoxy to CO oxidative pathway compared to similar Au/TiO_2 surfaces.

6.3.6 Mechanistic Studies of Methoxy Oxidation

In light of our recent work on methanol oxidation over Au/TiO_2 catalysts,[221] infrared spectroscopic measurements of methanol adsorption and oxidation over the Cu/TiO_2 aerogel were

performed to confirm the methoxy to CO pathway during DMCP decomposition. We expect these experiments to provide mechanistic insight into the fate of the methoxy (that originates from DMCP decomposition) when exposed to molecular oxygen.

The Cu/TiO_2 aerogel was exposed to 500 mTorr of methanol. After a few minutes of methanol equilibrium, the chamber was subsequently evacuated leaving only the strongly bound, molecularly adsorbed methanol and dissociated products, including methoxy species and thermally converted formate species on the surface (Figure 6.12). Upon adsorption, previous studies have shown that a fraction of methanol dissociates on metal oxides surfaces to form a methoxy species and a hydroxyl group.[221,243-244]

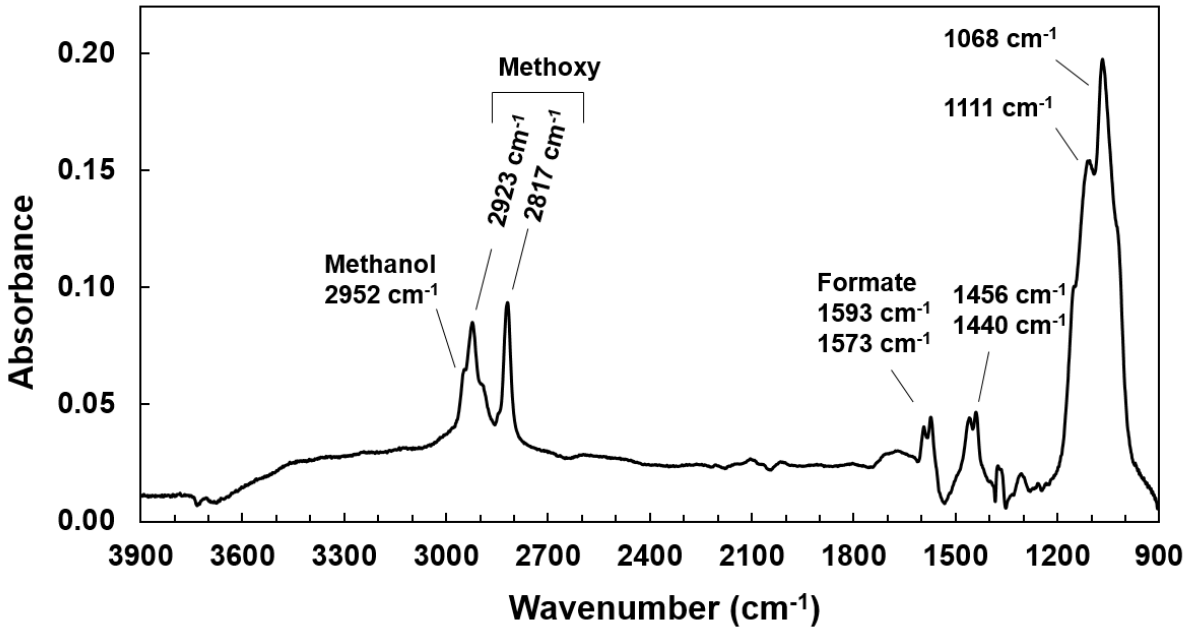

Figure 6.12. Infrared spectrum upon the adsorption and evacuation of methanol onto Cu/TiO_2.

Methanol coadsorption studies with carbon monoxide confirmed the presence of methanol and methoxy species on the copper. Carbon monoxide was pre-adsorbed onto the Cu/TiO_2 aerogel and subsequent additions of the methanol (Fig. 6.13, spectrum ii – iv) effectively displaced the

copper-bound CO adsorbates. Therefore, methanol is shown to bind strongly to Cu^{1+} and Cu^{0} regions of the sample. This adsorption behavior is unlike previous experiments of methanol adsorption onto Au/TiO_2 in which methanol does not bind to the metallic gold particles.[221]

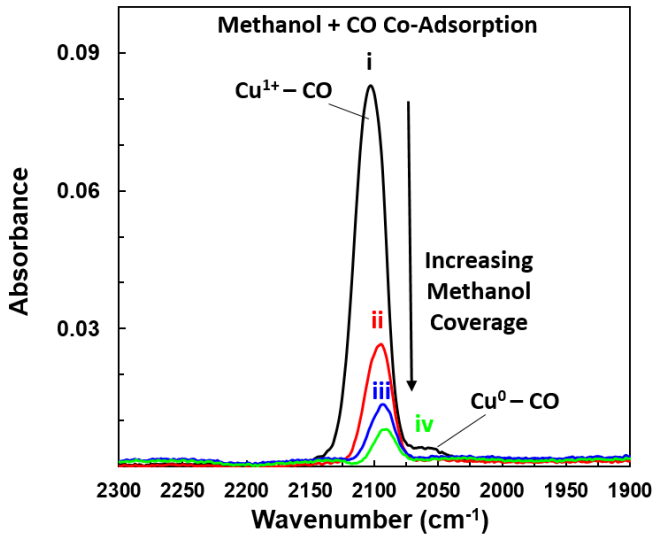

Figure 6.13. CO and methanol coadsorption on a Cu/TiO_2 aerogel (i) 0 Torr methanol, (ii) 500 mTorr methanol, (iii) 1 Torr methanol, (iv) 2 Torr methanol. The sample was pre-saturated with 1 Torr of CO and then gas phase CO was removed from the chamber prior to methanol adsorption. Spectra acquired at 300 K.

Upon exposure of O_2 to the methoxy-saturated Cu/TiO_2 surface, significant methanol and methoxy oxidation occurs. The negative features at 2946 cm^{-1} and 2841 cm^{-1} in the infrared spectra indicate the loss of ν(C-H) features associated with methanol and the negative features at 2911 cm^{-1} and 2810 cm^{-1} indicate the loss of ν(C-H) features associated with methoxy adsorbates. Positive-going infrared features at 2863 cm^{-1}, 1592 cm^{-1}, 1570 cm^{-1}, 1377 cm^{-1} and 1360 cm^{-1} suggested the formation of surface formate groups bound to both Cu and Ti regions of the surface. The emergence of the vibrational feature at 2098 cm^{-1} was attributed to the formation of Cu^{1+}-CO. The broad positive-going feature at 3560 cm^{-1} indicated an increase in the concentration of surface

hydroxyls as a result of the oxidation reaction—likely found on Cu_2O regions as TiO_2 hydroxyls adsorb photons between 3645 – 3700 cm^{-1}. It should also be noted that no reactivity (formate or CO production) was identified on the surface of TiO_2 aerogels and that other supported-metal surfaces, such as Au/TiO_2, have only shown methoxy conversion to formate at 300 K in the absence of light.[221] The oxidation of methanol and methoxy-bound species suggests the formation of CO (via the increase in vibrational feature at 2100 cm^{-1})—a process also identified during the oxidation of DMCP.

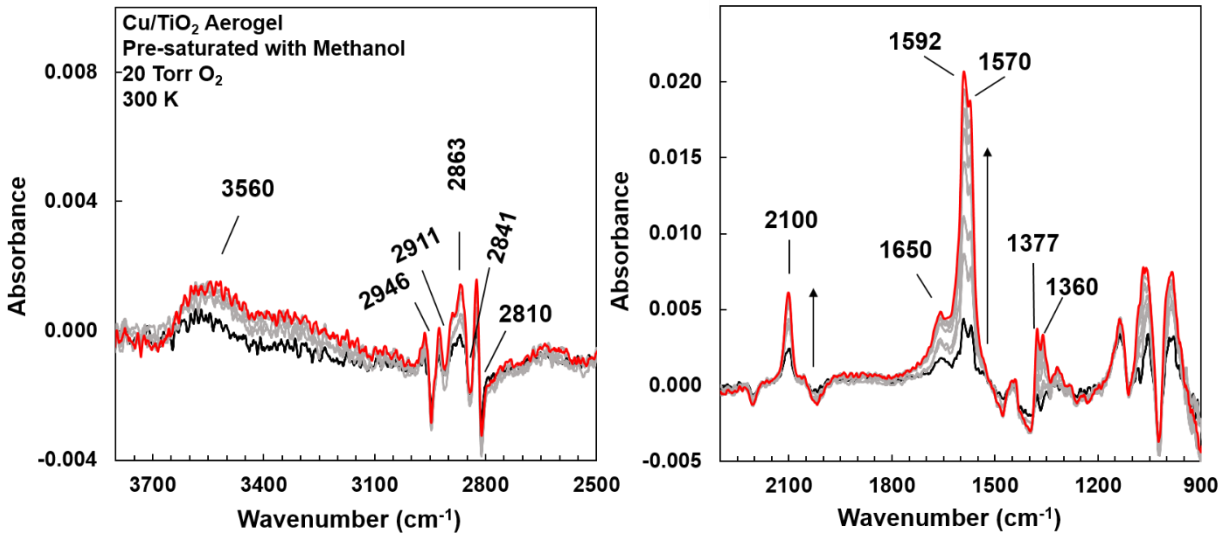

Figure 6.14. Infrared spectra acquired during the oxidation of methanol on the surface of Cu/TiO_2 for 1 hour. All spectra are referenced to the spectrum of the methanol adsorbed onto Cu/TiO_2.

The conversion of methanol into both formate and carbon monoxide confirms the role of the methoxy intermediate in the DMCP oxidation pathway to form CO. We speculate that molecular oxygen from the gas phase binds as $O_{2(ads)}$ at the Cu/Ti interface. This process has been previously shown on titania-supported Au interfaces.[18,23] The bound-O_2 readily dissociates on these dual-metal sites due to electron donation to the $2\pi^*$ antibonding orbital, which weakens the

O-O bond and promotes interfacial reactivity.[23-25,245] O_2 can also adsorb at oxygen vacancies on the TiO_2 lattice, near the copper nanoparticles and exhibit similar reactive tendencies.[246-248] We speculate that the production of the formate occurs with both the Cu/Ti interfacial oxygen (eqn. 6.3) and $O_{2(ads)}$ at oxygen vacancies (eqn. 6.4) as evidenced by the two formate ($\nu_{as}OCO$) motions centered at 1592 and 1570 cm^{-1} attributed to formate on TiO_2 and formate on Cu_2O.

$$Cu^{1+}–OCH_3 + O_{2(ads)} + 2Cu^{1+} \rightarrow Cu^{1+}–OOCH + 2(Cu^{1+}–OH) \quad (6.3)$$

$$Ti^{4+}\text{-}OCH_3 + O_{2(ads)} + 2Cu^{1+} \rightarrow Ti^{4+}–OOCH + 2(Cu^{1+}–OH) \quad (6.4)$$

The production of copper-bound carbon monoxide utilizes the same reactive $O_{2(ads)}$—likely adsorbed to the Cu/Ti interface and can be summarized in the following equation:

$$Cu^{1+}–OCH_3 + 2O_{2(ads)} + 2Cu^{1+} \rightarrow Cu^{1+}–CO + 3(Cu^{1+}–OH) \quad (6.5)$$

The concentration of CO on the Cu/TiO_2 aerogel was stable (did not increase or decrease) after 30 minutes of aerobic exposure and therefore we do not expect CO to participate in the methanol to formate pathway.

Further evaluation of the methanol oxidation reaction was performed through isotopically labeled studies of methanol and O_2. Figure 6.15 provides the infrared spectra associated with methanol oxidation using different isotopically-label reactants. When $CH_3{}^{18}OH$ was added to the reaction, we identified no shift in the produced CO feature. Therefore, we can conclude that the methoxy oxygen does not react to form the surface-bound CO species. In fact, a small redshift (~10cm^{-1}) in the formate vibrational feature at 1592 cm^{-1}, shown in Figure 6.15B, suggested an ^{18}O-labeled formate vibrational product on the surface in the presence of $CH_3{}^{18}OH$. However, when $^{18}O_2$ was added to the reaction, we identified a 60 cm^{-1} redshift in 60% of the adsorbed CO produced on the surface. This redshift occurs because the CO species bound to Cu is $C^{18}O$. Therefore, we can confirm the oxygen originating from the adsorbed O_2 is the species that produces

Cu-bound CO. We also speculate that $^{18}O_2$ is able to exchange with lattice oxygen on the surface of Cu/TiO_2 and is the reason why we observe two CO features associated with $C^{16}O$ and $C^{18}O$ when $^{18}O_2$ is added to the reaction feed.[238] Through the aid of the isotopically labelled studies, we can identify the adsorbed atoms that react and form isotopically labeled products. Specifically, the methoxy oxygen atom reacts to form formate-bound species while the O_2 adsorbates react to form the surface-bound CO. Throughout this process, a significant portion of the catalyst will be saturated with hydroxyl groups and potential side-reactions could occur.

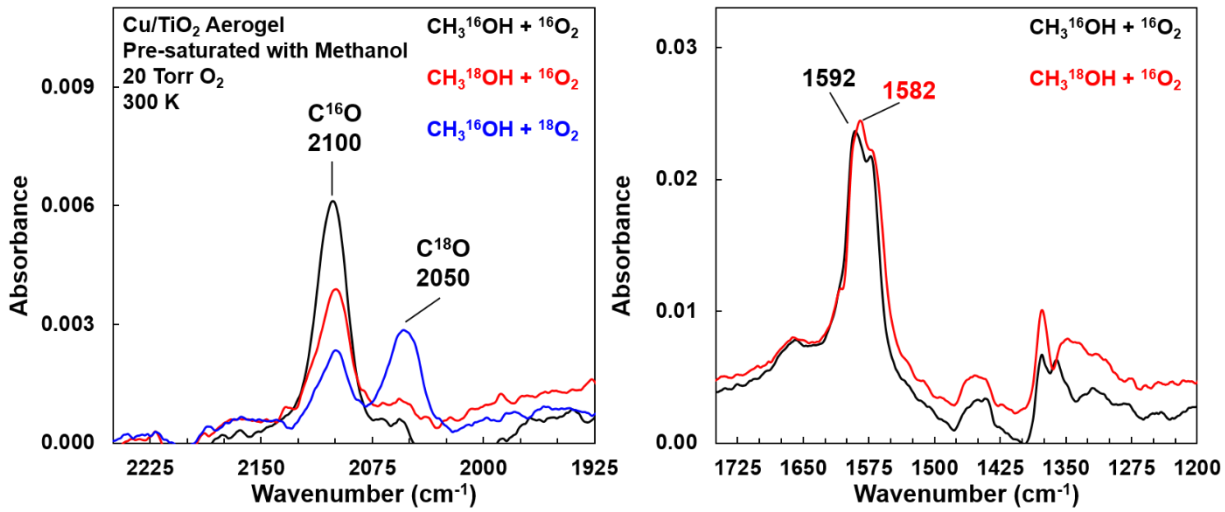

Figure 6.15. Infrared spectrum acquired after 30 minutes during the oxidation of $^{16}O_2$ and $CH_3{}^{16}OH$ (black trace), $^{16}O_2$ and $CH_3{}^{18}OH$ (red trace), and $^{18}O_2$ and $CH_3{}^{16}OH$ (blue trace). Each spectrum references the methanol-saturated surface.

Competition between the production of formate and the production of CO is likely to occur and may deactivate the CO pathway. Future studies will further investigate how competition between these two pathways impact the overall mechanism of DMCP oxidation. The methanol oxidation studies combined with the DMCP oxidation studies provide the specific decomposition

steps that occur when DMCP first dissociates upon adsorption and then reacts with surface-bound oxygen to produce CO.

6.4 Summary

Dimethyl chlorophosphate (DMCP) dissociatively adsorbs onto a Cu/TiO_2 aerogel and in the presence of oxygen reacts to produce surface bound CO at atmospherically relevant temperatures. *In situ* spectroscopic measurements of DMCP oxidation and methanol oxidation confirmed a methoxy intermediate, produced during DMCP dissociation, is required to form copper-bound CO. The methoxy adsorbate reacts with a reactive oxygen species, $O_{2(ads)}$, located at both interfacial Cu/Ti sites and TiO_2 oxygen vacancy sites to produce CO and bidentate formate. Upon regeneration of the aerogel, both phosphorus and chlorine species remain on the surface, indicating the inability to drive off strongly-bound oxidized products. Therefore, the deactivation of the aerogel occurs through the production of oxidized phosphate species and surface-bound formate—both limit the production of Cu^{1+}-CO by adsorbing near Cu/Ti interfacial sites and over time completely deactivating CO production.

Chapter 7

Characterization of Zr-based Metal-Organic Frameworks with the Probe Molecule, CO

Adapted with permission from Driscoll et al., Characterization of Undercoordinated Zr Defect Sites in UiO-66 with Vibrational Spectroscopy of Adsorbed CO. Journal of Physical Chemistry C, 2018, 122, 14582-14589. Copyright 2018 American Chemical Society. Adapted from Driscoll et al., Geometry and Energetic of CO Adsorption on Hydroxylated UiO-66. Physical Chemistry Chemical Physics, 2019, 21, 5078-5085 with permission the Royal Society of Chemistry.

7.1 Introduction to MOF Application

Zr-based metal-organic frameworks (MOFs) are robust, thermally stable materials that have found applications in a wide range of processes, from the destruction of chemical warfare agents to the separation of industrially relevant reactions gas molecules.[42,89] The Zr-MOFs are well known to retain their porous structure upon the introduction of significant defects, including both missing linker and missing node defects, and ligand modification.[41,90,249] In addition, Zr-MOFs exhibit unique chemical heterogeneity that can generate an abundance of Lewis acid sites (coordinatively unsaturated Zr, Zr_{cus}) and Brønsted acid sites (bridging hydroxyls between Zr atoms, or functionalized linkers) that have been cited as critical in catalytic processes and enhanced proton mobility.[250-254]

MOFs contain intrinsic acid sites useful for adsorption, separation and catalysis. Improvements to materials for gas storage and separation have been previously identified through tuning reactive metal centers or functionalized ligands that bind to gas molecules.[255-258] For instance, a recent study by Andonova et al. found that the incorporation of excess hydroxyl groups

onto MIL-53-Al improved CO_2 adsorption capacity relative to the non-functionalized material.[259] Recent research has focused on the importance of hydrogen bonding for gas adsorption and separation between the native hydroxyl groups in many of these porous materials and small molecules such as CO, CO_2, SO_2, NO_2, and organic compounds.[209-210,259-262] However, a molecular-level understanding of the energetics of small molecule adsorption is still lacking.

7.1.1 Defects within Zr-MOFs Drive Chemistry

Mechanistically, Zr-based MOFs have been shown to activate chemical change through undercoordinated metal sites located on the structural nodes that result from missing linker defects.[41-42,89-90] Traditionally, characterization techniques such as powder X-ray diffraction (PXRD) and surface area measurements are used to probe general defect density. However, these techniques interrogate only the type of defects that affect the long range order of the framework. They do not easily lend insight into the types of defects that have minimal effects on the overall structure of the MOF. Further, they do not directly determine the defects accompanied by coordinatively unsaturated zirconium (Zr_{cus}) sites.

Determination of the linker defect concentration and characterization of associated undercoordinated Zr centers is paramount in predicting the potential catalytic capacity of MOFs. Undercoordinated Zr has been shown, through experimental and computational studies, to be the main active site for the degradation of chemical warfare agents.[81,84,263-265] A computational study by Troya suggests the decomposition of sarin on UiO-66 involves the activation of the nerve agent on an undercoordinated Zr atom, a product of missing linker defects.[264] Mondloch et al. suggest that accessible Lewis-acidic Zr(IV) ions on the MOF, NU-1000, are responsible for fast degradation of the nerve agent, sarin. The phosphoester hydrolysis reaction was shown to occur up to 30 times faster, on the order of minutes, when exposed to the dehydrated NU-1000 material

(4 exposed Lewis acid Zr atoms) compared to more heavily coordinated Zr-based MOF materials.[84]

Many recent studies have focused on developing methods to engineer defects into MOF structures. These studies show that the relative Zr_{cus} density is highly dependent upon the synthetic conditions and thermal treatment used to activate the framework.[266-268] Synthesis precursors, acid modulators, and environmental contaminants can all affect the accessibility of coordinatively unsaturated Zr sites to reactants.

7.1.2 Characterization of the Zr-MOF, UiO-66

A prime example of synthetically controlled defect incorporation can be found in recent studies of the Zr-based MOF, UiO-66 ($Zr_6(OH)_4O_4(BDC)_6$, BDC = benzene-1,4 dicarboxylate). UiO-66, one of the most widely investigated Zr MOFs, displays exceptional stability in a wide range of thermal, chemical, and physical environments.[86,269] In the ideal UiO-66 structure, each $Zr_6(OH)_4O_4$ core is coordinated to 12 BDC linkers, and each Zr ion within the core is coordinated to eight oxygen atoms. The hydroxylated (as-synthesized) UiO-66 node contains four μ_3-OH groups that reside at the corners of the MOF's tetrahedral cavity. Previous literature has focused on modulating the synthesis of UiO-66 to generate both missing linker defects and missing node defects (Zr_6 cluster + 12 surrounding BDC) in attempts to alter the overall stability, reactivity, and porosity of the MOF.[266,270-271] In particular, missing linker defects are thought to be critical in UiO-66 reactivity because they afford Zr_{cus}–a highly active and strong Lewis acid site.[250-251]

Previous studies have probed defect density within MOFs via a variety of techniques; however, these methods often lack sufficient chemical specificity and sensitivity to pinpoint the density of available Zr_{cus} sites within UiO-66 (or open metal sites within other MOFs). For example, potentiometric acid-base titrations have been used to quantify the number of missing

linkers in a variety of Zr/Hf-based MOFs.[252,272] Although this technique determines the amount of water, defect hydroxyl, acid modulator, and solvent that interacts with Zr_{cus}, the approach does not directly probe the Zr_{cus} species. In-depth thermogravimetric analysis (TGA) has also been shown to provide a quantitative measure of missing linkers.[266-267,270,273] While effective in many applications, TGA analysis is subject to significant experimental uncertainty that can propagate to large variability in the accuracy of defect density determinations.[268] Further, TGA methods do not directly identify the chemical nature of defect sites within the MOFs. To date, only a few experimental techniques have provided a direct *in situ* probe of the undercoordinated Zr centers that are accessible for catalytic and adsorptive processes.[267]

7.1.3 CO as a Probe of Surface Sites

For decades, the surface science community has used carbon monoxide as a sensitive molecular probe of exposed metal and metal oxide surface sites, and more recently, also of MOFs.[42,96,274-275] For example, CO has also been recently employed to investigate the Brønsted acidity of hydroxyl moieties on the nodes of MIL-53(Al).[259] Wiersum et al. previously studied the interaction between CO and UiO-66 through FTIR measurements.[276] They found that CO binds with the μ_3-OH groups of UiO-66 through the carbon end of the molecule, but they only speculated on the presence of CO coordinated directly to Zr, as evidenced by a very weak feature in their spectra at 2172 cm^{-1}.[276] When binding to exposed metal sites inside frameworks, the CO stretching vibration is blue-shifted relative to the gas molecule due to a transfer of electron density from CO's carbon atom putative lone pair to the electron deficient Lewis acid metal.[260-261,277-278] These previous studies suggest that CO may be an effective probe of both hydroxyl groups and undercoordinated Zr sites within MOFs, the primary focus of the current work.

We have applied *in situ* vibrational spectroscopic studies of CO to identify the binding geometry and characterize the adsorption onto both μ_3-OH and Zr_{cus} sites located within the porous structure of UiO-66 and a few synthetic derivatives. Supported by electronic structure calculations, we provide evidence of CO binding to undercoordinated Zr in UiO-66 samples that were synthesized with either low or high defect densities. Thermal treatment of a pristine MOF sample is shown to actively generate greater undercoordinated metal sites, which can be identified and quantified with the probe molecule, CO. These studies provide insight into the relative defect density in various forms of UiO-66 and demonstrate that infrared spectroscopy of adsorbed CO effectively identifies and quantifies open metal sites and hydroxyl groups within MOFs.

7.2 Procedural Methods

7.2.1 Synthesis of Metal-Organic Frameworks

The synthesis of low defect density UiO-66 was based on an established literature procedure.[266] $ZrCl_4$ (378 mg, 1.62 mmol) and terephthalic acid (539 mg, 3.24 mmol) were suspended in dimethylformamide (DMF) (10 mL) inside a 6 dram vial. 37 % HCl (0.286 mL, 3.24 mmol) was added to the reaction mixture and stirred at 343 K for 30 min to ensure complete dissolution of the starting materials. The resultant solution was transferred into a Teflon-lined Parr reactor, which was heated at 493 K for 24 hours. After cooling to room temperature, a white powder was isolated by centrifugation, washed with fresh DMF (4 × 10 mL), and then soaked in DMF (10 mL) for 4 days. The solvent was replaced every 24 hours. The resultant framework was dried in air at 333 K for 24 hours, followed by 473 K for 1 hour. The MOF powder was further washed with acetone using a Soxhlet extractor for 24 hours followed by drying in air at 473 K for 1 hour. All synthesis procedures were performed by the Amanda Morris research group at Virginia

Tech. The calcined UiO-66 sample was obtained by heating the low defect density UiO-66 powder in air at 543 K for 24 hours.

The synthesis of the highly defective UiO-66 utilized trifluoroacetic acid (TFA) as an acid modulator during the same synthetic steps as described above. The TFA modulated (with 36 molar equivalents of TFA used during the synthesis) UiO-66 sample provides a highly defective framework that induces both missing node and missing linker defects.[266] The synthesis of UiO-66-NH_2, where a 2-amino-benzenedicarboxylic acid (H_2-N-H_2BDC) is used in the original synthesis, followed previous literature precedent.[279] Finally, NU-1000 was provided by the Omar Farha research group at Northwestern and was produced following an established literature procedure.[280]

7.2.2 Characterization

The Powder X-ray diffraction (PXRD) was measured using a Rigaku MiniFlex 600 with Cu(Kα) radiation (1.5418 Å). The patterns were collected over a 2θ range of 2−50° with a 0.05° step size at a 10°/min scan rate. The powdered samples were mounted onto reflective Si (510) disks. Thermogravimetric Analysis (TGA) was performed using TA Q500 analyzer. The UiO-66 sample was loaded in a platinum pan and heated at 2 deg/min under a flow of air. XPS characterization was performed on a PHI VersaProbe III scanning XPS microscope using monochromatic Al K-alpha X-ray source (1486.6 eV). C 1s and Zr 3d XPS spectra were acquired at 50 μm/12.5 W/15 kV using 26 eV pass energy, which gives a Ag $3d_{5/2}$ full width at half maximum of 0.59 eV. All binding energies are referenced to adventitious C-C at 284.8 eV.

7.2.3 Infrared Studies of Adsorption

Infrared spectroscopic experiments were performed in a stainless-steel high vacuum cell with a base pressure of 1×10^{-8} Torr. The UiO-66 sample installed into vacuum chamber as previously described in Chapter 2. Previous characterization suggests no structural change to the

underlying UiO-66 framework as a result of a pelletization pressure up to 10,000 psi.[269] The resistively heated tungsten mesh was attached to an external power supply and cooled using a liquid-nitrogen reservoir. A K-type thermocouple, spot welded directly to the mesh was used to monitor the sample temperature. For infrared analysis, we employed an FTIR spectrometer (Thermo, Nicolet Nexus 470 FTIR) that was mounted on the side of the vacuum chamber with an external MCT-A detector and spectral resolution of 2 cm^{-1}.

Vacuum annealing of samples at 473 K effectively removed weakly bound adsorbates for each experiment. The dehydroxylation of UiO-66 required a pretreatment temperature of 573 K, which easily removed the μ_3-hydroxyls located in the tetrahedral cavities of the MOF without the added addition of defects.[281] A filter (NANOCHEM Purifilter, Matheson Tri Gas) was attached to the manifold to remove any metal carbonyls from the gas stream. Systematic introduction of CO (Airgas, 99.3%) onto the liquid-nitrogen cooled sample at temperatures ranging from 100 K to 250 K was used to observe CO adsorption onto defect sites and hydroxyl groups on UiO-66.

7.2.4 Variable-Temperature Infrared Spectroscopy

Variable-temperature infrared spectroscopic (VTIR) measurements characterized the energetics of CO-surface interations.[106] VTIR requires a fixed partial pressure of CO interacting with the UiO-66 sample within a closed system. The equilibrium constant for CO adsorption depends on temperature according to the van't Hoff equation (eqn. 2.3). Experimentally, the energetics of CO–surface interactions were attained by introducing 4 Torr of CO into the vacuum chamber at 183 K. Following CO introduction, the sealed chamber equilibrated at a given temperature for a ten-minute period prior to data collection. The acquisition of infrared spectra ranged from 183 K – 233 K and composed of an average of 250 scans.

7.2.5 Density Functional Theory of CO Adsorption

All DFT calculations were performed by Diego Troya in the Chemistry Department at Virginia Tech. Determination of the binding geometry and energy of CO on the μ_3-OH groups of UiO-66 used a fully relaxed cluster model consisting of a $Zr_6(OH)_4O_4$ capped by 12 benzoate ligands with heavy atoms frozen at the experimental crystallographic coordinates. Geometry optimizations and harmonic vibrational frequency calculations were carried out with the M06-L functional[282] using a 6-31G* basis set for C, O, and H atoms of the cluster and ligands other than the μ_3-OH and CO adsorbate, an aug-cc-pVTZ basis set for the μ_3-OH and CO atoms, and the Lanl2dz basis set and pseudopotentials for Zr atoms. Using these geometries, single point calculations with the M06-2X functional[283] and the same basis set were conducted to further refine the electronic energies, which were corrected by the basis set superposition error using the counterpoise scheme. All calculation incorporated a superfine integration grid. The reported energetic data correspond to adsorption enthalpies at 200 K.

7.3 Results and Discussion

Over the past sixty years,[93,96,98,284] the surface science community has employed CO as a highly effective molecular probe because the vibrational frequency of the adsorbed molecule, $\nu(CO)_{ads}$, depends strongly on the electronic character of the site to which it is bound. Specifically, π back-donation of electrons from the adsorption site into an antibonding orbital of CO results in a shift of the CO vibrational mode to lower frequency; whereas, σ-donation from CO to the surface site increases the CO vibrational frequency. These effects, along with the molecule's stability and strong transition dipole moment in the mid-infrared range, make CO an excellent probe molecule for characterizing the electronic nature of a variety of surfaces.[18,26,28,159,261,285] We have applied

this strategy, in conjunction with DFT calculations, to characterize the nature of metallic binding sites within the Zr-MOFs and specifically UiO-66.

7.3.1 Characterization of UiO-66 through Traditional Techniques

Infrared spectroscopic characterization of the low defect density UiO-66 framework, shown in Figure 7.1, revealed that the MOF retained sharp, narrow spectroscopic features associated with the linker vibrational motions in vacuum and following a thermal treatment at 473 K. The full width at half max (FWHM) of the linker vibrational band assigned to the aromatic breathing motion (1020 cm^{-1} vibration with a FWHM ~10 cm^{-1}) indicated that UiO-66 retained a framework structure under the high vacuum experimental conditions.[82,209] In addition to the carbon-containing linker vibrations, the sharp vibrational feature at 3674 cm^{-1} has been identified as the μ_3-hydroxyl groups of the zirconium nodes located in the tetrahedral cavity (Figure 7.1, black trace).[82,209] The crystalline nature of the MOF is also reflected in the PXRD pattern of the low defect density material (see Fig. 7.1 B, black trace), and through TGA analysis, which confirmed a defect-free MOF within experimental uncertainty (Fig. 7.2B). As previously shown, we found UiO-66 to be thermally stable between 100 K and 475 K.[82,209] Upon an increase in the vacuum pretreatment temperature to 573 K (Figure 7.1, red trace), the material rapidly desorbed water and produced the dehydroxylated form of UiO-66. The infrared spectrum of the dehydroxylated UiO-66 material showed a significant depletion of the 3674 cm^{-1} feature while retaining the sharp vibrational features of the organic linkers. These results are consistent with

acquired TGA and PXRD patterns, shown in Figure 7.2 that suggest the underling framework remains intact at temperatures up to 573 K in vacuum.[269,281]

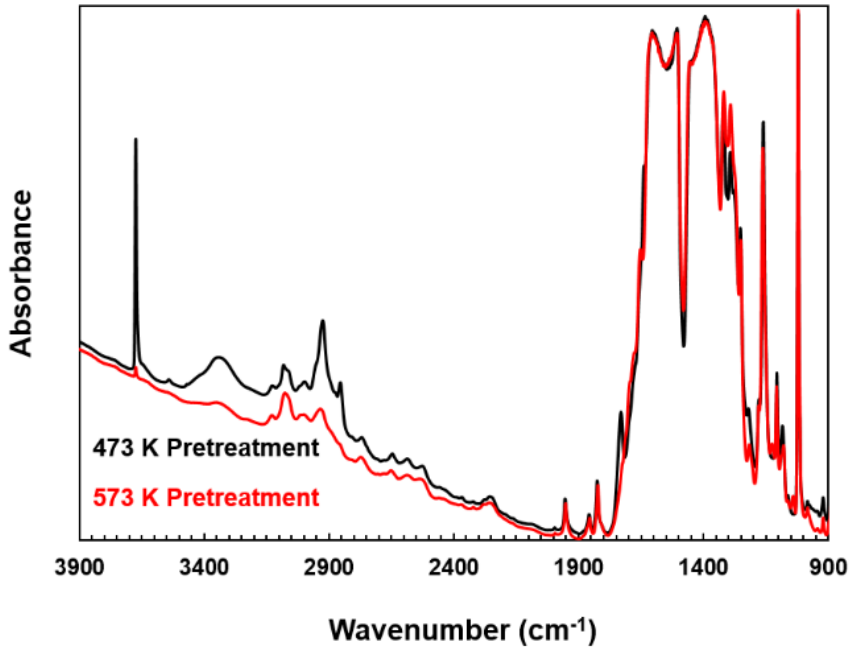

Figure 7.1. Infrared spectra of the MOF, low-defect UiO-66, acquired after pretreatment temperatures of 473 K (black) and 573 K (red).

The crystalline nature of the MOF is also reflected in the PXRD pattern of the "as synthesized" low defect density material (see Fig. 7.2 A, black trace), the PXRD pattern of the low defect density materials after pelletization and vacuum treatment, and through TGA analysis (Fig. 7.2B, black trace), which confirmed a defect-free MOF within experimental uncertainty. The defectivity of UiO-66 was assessed from the TGA data.[266] Briefly, the weight loss was normalized with respect to ZrO_2, where the end plateau was set to 100%. The 370 °C plateau corresponds to the dehydroxylated UiO-66 with the formula of $[Zr_6O_6(BDC)_6]$ for an ideal framework. The weight of this structure should be 220% relative to ZrO_2. If missing-linkers defects are present, the

framework would appear lighter and this plateau would deviate from the ideal value. Therefore, by measuring this difference the amount of missing linkers per formula unit can be calculated. The TGA analysis suggested the low defect UiO-66 sample had zero missing linkers per node (within experimental uncertainty) whereas the calcined UiO-66 sample contained a defect density of 0.56 missing linkers per molecular formula unit (or 1.12 missing linkers out of 12 linkers surrounding each Zr_6 node).

Apart from dehydroxylation, the low defect density UiO-66 sample appears to be stable well above 600 K. Others have suggested that under an argon atmosphere, BDC linkers are lost between 723 K and 923 K.[286] The infrared spectrum and PXRD pattern of the same low defect density UiO-66 sample following calcination ("calcined UiO-66", hereafter) in the presence of oxygen, are nearly identical to the original sample, with a few key exceptions (Fig. 7.2, red trace). Consistent with other work,[266] we find that calcination removes the excess organic precursors and solvent that post-synthesis rinsing and activation techniques leave behind. Therefore, the infrared spectrum of the calcined UiO-66 sample shows decreased vibrational features at 3300 cm^{-1} and below 3000 cm^{-1} associated with hydrogen bonded hydroxyl groups and synthetic precursors, respectively.

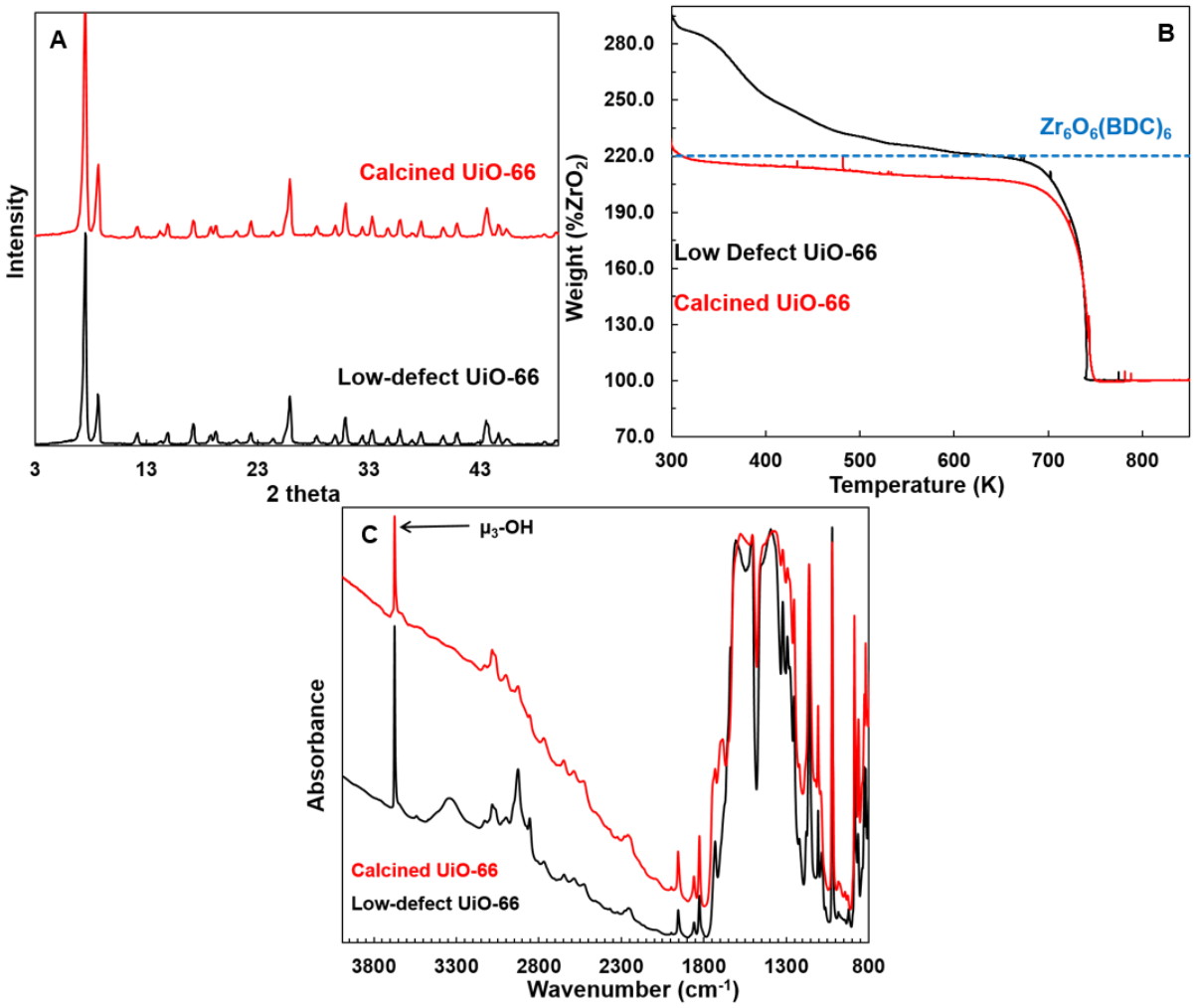

Figure 7.2. Characterization of the low-defect UiO-66 (black traces) and the calcined UiO-66 (red traces) with (A) PXRD, (B) TGA, and (C) transmission-infrared spectroscopy. The blue dashed line on the TGA data represents the weight percent of an ideal UiO-66 framework with 12 BDC linkers coordinated to each Zr_6O_6 node.

7.3.2 CO Adsorption and Energetics onto the Hydroxyl Groups of UiO-66

CO adsorption on UiO-66 has been characterized via infrared spectroscopy of adsorbed CO. The unique vibrational character of adsorbed CO not only probes the molecular nature of

acidic sites,[18,93,96,276,281] but also provides the thermodynamics of CO uptake and transport within materials.[94,106,287-288] Rational development of next-generation materials for the sorption and separation of small gas molecules, such as CO, requires a fundamental understanding of the interactions between the abundant hydroxyl groups of materials and the gas molecules of interest.[260-261,276,289] Hydroxyl–CO interactions result from electrostatic forces that cause significant perturbation to the vibrational stretching frequency of the C-O bond. In addition, the frequency of ν(C-O) provides insight into the binding geometry and specifically the orientation of CO adsorption (through the C- end or the O- end of the adsorbate).[101] The binding complexity of CO adsorption and the applications in small molecule adsorption stimulate the detailed studies presented below.

7.3.2.1 CO Adsorption Geometry

Adsorbed CO is an excellent probe molecule due to the sensitivity of $\nu(C\text{-}O)_{ads}$ when the adsorbate interacts with acidic binding sites on MOFs.[259,275-276,281] Carbon monoxide adsorption was performed under varying CO pressures at 183 K, a temperature low enough to achieve extended surface residence time. Infrared spectra of CO adsorption, shown in Figure 7.3, were recorded *in situ* and referenced to the clean UiO-66. Upon CO exposure at 50 mTorr (Figure 7.3A), two prominent features appeared at 2152 cm^{-1} and 2124 cm^{-1}. As the pressure of CO increased inside the chamber, the integrated area under both the 2152 cm^{-1} and 2124 cm^{-1} features increased. The large positive absorbance feature at 2152 cm^{-1} has been previously proposed to be CO interacting with μ_3-hydroxyl groups through the carbon end of the adsorbate (ZrOH···CO).[276] The interaction between CO and the μ_3-OH is electrostatic and the magnitude of the change in vibrational frequency compared to the gas phase fundamental vibration at 2143 cm^{-1} [$\Delta\nu$(CO)] depends on the strength of the electrostatic field according to the Stark effect.[96] The observed CO

stretching frequency on UiO-66 agrees with previous reported studies of CO binding to hydroxylated surfaces such as silicates and zirconia.[94,100-101,213]

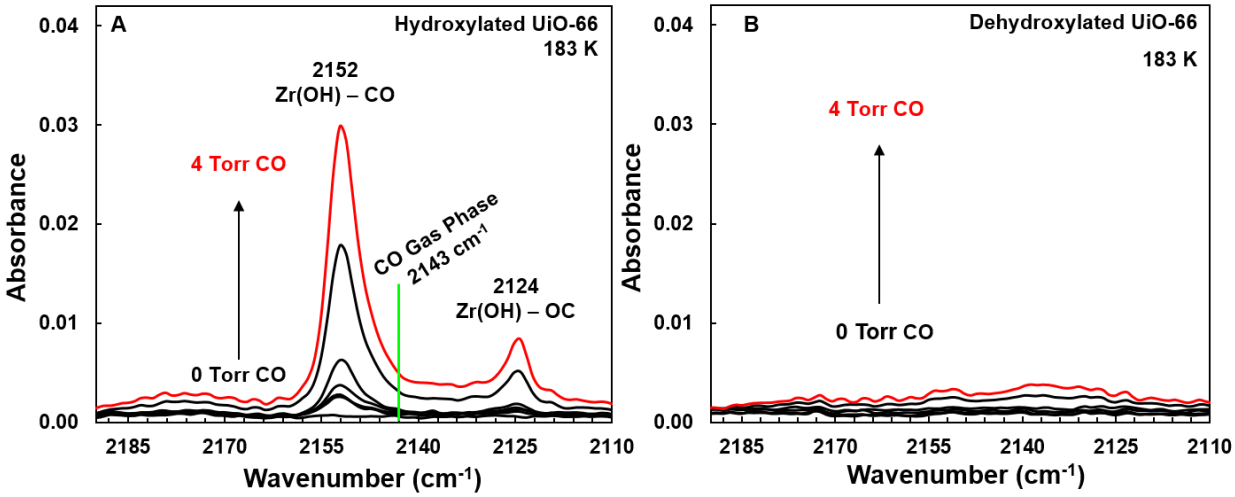

Figure 7.3. Infrared spectra of CO adsorption at increasing pressures ranging from 0 Torr up to 4 Torr. Panel A provides CO adsorption on the low defect-hydroxylated UiO-66 sample. Panel B provides infrared spectra of CO adsorption under the same experimental conditions on the dehydroxylated low defect density UiO-66 sample.

Unlike the 2152 cm^{-1} CO-hydroxyl feature, the CO-MOF vibrational feature at 2124 cm^{-1} (shown in Figure 7.3A) has not been previously reported for CO uptake within UiO-66. The observed infrared feature redshifted 19 cm^{-1} from the gas phase fundamental frequency of CO. We hypothesize that the redshift of the CO vibrational frequency is due to a μ_3-OH···OC binding geometry. This isocarbonyl binding configuration is most commonly observed spectroscopically when CO interacts with alkali-metal cations in zeolites,[96,290] and has also been identified in CO adsorption onto hydroxyl groups of silica[100] and the MOF, MIL-53.[291]

Analogous experiments with the dehydroxylated UiO-66 framework verified the assignment of the 2124 cm^{-1} feature in the infrared absorption spectrum to the μ_3-OH⋯OC binding geometry. Upon CO exposure to the dehydroxylated UiO-66 sample at identical concentrations of CO within the chamber, both vibrational features at 2152 cm^{-1} and 2124 cm^{-1} remained absent in the infrared difference spectra (Figure 7.3B). The absence of CO vibrational features upon dehydroxylation of UiO-66 suggests the μ_3-hydroxyl is required for the small molecule to bind within tetrahedral cavities (the location of the μ_3-OH groups) of the porous structure. In addition, these studies provide evidence that weakly-bound physisorbed CO molecules are not present, in measureable quantities, under our experimental conditions. The dehydroxylated UiO-66 studies also lend support to the attribution of the 2124 cm^{-1} vibration to CO interacting with the μ_3-OH groups through the oxygen atom.

7.3.2.2 CO Adsorption Energetics

The binding energetics of CO on the μ_3-hydroxyl groups of UiO-66 were measured utilizing variable temperature infrared spectroscopy (VTIR). The introduction of 4 Torr of CO adsorbed onto UiO-66 over a wide range of temperatures provided a closed gas–surface system to initiate the van't Hoff analysis. The infrared spectra acquired at each temperature are shown in Figure 7.4A. As the temperature of the sample increased, the equilibrium between $CO_{(ads)}$ and $CO_{(g)}$ shifted to the gas phase and the CO-μ_3 hydroxyl concentration diminished.

The energetics of the CO-hydroxyl interaction were quantified through a van't Hoff analysis of the VTIR experimental data. This analysis has been shown to be highly successful in characterizing gas–surface binding energetics in a number of studies, and reviewed here.[106] In this study, we increased the temperature of the sample while acquiring infrared spectra at each temperature and subsequently observed a decrease in the concentration of μ_3-OH⋯CO

interactions, shown in Figure 7.4. No measurable pressure increases within the chamber accompanied the decrease in concentration of the μ_3-OH$\cdots$CO configuration and as a result, the relationship between integrated absorbance and the standard enthalpy of adsorption ($\Delta H°_{ads}$) eqn. 2.2 can be written as eqn. 2.3.

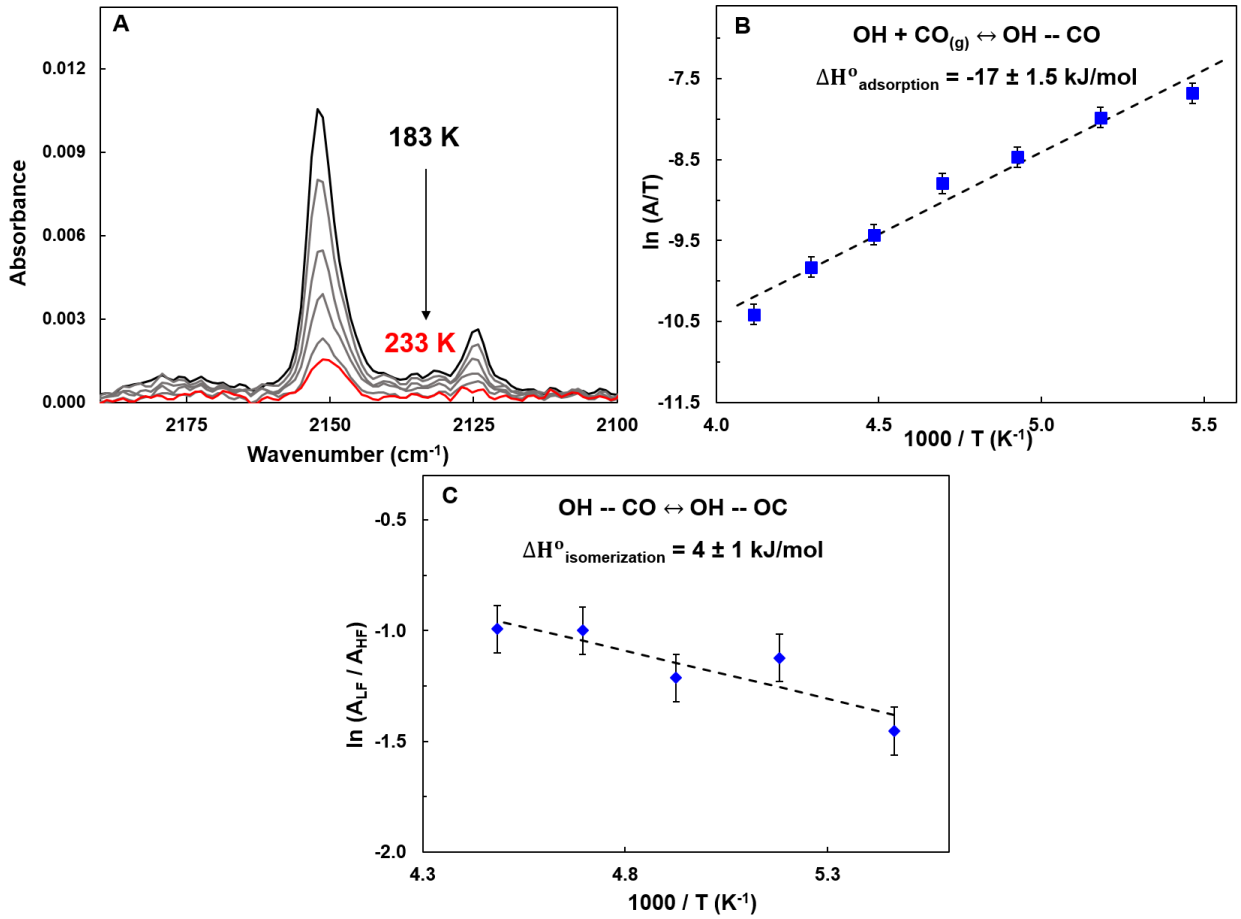

Figure 7.4. CO adsorption on UiO-66 under varying temperatures in a closed equilibrium environment. Panel A provides the infrared spectra acquired at each temperature (183 K, 193 K, 203 K, 213 K, 223 K and 233 K). Panel B provides a van't Hoff plot of the integrated absorbance of the 2152 cm^{-1} ZrOH ⋯ CO feature with the linear slope to provide $\Delta H°_{ads}$. Panel C is the ratio of the natural log of the integrated absorbance of the 2124 cm^{-1} and 2152 cm^{-1} CO features with a linear model to provide the $\Delta H°_{isomerization}$. Error bars represent the standard deviation of triplicate data points.

Figure 7.4B provides a van't Hoff plot and, under the assumption of low surface coverage, the standard enthalpy of adsorption for the ZrOH⋯CO interaction was found to be -17 ± 1.5 kJ/mol. The experimentally attained $\Delta H°_{ads}$ for the ZrOH⋯CO agrees with the

energetics of other weak Brønsted acid–CO interactions including silica (-11 kJ/mol $\Delta H°_{ads}$)[94] and H-ZSM-5 (-25.5 kJ/mol $\Delta H°_{ads}$).[292] The relatively weak standard enthalpy of adsorption, as determined by VTIR, for the ZrOH···CO interaction is consistent with previous adsorption calorimetry experiments for CO on UiO-66 that were observed to be between 16.0 – 16.6 kJ/mol.[276] The main adsorption pathway for CO on a non-defective UiO-66 framework occurs through the μ_3-OH group.[293] However, CO interacts weakly compared to the CO interactions with coordinatively unsaturated metal sites (calculated binding energy of 81 kJ/mol on Zr_{cus}).[281]

In addition to the energetics of CO adsorption, VTIR can be employed to investigate the enthalpic difference between CO bound through the carbon and oxygen atoms.[106] In the closed chamber environment, an increase in temperature of the material resulted in the concentrations of both the μ_3OH···CO geometry (referred to as high frequency: HF) and the low frequency (LF) μ_3OH···OC geometry to decrease. However, the ratio of A_{LF} / A_{HF} increased over that same range and therefore provided the enthalpic energy difference ($\Delta H°_{iso}$) from the more energetically stable carbonyl configuration to isocarbonyl configuration (μ_3OH···CO ↔ μ_3OH···OC). Integration of both the HF and the LF CO features is used to determine the standard enthalpy of isomerization, $\Delta H°_{iso}$, as shown below[106]:

$$\ln\left(\frac{A_{LF}}{A_{HF}}\right) = \left(-\frac{\Delta H^{\circ}_{iso}}{RT}\right) + \left(\frac{\Delta S^{\circ}_{iso}}{R}\right) + \ln\left(\frac{\varepsilon_{LF}}{\varepsilon_{HF}}\right) \qquad (7.1)$$

where ε represents the molar extinction coefficient for each CO vibration. The relationship between $1/T$ and $\ln(A_{LF} / A_{HF})$ (shown in Fig. 7.4C) identifies the isomerization enthalpy as 4 ± 1 kJ/mol while the ΔS°_{iso} cannot be attained without molar extinction coefficients for each unique CO–surface vibration.

The strength and binding geometries of the CO···μ_3-hydroxyl interactions were further explored computationally. Figure 7.5 shows calculated structures of CO hydrogen bonding to the

μ_3-OH group of UiO-66 through its carbon and oxygen ends. The calculations also predicted the experimentally confirmed blueshift in vibrational frequency for the ν(CO) vibration when bound through the carbon atom (2179 cm^{-1}) and redshift when bound through the oxygen atom (2121 cm^{-1}, both consider a 0.9744 scaling factor obtained from the ratio of the experimental to calculated gas-phase CO stretch at the same level of theory). The enthalpies of adsorption computed at 200 K for each calculated geometry, corrected by the basis set superposition error, were also calculated to be -31.8 kJ/mol and -21.8 kJ/mol for the μ_3-OH···OC and μ_3-OH···CO configurations, respectively. While the relative strength of the two binding geometries measured by the experiment is nicely captured by the calculations, the calculated enthalpies overestimate the measured values by 8-15 kJ/mol, indicating incompleteness of the basis set, inadequacy of the DFT functional chosen to recover all electron correlation, or a combination of both.

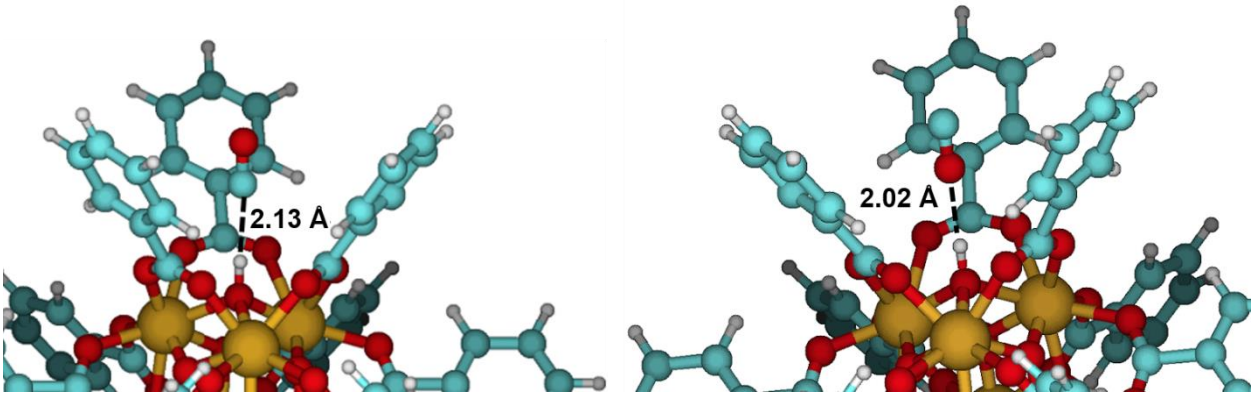

Figure 7.5. Calculated geometries of CO hydrogen bonding to a μ_3-OH site through its carbon end (a) and through its oxygen end (b). The Zr, O, H, and C atoms are shown in gold, red, white, and teal, respectively.

The spectroscopic analysis of CO interacting with UiO-66, in conjunction with DFT calculations, provides clear evidence of unique geometries and energetics of two well-resolved adsorption events that are mediated by selective binding to the weakly acidic μ_3-OH groups located

within tetrahedral cavities of the MOF UiO-66. As new materials are produced for gas storage and transport applications, variable-temperature spectroscopic methods can help identify binding configurations and provide energetic information for each specific site. These studies will help identify and optimize materials capable of increased sorption capacity for a specific small molecule.

7.3.3 CO as a Probe of Brønsted Acidity

Probe molecules, such as CO, are able to bind to a single hydroxyl site as shown in the infrared spectra above. Upon adsorption, the shift in vibrational frequency of both the hydroxyl, $\Delta\nu$(OH), and the probe molecule give insight into the strength of the interaction (probe–hydroxyl) as well as the intrinsic strength of the acid site.[101,276,291,294-295] In fact, a correlation between the vibrational shift of the hydroxyl and the adsorption enthalpy of the probe molecule can be found across a series of probe-surface interfaces.[101] This has led some researchers to speculate that the shift of the hydroxyl group when bound to a single probe molecule can identify the acidity of that surface site relative to another similar acidic system.[296]

Infrared spectroscopy of the high wavenumber region (> 3000 cm^{-1}) confirms the presence of the CO – hydroxyl interaction and also provides some general insight into the acidity of the MOF hydroxyl. Perturbation of the free μ_3-hydroxyl groups appears in the presence of CO on UiO-66 as a small, broad feature at 3605 cm^{-1} (Fig. 7.6A). The feature at 3605 cm^{-1} can be attributed to a hydrogen bonded μ_3-hydroxyl [ν(OH)]. The same experimental methodology was performed on the UiO-66-NH_2 sample (Figure 7.6B). Upon CO adsorption, a pronounced hydrogen-bonded feature appeared at 3587 cm^{-1} and is centered 87 cm^{-1} redshifted relative to the free μ_3-hydroxyl. We speculate the incorporation of the NH_2 into UiO-66 linker induces a drastic effect on the confined pore environment of UiO-66 but does not necessarily indicate that the hydroxyl groups

of UiO-66-NH_2 are more acidic than UiO-66. This is because the change in a confined-cavity environment can have a significant effect on the adsorption properties of CO with hydroxyl groups.[297] In order to fully understand the effect of the amine functionalization on the acidic adsorption properties of the UiO-series of MOFs, further studies are needed.

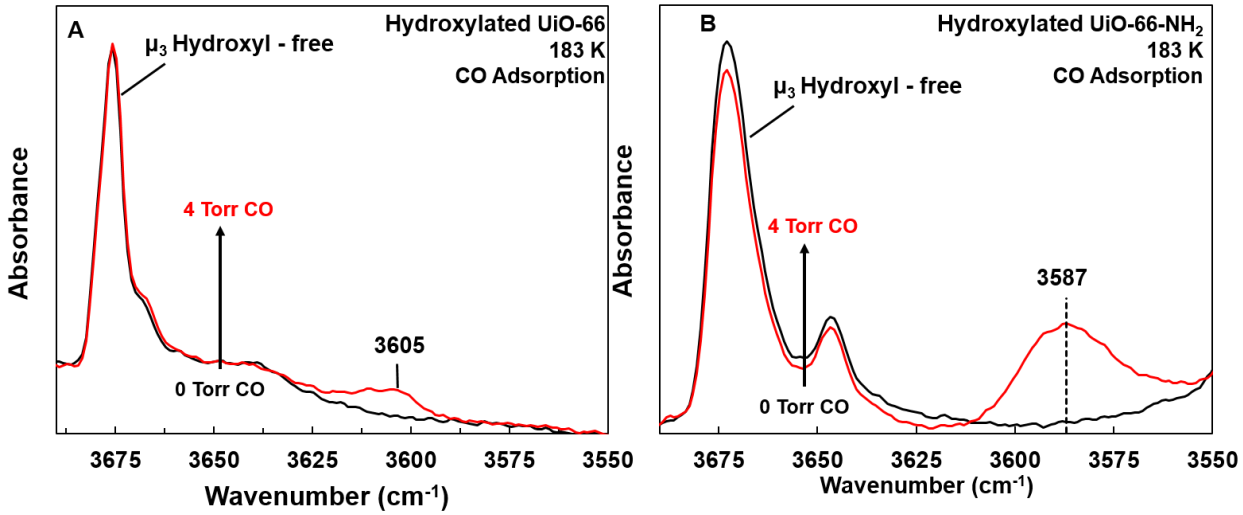

Figure 7.6. Infrared spectra acquired prior to (black trace) and during CO adsorption (red trace) on the low defect, hydroxylated UiO-66 (A) and the hydroxylated UiO-66-NH_2 (B).

Some studies do suggest the Brønsted acidity of a hydroxyl on a specific material can be directly related to the redshift in the ν(OH) as a result of CO-hydroxyl interactions.[101,295] Paukshtis and Yurchenko[295] proposed a correlation for a specific weak hydrogen-bonding probe molecule ($\Delta\nu_{OH}$ < 400 cm^{-1}) that relates the proton affinity (PA) of the surface hydroxyl to the PA of an isolated hydroxyl group of silica (PA^{SiOH}). As shown in equation 7.2, the log of the ratio between vibrational shifts for the probe-hydroxyl interaction ($\Delta\nu_{OH}/\Delta\nu_{SiOH}$) can be directly related to the proton affinity of the surface hydroxyl (PA^{OH}) of interest.

$$PA^{OH} = PA^{SiOH} - 442.5log\left(\frac{\Delta\nu OH}{\Delta\nu SiOH}\right) \qquad (7.2)$$

The PA^{SiOH} is provided from literature and assumed to be 1390 kJ/mol.[295] The experimental vibrational shift ($\Delta\nu_{OH}$) of ~69 cm^{-1} for the Zr-MOF during CO adsorption, shown in Figure 7.6A, suggests the PA of the μ_3-OH for UiO-66 is 1441 kJ/mol (Table 1). The same evaluation of the hydroxyl group on UiO-66-NH_2 is not performed because of the ambiguity the effect pore confinement has on Brønsted acidity calculations.

Table 1. Experimentally attained vibrational shifts and proton affinity of the μ_3-OH for UiO-66 using two separate probe molecules. Experimentally attained vibrational shifts for each respective probe molecule on silica are provided by ref. [295]

Probe Molecule	$\Delta\nu_{Zr\text{-}OH}$ (cm^{-1})	PA^{ZrOH} (kJ mol^{-1})	$\Delta\nu_{SiOH}$ (cm^{-1})[295]
CO	69	1441	90
N_2	20	1425	24

A second probe molecule, N_2, was used to further study the acidity of the μ_3-OH. Gas phase N_2 was dosed onto UiO-66 under the same experimental conditions and the $\Delta\nu_{OH}$ shifted 20 cm^{-1} (Fig. 7.7). Based on the relationship provided in equation 7.2, the PA of the μ_3-hydroxyl was found to be 1425 kJ/mol. The PA calculated for the μ_3-OH groups using N_2 and CO are similar and would suggest that this method has quantitative merit. However, many more probe molecules (such as Xe, NH_3) are needed to confirm the validity of the analysis. Both probe molecules do suggest the bridging hydroxyls of UiO-66 are weak Brønsted acids, consistent with previous literature of UiO-66 acidity[276] as well as type I zirconium hydroxides.[213] Further study into similar probe molecules are required to validate the PA analysis in these small, confined pore environments.

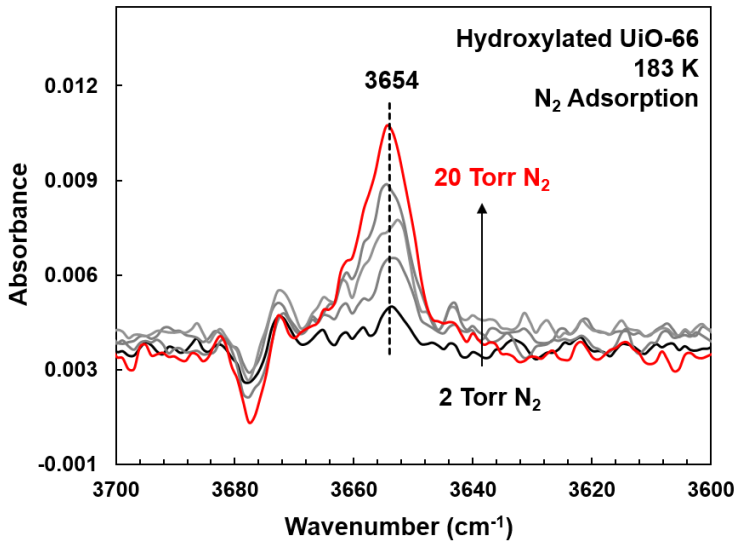

Figure 7.7. Infrared spectra acquired during N_2 adsorption on the low defect, hydroxylated UiO-66 and varying pressures between 2 – 20 Torr.

7.3.4 CO Characterization of Coordinatively Unsaturated Zr

Coordinatively unsaturated Zr sites within the UiO-66 MOF have been characterized and quantified via infrared spectroscopic studies of CO uptake. Specifically, σ-donation from CO to the surface site increases the CO vibrational frequency. This effect, along with the molecule's stability and strong transition dipole moment in the mid-infrared range, make CO an excellent probe molecule for characterizing the electronic nature of a variety of surfaces and specifically undercoordinated Zr atoms.[18,26,28,159,261,285] We have applied this strategy, in conjunction with DFT calculations, to characterize the nature of metallic binding sites within the MOF, UiO-66.

7.3.4.1 CO Uptake at Low Temperatures

While our low defect density MOF exhibits sharp diffraction patterns and TGA data indicative of a "pristine" material, the MOF certainly contains defects that are not detected by these traditional characterization methods. Therefore, we employed infrared spectroscopic studies of

carbon monoxide adsorption at very low temperatures to identify the nature of those defects. These experiments were conducted by exposing the hydroxylated (prior to extensive thermal treatment) UiO-66 samples to 1×10^{-5} Torr of CO at 103 K. Infrared spectra, recorded *in situ* with CO exposure, were acquired and referenced to the infrared spectrum of a clean UiO-66 sample (Fig. 7.1).

Upon CO uptake, three key features appear in the infrared spectrum (Fig.7.8, black trace). The absorbance feature at 2154 cm^{-1} is consistent with a hydrogen bond between CO and the μ_3-hydroxyl moiety located on the MOF nodes.[276,298-299] A slightly red-shifted feature relative to the CO–hydroxyl interaction, which appears as a shoulder at 2148 cm^{-1}, is assigned to the stretch of CO molecules that are physisorbed inside the pore environment of the UiO-66 structure and only present because of the very low temperatures used in the adsorption studies. In addition to these IR bands, we find an additional, highly blue-shifted band (relative to gas-phase CO) that is suggestive of CO establishing a σ-bond through its C atom.[96] We assign this highly blue-shifted band at 2180 cm^{-1} to CO in a dative covalent bond with a coordinatively unsaturated Zr atom at a missing-liker defect. In addition to missing linker defects, CO is expected to bind at Zr_{cus} that may exist within the MOF due to small quantities of ZrO_2 impurities. The CO vibrational frequency observed here for a Zr_{cus}-CO bond is consistent with analogous experimental studies of CO bound to a variety of zirconia materials.[96,300] The intensity of the CO-Zr_{cus} interaction band is significantly lower than that of the band assigned to CO interactions with the μ_3-hydroxl groups due to the low defect density of the as-synthesized MOF. Upon evacuation of the CO from the chamber, the infrared absorbance features associated with both the CO-Zr_{cus} interaction and the CO-hydroxyl interaction diminished below our detection limit. The rapid desorption rate of CO from the MOF

further evidences the relatively weak interaction that occurs between the CO and the coordinatively unsaturated Zr sites in UiO-66.

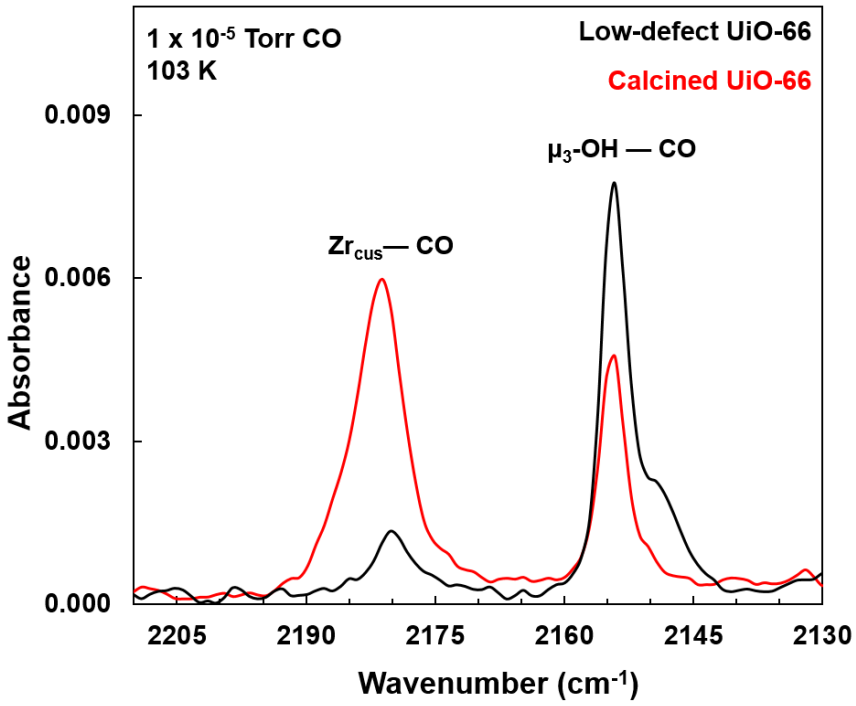

Figure 7.8. Infrared spectra recorded during the adsorption of CO onto the low defect density UiO-66 (black) and calcined UiO-66 (red). Each spectrum represents an average of 250 scans.

7.3.4.2 Sequestration of Zr_{cus} with a Lewis Base

To further verify the assignment of the infrared bands above 2175 cm^{-1} to CO bound at Zr_{cus} sites, D_2O was employed as a small-molecule Lewis base that is expected to occupy accessible Zr_{cus} sites[286,301] on the MOF and therefore, block CO binding to these sites. This hypothesis was tested by exposing the hydroxylated MOF sample to 500 mTorr of D_2O at 300 K for 5 minutes followed by evacuation. Bulk D_2O that persisted in the UiO-66 pore structure was confirmed with *in situ* infrared spectroscopy by the presence of a broad absorbance feature between 2500 and 2000 cm^{-1} (Fig. 7.9B). The appearance of a sharp feature at 2708 cm^{-1} in Figure 7.9B

indicates that, along with bulk D_2O, some D_2O molecules react to further hydroxylate UiO-66.[302] Following D_2O saturation of the Zr_{cus} sites, the sample was re-exposed to CO at low temperatures. The resulting spectrum, shown in Figure 7.9A (blue trace), revealed that there is no indication of CO binding at the now-D_2O-occupied Zr_{cus} sites.

In addition to blocking the Lewis acid sites, bulk D_2O is expected to interact with the μ_3-hydroxyl groups within the MOF. These interactions are evidenced in the spectrum of Figure 7.9A, which reveals a decrease in CO intensity associated with binding to the μ_3-hydroxyl groups. CO can more easily displace the D_2O that interacts with the Brønsted acid sites at the μ_3-hydroxyl groups. As expected based on previous works,[276,301] the binding energy between D_2O and Zr_{cus} is much stronger than that between CO and Zr_{cus} sites. Upon annealing the sample to 448 K, molecular D_2O was removed from the structure (Fig. 7.9B, red trace) and the Zr_{cus} sites were once again available to bind CO while the μ_3-hydroxyl groups were fully saturated by CO (Fig. 7.9A, red trace). The set of experiments employing the Lewis acid site blocker, D_2O, demonstrates both that water binds strongly to Zr_{cus} sites, thereby outcompeting CO coordination, and that relatively mild thermal treatment of the sample regenerates the Zr_{cus} active sites.

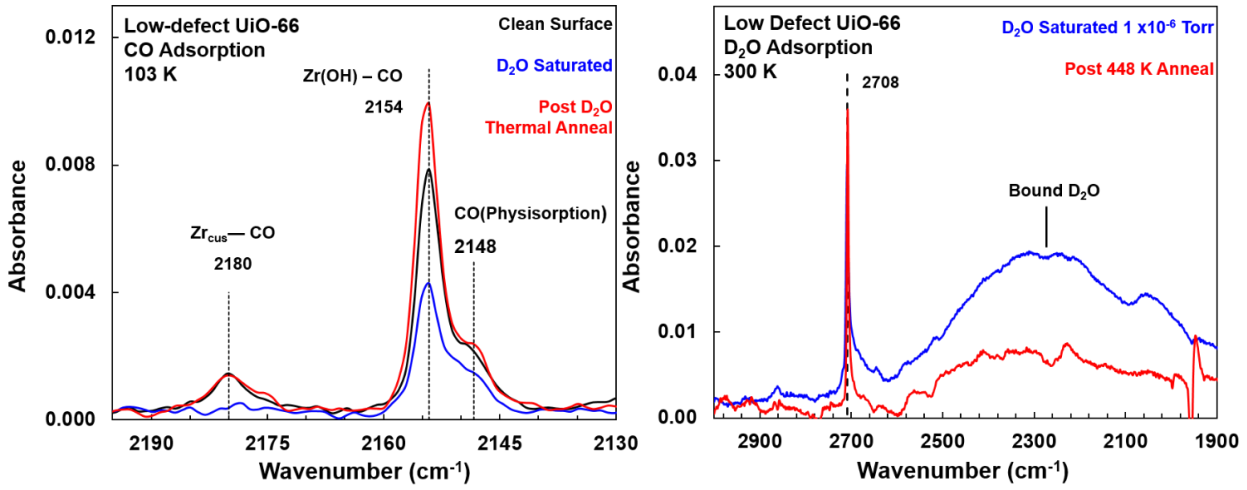

Figure 7.9. (A) Infrared spectra recorded during low temperature adsorption of CO prior to D_2O (black), D_2O saturated (blue) and after a 448 K thermal anneal (red) of the low defect density UiO-66 sample. (B) Infrared spectra recorded in vacuum after the adsorption of D_2O (blue trace) and upon vacuum annealing at 448 K (red trace).

7.3.4.3 Tracking the Development of Missing Linker Defects with Adsorbed CO

The concentration of coordinatively unsaturated Zr sites within MOFs depends strongly on sample synthesis procedure and history (storage conditions, humidity, time, temperature, etc.); therefore, we hypothesis that CO adsorption is a reliable and non-destructive method for analysis of the relative number of defects within MOF nodes. Here, the simplicity, accuracy, and non-invasive nature of IR spectroscopy of CO adsorption transcends prior techniques as a means to conveniently characterize the systematic development of defects within UiO-66.

Controlled heating of UiO-66 under vacuum has been employed to first desolvate, then dehydroxylate, and finally drive linkers from the MOF. For each stage, the UiO-66 sample was heated under vacuum to a pre-determined temperature and maintained at that temperature for 30 minutes before cooling back to 103 K, where CO adsorption was performed. The concentration of

linkers present after each thermal treatment was monitored by tracking the absorbance of the ρ(C-H) vibrational modes (825 – 810 cm^{-1}) (see Fig. 7.10).

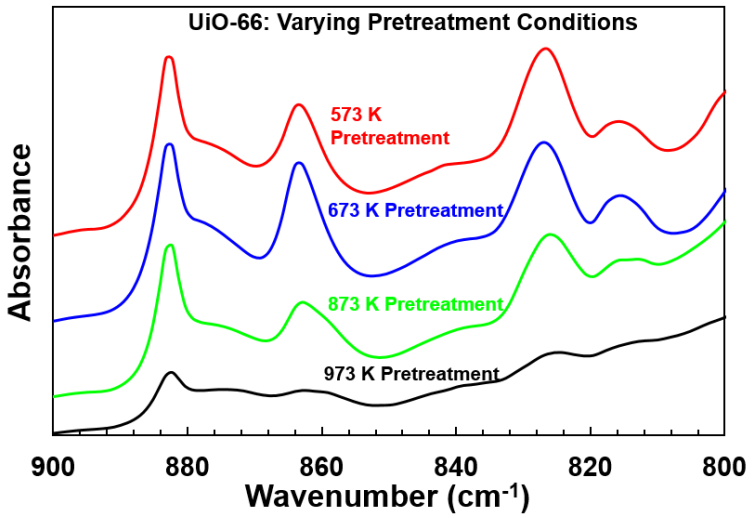

Figure 7.10. Infrared spectra of the low-defect density UiO-66 after different thermal pretreatments. The zoomed in x-axis highlights the C—H bending motions of the benzoate linkers.

Figure 7.11A shows how varying the pretreatment temperature affects the uptake of CO at 103 K. As described above, desolvation, which occurs at mild temperatures, opens a very limited number of Zr_{cus} as evidenced by the small CO absorbance band at 2180 cm^{-1} (see spectra *i* and *ii* in Fig. 7.11A). In addition, the mild-temperature treatment leaves a large number of μ_3-hydroxl groups intact for hydrogen bonding to the CO, as revealed by the larger band in spectra *i* and *ii* at 2154 cm^{-1}. As the μ_3-hydroxyl groups are thermally removed from the MOF at temperatures above 550 K, the IR spectra change in a number of ways. First, the band assigned to the free μ_3-OH groups above 3600 cm^{-1} diminishes (black points in Fig. 7.11B). Secondly, the IR signal at 2154 cm^{-1}, responsible for CO hydrogen bonded to μ_3-OH, also diminishes. Thirdly, the 2180 cm^{-1} CO-Zr_{cus} band grows with temperature until it becomes the only infrared absorbance feature for CO at

high temperatures, signaling the continued presence of Zr_{cus} sites within the MOF (spectra iii, iv, and v).

Upon raising the thermal pretreatment above 800 K, we observed several key changes in the MOF infrared spectrum. The bands assigned to the ρ(C-H) modes associated with the BDC linkers decreased in intensity (red data in Fig. 7.11B) due to the desorption of linkers from the MOF. During this process, many more defect sites within the MOF are generated. That is, spectra *vi* and *vii* in Figure 7.11A exhibit a large increase in the intensity of the band assigned to the CO-Zr_{cus} feature. The plot of IR band intensities versus pretreatment temperature in Figure 7.11B shows a direct correlation between the quantity of CO adsorbed on the Zr_{cus} sites and the loss of the organic linkers. The pretreatment temperature of 873 K released a significant portion of the organic linkers from the MOF (~ 40%), which led to a factor of 43 increase and significant broadening (relative to the as-prepared MOF) in the infrared absorbance of CO bound to Zr_{cus} sites (spectrum vii). At such high temperatures, decomposition of the UiO-66 framework begins to occur. The final pretreatment temperature of 973 K induced complete destruction of the framework as evidenced by the disappearance of ρ(C-H) modes associated with the BDC linkers and verified by *ex situ* XPS analysis of the sample (Fig. 7.12). We note that the MOF appears more stable upon thermal treatment in vacuum than during the ambient-pressure TGA characterization, where atmospheric gases may contribute to the reactivity of the MOF at elevated temperatures.

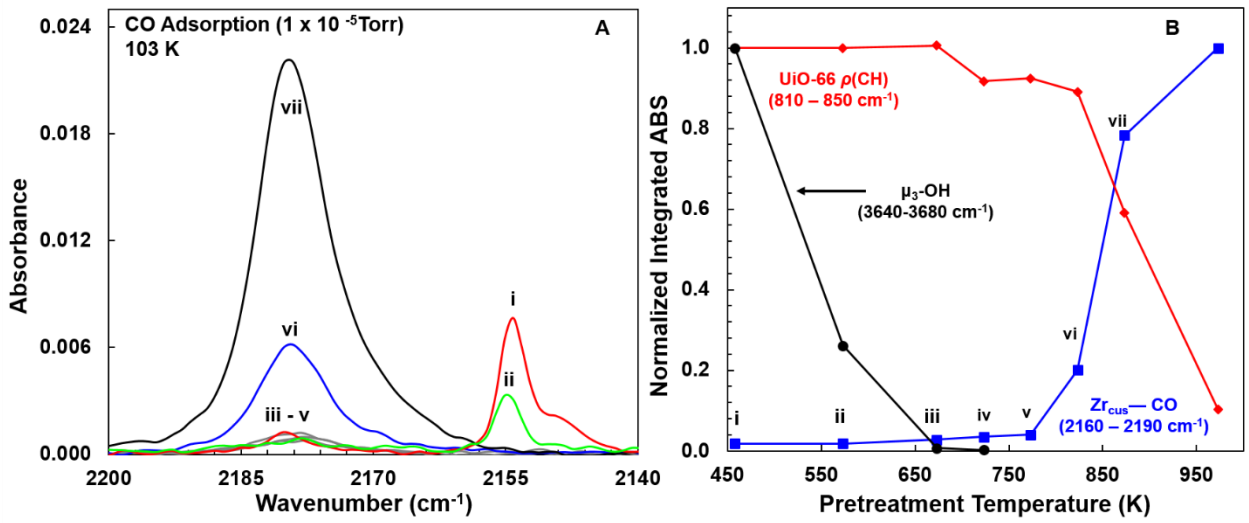

Figure 7.11. Probing the concentration of missing linkers as a function of the pretreatment temperature. Panel A provides the infrared spectra recorded during CO adsorption at 103 K. Panel B provides the integrated absorbance of the ρ(CH) modes of UiO-66 (red), the μ_3 hydroxyl (black) and the CO uptake at each corresponding pretreatment temperature (blue). Each data point is normalized relative to the maximum absorbance achieved during thermal treatment for the ρ(CH) modes, μ3 hydroxyl, and CO bound to Zr, respectively. The labels correspond to the pretreatment temperatures: (i) 448 K, (ii) 573 K, (iii) 673 K, (iv) 723 K, (v) 773 K, (vi) 823 K and (vii) 873 K.

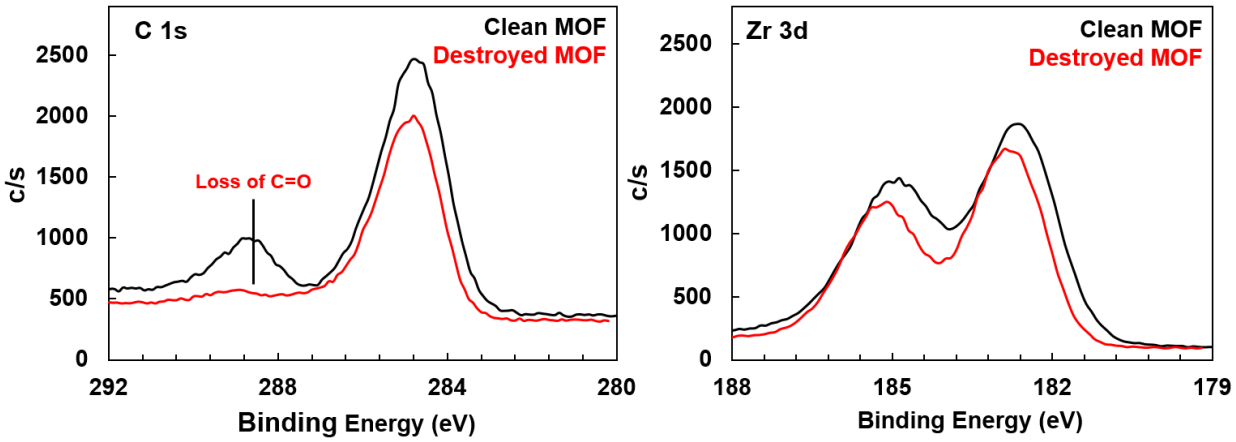

Figure 7.12. XPS of the low-defect density UiO-66 sample before thermal treatment (black) and after a 973 K thermal treatment (red).

Under the assumption that the CO absorbance is proportional to concentration, the data in Figures 7.8 and 7.11 can be directly correlated to the number of Zr_{cus} defect sites within the MOF. Specifically, once normalized to the mass of each sample, the spectra in Figure 7.8 illustrate an increase in the CO-Zr_{cus} infrared feature by a factor of 10.8 for the calcined UiO-66 sample relative to the low-defect density sample. Based upon TGA analysis, the calcined UiO-66 sample contains a defect density of 0.56 missing linkers per molecular formula unit. The defect density, as determined from the TGA data for the calcined MOF, was employed as a reference to calibrate the relative infrared intensities of the CO bands. Therefore, we calculate the defect density for the fully hydroxylated low-defect density UiO-66 sample to be 0.1 missing linkers per node. Traditional experimental approaches used to determine the defect density, such as TGA or PXRD, are not sufficiently sensitive to identify or characterize defects at such low concentrations. However, the work presented here suggests that infrared spectroscopic analysis of $CO_{(ads)}$ is sensitive from less than 1% up to 30% (calculated from Fig. 7.11A, spectrum vii) defect density in UiO-66.

7.3.4.4 Future Work of CO Adsorption to Distinguish and Further Characterize Zr_{cus} Sites

Based on these results, the stretching vibration of CO is a highly effective probe of the chemical nature of the node structure in UiO-66. Importantly, CO can simultaneously track changes in the concentration of node-bound hydroxyl groups as well as the presence of undercoordinated zirconium sites and how both respond to an external perturbation (water adsorption or thermal pretreatment). Preliminary CO adsorption performed on materials such as, NU-1000 and a TFA modulated UiO-66 highlight the ability of CO to probe the coordination environment of exposed metal atoms within systems under development for catalysis (Fig. 7.13).[60,84] In fact, CO adsorption on NU-1000 suggests two Zr adsorption sites with slightly different electronic structure. We speculate that the nodes of NU-1000 become distorted upon dehydroxylation as suggested by other research.[303] In addition, we anticipate that CO will serve as an equally effective tool to interrogate the defect properties within MOFs featuring open metal centers, such as PCN-222, HKUST-1, and MOF-808.

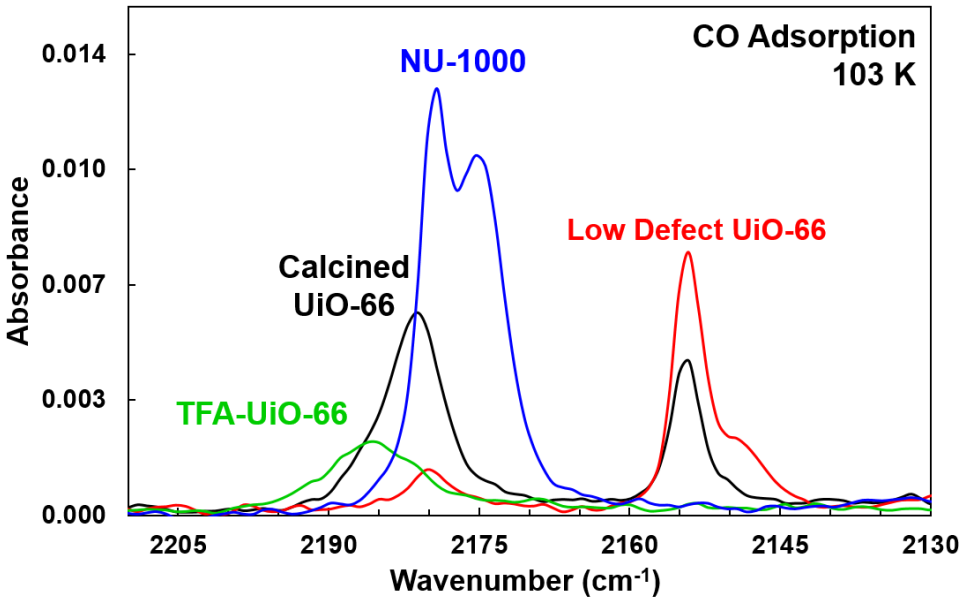

Figure 7.13. Infrared spectra acquired during the adsorption of CO on a variety of Zr-based MOFs

7.4 Summary

In summary, we have provided spectroscopic and computational evidence that the gas phase molecule, CO, binds to coordinatively unsaturated Zr and μ_3-hydroxyl groups in the metal-organic framework, UiO-66. These interactions have been elucidated through the $CO_{(ads)}$ stretching frequency. We utilized variable temperature infrared spectroscopy to evaluate the energetics of CO-hydroxyl interactions and suggest under certain situations that the acidity of unique hydroxyl groups within these frameworks can be quantified with small basic probe molecules. The Lewis-base, D_2O, was used to confirm the presence of Zr_{cus} on a low defect density, hydroxylated UiO-66 MOF. Missing linker defects were systematically produced through thermal treatment and correlated to the emergence of CO-Zr_{cus} species. Finally, this work suggests that CO is a superior probe of Zr_{cus} compared to traditional methods such as PXRD and TGA and can identify relative Zr_{cus} sites as low as 1% and up to 30% in UiO-66 samples. Insight into the defect density and associated Zr_{cus}, as well as the presence of μ_3-OH sites within Zr-based MOFs, will be important for predicting the outcome of MOF chemistry and for the development of more complete mechanistic descriptions of catalytic cycles on these tunable materials.

Chapter 8

Conclusion and Future Work

8.1 Conclusion

The main goal of this work was to develop a fundamental understanding of the adsorption and reaction processes that occur between small gas molecules and catalytic surfaces. Such fundamental studies are imperative to the generation and production of new catalytic materials for future industrial and environmental applications. This thesis focused on two different oxidation pathways: the epoxidation of the propene into propene oxide and the decomposition of chemical warfare agent simulants in aerobic environments. In order to investigate these two reaction pathways over heterogeneous surfaces, *in situ* vibrational spectroscopy within a well-defined vacuum environment was employed.

Through this spectroscopic approach, it was found that propene binds in multiple configurations on the surface of a TiO_2-supported Au nanocatalyst. These binding configurations were distinguishable through the ν(C=C) of propene when bound to an undercoordinated Au surface site and when bound to a Ti^{4+} surface site. The strength of propene binding to each site was further investigated and it determined that the propene–Au complex was more strongly bound compared to the propene–TiO_2 interaction. These results suggest that the gold nanoparticles play an important role in the epoxidation process—specifically in propene activation. To validate the propene adsorption studies, the same Au/TiO_2 nanocatalyst was studied under an environment of propene, O_2, H_2—the necessary feedstock to produce propene oxide. Through vibrational signatures of adsorbed propene oxide on the Au/TiO_2 surface, PO was identified on the Au particles near the TiO_2 interface. A systematic evaluation of the reactants identified the hydroperoxide intermediate, OOH, at room temperature—a novel result for the catalysis

community. Finally, in an attempt to remove the hydrogen requirement from the feedstock, a series of TiO_2-SiO_2 catalysts with isolated Ti^{4+} sites were synthesized. These materials were shown to produce propene oxide in the presence of the propene, oxygen and UV light; however, the extended TiO_2 regions of the materials were shown to significantly degrade propene oxide. In all, these studies provided new insight into the overall mechanism of propene epoxidation over TiO_2-supported catalysts.

The decomposition of organophosphate-based materials was investigated through similar experimental measures. A TiO_2-supported Cu aerogel catalyst, containing multiple Ti-Cu interfacial planes, was shown to convert the chemical warfare agent simulant, dimethyl chlorophosphate into surface bound CO. This unique reactivity was exhibited by only the Cu/TiO_2 aerogel and not seen on the TiO_2 aerogel or Cu_2O surface and thus, it was speculated that the Cu/Ti interfacial regions are critical in the reactivity. Through a systematic approach to the adsorption and oxidation of the CWA simulant, the reaction mechanism was confirmed to proceed through a methoxy intermediate located near the Cu/Ti interface.

Another class of materials known to degrade chemical warfare agents, Zr-based metal organic frameworks, were characterized with the probe molecule, CO. These Zr-based materials have been previously shown to bind and react CWAs through adsorption at undercoordinated Zr atoms on the nodes of these framework structures. Therefore, the coordinatively unsaturated Zr atoms were investigated through the vibrational frequency of ν(CO) adsorbed on the surface. The adsorption of CO onto Zr_{cus} was confirmed through a vibrational blueshift of CO when bound to the Lewis acidic Zr^{4+} surface site. The increase in the concentration of defects within the porous framework, induced by a systematic increase in temperature, was found to trend linearly with the concentration of adsorbed CO molecules bound to these undercoordinated sites. Additionally, I

show how CO can characterize both the hydroxyl groups of UiO-66 and potentially provide insight into the Brønsted acidity of these fascinating, porous materials.

8.2 Future Work

The work presented in this thesis leads well into more fundamental studies of gas adsorption and reaction on surfaces. Specifically, propene oxidation onto inverted Au/TiO_2 materials (also known as TiO_2 decorated Au surfaces) have shown promising activity under reaction feed environments of a hydrogen source, O_2, and propene.[170] These materials may exhibit similar or different binding configurations for reaction intermediates on the surface, such as propene and OOH. Additionally, Cu/TiO_2 aerogels have shown significant progress in the adsorption and oxidation of CWAs however, the state of the copper that remains active over time is not well known. Vibrational spectroscopy in conjunction with other surface sensitive techniques could help elucidate the oxidation state of Cu at interfacial regions vs. terrace-like Cu structures. Also, the role of lattice oxygen vacancies or the exposed Ti^{3+} surface sites as a result of these vacancies is unknown. I believe vibrational spectroscopy of probe molecules like CO or O_2 could help to identify Ti^{3+} sites on these aerogel metal-oxide surfaces. Finally, the adsorption of small probe molecules onto active surfaces sites, like those on metal-organic frameworks may provide insightful characterization throughout surface adsorption and reaction events and answer the question of where and how the organophosphorus-based compounds bind within this class of porous materials.

Appendix A

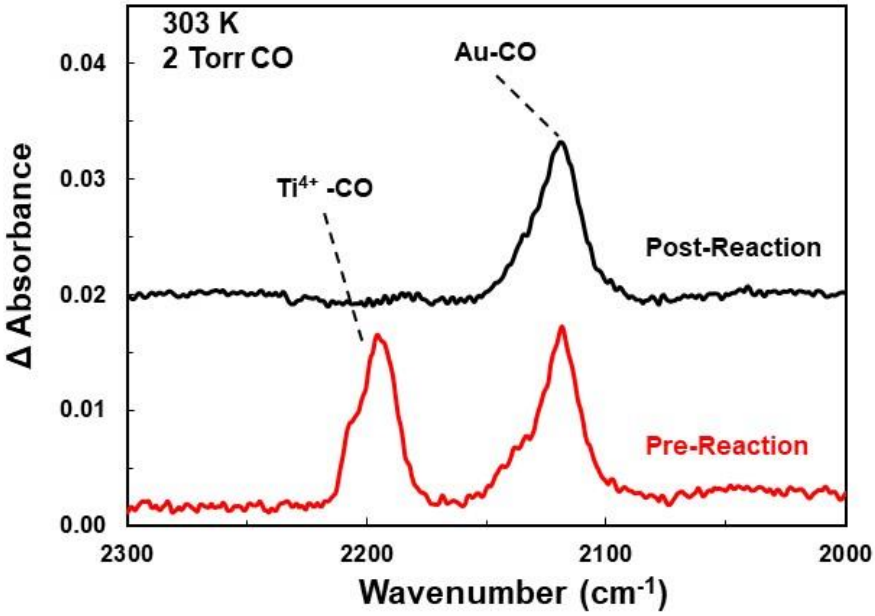

Figure i. Adsorption of CO on a clean Au/TiO_2 aerogel (red trace) and after the introduction of 2 Torr H_2 and 2 Torr O_2 (black trace). The reaction of H_2 and O_2 produces significant amounts of water (shown in Ch. 4) and blocks all the Ti^{4+} from binding CO.

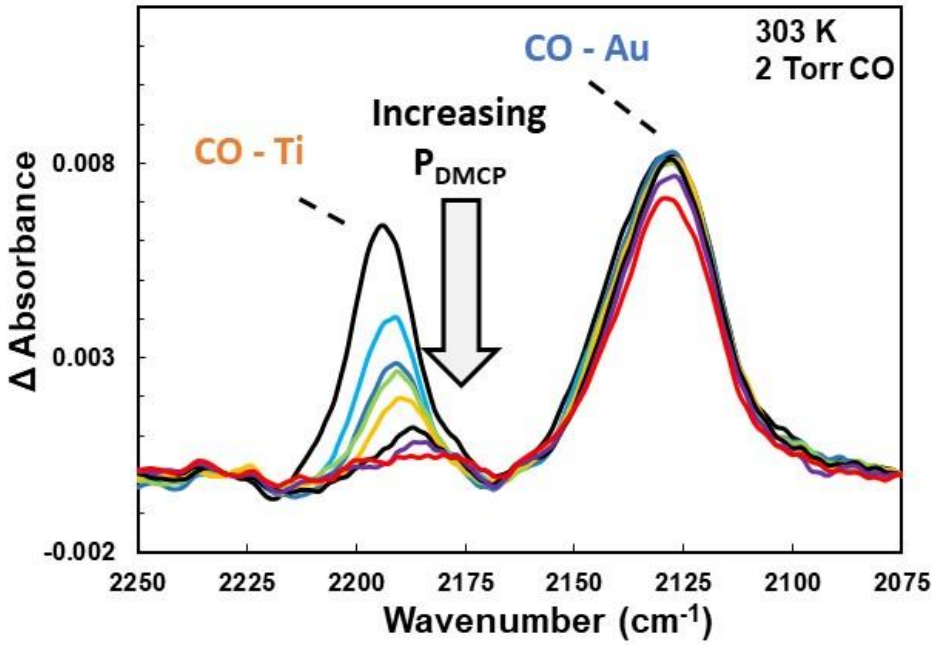

Figure ii. Co-adsorption studies between DMCP and CO on a Au/TiO_2 aerogel. DMCP easily removes CO from Ti sites however do not prefer to bind on Au particles.

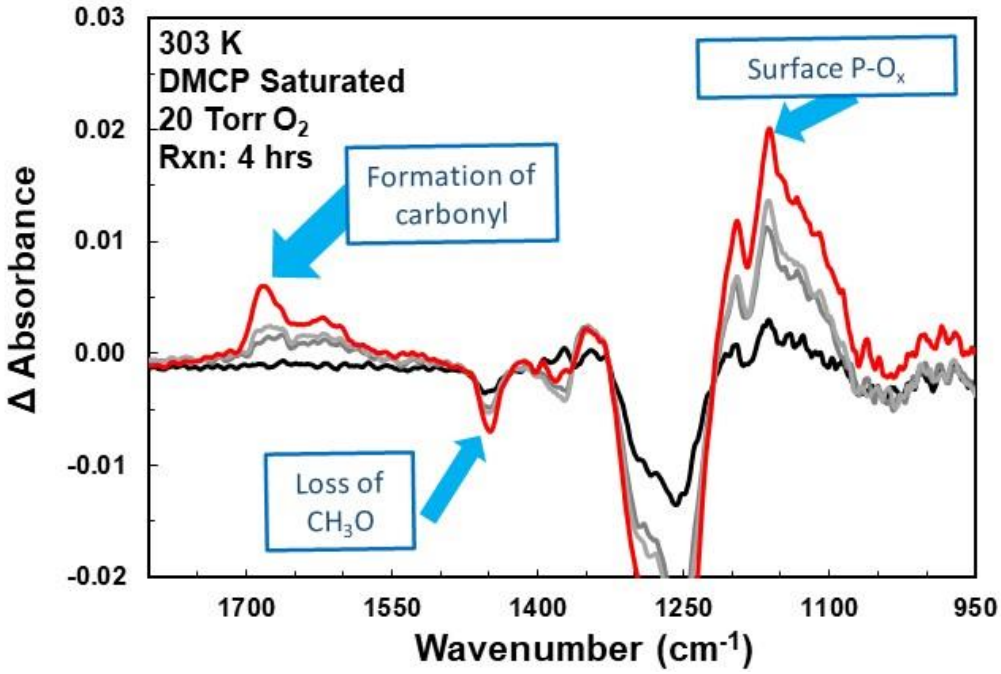

Figure iii. Infrared spectra of the oxidation of DMCP over a Au/TiO_2 aerogel. No surface-bound CO was identified.

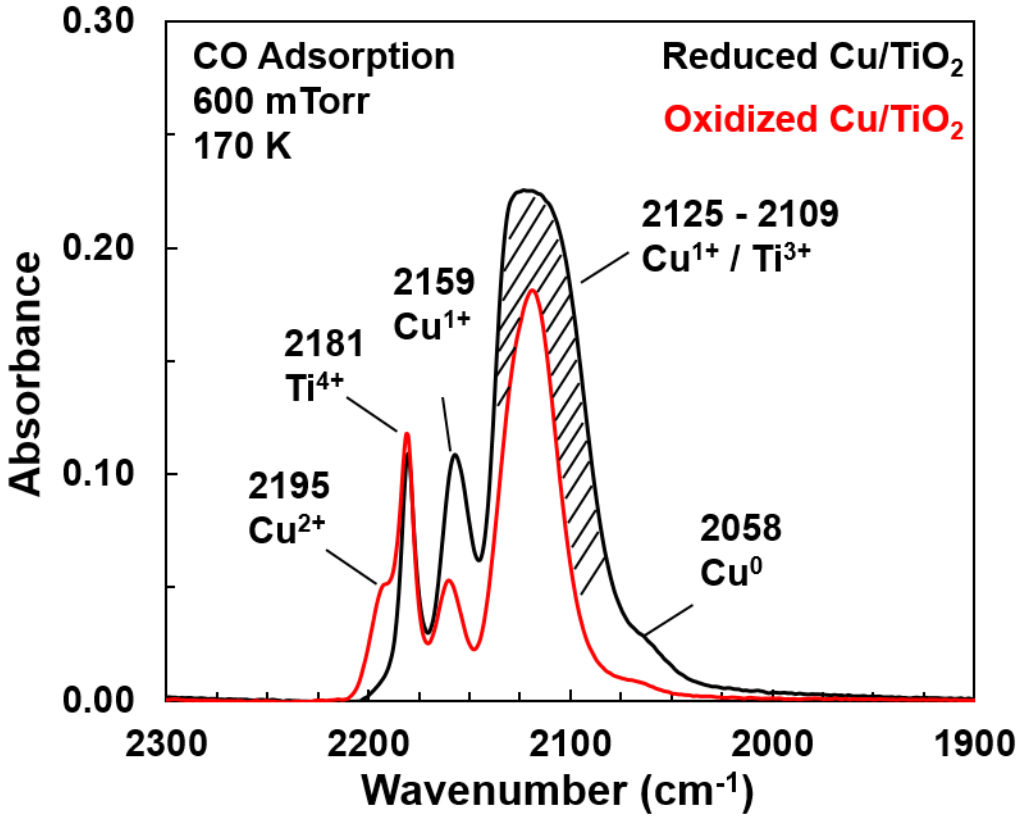

Figure iv. CO adsorption onto a Cu/TiO_2 aerogel that has been reduced in vacuum at 673 K (black trace) and oxidized in O_2 at 673 K. The decrease in the large feature at 2125-2109 upon oxidation would suggest that Ti^{3+} (present when reduced) are quenched by adsorbed oxygen species. Additionally, some Cu^{2+} surface species appear at high wavenumbers.

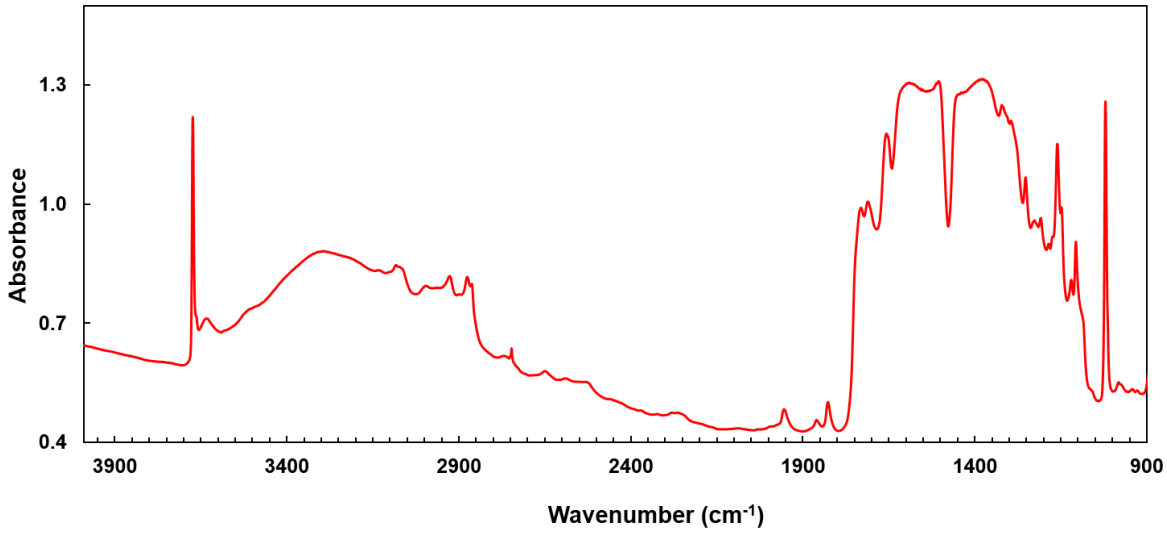

Figure v. Infrared spectrum of the MOF, UiO-66-TFA. The TFA is used as a modulator to add significant defects into the framework. Note the small, sharp feature around 2700 cm^{-1}, the second hydroxyl group 3600 cm^{-1}, and the broad hydrogen bonded feature.

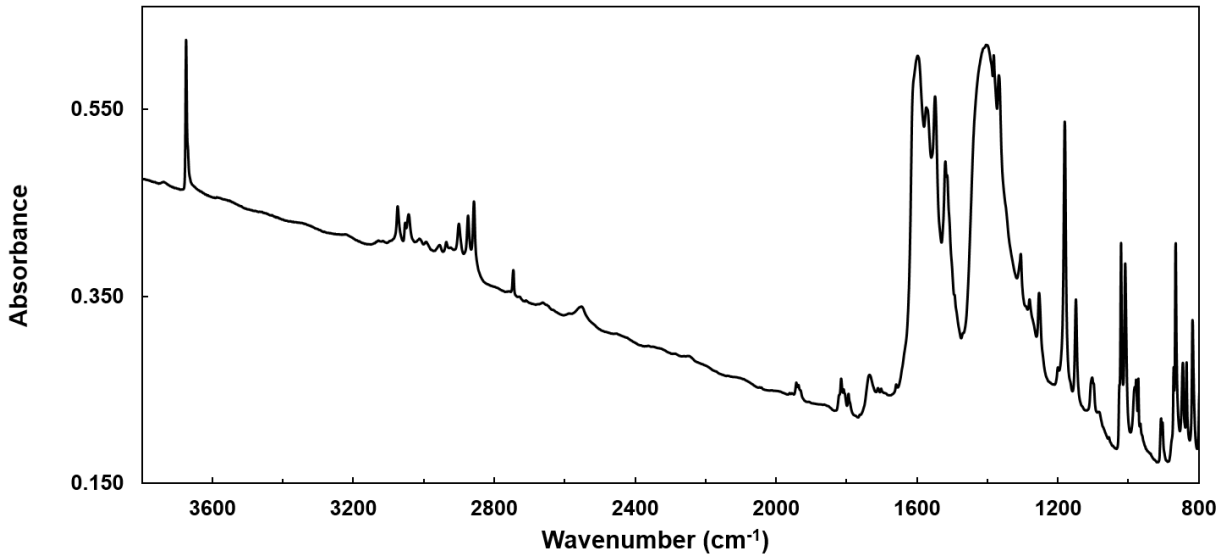

Figure vi. Infrared spectrum of the MOF, NU-1000

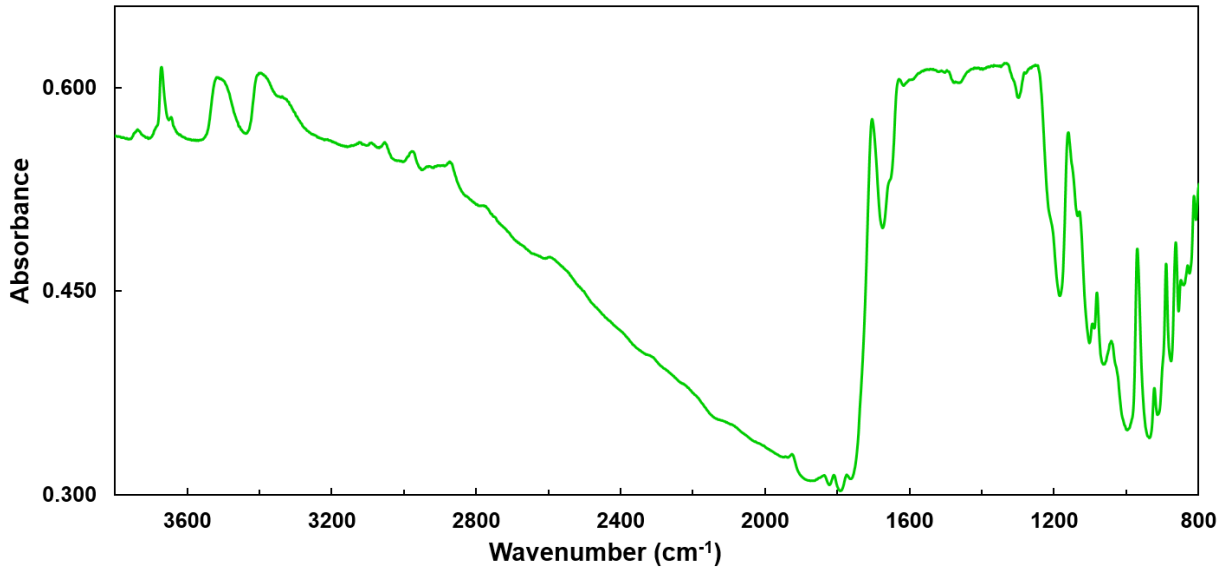

Figure vii. Infrared spectrum of the MOF, UiO-66-NH_2.

References

1. Zaera, F., The Surface Chemistry of Catalysis: New Challenges Ahead. *Surf. Sci.* **2002**, *500*, 947-965.
2. Somorjai, G. A., Modern Concepts in Surface Science and Heterogeneous Catalysis. *J. Phys. Chem.* **1990**, *94*, 1013-1023.
3. Hemmingson, S. L.; Campbell, C. T., Trends in Adhesion Energies of Metal Nanoparticles on Oxide Surfaces: Understanding Support Effects in Catalysis and Nanotechnology. *ACS Nano* **2017**, *11*, 1196-1203.
4. Hammer, B.; Norskov, J. K., Why Gold is the Noblest of all the Metals. *Nature* **1995**, *376*, 238-240.
5. Newns, D. M., Self-Consistent Model of Hydrogen Chemisorption. *Phys. Rev.* **1969**, *178*, 1123-1135.
6. Greiner, M. T.; Jones, T. E.; Beeg, S.; Zwiener, L.; Scherzer, M.; Girgsdies, F.; Piccinin, S.; Armbrüster, M.; Knop-Gericke, A., et al., Free-atom-like d states in single-atom alloy catalysts. *Nat. Chem.* **2018**, *10*, 1008-1015.
7. Nilsson, A.; Pettersson, L. G. M.; Hammer, B.; Bligaard, T.; Christensen, C. H.; Nørskov, J. K., The electronic structure effect in heterogeneous catalysis. *Catal. Lett.* **2005**, *100*, 111-114.
8. Hammer, B.; Nørskov, J. K., Theoretical surface science and catalysis—calculations and concepts. In *Advances in Catalysis*, Academic Press: 2000; Vol. 45, pp 71-129.
9. Haruta, M., Size- and Support-Dependency in the Catalysis of Gold. *Catal. Today* **1997**, *36*, 153-166.
10. Haruta, M.; Kobayashi, T.; Sano, H.; Yamada, N., Novel Gold Catalysts for the Oxidation of Carbon Monoxide at a Temperature far Below 0 °C. *Chem. Lett.* **1987**, *16*, 405-408.
11. Haruta, M.; Tsubota, S.; Kobayashi, T.; Kageyama, H.; Genet, M. J.; Delmon, B., Low-Temperature Oxidation of CO over Gold Supported on TiO2, α-Fe2O3, and Co3O4. *J. Catal.* **1993**, *144*, 175-192.
12. Panayotov, D. A.; Morris, J. R., Surface Chemistry of Au/TiO_2: Thermally and Photolytically Activated Reactions. *Surf. Sci. Rep.* **2016**, *71*, 77-271.
13. Pettersson, L. G. M.; Nilsson, A., A Molecular Perspective on the d-Band Model: Synergy Between Experiment and Theory. *Top. Catal.* **2014**, *57*, 2-13.
14. Gross, A., Adsorption at Nanostructured Surfaces from First Principles. *Journal of Computational and Theoretical Nanoscience* **2008**, *5*, 894-922.
15. Zhou, Y.; Lawrence, N. J.; Wang, L.; Kong, L.; Wu, T.-S.; Liu, J.; Gao, Y.; Brewer, J. R.; Lawrence, V. K., et al., Resonant Photoemission Observations and DFT Study of s–d Hybridization in Catalytically Active Gold Clusters on Ceria Nanorods. *Angew. Chem. Int. Ed.* **2013**, *52*, 6936-6939.
16. Chen, M. S.; Goodman, D. W., The Structure of Catalytically Active Gold on Titania. *Science* **2004**, *306*, 252-255.
17. Chusuei, C. C.; Lai, X.; Luo, K.; Goodman, D. W., Modeling Heterogeneous Catalysts: Metal Clusters on Planar Oxide Supports. *Top. Catal.* **2000**, *14*, 71-83.
18. Green, I. X.; Tang, W. J.; Neurock, M.; Yates, J. T., Spectroscopic Observation of Dual Catalytic Sites During Oxidation of CO on a Au/TiO_2 Catalyst. *Science* **2011**, *333*, 736-739.

19. Panayotov, D. A.; Frenkel, A. I.; Morris, J. R., Catalysis and Photocatalysis by Nanoscale Au/TiO_2: Perspectives for Renewable Energy. *ACS Energy Letters* **2017**, *2*, 1223-1231.
20. Lu, Y.; Wang, J.; Yu, L.; Kovarik, L.; Zhang, X.; Hoffman, A. S.; Gallo, A.; Bare, S. R.; Sokaras, D., et al., Identification of the Active Complex for CO Oxidation over Single-Atom Ir-on-$MgAl_2O_4$ Catalysts. *Nature Catalysis* **2018**.
21. Masel, R. I., *Chemical Kinetics and Catalysis*; Wiley-Interscience: New York, 2001.
22. Saavedra, J.; Doan, H. A.; Pursell, C. J.; Grabow, L. C.; Chandler, B. D., The Critical Role of Water at the Gold-Titania Interface in Catalytic CO Oxidation. *Science* **2014**, *345*, 1599.
23. Green, I. X.; Tang, W.; Neurock, M.; Yates, J. T., Insights into Catalytic Oxidation at the Au/TiO_2 Dual Perimeter Sites. *Acc. Chem. Res.* **2014**, *47*, 805-815.
24. Green, I. X.; McEntee, M.; Tang, W. J.; Neurock, M.; Yates, J. T., Direct Formation of Acetate from the Partial Oxidation of Ethylene on a Au/TiO_2 Catalyst. *Top. Catal.* **2013**, *56*, 1512-1524.
25. McEntee, M.; Tang, W. J.; Neurock, M.; Yates, J. T., Mechanistic Insights into the Catalytic Oxidation of Carboxylic Acids on Au/TiO_2: Partial Oxidation of Propionic and Butyric Acid to Gold Ketenylidene through Unsaturated Acids. *ACS Catal.* **2015**, *5*, 744-753.
26. Matsubu, J. C.; Zhang, S.; DeRita, L.; Marinkovic, N. S.; Chen, J. G.; Graham, G. W.; Pan, X.; Christopher, P., Adsorbate-Mediated Strong Metal–Support Interactions in Oxide-Supported Rh Catalysts. *Nat Chem* **2016**, *9*, 120-127.
27. Kale, M. J.; Christopher, P., Utilizing Quantitative in Situ FTIR Spectroscopy To Identify Well-Coordinated Pt Atoms as the Active Site for CO Oxidation on Al_2O_3-Supported Pt Catalysts. *ACS Catal.* **2016**, *6*, 5599-5609.
28. McEntee, M.; Stevanovic, A.; Tang, W. J.; Neurock, M.; Yates, J. T., Electric Field Changes on Au Nanoparticles on Semiconductor Supports - The Molecular Voltmeter and Other Methods to Observe Adsorbate-Induced Charge-Transfer Effects in Au/TiO_2 Nanocatalysts. *J. Am. Chem. Soc.* **2015**, *137*, 1972-1982.
29. Tang, H.; Su, Y.; Zhang, B.; Lee, A. F.; Isaacs, M. A.; Wilson, K.; Li, L.; Ren, Y.; Huang, J., et al., Classical Strong Metal–Support Interactions Between Gold Nanoparticles and Titanium Dioxide. *Science Advances* **2017**, *3*.
30. DeSario, P. A.; Pietron, J. J.; Taffa, D. H.; Compton, R.; Schünemann, S.; Marschall, R.; Brintlinger, T. H.; Stroud, R. M.; Wark, M., et al., Correlating Changes in Electron Lifetime and Mobility on Photocatalytic Activity at Network-Modified TiO_2 Aerogels. *J. Phys. Chem. C* **2015**, *119*, 17529-17538.
31. DeSario, P. A.; Pietron, J. J.; DeVantier, D. E.; Brintlinger, T. H.; Stroud, R. M.; Rolison, D. R., Plasmonic Enhancement of Visible-Light Water Splitting with $Au\text{-}TiO_2$ Composite Aerogels. *Nanoscale* **2013**, *5*, 8073-8083.
32. DeSario, P. A.; Pietron, J. J.; Brintlinger, T. H.; McEntee, M.; Parker, J. F.; Baturina, O.; Stroud, R. M.; Rolison, D. R., Oxidation-Stable Plasmonic Copper Nanoparticles in Photocatalytic TiO_2 Nanoarchitectures. *Nanoscale* **2017**, *9*, 11720-11729.
33. Diebold, U., The Surface Science of Titanium Dioxide. *Surf. Sci. Rep.* **2003**, *48*, 53-229.
34. Vijay, A.; Mills, G.; Metiu, H., Adsorption of Gold on Stoichiometric and Reduced Rutile TiO_2 (110) Surfaces. *J. Chem. Phys.* **2003**, *118*, 6536-6551.
35. Tosoni, S.; Pacchioni, G., Trends in Adhesion Energies of Gold on MgO(100), Rutile TiO_2(110), and CeO_2(111) Surfaces: A Comparative DFT Study. *J. Phys. Chem. C* **2017**, *121*, 28328-28338.

36. Zanella, R.; Giorgio, S.; Henry, C. R.; Louis, C., Alternative methods for the preparation of gold nanoparticles supported on TiO_2. *J. Phys. Chem. B* **2002**, *106*, 7634-7642.
37. Driscoll, D. M.; Tang, W.; Burrows, S. P.; Panayotov, D. A.; Neurock, M.; McEntee, M.; Morris, J. R., Binding Sites, Geometry, and Energetics of Propene at Nanoparticulate Au/TiO_2. *J. Phys. Chem. C* **2017**, *121*, 1683-1689.
38. Panayotov, D.; McEntee, M.; Burrows, S.; Driscoll, D.; Tang, W.; Neurock, M.; Morris, J., Infrared Studies of Propene and Propene Oxide Adsorption on Nanoparticulate Au/TiO_2. *Surf. Sci.* **2016**, *652*, 172-182.
39. Klimev, H.; Fajerwerg, K.; Chakarova, K.; Delannoy, L.; Louis, C.; Hadjiivanov, K., Oxidation of Gold Metal Particles Supported on TiO_2: An FTIR Study by Means of Low-Temperature CO Adsorption. *J. Mater. Sci.* **2007**, *42*, 3299-3306.
40. Venkov, T.; Fajerwerg, K.; Delannoy, L.; Klimev, H.; Hadjiivanov, K.; Louis, C., Effect of the Activation Temperature on the State of Gold Supported on Titania: An FT-IR Spectroscopic Study. *Appl. Catal., A* **2006**, *301*, 106-114.
41. Ren, J.; Ledwaba, M.; Musyoka, N. M.; Langmi, H. W.; Mathe, M.; Liao, S.; Pang, W., Structural Defects in Metal–Organic Frameworks (MOFs): Formation, Detection and Control Towards Practices of Interests. *Coord. Chem. Rev.* **2017**, *349*, 169-197.
42. Bobbitt, N. S.; Mendonca, M. L.; Howarth, A. J.; Islamoglu, T.; Hupp, J. T.; Farha, O. K.; Snurr, R. Q., Metal-Organic Frameworks for the Removal of Toxic Industrial Chemicals and Chemical Warfare Agents. *Chem. Soc. Rev.* **2017**, *46*, 3357-3385.
43. Lee, J.; Farha, O. K.; Roberts, J.; Scheidt, K. A.; Nguyen, S. T.; Hupp, J. T., Metal–Organic Framework Materials as Catalysts. *Chem. Soc. Rev.* **2009**, *38*, 1450-1459.
44. Isaeva, V. I.; Kustov, L. M., The Application of Metal-Organic Frameworks in Catalysis (Review). *Petroleum Chemistry* **2010**, *50*, 167-180.
45. Kahlich, D.; Wiechern, U.; Lindner, J., Propylene Oxide. In *Ullmann's Encyclopedia of Industrial Chemistry*, Wiley-VCH Verlag GmbH & Co. KGaA: 2000.
46. Nijhuis, T. A.; Makkee, M.; Moulijn, J. A.; Weckhuysen, B. M., The Production of Propene Oxide: Catalytic Processes and Recent Developments. *Ind. Eng. Chem. Res.* **2006**, *45*, 3447-3459.
47. Trent, D. L., Propylene Oxide. In *Kirk-Othmer Encyclopedia of Chemical Technology*, Wiley: 2001.
48. Nijhuis, T. A.; Huizinga, B. J.; Makkee, M.; Moulijn, J. A., Direct Epoxidation of Propene Using Gold Dispersed on TS-1 and Other Titanium-Containing Supports. *Ind. Eng. Chem. Res.* **1999**, *38*, 884-891.
49. Suo, Z.; Jin, M.; Lu, J.; Wei, Z.; Li, C., Direct Gas-Phase Epoxidation of Propylene to Propylene Oxide using Air as Oxidant on Supported Gold Catalyst. *Journal of Natural Gas Chemistry* **2008**, *17*, 184-190.
50. Stangland, E. E.; Stavens, K. B.; Andres, R. P.; Delgass, W. N., Characterization of Gold–Titania Catalysts via Oxidation of Propylene to Propylene Oxide. *J. Catal.* **2000**, *191*, 332-347.
51. Hayashi, T.; Tanaka, K.; Haruta, M., Selective Vapor-Phase Epoxidation of Propylene over Au/TiO_2 Catalysts in the Presence of Oxygen and Hydrogen. *J. Catal.* **1998**, *178*, 566-575.
52. Mul, G.; Zwijnenburg, A.; van der Linden, B.; Makkee, M.; Moulijn, J. A., Stability and Selectivity of Au/TiO_2 and $Au/TiO_2/SiO_2$ Catalysts in Propene Epoxidation: An In Situ FT-IR Study. *J. Catal.* **2001**, *201*, 128-137.

53. Nijhuis, T. A.; Visser, T.; Weckhuysen, B. M., Mechanistic Study into the Direct Epoxidation of Propene over Gold/Titania Catalysts. *J. Phys. Chem. B* **2005**, *109*, 19309-19319.
54. Taylor, B.; Lauterbach, J.; Delgass, W. N., Gas-Phase Epoxidation of Propylene over Small Gold Ensembles on TS-1. *Appl. Catal., A* **2005**, *291*, 188-198.
55. Nijhuis, T. A.; Visser, T.; Weckhuysen, B. M., The Role of Gold in Gold–Titania Epoxidation Catalysts. *Angew. Chem. Int. Ed.* **2005**, *44*, 1115-1118.
56. Ojeda, M.; Iglesia, E., Catalytic Epoxidation of Propene with H_2O-O_2 Reactants on Au/TiO_2. *Chem. Commun.* **2009**, 352-354.
57. Friboulet, A.; Rieger, F.; Goudou, D.; Amitai, G.; Taylor, P., Interaction of an Organophosphate with a Peripheral Site on Acetylcholinesterase. *Biochemistry* **1990**, *29*, 914-920.
58. Davis, E. D.; Gordon, W. O.; Wilmsmeyer, A. R.; Troya, D.; Morris, J. R., Chemical Warfare Agent Surface Adsorption: Hydrogen Bonding of Sarin and Soman to Amorphous Silica. *J. Phys. Chem. Lett.* **2014**, *5*, 1393-1399.
59. Quintero, Y. C.; Nagarajan, R., Molecular and Dissociative Adsorption of DMMP, Sarin and Soman on Dry and Wet TiO_2(110) using Density Functional Theory. *Surf. Sci.* **2018**, *675*, 26-35.
60. de Koning, M. C.; van Grol, M.; Breijaert, T., Degradation of Paraoxon and the Chemical Warfare Agents VX, Tabun, and Soman by the Metal–Organic Frameworks UiO-66-NH_2, MOF-808, NU-1000, and PCN-777. *Inorg. Chem.* **2017**, *56*, 11804-11809.
61. Kim, K.; Tsay, O. G.; Atwood, D. A.; Churchill, D. G., Destruction and Detection of Chemical Warfare Agents. *Chem. Rev.* **2011**, *111*, 5345-5403.
62. Templeton, M. K.; Weinberg, W. H., Adsorption and Decomposition of Dimethyl Methylphosphonate on an Aluminum Oxide Surface. *J. Am. Chem. Soc.* **1985**, *107*, 97-108.
63. Mitchell, M. B.; Sheinker, V. N.; Mintz, E. A., Adsorption and Decomposition of Dimethyl Methylphosphonate on Metal Oxides. *J. Phys. Chem. B* **1997**, *101*, 11192-11203.
64. Ekerdt, J. G.; Klabunde, K. J.; Shapley, J. R.; White, J. M.; Yates, J. T., Surface Chemistry of Organophosphorus Compounds. *J. Phys. Chem.* **1988**, *92*, 6182-6188.
65. Wilmsmeyer, A. R.; Gordon, W. O.; Davis, E. D.; Troya, D.; Mantooth, B. A.; Lalain, T. A.; Morris, J. R., Infrared Spectra and Binding Energies of Chemical Warfare Nerve Agent Simulants on the Surface of Amorphous Silica. *J. Phys. Chem. C* **2013**, *117*, 15685-15697.
66. Kanan, S. M.; Tripp, C. P., An Infrared Study of Adsorbed Organophosphonates on Silica: A Prefiltering Strategy for the Detection of Nerve Agents on Metal Oxide Sensors. *Langmuir* **2001**, *17*, 2213-2218.
67. Panayotov, D. A.; Morris, J. R., Thermal Decomposition of a Chemical Warfare Agent Simulant (DMMP) on TiO_2: Adsorbate Reactions with Lattice Oxygen as Studied by Infrared Spectroscopy. *J. Phys. Chem. C* **2009**, *113*, 15684-15691.
68. Panayotov, D. A.; Morris, J. R., Uptake of a Chemical Warfare Agent Simulant (DMMP) on TiO_2: Reactive Adsorption and Active Site Poisoning. *Langmuir* **2009**, *25*, 3652-3658.
69. Rusu, C. N.; Yates, J. T., Adsorption and Decomposition of Dimethyl Methylphosphonate on TiO_2. *J. Phys. Chem. B* **2000**, *104*, 12292-12298.
70. Balow, R. B.; Lundin, J. G.; Daniels, G. C.; Gordon, W. O.; McEntee, M.; Peterson, G. W.; Wynne, J. H.; Pehrsson, P. E., Environmental Effects on Zirconium Hydroxide

Nanoparticles and Chemical Warfare Agent Decomposition: Implications of Atmospheric Water and Carbon Dioxide. *ACS Applied Materials & Interfaces* **2017**, *9*, 39747-39757.
71. Gordon, W. O.; Tissue, B. M.; Morris, J. R., Adsorption and Decomposition of Dimethyl Methylphosphonate on Y_2O_3 Nanoparticles. *J. Phys. Chem. C* **2007**, *111*, 3233-3240.
72. Chen, D. A.; Ratliff, J. S.; Hu, X.; Gordon, W. O.; Senanayake, S. D.; Mullins, D. R., Dimethyl Methylphosphonate Decomposition on Fully Oxidized and Partially Reduced Ceria Thin Films. *Surf. Sci.* **2010**, *604*, 574-587.
73. Head, A. R.; Tsyshevsky, R.; Trotochaud, L.; Yu, Y.; Karslıoğlu, O.; Eichhorn, B.; Kuklja, M. M.; Bluhm, H., Dimethyl Methylphosphonate Adsorption and Decomposition on MoO_2 as Studied by Ambient Pressure X-Ray Photoelectron Spectroscopy and DFT Calculations. *J. Phys.: Condens. Matter* **2018**, *30*, 134005.
74. Head, A. R.; Tsyshevsky, R.; Trotochaud, L.; Yu, Y.; Kyhl, L.; Karslıoğlu, O.; Kuklja, M. M.; Bluhm, H., Adsorption of Dimethyl Methylphosphonate on MoO_3: The Role of Oxygen Vacancies. *J. Phys. Chem. C* **2016**, *120*, 29077-29088.
75. Tang, X.; Hicks, Z.; Ganteför, G.; Eichhorn, B. W.; Bowen, K. H., Adsorption and Decomposition of DMMP on Size-Selected $(WO_3)_3$ Clusters. *ChemistrySelect* **2018**, *3*, 3718-3721.
76. Head, A. R.; Trotochaud, L.; Tsyshevsky, R.; Fears, K.; Eichhorn, B.; Kuklja, M. M.; Bluhm, H., Coupling Ambient Pressure X-ray Photoelectron Spectroscopy with Density Functional Theory to Study Complex Surface Chemistry and Catalysis. *Top. Catal.* **2018**, *61*, 2175-2184.
77. Trotochaud, L.; Head, A. R.; Büchner, C.; Yu, Y.; Karslıoğlu, O.; Tsyshevsky, R.; Holdren, S.; Eichhorn, B.; Kuklja, M. M., et al., Room Temperature Decomposition of Dimethyl Methylphosphonate on Cuprous Oxide Yields Atomic Phosphorus. *Surf. Sci.* **2019**, *680*, 75-87.
78. Schuschke, C.; Schwarz, M.; Hohner, C.; Silva, T. N.; Libuda, J., Phosphonic Acids on Well-Ordered CoO Surfaces: The Binding Motif Depends on the Surface Structure. *J. Phys. Chem. C* **2018**, *122*, 16221-16233.
79. Florent, M.; Giannakoudakis, D. A.; Wallace, R.; Bandosz, T. J., Mixed CuFe and ZnFe (hydr)oxides as reactive adsorbents of chemical warfare agent surrogates. *J. Hazard. Mater.* **2017**, *329*, 141-149.
80. Katz, M. J.; Klet, R. C.; Moon, S.-Y.; Mondloch, J. E.; Hupp, J. T.; Farha, O. K., One Step Backward Is Two Steps Forward: Enhancing the Hydrolysis Rate of UiO-66 by Decreasing $[OH^-]$. *ACS Catal.* **2015**, *5*, 4637-4642.
81. Plonka, A. M.; Wang, Q.; Gordon, W. O.; Balboa, A.; Troya, D.; Guo, W.; Sharp, C. H.; Senanayake, S. D.; Morris, J. R., et al., In Situ Probes of Capture and Decomposition of Chemical Warfare Agent Simulants by Zr-Based Metal Organic Frameworks. *J. Am. Chem. Soc.* **2017**, *139*, 599-602.
82. Wang, G.; Sharp, C.; Plonka, A. M.; Wang, Q.; Frenkel, A. I.; Guo, W.; Hill, C.; Smith, C.; Kollar, J., et al., Mechanism and Kinetics for Reaction of the Chemical Warfare Agent Simulant, DMMP(g), with Zirconium(IV) MOFs: An Ultrahigh-Vacuum and DFT Study. *J. Phys. Chem. C* **2017**, *121*, 11261-11272.
83. Sava Gallis, D. F.; Harvey, J. A.; Pearce, C. J.; Hall, M. G.; DeCoste, J. B.; Kinnan, M. K.; Greathouse, J. A., Efficient MOF-Based Degradation of Organophosphorus Compounds in Non-Aqueous Environments. *J. Mater. Chem. A* **2018**, *6*, 3038-3045.

84. Mondloch, J. E.; Katz, M. J.; Isley Iii, W. C.; Ghosh, P.; Liao, P.; Bury, W.; Wagner, G. W.; Hall, M. G.; DeCoste, J. B., et al., Destruction of Chemical Warfare Agents Using Metal–Organic Frameworks. *Nat. Mater.* **2015**, *14*, 512.
85. Moon, S.-Y.; Liu, Y.; Hupp, J. T.; Farha, O. K., Instantaneous Hydrolysis of Nerve-Agent Simulants with a Six-Connected Zirconium-Based Metal–Organic Framework. *Angew. Chem. Int. Ed.* **2015**, *54*, 6795-6799.
86. Cavka, J. H.; Jakobsen, S.; Olsbye, U.; Guillou, N.; Lamberti, C.; Bordiga, S.; Lillerud, K. P., A New Zirconium Inorganic Building Brick Forming Metal Organic Frameworks with Exceptional Stability. *J. Am. Chem. Soc.* **2008**, *130*, 13850-13851.
87. Katz, M. J.; Brown, Z. J.; Colon, Y. J.; Siu, P. W.; Scheidt, K. A.; Snurr, R. Q.; Hupp, J. T.; Farha, O. K., A Facile Synthesis of UiO-66, UiO-67 and their Derivatives. *Chem. Commun.* **2013**, *49*, 9449-9451.
88. St. Petkov, P.; Vayssilov, G. N.; Liu, J.; Shekhah, O.; Wang, Y.; Wöll, C.; Heine, T., Defects in MOFs: A Thorough Characterization. *ChemPhysChem* **2012**, *13*, 2025-2029.
89. Taddei, M., When Defects Turn into Virtues: The Curious Case of Zirconium-Based Metal-Organic Frameworks. *Coord. Chem. Rev.* **2017**, *343*, 1-24.
90. Canivet, J.; Vandichel, M.; Farrusseng, D., Origin of Highly Active Metal-Organic Framework Catalysts: Defects? Defects! *Dalton Transactions* **2016**, *45*, 4090-4099.
91. Ryu, S. G.; Kim, M.-K.; Park, M.; Jang, S. O.; Kim, S. H.; Jung, H., Availability of Zr-Based MOFs for the Degradation of Nerve Agents in all Humidity Conditions. *Microporous Mesoporous Mater.* **2019**, *274*, 9-16.
92. Cho, K. Y.; Seo, J. Y.; Kim, H.-J.; Pai, S. J.; Do, X. H.; Yoon, H. G.; Hwang, S. S.; Han, S. S.; Baek, K.-Y., Facile Control of Defect Site Density and Particle Size of UiO-66 for Enhanced Hydrolysis Rates: Insights into Feasibility of Zr(IV)-Based Metal-Organic Framework (MOF) Catalysts. *Appl. Catal., B* **2019**, *245*, 635-647.
93. Eischens, R.; Pliskin, W.; Francis, S., Infrared Spectra of Chemisorbed Carbon Monoxide. *J. Chem. Phys.* **1954**, *22*, 1786-1787.
94. Beebe, T. P.; Yates, J. T., Competitive Physisorption: The Interaction of CO and N_2 with Silica Surfaces as Studied by IR Spectroscopy. *Surf. Sci.* **1985**, *159*, 369-380.
95. Angell, C. L.; Schaffer, P. C., Infrared Spectroscopic Investigations of Zeolites and Adsorbed Molecules. II. Adsorbed Carbon Monoxide1. *J. Phys. Chem.* **1966**, *70*, 1413-1418.
96. Hadjiivanov, K. I.; Vayssilov, G. N., Characterization of Oxide Surfaces and Zeolites by Carbon Monoxide as an IR Probe Molecule. In *Advances in Catalysis, Vol 47*, Gates, B. C.; Knozinger, H., Eds. Elsevier Academic Press Inc: San Diego, 2002; Vol. 47, pp 307-511.
97. Katoh, M.; Yamazaki, T.; Ozawa, S., IR Spectra for Adsorbed CO on Various Alkali Metal Ion-Exchanged ZSM-5 Zeolites. *Bull. Chem. Soc. Jpn.* **1994**, *67*, 1246-1253.
98. Fohlisch, A.; Nyberg, M.; Bennich, P.; Triguero, L.; Hasselstrom, J.; Karis, O.; Pettersson, L. G. M.; Nilsson, A., The Bonding of CO to Metal Surfaces. *J. Chem. Phys.* **2000**, *112*, 1946-1958.
99. Lamberti, C.; Zecchina, A.; Groppo, E.; Bordiga, S., Probing the Surfaces of Heterogeneous Catalysts by In Situ IR Spectroscopy. *Chem. Soc. Rev.* **2010**, *39*, 4951-5001.

100. Storozhev, P. Y.; Otero Areán, C.; Garrone, E.; Ugliengo, P.; Ermoshin, V. A.; Tsyganenko, A. A., FTIR Spectroscopic and Ab Initio Evidence for an Amphipathic Character of CO Bonding with Silanol Groups. *Chem. Phys. Lett.* **2003**, *374*, 439-445.
101. Hadjiivanov, K., Chapter Two - Identification and Characterization of Surface Hydroxyl Groups by Infrared Spectroscopy. In *Advances in Catalysis*, Jentoft, F. C., Ed. Academic Press: 2014; Vol. 57, pp 99-318.
102. Libuda, J.; Meusel, I.; Hartmann, J.; Freund, H.-J., A Molecular Beam/Surface Spectroscopy Apparatus for the Study of Reactions on Complex Model Catalysts. *Rev. Sci. Instrum.* **2000**, *71*, 4395-4408.
103. Abdelrehim, I. M.; Thornburg, N. A.; Land, D. P., An Ultrahigh Vacuum Surface Analysis Instrument Incorporating a Fourier Transform Mass Spectrometer and a Fourier Transform Infrared Spectrometer. *Rev. Sci. Instrum.* **1997**, *68*, 4572-4582.
104. Basu, P.; Ballinger, T. H.; Yates, J. T., Wide Temperature-Range IR Spectroscopy Cell for Studies of Adsorption and Desorption on High Area Solids. *Rev. Sci. Instrum.* **1988**, *59*, 1321-1327.
105. Wilmsmeyer, A. R.; Gordon, W. O.; Davis, E. D.; Mantooth, B. A.; Lalain, T. A.; Morris, J. R., Multifunctional Ultra-High Vacuum Apparatus for Studies of the Interactions of Chemical Warfare Agents on Complex Surfaces. *Rev. Sci. Instrum.* **2014**, *85*.
106. Garrone, E.; Otero Arean, C., Variable Temperature Infrared Spectroscopy: A Convenient Tool for Studying the Thermodynamics of Weak Solid-Gas Interactions. *Chem. Soc. Rev.* **2005**, *34*, 846-857.
107. Khatib, S. J.; Oyama, S. T., Direct Oxidation of Propylene to Propylene Oxide with Molecular Oxygen: A Review. *Catal. Rev.* **2015**, *57*, 306-344.
108. Kung, M. C.; Davis, R. J.; Kung, H. H., Understanding Au-Catalyzed Low-Temperature CO Oxidation. *J. Phys. Chem. C* **2007**, *111*, 11767-11775.
109. Panayotov, D. A.; Yates, J. T., Jr., Spectroscopic Detection of Hydrogen Atom Spillover from Au Nanoparticles Supported on TiO_2: Use of Conduction Band Electrons. *J. Phys. Chem. C* **2007**, *111*, 2959-2964.
110. Remediakis, I. N.; Lopez, N.; Nørskov, J. K., CO Oxidation on Gold Nanoparticles: Theoretical Studies. *Appl. Catal., A* **2005**, *291*, 13-20.
111. Reinecke, B. N.; Kuhl, K. P.; Ogasawara, H.; Li, L.; Voss, J.; Abild-Pedersen, F.; Nilsson, A.; Jaramillo, T. F., Elucidating the Electronic Structure of Supported Gold Nanoparticles and its Relevance to Catalysis by Means of Hard X-ray Photoelectron Spectroscopy. *Surf. Sci.* **2016**, *650*, 24-33.
112. Nijhuis, T. A.; Sacaliuc, E.; Beale, A. M.; van der Eerden, A. M. J.; Schouten, J. C.; Weckhuysen, B. M., Spectroscopic Evidence for the Adsorption of Propene on Gold Nanoparticles during the Hydro-Epoxidation of Propene. *J. Catal.* **2008**, *258*, 256-264.
113. Mijovilovich, A., Delta-mu XANES Reveals the Electronic Structure of the Adsorption of Propene on Gold Nanoparticles. *RSC Adv.* **2014**, *4*, 12293-12297.
114. Zhang, Q.; Zhao, X.; Yang, J.; Zheng, M.; Fan, W., Theoretical Insights into Propene Epoxidation on Au7/Anatase TiO2–x(001) Catalysts: Effect of the Interface and Reaction Atmosphere. *J. Phys. Chem. C* **2019**, *123*, 3568-3578.
115. Kanungo, S.; Perez Ferrandez, D. M.; Neira d'Angelo, F.; Schouten, J. C.; Nijhuis, T. A., Kinetic Study of Propene Oxide and Water Formation in Hydro-Epoxidation of Propene on Au/Ti–SiO_2 Catalyst. *J. Catal.* **2016**, *338*, 284-294.

116. Baker, T. A.; Xu, B.; Jensen, S. C.; Friend, C. M.; Kaxiras, E., Role of Defects in Propene Adsorption and Reaction on a Partially O-Covered Au(111) Surface. *Catal. Sci. Technol.* **2011**, *1*, 1166-1174.
117. Deng, X.; Min, B. K.; Liu, X.; Friend, C. M., Partial Oxidation of Propene on Oxygen-Covered Au(111). *J. Phys. Chem. B* **2006**, *110*, 15982-15987.
118. Ji, J.; Lu, Z.; Lei, Y.; Turner, C. H., Mechanistic Insights into the Direct Propylene Epoxidation using Au Nanoparticles Dispersed on TiO_2/SiO_2. *Chem. Eng. Sci.* **2018**, *191*, 169-182.
119. Ji, J.; Lu, Z.; Lei, Y.; Turner, C., Theoretical Studies on the Direct Propylene Epoxidation Using Gold-Based Catalysts: A Mini-Review. *Catalysts* **2018**, *8*, 421.
120. Lee, S.; Molina, L. M.; López, M. J.; Alonso, J. A.; Hammer, B.; Lee, B.; Seifert, S.; Winans, R. E.; Elam, J. W., et al., Selective Propene Epoxidation on Immobilized $Au_{6–10}$ Clusters: The Effect of Hydrogen and Water on Activity and Selectivity. *Angew. Chem. Int. Ed.* **2009**, *48*, 1467-1471.
121. Song, W.; Perez Ferrandez, D. M.; van Haandel, L.; Liu, P.; Nijhuis, T. A.; Hensen, E. J. M., Selective Propylene Oxidation to Acrolein by Gold Dispersed on $MgCuCr_2O_4$ Spinel. *ACS Catal.* **2015**, *5*, 1100-1111.
122. Chen, J. Q.; Pidko, E. A.; Ordomsky, V. V.; Verhoeven, T.; Hensen, E. J. M.; Schouten, J. C.; Nijhuis, T. A., How Metallic is Gold in the Direct Epoxidation of Propene: An FTIR Study. *Catal. Sci. Technol.* **2013**, *3*, 3042-3055.
123. Pulido, A.; Boronat, M.; Corma, A., Propene Epoxidation with $H_2/H_2O/O_2$ Mixtures Over Gold Atoms Supported on Defective Graphene: A Theoretical Study. *J. Phys. Chem. C* **2012**, *116*, 19355-19362.
124. Chang, C.-R.; Wang, Y.-G.; Li, J., Theoretical Investigations of the Catalytic Role of Water in Propene Epoxidation on Gold Nanoclusters: A Hydroperoxyl-Mediated Pathway. *Nano Res.* **2011**, *4*, 131-142.
125. Chrétien, S.; Gordon, M. S.; Metiu, H., Binding of Propene on Small Gold Clusters and on Au(111): Simple Rules for Binding Sites and Relative Binding Energies. *J. Chem. Phys.* **2004**, *121*, 3756-3766.
126. Ajo, H. M.; Bondzie, V. A.; Campbell, C. T., Propene Adsorption on Gold Particles on TiO_2(110). *Catal. Lett.* **2002**, *78*, 359-368.
127. Davis, K. A.; Goodman, D. W., Propene Adsorption on Clean and Oxygen-Covered Au(111) and Au(100) Surfaces. *J. Phys. Chem. B* **2000**, *104*, 8557-8562.
128. Green, I. X.; Tang, W. J.; McEntee, M.; Neurock, M.; Yates, J. T., Inhibition at Perimeter Sites of Au/TiO_2 Oxidation Catalyst by Reactant Oxygen. *J. Am. Chem. Soc.* **2012**, *134*, 12717-12723.
129. Ramamoorthy, M.; Vanderbilt, D.; King-Smith, R. D., First-Principles Calculations of the Energetics of Stoichiometric TiO_2 Surfaces. *Phys. Rev. B* **1994**, *49*, 16721-16727.
130. Yang, K.; Huang, K.; He, Z.; Chen, X.; Fu, X.; Dai, W., Promoted Effect of PANI as Electron Transfer Promoter on CO Oxidation over Au/TiO_2. *Appl. Catal., B* **2014**, *158–159*, 250-257.
131. Laursen, S.; Linic, S., Geometric and Electronic Characteristics of Active Sites on TiO_2-Supported Au Nano-Catalysts: Insights from First Principles. *Phys. Chem. Chem. Phys.* **2009**, *11*, 11006-11012.
132. Molina, L. M.; Rasmussen, M. D.; Hammer, B., Adsorption of O_2 and oxidation of CO at Au nanoparticles supported by TiO_2(110). *J. Chem. Phys.* **2004**, *120*, 7673-7680.

133. Kresse, G., Dissociation and Sticking of H_2 on the Ni(111), (100), and (110) Substrate. *Phys. Rev. B* **2000**, *62*, 8295-8305.
134. Kresse, G.; Hafner, J., Ab Initio Molecular Dynamics for Liquid Metals. *Phys. Rev. B* **1993**, *47*, 558-561.
135. Kresse, G.; Hafner, J., Ab Initio Molecular-Dynamics Simulation of the Liquid-Metal-Amorphous-Semiconductor Transition in Germanium. *Phys. Rev. B* **1994**, *49*, 14251-14269.
136. Kresse, G.; Joubert, D., From Ultrasoft Pseudopotentials to the Projector Augmented-Wave Method. *Phys. Rev. B* **1999**, *59*, 1758-1775.
137. Blöchl, P. E., Projector Augmented-Wave Method. *Phys. Rev. B* **1994**, *50*, 17953-17979.
138. Perdew, J. P.; Wang, Y., Accurate and Simple Analytic Representation of the Electron-Gas Correlation Energy. *Phys. Rev. B* **1992**, *45*, 13244-13249.
139. Dudarev, S. L.; Botton, G. A.; Savrasov, S. Y.; Humphreys, C. J.; Sutton, A. P., Electron-Energy-Loss Spectra and the Structural Stability of Nickel Oxide: An LSDA+U Study. *Phys. Rev. B* **1998**, *57*, 1505-1509.
140. Morgan, B. J.; Watson, G. W., A DFT + U Description of Oxygen Vacancies at the TiO_2 Rutile (1 1 0) Surface. *Surf. Sci.* **2007**, *601*, 5034-5041.
141. Monkhorst, H. J.; Pack, J. D., Special points for Brillouin-zone integrations. *Phys. Rev. B* **1976**, *13*, 5188-5192.
142. Lord, R. C.; Venkateswarlu, P., The Infrared Spectra of Propylene and Propylene-d_6. *J. Opt. Soc. Am.* **1953**, *43*, 1079-1085.
143. Sheppard, N.; De La Cruz, C., Vibrational Spectra of Hydrocarbons Adsorbed on Metals: Part I. Introductory Principles, Ethylene, and the Higher Acyclic Alkenes. In *Advances in Catalysis*, D.D. Eley, W. O. H.; Bruce, G., Eds. Academic Press: 1996; Vol. Volume 41, pp 1-112.
144. Kokes, R. J.; Dent, A. L., Hydrogenation and Isomerization over Zinc Oxide. In *Advances in Catalysis*, Eley, D. D.; Pines, H.; Weisz, P. B., Eds. Academic Press: 1972; Vol. 22, pp 1-50.
145. Frank, M.; Baumer, M., From Atoms to Crystallites: Adsorption on Oxide-Supported Metal Particles. *Phys. Chem. Chem. Phys.* **2000**, *2*, 3723-3737.
146. Lee, C.-C.; Chen, H.-T., Adsorption and Reaction of C_2H_4 and O_2 on a Nanosized Gold Cluster: A Computational Study. *J. Phys. Chem. A* **2015**, *119*, 8547-8555.
147. Ruiz, A.; van der Linden, B.; Makkee, M.; Mul, G., Acrylate and Propoxy-Groups: Contributors to Deactivation of Au/TiO_2 in the Epoxidation of Propene. *J. Catal.* **2009**, *266*, 286-290.
148. Boccuzzi, F.; Chiorino, A.; Manzoli, M., FTIR Study of the Electronic Effects of CO Adsorbed on Gold Nanoparticles Supported on Titania. *Surf. Sci.* **2000**, *454-456*, 942-946.
149. Boronat, M.; Concepcion, P.; Corma, A., Unravelling the Nature of Gold Surface Sites by Combining IR Spectroscopy and DFT Calculations. Implications in Catalysis. *J. Phys. Chem. C* **2009**, *113*, 16772-16784.
150. Boronat, M.; Illas, F.; Corma, A., Active Sites for H_2 Adsorption and Activation in Au/TiO_2 and the Role of the Support. *J. Phys. Chem. A* **2009**, *113*, 3750-3757.
151. Boccuzzi, F.; Cerrato, G.; Pinna, F.; Strukul, G., FTIR, UV−Vis, and HRTEM Study of Au/ZrO_2 Catalyst: Reduced Reactivity in the $CO-O_2$ Reaction of Electron-Deficient Gold Sites Present on the Used Samples. *J. Phys. Chem. B* **1998**, *102*, 5733-5736.

152. Mihaylov, M.; Knözinger, H.; Hadjiivanov, K.; Gates, B. C., Characterization of the Oxidation States of Supported Gold Species by IR Spectroscopy of Adsorbed CO. *Chem. Ing. Tech.* **2007**, *79*, 795-806.
153. Besson, M.; Gallezot, P., Selective Oxidation of Alcohols and Aldehydes on Metal Catalysts. *Catal. Today* **2000**, *57*, 127-141.
154. Enthaler, S.; Junge, K.; Beller, M., Sustainable Metal Catalysis with Iron: From Rust to a Rising Star? *Angew. Chem. Int. Ed.* **2008**, *47*, 3317-3321.
155. Kim, J.; Samano, E.; Koel, B. E., Oxygen Adsorption and Oxidation Reactions on Au(211) Surfaces: Exposures using O_2 at High Pressures and Ozone (O_3) in UHV. *Surf. Sci.* **2006**, *600*, 4622-4632.
156. Deng, X.; Min, B. K.; Guloy, A.; Friend, C. M., Enhancement of O_2 Dissociation on Au(111) by Adsorbed Oxygen: Implications for Oxidation Catalysis. *J. Am. Chem. Soc.* **2005**, *127*, 9267-9270.
157. Farnesi Camellone, M.; Zhao, J.; Jin, L.; Wang, Y.; Muhler, M.; Marx, D., Molecular Understanding of Reactivity and Selectivity for Methanol Oxidation at the Au/TiO_2 Interface. *Angew. Chem. Int. Ed.* **2013**, *52*, 5780-5784.
158. Green, I. X.; Tang, W.; Neurock, M.; Yates, J. T., Low-Temperature Catalytic H_2 Oxidation over Au Nanoparticle/TiO_2 Dual Perimeter Sites. *Angew. Chem. Int. Ed.* **2011**, *50*, 10186-10189.
159. Panayotov, D. A.; Burrows, S. P.; Yates, J. T., Jr.; Morris, J. R., Mechanistic Studies of Hydrogen Dissociation and Spillover on Au/TiO_2: IR Spectroscopy of Coadsorbed CO and H-Donated Electrons. *J. Phys. Chem. C* **2011**, *115*, 22400-22408.
160. Fujitani, T.; Nakamura, I.; Akita, T.; Okumura, M.; Haruta, M., Hydrogen Dissociation by Gold Clusters. *Angew. Chem.* **2009**, *121*, 9679-9682.
161. Whittaker, T.; Kumar, K. B. S.; Peterson, C.; Pollock, M. N.; Grabow, L. C.; Chandler, B. D., H_2 Oxidation over Supported Au Nanoparticle Catalysts: Evidence for Heterolytic H_2 Activation at the Metal–Support Interface. *J. Am. Chem. Soc.* **2018**, *140*, 16469-16487.
162. Chen, J.; Halin, S. J. A.; Pidko, E. A.; Verhoeven, M. W. G. M.; Ferrandez, D. M. P.; Hensen, E. J. M.; Schouten, J. C.; Nijhuis, T. A., Enhancement of Catalyst Performance in the Direct Propene Epoxidation: A Study into Gold–Titanium Synergy. *ChemCatChem* **2013**, *5*, 467-478.
163. Bravo-Suárez, J. J.; Bando, K. K.; Lu, J.; Fujitani, T.; Oyama, S. T., Oxidation of Propane to Propylene Oxide on Gold Catalysts. *J. Catal.* **2008**, *255*, 114-126.
164. Kanungo, S.; Su, Y.; Neira d'Angelo, M. F.; Schouten, J. C.; Hensen, E. J. M., Epoxidation of Propene using Au/TiO_2: On the Difference Between H_2 and CO as a Co-Reactant. *Catal. Sci. Technol.* **2017**, *7*, 2252-2261.
165. Lee, W.-S.; Cem Akatay, M.; Stach, E. A.; Ribeiro, F. H.; Nicholas Delgass, W., Gas-Phase Epoxidation of Propylene in the Presence of H_2 and O_2 over Small Gold Ensembles in Uncalcined TS-1. *J. Catal.* **2014**, *313*, 104-112.
166. Lee, W.-S.; Zhang, R.; Akatay, M. C.; Baertsch, C. D.; Stach, E. A.; Ribeiro, F. H.; Delgass, W. N., Differences in Catalytic Sites for CO Oxidation and Propylene Epoxidation on Au Nanoparticles. *ACS Catal.* **2011**, *1*, 1327-1330.
167. Bravo-Suárez, J. J.; Bando, K. K.; Lu, J.; Haruta, M.; Fujitani, T.; Oyama, T., Transient Technique for Identification of True Reaction Intermediates: Hydroperoxide Species in Propylene Epoxidation on Gold/Titanosilicate Catalysts by X-ray Absorption Fine Structure Spectroscopy. *J. Phys. Chem. C* **2008**, *112*, 1115-1123.

168. Lu, J.; Zhang, X.; Bravo-Suárez, J. J.; Tsubota, S.; Gaudet, J.; Oyama, S. T., Kinetics of Propylene Epoxidation using H_2 and O_2 over a Gold/Mesoporous Titanosilicate Catalyst. *Catal. Today* **2007**, *123*, 189-197.
169. Feng, X.; Sheng, N.; Liu, Y.; Chen, X.; Chen, D.; Yang, C.; Zhou, X., Simultaneously Enhanced Stability and Selectivity for Propene Epoxidation with H_2 and O_2 on Au Catalysts Supported on Nano-Crystalline Mesoporous TS-1. *ACS Catal.* **2017**, *7*, 2668-2675.
170. Lu, Z.; Piernavieja-Hermida, M.; Turner, C. H.; Wu, Z.; Lei, Y., Effects of TiO_2 in Low Temperature Propylene Epoxidation Using Gold Catalysts. *J. Phys. Chem. C* **2018**, *122*, 1688-1698.
171. Yao, S.; Xu, L.; Wang, J.; Jing, X.; Odoom-Wubah, T.; Sun, D.; Huang, J.; Li, Q., Activity and Stability of Titanosilicate Supported Au Catalyst for Propylene Epoxidation with H_2 and O_2. *Molecular Catalysis* **2018**, *448*, 144-152.
172. Delannoy, L.; Fajerwerg, K.; Lakshmanan, P.; Potvin, C.; Méthivier, C.; Louis, C., Supported Gold Catalysts for the Decomposition of VOC: Total Oxidation of Propene in Low Concentration as Model Reaction. *Appl. Catal., B* **2010**, *94*, 117-124.
173. Leerat, J.; Osuwan, S.; Gulari, E., Lean-burn NO_x Reduction by Propene over Gold Supported on Alumina Catalysts Derived from the Sol–Gel Method. *Catal. Lett.* **2011**, *141*, 62-67.
174. Wang, L.; Xiong, G.; Su, J.; Li, P.; Guo, H., In Situ UV Raman Spectroscopic Study on the Reaction Intermediates for Propylene Epoxidation on TS-1. *J. Phys. Chem. C* **2012**, *116*, 9122-9131.
175. Sivadinarayana, C.; Choudhary, T. V.; Daemen, L. L.; Eckert, J.; Goodman, D. W., The Nature of the Surface Species Formed on Au/TiO_2 during the Reaction of H_2 and O_2: An Inelastic Neutron Scattering Study. *J. Am. Chem. Soc.* **2004**, *126*, 38-39.
176. Henkelman, G.; Uberuaga, B. P.; Jónsson, H., A Climbing Image Nudged Elastic Band Method for Finding Saddle Points and Minimum Energy Paths. *J. Chem. Phys.* **2000**, *113*, 9901-9904.
177. Henkelman, G.; Jónsson, H., Improved Tangent Estimate in the Nudged Elastic Band Method for Finding Minimum Energy Paths and Saddle Points. *J. Chem. Phys.* **2000**, *113*, 9978-9985.
178. Henkelman, G.; Jónsson, H., A Dimer Method for Finding Saddle Points on High Dimensional Potential Surfaces Using only First Derivatives. *J. Chem. Phys.* **1999**, *111*, 7010-7022.
179. Panayotov, D. A.; Yates, J. T., n-Type Doping of TiO_2 with Atomic Hydrogen-Observation of the Production of Conduction Band Electrons by Infrared Spectroscopy. *Chem. Phys. Lett.* **2007**, *436*, 204-208.
180. Powell, C. D.; Daigh, A. W.; Pollock, M. N.; Chandler, B. D.; Pursell, C. J., CO Adsorption on Au/TiO_2 Catalysts: Observations, Quantification, and Explanation of a Broad-Band Infrared Signal. *J. Phys. Chem. C* **2017**, *121*, 24541-24547.
181. Panayotov, D. A.; Morris, J. R., Catalytic Degradation of a Chemical Warfare Agent Simulant: Reaction Mechanisms on TiO_2-Supported Au Nanoparticles. *J. Phys. Chem. C* **2008**, *112*, 7496-7502.
182. Sun, K.; Kohyama, M.; Tanaka, S.; Takeda, S., A Study on the Mechanism for H2 Dissociation on Au/TiO2 Catalysts. *J. Phys. Chem. C* **2014**, *118*, 1611-1617.

183. Moskaleva, L. V., Theoretical Mechanistic Insights into Propylene Epoxidation on Au-Based Catalysts: Surface O Versus OOH as Oxidizing Agents. *Catal. Today* **2016**, *278*, 45-55.
184. Chen, J. Q.; Halin, S. J. A.; Perez Ferrandez, D. M.; Schouten, J. C.; Nijhuis, T. A., Switching Off Propene Hydrogenation in the Direct Epoxidation of Propene over Gold-Titania Catalysts. *J. Catal.* **2012**, *285*, 324-327.
185. Pichat, P.; Herrmann, J. M.; Disdier, J.; Mozzanega, M. N., Photocatalytic Oxidation of Propene over Various Oxides at 320 K. Selectivity. *J. Phys. Chem.* **1979**, *83*, 3122-3126.
186. Murata, C.; Yoshida, H.; Hattori, T., Visible Light-Induced Photoepoxidation of Propene by Molecular Oxygen over Chromia-Silica Catalysts. *Chem. Commun.* **2001**, 2412-2413.
187. Yoshida, H.; Tanaka, T.; Yamamoto, M.; Funabiki, T.; Yoshida, S., Photooxidation of Propene by O_2 over Silica and Mg-Loaded Silica. *Chem. Commun.* **1996**, 2125-2126.
188. Yoshida, H.; Tanaka, T.; Yamamoto, M.; Yoshida, T.; Funabiki, T.; Yoshida, S., Epoxidation of Propene by Gaseous Oxygen over Silica and Mg-Loaded Silica under Photoirradiation. *J. Catal.* **1997**, *171*, 351-357.
189. Yoshida, H.; Murata, C.; Hattori, T., Photooxidation of Propene to Propene Oxide by Molecular Oxygen over Zinc Oxide Dispersed on Silica. *Chem. Lett.* **1999**, *28*, 901-902.
190. Yoshida, H.; Shimizu, T.; Murata, C.; Hattori, T., Highly Dispersed Zinc Oxide Species on Silica as Active Sites for Photoepoxidation of Propene by Molecular Oxygen. *J. Catal.* **2003**, *220*, 226-232.
191. Amano, F.; Tanaka, T.; Funabiki, T., Steady-State Photocatalytic Epoxidation of Propene by O_2 over V_2O_5/SiO_2 Photocatalysts. *Langmuir* **2004**, *20*, 4236-4240.
192. Amano, F.; Tanaka, T., Modification of Photocatalytic Center for Photo-Epoxidation of Propylene by Rubidium Ion Addition to V_2O_5/SiO_2. *Catal. Commun.* **2005**, *6*, 269-273.
193. Yoshida, H.; Murata, C.; Hattori, T., Screening Study of Silica-Supported Catalysts for Photoepoxidation of Propene by Molecular Oxygen. *J. Catal.* **2000**, *194*, 364-372.
194. Yoshida, H.; Murata, C.; Hattori, T., Photocatalytic Epoxidation of Propene by Molecular Oxygen over Highly Dispersed Titanium Oxide Species on Silica. *Chem. Commun.* **1999**, 1551-1552.
195. Kanai, H.; Shono, M.; Hamada, K.; Imamura, S., Photooxidation of Propylene with Oxygen over TiO_2–SiO_2- Composite Oxides Prepared by Rapid Hydrolysis. *J. Mol. Catal. A: Chem.* **2001**, *172*, 25-31.
196. Yoshida, H., Silica-Based Quantum Photocatalysts for Selective Reactions. *Curr. Opin. Solid State Mater. Sci.* **2003**, *7*, 435-442.
197. Amano, F.; Yamaguchi, T.; Tanaka, T., Photocatalytic Oxidation of Propylene with Molecular Oxygen over Highly Dispersed Titanium, Vanadium, and Chromium Oxides on Silica. *J. Phys. Chem. B* **2006**, *110*, 281-288.
198. Nguyen, V.-H.; Chan, H.-Y.; Wu, J. C. S.; Bai, H., Direct Gas-Phase Photocatalytic Epoxidation of Propylene with Molecular Oxygen by Photocatalysts. *Chem. Eng. J.* **2012**, *179*, 285-294.
199. Nguyen, V.-H.; Wu, J. C. S.; Bai, H., Temperature Effect on the Photo-Epoxidation of Propylene over V–Ti/MCM-41 Photocatalyst. *Catal. Commun.* **2013**, *33*, 57-60.
200. Nguyen, V.-H.; Lin, S. D.; Wu, J. C.-S.; Bai, H., Artificial Sunlight and Ultraviolet Light Induced Photo-Epoxidation of Propylene over V-Ti/MCM-41 Photocatalyst. *Beilstein Journal of Nanotechnology* **2014**, *5*, 566-576.

201. Nguyen, V.-H.; Lin, S. D.; Wu, J. C.-S., Synergetic Photo-Epoxidation of Propylene over V-Ti /MCM-41 Mesoporous Photocatalysts. *J. Catal.* **2015**, *331*, 217-227.
202. Rico-Santacruz, M.; Serrano, E.; Marcì, G.; García-López, E. I.; García-Martínez, J., Titania–Silica Materials for Enhanced Photocatalysis. *Chem. Eur. J.* **2015**, *21*, 18338-18344.
203. Murata, C.; Yoshida, H.; Kumagai, J.; Hattori, T., Active Sites and Active Oxygen Species for Photocatalytic Epoxidation of Propene by Molecular Oxygen over TiO_2−SiO_2 Binary Oxides. *J. Phys. Chem. B* **2003**, *107*, 4364-4373.
204. Murata, C.; Hattori, T.; Yoshida, H., Electrophilic Property of O_3^- Photoformed on Isolated Ti Species in Silica Promoting Alkene Epoxidation. *J. Catal.* **2005**, *231*, 292-299.
205. Carter, E. A.; Goddard, W. A., The Surface Atomic Oxyradical Mechanism for Ag-Catalyzed Olefin Epoxidation. *J. Catal.* **1988**, *112*, 80-92.
206. Kim, S.; Wang, X.; Buda, C.; Neurock, M.; Koper, O. B.; Yates, J. T., IR Spectroscopic Measurement of Diffusion Kinetics of Chemisorbed Pyridine through Nanocrystalline MgO Particles. The Involvement of Surface Defect Sites in Slow Diffusion. *J. Phys. Chem. C* **2009**, *113*, 2219-2227.
207. Kim, S.; Byl, O.; Liu, J.-C.; Johnson, J. K.; Yates, J. T., Spectroscopic Measurement of Diffusion Kinetics through Subnanometer and Larger Al_2O_3 Particles by a New Method: The Interaction of 2-Chloroethylethyl Sulfide with γ-Al_2O_3. *J. Phys. Chem. B* **2006**, *110*, 9204-9210.
208. Green, I. X.; Buda, C.; Zhang, Z.; Neurock, M.; Yates, J. T., IR Spectroscopic Measurement of Diffusion Kinetics of Chemisorbed Pyridine through TiO_2 Particles. *J. Phys. Chem. C* **2010**, *114*, 16649-16659.
209. Sharp, C. H.; Abelard, J.; Plonka, A. M.; Guo, W.; Hill, C. L.; Morris, J. R., Alkane–OH Hydrogen Bond Formation and Diffusion Energetics of n-Butane within UiO-66. *J. Phys. Chem. C* **2017**, *121*, 8902-8906.
210. Grissom, T. G.; Sharp, C. H.; Usov, P. M.; Troya, D.; Morris, A. J.; Morris, J. R., Benzene, Toluene, and Xylene Transport through UiO-66: Diffusion Rates, Energetics, and the Role of Hydrogen Bonding. *J. Phys. Chem. C* **2018**, *122*, 16060-16069.
211. Jensen, H.; Soloviev, A.; Li, Z.; Søgaard, E. G., XPS and FTIR Investigation of the Surface Properties of Different Prepared Titania Nano-Powders. *Appl. Surf. Sci.* **2005**, *246*, 239-249.
212. Biesinger, M. C.; Lau, L. W. M.; Gerson, A. R.; Smart, R. S. C., Resolving Surface Chemical States in XPS Analysis of First Row Transition Metals, Oxides and Hydroxides: Sc, Ti, V, Cu and Zn. *Appl. Surf. Sci.* **2010**, *257*, 887-898.
213. Hadjiivanov, K.; Lavalley, J.-C., FT–IR Spectroscopic Study of CO Adsorption on Monoclinic Zirconia of Different Hydroxylation Degrees. *Catal. Commun.* **2001**, *2*, 129-133.
214. Hadjiivanov, K.; Reddy, B. M.; Knözinger, H., FTIR study of low-temperature adsorption and co-adsorption of 12CO and 13CO on a TiO2–SiO2 mixed oxide. *Appl. Catal., A* **1999**, *188*, 355-360.
215. Abelard, J.; Wilmsmeyer, A. R.; Edwards, A. C.; Gordon, W. O.; Durke, E. M.; Karwacki, C. J.; Troya, D.; Morris, J. R., Adsorption of 2-Chloroethyl Ethyl Sulfide on Silica: Binding Mechanism and Energy of a Bifunctional Hydrogen-Bond Acceptor at the Gas–Surface Interface. *J. Phys. Chem. C* **2015**, *119*, 365-372.

216. Abelard, J.; Wilmsmeyer, A. R.; Edwards, A. C.; Gordon, W. O.; Durke, E. M.; Karwacki, C. J.; Troya, D.; Morris, J. R., Adsorption of Substituted Benzene Derivatives on Silica: Effects of Electron Withdrawing and Donating Groups. *J. Phys. Chem. C* **2016**, *120*, 13024-13031.
217. Ulrich, V.; Froese, C.; Moroz, B.; Pyrjaev, P.; Gerasimov, E.; Sinev, I.; Cuenya, B. R.; Muhler, M.; Bukhtiyarov, V., et al., Three-Way Catalysis with Supported Gold Catalysts: Poisoning Effects of Hydrocarbons. *Appl. Catal., B* **2018**, *237*, 1021-1032.
218. Jang, Y. J.; Kim, K.; Tsay, O. G.; Atwood, D. A.; Churchill, D. G., Update 1 of: Destruction and Detection of Chemical Warfare Agents. *Chem. Rev.* **2015**, *115*, PR1-PR76.
219. John, H.; van der Schans, M. J.; Koller, M.; Spruit, H. E. T.; Worek, F.; Thiermann, H.; Noort, D., Fatal Sarin Poisoning in Syria 2013: Forensic Verification within an International Laboratory Network. *Forensic Toxicology* **2018**, *36*, 61-71.
220. Stone, R., U.K. Attack Puts Nerve Agent in the Spotlight. *Science* **2018**, *359*, 1314.
221. Panayotov, D. A.; DeSario, P. A.; Pietron, J. J.; Brintlinger, T. H.; Szymczak, L. C.; Rolison, D. R.; Morris, J. R., Ultraviolet and Visible Photochemistry of Methanol at 3D Mesoporous Networks: TiO_2 and Au-TiO_2. *J. Phys. Chem. C* **2013**, *117*, 15035-15049.
222. Janssens, T. V. W.; Clausen, B. S.; Hvolbæk, B.; Falsig, H.; Christensen, C. H.; Bligaard, T.; Nørskov, J. K., Insights into the Reactivity of Supported Au Nanoparticles: Combining Theory and Experiments. *Top. Catal.* **2007**, *44*, 15.
223. Morrison, R. W. *NBC Filter Performance: ECBC-TR-135* U.S. Army Soldier and Biological Chemical Command: Aberdeen Proving Ground, MD: 2001.
224. Boccuzzi, F.; Chiorino, A.; Martra, G.; Gargano, M.; Ravasio, N.; Carrozzini, B., Preparation, Characterization, and Activity of Cu/TiO_2 Catalysts. I. Influence of the Preparation Method on the Dispersion of Copper in Cu/TiO_2. *J. Catal.* **1997**, *165*, 129-139.
225. Pedersen, D. B.; Wang, S.; Liang, S. H., Charge-Transfer-Driven Diffusion Processes in Cu@Cu-Oxide Core−Shell Nanoparticles: Oxidation of 3.0 ± 0.3 nm Diameter Copper Nanoparticles. *J. Phys. Chem. C* **2008**, *112*, 8819-8826.
226. Jernigan, G. G.; Somorjai, G. A., Carbon Monoxide Oxidation over Three Different Oxidation States of Copper: Metallic Copper, Copper (I) Oxide, and Copper (II) Oxide - A Surface Science and Kinetic Study. *J. Catal.* **1994**, *147*, 567-577.
227. Kaatz, F. H.; Harris, V. G.; Kurihara, L.; Rolison, D. R.; Edelstein, A. S., Slowing the Oxidation of Cu in Cu–Co Nanocrystals by Co Surface Passivation. *Appl. Phys. Lett.* **1995**, *67*, 3807-3809.
228. Marimuthu, A.; Zhang, J. W.; Linic, S., Tuning Selectivity in Propylene Epoxidation by Plasmon Mediated Photo-Switching of Cu Oxidation State. *Science* **2013**, *339*, 1590-1593.
229. Trotochaud, L.; Tsyshevsky, R.; Holdren, S.; Fears, K.; Head, A. R.; Yu, Y.; Karslıoğlu, O.; Pletincx, S.; Eichhorn, B., et al., Spectroscopic and Computational Investigation of Room-Temperature Decomposition of a Chemical Warfare Agent Simulant on Polycrystalline Cupric Oxide. *Chem. Mater.* **2017**, *29*, 7483-7496.
230. Florent, M.; Giannakoudakis, D. A.; Wallace, R.; Bandosz, T. J., Carbon Textiles Modified with Copper-Based Reactive Adsorbents as Efficient Media for Detoxification of Chemical Warfare Agents. *ACS Applied Materials & Interfaces* **2017**, *9*, 26965-26973.
231. Dagan, G.; Tomkiewicz, M., Titanium Dioxide Aerogels for Photocatalytic Decontamination of Aquatic Environments. *J. Phys. Chem.* **1993**, *97*, 12651-12655.
232. Wu, G.; Guan, N.; Li, L., Low Temperature CO Oxidation on Cu-Cu_2O/TiO_2 Catalyst Prepared by Photodeposition. *Catal. Sci. Technol.* **2011**, *1*, 601-608.

233. Kozlov, D. V.; Paukshtis, E. A.; Savinov, E. N., The comparative studies of titanium dioxide in gas-phase ethanol photocatalytic oxidation by the FTIR in situ method. *Appl. Catal., B* **2000**, *24*, L7-L12.
234. Busca, G.; Saussey, H.; Saur, O.; Lavalley, J. C.; Lorenzelli, V., FT-IR characterization of the surface acidity of different titanium dioxide anatase preparations. *Applied Catalysis* **1985**, *14*, 245-260.
235. Trotochaud, L.; Head, A. R.; Pletincx, S.; Karslıoğlu, O.; Yu, Y.; Waldner, A.; Kyhl, L.; Hauffman, T.; Terryn, H., et al., Water Adsorption and Dissociation on Polycrystalline Copper Oxides: Effects of Environmental Contamination and Experimental Protocol. *J. Phys. Chem. B* **2018**, *122*, 1000-1008.
236. Holdren, S.; Tsyshevsky, R.; Fears, K.; Owrutsky, J.; Wu, T.; Wang, X.; Eichhorn, B. W.; Kuklja, M. M.; Zachariah, M. R., Adsorption and Destruction of the G-Series Nerve Agent Simulant Dimethyl Methylphosphonate on Zinc Oxide. *ACS Catal.* **2019**, *9*, 902-911.
237. Liu, H.; Kozlov, A. I.; Kozlova, A. P.; Shido, T.; Asakura, K.; Iwasawa, Y., Active Oxygen Species and Mechanism for Low-Temperature CO Oxidation Reaction on a TiO_2-Supported Au Catalyst Prepared from $Au(PPh_3)(NO_3)$ and As-Precipitated Titanium Hydroxide. *J. Catal.* **1999**, *185*, 252-264.
238. Boccuzzi, F.; Chiorino, A., FTIR Study of Carbon Monoxide Oxidation and Scrambling at Room Temperature over Copper Supported on ZnO and TiO_2. 1. *J. Phys. Chem.* **1996**, *100*, 3617-3624.
239. Dahlang, T.; Sven, T., Electronic and Optical Properties of Cu, CuO and Cu_2O Studied by Electron Spectroscopy. *J. Phys.: Condens. Matter* **2012**, *24*, 175002.
240. Deshmane, V. G.; Owen, S. L.; Abrokwah, R. Y.; Kuila, D., Mesoporous Nanocrystalline TiO_2 Supported Metal (Cu, Co, Ni, Pd, Zn, and Sn) Catalysts: Effect of Metal-Support Interactions on Steam Reforming of Methanol. *J. Mol. Catal. A: Chem.* **2015**, *408*, 202-213.
241. Araiza, D. G.; Gómez-Cortés, A.; Díaz, G., Partial Oxidation of Methanol Over Copper Supported on Nanoshaped Ceria for Hydrogen Production. *Catal. Today* **2017**, *282*, 185-194.
242. Alejo, L.; Lago, R.; Peña, M. A.; Fierro, J. L. G., Partial Oxidation of Methanol to Produce Hydrogen over Cu-Zn-Based Catalysts. *Appl. Catal., A* **1997**, *162*, 281-297.
243. Panayotov, D. A.; Burrows, S. P.; Morris, J. R., Photooxidation Mechanism of Methanol on Rutile TiO_2 Nanoparticles. *J. Phys. Chem. C* **2012**, *116*, 6623-6635.
244. Panayotov, D. A.; Burrows, S.; Mihaylov, M.; Hadjiivanov, K.; Tissue, B. M.; Morris, J. R., Effect of Methanol on the Lewis Acidity of Rutile TiO_2 Nanoparticles Probed through Vibrational Spectroscopy of Coadsorbed CO. *Langmuir* **2010**, *26*, 8106-8112.
245. McEntee, M.; Tang, W. J.; Neurock, M.; Yates, J. T., Selective Catalytic Oxidative-Dehydrogenation of Carboxylic Acids-Acrylate and Crotonate Formation at the Au/TiO_2 Interface. *J. Am. Chem. Soc.* **2014**, *136*, 5116-5120.
246. Lee, I.; Zaera, F., Catalytic Oxidation of Carbon Monoxide at Cryogenic Temperatures. *J. Catal.* **2014**, *319*, 155-162.
247. Zaera, F., Gold-Titania Catalysts for Low-Temperature Oxidation and Water Splitting. *Top. Catal.* **2018**, *61*, 336-347.
248. Green, I. X.; Yates, J. T., Vibrational Spectroscopic Observation of Weakly Bound Adsorbed Molecular Oxygen on Powdered Titanium Dioxide. *J. Phys. Chem. C* **2010**, *114*, 11924-11930.

249. Fang, Z.; Bueken, B.; De Vos, D. E.; Fischer, R. A., Defect-Engineered Metal–Organic Frameworks. *Angew. Chem. Int. Ed.* **2015**, *54*, 7234-7254.
250. Rimoldi, M.; Howarth, A. J.; DeStefano, M. R.; Lin, L.; Goswami, S.; Li, P.; Hupp, J. T.; Farha, O. K., Catalytic Zirconium/Hafnium-Based Metal–Organic Frameworks. *ACS Catal.* **2017**, *7*, 997-1014.
251. Vermoortele, F.; Ameloot, R.; Vimont, A.; Serre, C.; De Vos, D., An Amino-Modified Zr-Terephthalate Metal-Organic Framework as an Acid-Base Catalyst for Cross-Aldol Condensation. *Chem. Commun.* **2011**, *47*, 1521-1523.
252. Liu, Y.; Klet, R. C.; Hupp, J. T.; Farha, O., Probing the Correlations between the Defects in Metal-Organic Frameworks and Their Catalytic Activity by an Epoxide Ring-Opening Reaction. *Chem. Commun.* **2016**, *52*, 7806-7809.
253. Taylor, J. M.; Dekura, S.; Ikeda, R.; Kitagawa, H., Defect Control To Enhance Proton Conductivity in a Metal–Organic Framework. *Chem. Mater.* **2015**, *27*, 2286-2289.
254. Ardila-Suarez, C.; Perez-Beltran, S.; Ramirez-Caballero, G. E.; Balbuena, P. B., Enhanced Acidity of Defective MOF-808: Effects of the Activation Process and Missing Linker Defects. *Catal. Sci. Technol.* **2018**, *8*, 847-857.
255. Sumida, K.; Rogow, D. L.; Mason, J. A.; McDonald, T. M.; Bloch, E. D.; Herm, Z. R.; Bae, T.-H.; Long, J. R., Carbon Dioxide Capture in Metal–Organic Frameworks. *Chem. Rev.* **2012**, *112*, 724-781.
256. Cohen, S. M., Postsynthetic Methods for the Functionalization of Metal–Organic Frameworks. *Chem. Rev.* **2012**, *112*, 970-1000.
257. Evans, A.; Luebke, R.; Petit, C., The Use of Metal–Organic Frameworks for CO Purification. *J. Mater. Chem. A* **2018**, *6*, 10570-10594.
258. Campbell, C.; Gomes, J. R. B.; Fischer, M.; Jorge, M., New Model for Predicting Adsorption of Polar Molecules in Metal–Organic Frameworks with Unsaturated Metal Sites. *J. Phys. Chem. Lett.* **2018**, *9*, 3544-3553.
259. Andonova, S.; Ivanova, E.; Yang, J.; Hadjiivanov, K., Adsorption Forms of CO_2 on MIL-53(Al) and MIL-53(Al)–OHx As Revealed by FTIR Spectroscopy. *J. Phys. Chem. C* **2017**, *121*, 18665-18673.
260. Tan, K.; Zuluaga, S.; Fuentes, E.; Mattson, E. C.; Veyan, J.-F.; Wang, H.; Li, J.; Thonhauser, T.; Chabal, Y. J., Trapping Gases in Metal-Organic Frameworks with a Selective Surface Molecular Barrier Layer. *Nature Communication* **2016**, *7*, 13871.
261. Tan, K.; Jensen, S.; Zuluaga, S.; Chapman, E. K.; Wang, H.; Rahman, R.; Cure, J.; Kim, T.-H.; Li, J., et al., Role of Hydrogen Bonding on Transport of Coadsorbed Gases in Metal–Organic Frameworks Materials. *J. Am. Chem. Soc.* **2018**, *140*, 856-859.
262. Zhang, W.; Ma, Y.; Santos-López, I. A.; Lownsbury, J. M.; Yu, H.; Liu, W.-G.; Truhlar, D. G.; Campbell, C. T.; Vilches, O. E., Energetics of van der Waals Adsorption on the Metal–Organic Framework NU-1000 with Zr_6-oxo, Hydroxo, and Aqua Nodes. *J. Am. Chem. Soc.* **2018**, *140*, 328-338.
263. Stassen, I.; Bueken, B.; Reinsch, H.; Oudenhoven, J. F. M.; Wouters, D.; Hajek, J.; Van Speybroeck, V.; Stock, N.; Vereecken, P. M., et al., Towards Metal-Organic Framework Based Field Effect Chemical Sensors: UiO-66-NH_2 for Nerve Agent Detection. *Chem. Sci.* **2016**, *7*, 5827-5832.
264. Troya, D., Reaction Mechanism of Nerve-Agent Decomposition with Zr-Based Metal Organic Frameworks. *J. Phys. Chem. C* **2016**, *120*, 29312-29323.

265. López-Maya, E.; Montoro, C.; Rodríguez-Albelo, L. M.; Aznar Cervantes, S. D.; Lozano-Pérez, A. A.; Cenís, J. L.; Barea, E.; Navarro, J. A. R., Textile/Metal–Organic-Framework Composites as Self-Detoxifying Filters for Chemical-Warfare Agents. *Angew. Chem. Int. Ed.* **2015**, *54*, 6790-6794.
266. Shearer, G. C.; Chavan, S.; Bordiga, S.; Svelle, S.; Olsbye, U.; Lillerud, K. P., Defect Engineering: Tuning the Porosity and Composition of the Metal–Organic Framework UiO-66 via Modulated Synthesis. *Chem. Mater.* **2016**, *28*, 3749-3761.
267. Vermoortele, F.; Bueken, B.; Le Bars, G.; Van de Voorde, B.; Vandichel, M.; Houthoofd, K.; Vimont, A.; Daturi, M.; Waroquier, M., et al., Synthesis Modulation as a Tool to Increase the Catalytic Activity of Metal–Organic Frameworks: The Unique Case of UiO-66(Zr). *J. Am. Chem. Soc.* **2013**, *135*, 11465-11468.
268. Wu, H.; Chua, Y. S.; Krungleviciute, V.; Tyagi, M.; Chen, P.; Yildirim, T.; Zhou, W., Unusual and Highly Tunable Missing-Linker Defects in Zirconium Metal–Organic Framework UiO-66 and Their Important Effects on Gas Adsorption. *J. Am. Chem. Soc.* **2013**, *135*, 10525-10532.
269. Peterson, G. W.; DeCoste, J. B.; Glover, T. G.; Huang, Y.; Jasuja, H.; Walton, K. S., Effects of Pelletization Pressure on the Physical and Chemical Properties of the Metal–Organic Frameworks $Cu_3(BTC)_2$ and UiO-66. *Microporous Mesoporous Mater.* **2013**, *179*, 48-53.
270. Valenzano, L.; Civalleri, B.; Chavan, S.; Bordiga, S.; Nilsen, M. H.; Jakobsen, S.; Lillerud, K. P.; Lamberti, C., Disclosing the Complex Structure of UiO-66 Metal Organic Framework: A Synergic Combination of Experiment and Theory. *Chem. Mater.* **2011**, *23*, 1700-1718.
271. Cliffe, M. J.; Wan, W.; Zou, X.; Chater, P. A.; Kleppe, A. K.; Tucker, M. G.; Wilhelm, H.; Funnell, N. P.; Coudert, F.-X., et al., Correlated Defect Nanoregions in a Metal–Organic Framework. *Nature Communications* **2014**, *5*, 4176.
272. DeStefano, M. R.; Islamoglu, T.; Garibay, S. J.; Hupp, J. T.; Farha, O. K., Room-Temperature Synthesis of UiO-66 and Thermal Modulation of Densities of Defect Sites. *Chem. Mater.* **2017**, *29*, 1357-1361.
273. Shearer, G. C.; Chavan, S.; Ethiraj, J.; Vitillo, J. G.; Svelle, S.; Olsbye, U.; Lamberti, C.; Bordiga, S.; Lillerud, K. P., Tuned to Perfection: Ironing Out the Defects in Metal–Organic Framework UiO-66. *Chem. Mater.* **2014**, *26*, 4068-4071.
274. Reed, D. A.; Xiao, D. J.; Gonzalez, M. I.; Darago, L. E.; Herm, Z. R.; Grandjean, F.; Long, J. R., Reversible CO Scavenging via Adsorbate-Dependent Spin State Transitions in an Iron(II)–Triazolate Metal–Organic Framework. *J. Am. Chem. Soc.* **2016**, *138*, 5594-5602.
275. Drenchev, N.; Mihaylov, M.; Dietzel, P. D. C.; Albinati, A.; Georgiev, P. A.; Hadjiivanov, K., Low-Temperature Adsorption of H_2 and D_2 on Dehydrated and Water Precovered CPO-27-Ni. *J. Phys. Chem. C* **2016**, *120*, 23083-23092.
276. Wiersum, A. D.; Soubeyrand-Lenoir, E.; Yang, Q.; Moulin, B.; Guillerm, V.; Yahia, M. B.; Bourrelly, S.; Vimont, A.; Miller, S., et al., An Evaluation of UiO-66 for Gas-Based Applications. *Chemistry – An Asian Journal* **2011**, *6*, 3270-3280.
277. Bordiga, S.; Regli, L.; Bonino, F.; Groppo, E.; Lamberti, C.; Xiao, B.; Wheatley, P. S.; Morris, R. E.; Zecchina, A., Adsorption Properties of HKUST-1 Toward Hydrogen and Other Small Molecules Monitored by IR. *Phys. Chem. Chem. Phys.* **2007**, *9*, 2676-2685.
278. Sato, H.; Kosaka, W.; Matsuda, R.; Hori, A.; Hijikata, Y.; Belosludov, R. V.; Sakaki, S.; Takata, M.; Kitagawa, S., Self-Accelerating CO Sorption in a Soft Nanoporous Crystal. *Science* **2014**, *343*, 167.

279. Kandiah, M.; Nilsen, M. H.; Usseglio, S.; Jakobsen, S.; Olsbye, U.; Tilset, M.; Larabi, C.; Quadrelli, E. A.; Bonino, F., et al., Synthesis and Stability of Tagged UiO-66 Zr-MOFs. *Chem. Mater.* **2010**, *22*, 6632-6640.
280. Mondloch, J. E.; Bury, W.; Fairen-Jimenez, D.; Kwon, S.; DeMarco, E. J.; Weston, M. H.; Sarjeant, A. A.; Nguyen, S. T.; Stair, P. C., et al., Vapor-Phase Metalation by Atomic Layer Deposition in a Metal–Organic Framework. *J. Am. Chem. Soc.* **2013**, *135*, 10294-10297.
281. Driscoll, D. M.; Troya, D.; Usov, P. M.; Maynes, A. J.; Morris, A. J.; Morris, J. R., Characterization of Undercoordinated Zr Defect Sites in UiO-66 with Vibrational Spectroscopy of Adsorbed CO. *J. Phys. Chem. C* **2018**, *122*, 14582-14589.
282. Zhao, Y.; Truhlar, D. G., A New Local Density Functional for Main-Group Thermochemistry, Transition Metal Bonding, Thermochemical Kinetics, and Noncovalent Interactions. *J. Chem. Phys.* **2006**, *125*, 194101.
283. Zhao, Y.; Truhlar, D. G., The M06 Suite of Density Functionals for Main Group Thermochemistry, Thermochemical Kinetics, Noncovalent Interactions, Excited States, and Transition Elements: Two New Functionals and Systematic Testing of Four M06-Class Functionals and 12 Other Functionals. *Theor. Chem. Acc.* **2008**, *120*, 215-241.
284. Yates, J. T., Chemisorption on Surfaces — An Historical Look at a Representative Adsorbate: Carbon Monoxide. *Surf. Sci.* **1994**, *299-300*, 731-741.
285. Dumas, P.; Tobin, R. G.; Richards, P. L., Study of Adsorption States and Interactions of CO on Evaporated Noble Metal Surfaces by Infrared Absorption Spectroscopy: II. Gold and Copper. *Surf. Sci.* **1986**, *171*, 579-599.
286. Trickett, C. A.; Gagnon, K. J.; Lee, S.; Gándara, F.; Bürgi, H.-B.; Yaghi, O. M., Definitive Molecular Level Characterization of Defects in UiO-66 Crystals. *Angew. Chem. Int. Ed.* **2015**, *54*, 11162-11167.
287. Delgado, M. R.; de Yuso, A. M.; Bulánek, R.; Arean, C. O., Infrared Spectroscopic and Thermodynamic Assessment of Extraframework Cationic Adsorption Sites in the Zeolite K-L by using CO as Probe Molecule. *Chem. Phys. Lett.* **2015**, *639*, 195-198.
288. Otero Areán, C.; Tsyganenko, A. A.; Escalona Platero, E.; Garrone, E.; Zecchina, A., Two Coordination Modes of CO in Zeolites: A Temperature-Dependent Equilibrium. *Angew. Chem. Int. Ed.* **1998**, *37*, 3161-3163.
289. Jiang, J.; Yaghi, O. M., Brønsted Acidity in Metal–Organic Frameworks. *Chem. Rev.* **2015**, *115*, 6966-6997.
290. Manoilova, O. V.; Peñarroya Mentruit, M.; Turnes Palomino, G.; Tsyganenko, A. A.; Otero Areán, C., Variable-Temperature Infrared Spectrometry of Carbon Monoxide Adsorbed on the Zeolite K-ZSM-5. *Vib. Spectrosc* **2001**, *26*, 107-111.
291. Ravon, U.; Chaplais, G.; Chizallet, C.; Seyyedi , B.; Bonino , F.; Bordiga , S.; Bats, N.; Farrusseng, D., Investigation of Acid Centers in MIL-53(Al, Ga) for Brønsted-Type Catalysis: In Situ FTIR and Ab Initio Molecular Modeling. *ChemCatChem* **2010**, *2*, 1235-1238.
292. Otero Areán, C.; Manoilova, Olga V.; Tsyganenko, Alexey A.; Turnes Palomino, G.; Peñarroya Mentruit, M.; Geobaldo, F.; Garrone, E., Thermodynamics of Hydrogen Bonding between CO and the Supercage Brønsted Acid Sites of the H-Y Zeolite − Studies from Variable Temperature IR Spectrometry. *Eur. J. Inorg. Chem.* **2001**, *2001*, 1739-1743.
293. Driscoll, D. M.; Troya, D.; Usov, P. M.; Maynes, A. J.; Morris, A. J.; Morris, J. R., Geometry and Energetics of CO Adsorption on Hydroxylated UiO-66. *Phys. Chem. Chem. Phys.* **2019**, *21*, 5078-5085.

294. Hair, M. L.; Hertl, W., Acidity of Surface Hydroxyl Groups. *J. Phys. Chem.* **1970**, *74*, 91-94.
295. Evgenii, A. P.; Yurchenko, E. N., Study of the Acid–Base Properties of Heterogeneous Catalysts by Infrared Spectroscopy. *Russian Chemical Reviews* **1983**, *52*, 242.
296. Chakarova, K.; Strauss, I.; Mihaylov, M.; Drenchev, N.; Hadjiivanov, K., Evolution of acid and basic sites in UiO-66 and UiO-66-NH2 metal-organic frameworks: FTIR study by probe molecules. *Microporous Mesoporous Mater.* **2019**, *281*, 110-122.
297. Boronat, M.; Corma, A., What Is Measured When Measuring Acidity in Zeolites with Probe Molecules? *ACS Catal.* **2019**, *9*, 1539-1548.
298. Bordiga, S.; Turnes Palomino, G.; Pazè, C.; Zecchina, A., Vibrational Spectroscopy of H_2, N_2, CO and NO Adsorbed on H, Li, Na, K-Exchanged Ferrierite. *Microporous Mesoporous Mater.* **2000**, *34*, 67-80.
299. Hadjiivanov, K., FTIR Study of CO and NH_3 Co-Adsorption on TiO_2 (Rutile). *Appl. Surf. Sci.* **1998**, *135*, 331-338.
300. Morterra, C.; Cerrato, G.; Di Ciero, S., IR Study of the Low Temperature Adsorption of CO on Tetragonal Zirconia and Sulfated Tetragonal Zirconia. *Appl. Surf. Sci.* **1998**, *126*, 107-128.
301. Ghosh, P.; Colon, Y. J.; Snurr, R. Q., Water Adsorption in UiO-66: The Importance of Defects. *Chem. Commun.* **2014**, *50*, 11329-11331.
302. Kandiah, M.; Usseglio, S.; Svelle, S.; Olsbye, U.; Lillerud, K. P.; Tilset, M., Post-Synthetic Modification of the Metal-Organic Framework Compound UiO-66. *J. Mater. Chem.* **2010**, *20*, 9848-9851.
303. Platero-Prats, A. E.; Mavrandonakis, A.; Gallington, L. C.; Liu, Y.; Hupp, J. T.; Farha, O. K.; Cramer, C. J.; Chapman, K. W., Structural Transitions of the Metal-Oxide Nodes within Metal–Organic Frameworks: On the Local Structures of NU-1000 and UiO-66. *J. Am. Chem. Soc.* **2016**, *138*, 4178-4185.